Operational Baseline and Structural Health Monitoring for the 2nd Avenue Network Arch Bridge

DECEMBER 31, 2025

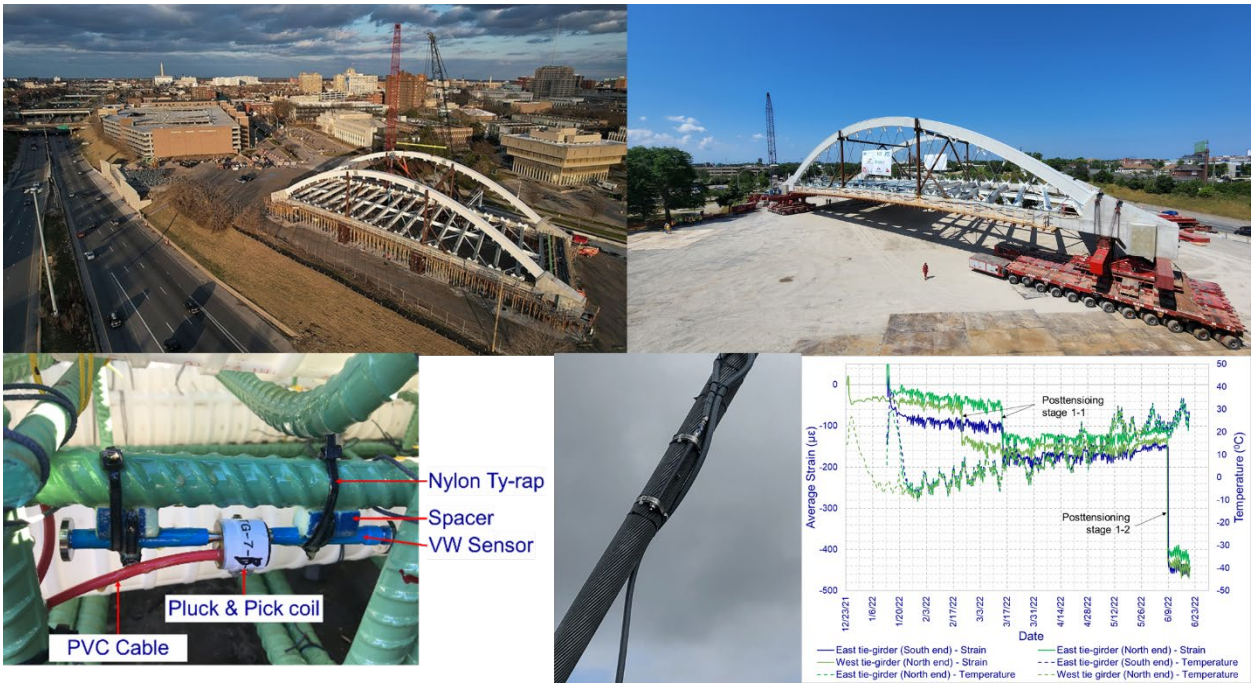

WESTERN MICHIGAN UNIVERSITY
Civil and Construction Engineering
Center of Excellence for Structural Durability

1. Report No. SPR-1762	**2. Government Accession No.** N/A	**3. Recipient's Catalog No.** N/A.
4. Title and Subtitle Operational Baseline and Structural Health Monitoring for the 2nd Avenue Network Arch Bridge		**5. Report Date** 12/31/2025
		6. Performing Organization Code N/A
7. Author(s) Upul Attanayake, Ph.D., P.E., Harsha Amunugama, M.Sc., and Kanchani Basnayake, Ph.D.		**8. Performing Org. Report No.** N/A
9. Performing Organization Name and Address Western Michigan University College of Engineering and Applied Sciences 1903 West Michigan Avenue Kalamazoo, Michigan 49008-5316		**10. Work Unit No.** N/A
		11. Contract or Grant No. Contract 2019-0313z8
12. Sponsoring Agency Name and Address Michigan Department of Transportation Research Administration 8885 Ricks Road P.O. Box 30049 Lansing, Michigan 48909		**13. Type of Report & Period Covered** Final Report 01/01/2022 – 12/31/2025
		14. Sponsoring Agency Code N/A

15. Supplementary Notes
Conducted in cooperation with the U.S. Department of Transportation, Federal Highway Administration. MDOT research reports are available at www.michigan.gov/mdotresearch.

16. Abstract
A unique network tied-arch bridge with free-standing arches was designed to carry 2nd Avenue traffic over Interstate (I-94) in Detroit, Michigan. This 245-ft-long, 96.5-ft-wide bridge, skewed at 18 degrees, is the first skewed, unbraced network arch bridge constructed in the United States. The superstructure frame was erected off-site at a bridge staging area and subsequently transported and placed over the I-94 freeway using self-propelled modular transporters and a lateral launching technique to complete construction. Based on observations from analytical models and discussions with the Engineer of Record (EOR), the peer review engineer, and the Michigan Department of Transportation (MDOT), an instrumentation system consisting of 112 vibrating wire sensors was designed to: (i) monitor strains in major structural components during construction to establish post-construction stress states; (ii) track strain changes during the service life to support bridge maintenance and load rating decisions; and (iii) collect sufficient data to verify key design assumptions. Of these sensors, 96 were embedded in the concrete during construction, and 16 were mounted on the hangers after erection of the arches and hangers. This instrumentation strategy enabled continuous monitoring of strains in the concrete frame and forces in the hangers, providing a clear understanding of the structural behavior throughout construction. The collection of a little more than two years of post-construction monitoring data provided valuable insight into the bridge's behavior under service conditions. Analysis of the monitoring data demonstrates that the structure is performing within established design limits, thereby increasing confidence in the implementation of innovative structural systems and complex construction methods that minimize traffic disruption and enhance safety. Load testing results indicate that the bridge exhibits minimal sensitivity to live loads, with seasonal temperature variations governing the stresses developed in the structure. A fully functional monitoring system, along with operational stress limits for each instrumented location, was delivered to MDOT. This system enables continuous, data-driven monitoring of the bridge, facilitating timely identification of maintenance, repair, and load rating needs over the long term without reliance solely on traditional visual inspection methods.

17. Key Words Accelerated bridge construction, concrete, load testing, network arch, post-tension, self-propelled modular transporter, structural health monitoring	**18. Distribution Statement** No restrictions. This document is available to the public through the Michigan Department of Transportation.

19. Security Classif. (of this report) Unclassified	**20. Security Classif. (of this page)** Unclassified	**21. No. of Pages** 172 (w/o appendices)	**22. Price** N/A

Operational Baseline and Structural Health Monitoring for the 2nd Avenue Network Arch Bridge

Final Report
(2022 - 2025)

Project Manager: Purushotham Pakala, Ph.D., P.E.

Submitted to:

Submitted by:

Upul Attanayake, Ph.D., P.E.
Professor and Director
Center of Excellence for Structural Durability
(269) 276 – 3217
upul.attanayake@wmich.edu

Harsha Amunugama, M.Sc.
Graduate Research Assistant
Center of Excellence for Structural Durability
(269) 276 – 3210
a.amunugama@wmich.edu

Kanchani Basnayake, Ph.D.
Engineer II
Parsons Corporation, East Hartford, CT
(269) 548 – 6198
kanchani.basnayake@parsons.com

WESTERN MICHIGAN UNIVERSITY
Civil and Construction Engineering
Center of Excellence for
Structural Durability

DISCLAIMER

"This publication is disseminated in the interest of information exchange. The Michigan Department of Transportation (hereinafter referred to as MDOT) expressly disclaims any liability, of any kind, or for any reason, that might otherwise arise out of any use of this publication or the information or data provided in the publication. MDOT further disclaims any responsibility for typographical errors or accuracy of the information provided or contained within this information. MDOT makes no warranties or representations whatsoever regarding the quality, content, completeness, suitability, adequacy, sequence, accuracy or timeliness of the information and data provided, or that the contents represent standards, specifications, or regulations."

"This material is based upon work supported by the Federal Highway Administration under SPR OR22-008. Any opinions, findings and conclusions or recommendations expressed in this publication are those of the author(s) and do not necessarily reflect the views of the Federal Highway Administration."

ACKNOWLEDGEMENTS

This research was funded by the Michigan Department of Transportation (MDOT). The authors gratefully acknowledge Mr. Bradley M. Wagner for initiating this research and Dr. Purushotham Pakala for coordinating and managing the project to its successful conclusion.

The authors wish to thank the Research Advisory Panel (RAP) members for their continuing guidance and contributions throughout the study. The project benefited significantly from the expertise and collaboration of John A. Belcher (MDOT); Mike LaViolette and Matt Longfield (HDR, Inc.); Christopher Bradshaw and Charles Esmacher (HNTB Corporation); Luke Cinader (OHM Advisors); and Blake Zapczynski and Pat Sullivan (Z Contractors, Inc.). The authors also acknowledge with gratitude the late Victor Judnic (HNTB Corporation), whose contributions to this project are remembered with appreciation.

Graduate students Sanjoy Bhowmik and Srikanth Vemula, and undergraduate students Naveen Ranasinghe and Uresh Wijesinghe, contributed substantially to the bridge instrumentation, monitoring, and experimental activities. Dr. Danush Wijekularathna's contribution to this study as the statistical consultant is greatly appreciated. Finally, the authors express their sincere appreciation to Professor Haluk Aktan for his support and guidance throughout the project.

EXECUTIVE SUMMARY

This research project investigated the structural performance of the 2nd Avenue Bridge in Detroit, Michigan - the first skewed, unbraced network tied-arch bridge in the United States. The 245-ft long, 96.5-ft wide bridge features an 18-degree skew and was constructed using accelerated bridge construction (ABC) techniques, including off-site fabrication at a bridge staging area (BSA) and installation via self-propelled modular transporters (SPMTs) and lateral launching. This approach enabled the completion of construction with minimal disruptions to I-94 traffic and improved safety.

Given the unique structural configuration of the bridge, the use of innovative construction techniques, and differences observed in structural responses predicted by three independent finite element models, this project was initiated to: (i) evaluate structural performance during construction using field data collected, (ii) conduct load testing to establish an operational baseline, (iii) characterize structural response under intrinsic and live loads, (iv) evaluate performance during seasonal temperature variations, and (v) identify instrumentation output envelopes within which the structure should be maintained.

Based on observations from the three independent finite element models and subsequent discussions with the Michigan Department of Transportation (MDOT), the Engineer of Record (EOR), and the peer reviewer, an instrumentation system was designed and installed on the bridge. The system consists of 96 vibrating wire (VW) strain sensors and 16 VW strandmeters to monitor strains and temperature.

During tie girder fabrication, specimens were prepared to evaluate compressive strength, modulus of elasticity (MOE), shrinkage, and creep of the project-specific concrete mix, which had a water-to-cement ratio of 0.3 and contained 47% slag and 20% Class F fly ash. This mix was used for the tie girders, knuckles, and end diaphragms. Although the design compressive strength was 8,000 psi, measured compressive strengths ranged from 11,823 psi to 15,113 psi.

The CEB-FIP 2010 model was identified as the most suitable for representing shrinkage behavior in this structure. Because the tie girders remained independent during initial post-tensioning, elastic shortening due to post-tensioning was used to calculate their effective MOE. The effective MOE values were compared with those obtained from cylinder testing. The results indicate that

the MOE of these concrete elements continued to increase for more than 150 days, consistent with the behavior of concrete mixes containing high proportions of supplementary cementitious materials.

Approximately two years of data were collected from the complete bridge, from September 28, 2023, to December 2, 2025. Both temperature and strain exhibit a periodic pattern resembling a sinusoidal function with a phase shift. Except for one sensor at the northwest knuckle and another at the tapered section of the west tie girder, all other sensors are functioning correctly and recording data indicating that the bridge behavior remains within the design limits.

A diagnostic static load test was conducted on August 7, 2024, ten months after the bridge opened to traffic, to verify analytical design assumptions and assess the bridge's real-time structural response under controlled loads. Eight tandem trucks, totaling approximately 416 kips (i.e., 50% of the HL-93 Mod design load), were arranged in six configurations to maximize strain at selected instrumented sections along the tie girders, end diaphragms, and hangers. The measured strain variations in concrete components were minimal, with a maximum of approximately 20 με, indicating the bridge's remarkable rigidity and minimal sensitivity to live loads.

Field data from VW strain sensors installed within a tapered section connecting the knuckle and the tie girder indicated that some areas of the cross-section were not compressed as anticipated during design. Although this does not compromise structural performance, it underscores the need for a refined finite element analysis that accounts for all local constraints and geometric irregularities to optimize the post-tension duct configuration and improve stress distribution in future designs. The modeling simplifications in LARSA 4D, particularly the representation of geometry, tendon grouting, and time-dependent behavior, did not significantly affect the predictions of stress changes along the tie girders. However, they limit the model’s ability to capture localized stresses in the knuckles. In contrast, the Abaqus model, with its detailed staged construction representation and three-dimensional mesh refinement, more accurately simulates the knuckle and tapered-section responses, as well as the influence of tendon profiles and grouting sequence on local stresses.

Overall, the LARSA 4D model remains a valuable tool for simulating global bridge response and construction sequencing. Still, the Abaqus model provides a more reliable framework for

assessing stress redistribution, time-dependent effects, and the behavior of geometrically complex structural elements.

The stress developed in the superstructure concrete frame during each construction activity was calculated from the change in strain recorded during that activity and the corresponding modulus of elasticity. The stress values obtained from the analysis are lower than the additional stresses required to reach the tensile and compressive stress limits while the bridge is in service. Therefore, even in the presence of temperature fluctuations, the structure remains safe as long as it exhibits strain patterns similar to those recorded over the past two years. If the strain variation deviates from the recorded patterns and exceeds the calculated maximum and minimum stresses, the causes of these changes and the strain patterns should be evaluated until damage signatures are developed and implemented in a future study to automate the monitoring process.

The 2nd Avenue Bridge represents a significant achievement in American bridge engineering - successfully demonstrating that complex network arch bridges can be constructed using accelerated techniques while incorporating comprehensive monitoring for long-term performance assessment. The knowledge gained from this project will inform future generations of innovative bridge designs and construction practices. Continued monitoring and analysis of this structure will yield insights valuable to the bridge engineering community for decades to come.

TABLE OF CONTENTS

LIST OF TABLES

LIST OF FIGURES

1 INTRODUCTION

1.1 OVERVIEW

The network arch bridge concept was first developed by Norwegian engineer Per Tveit in the late 1950s. A typical network arch bridge consists of two arch elements and a network of intersecting hangers, emulating a truss. A majority of bridges built worldwide include transverse/portal bracing between the arches and are called *braced network tied-arch bridges*. A unique bridge with free-standing arches was designed and constructed as a design-bid-build project to carry the 2nd Avenue traffic over the interstate (I) 94 in Detroit, Michigan, USA (Figure 1-1). This 245 ft long, 96.5 ft wide, and 18-degree skew bridge is the first skewed, unbraced, network arch bridge in the United States. The bridge was opened to traffic on December 22, 2022, but the project was completed on October 27, 2023.

Figure 1-1. The 2nd Avenue Bridge in Detroit, MI.

Figure 1-2 shows the structural elements of the bridge superstructure frame, including concrete knuckles (i.e., upper and lower knuckles), post-tensioned (PT) concrete tie girders, PT concrete end diaphragms, steel arch ribs, hangers, steel floorbeams, intermediate diaphragms, and lateral bracings. Two arches are connected to the PT frame, consisting of two tie girders and end diaphragms. The arches are held in-plane by concrete knuckles at each corner of the PT frame. Thirty (30) inclined hangers connect each arch rib to the respective tie girder, creating the network arch. A unique concrete mix with a water-to-cement ratio (w/c) of 0.3 and a high dose of supplementary cementitious materials (SCMs) (i.e., 47% slag and 20% Class F fly ash) is used for tie girders, knuckles, and end diaphragms.

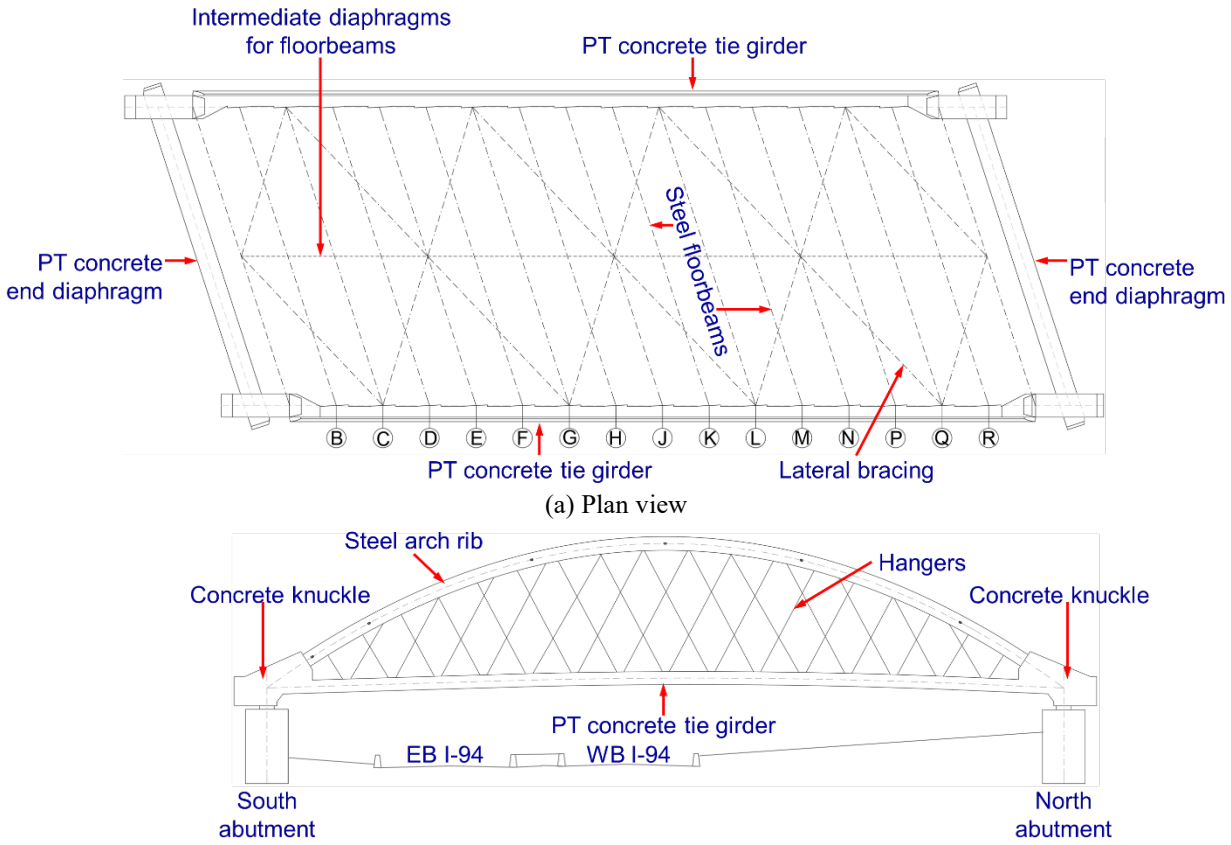

Figure 1-2. The plan and elevation views showing the major structural elements.

The frame of the superstructure was erected off-site at a bridge staging area (BSA) and then moved and placed over the I-94 freeway using self-propelled modular transporters (SPMTs) and the lateral launching technique, a combination of accelerated bridge construction (ABC) techniques, to complete the superstructure (Figure 1-3). Since the final alignment of the bridge is parallel to the north-south direction, PT tie girders are located on the east and west sides of the bridge. Please note that the bridge elements are labeled according to their position at the final alignment of the bridge over the freeway. For example, tie girders on the east and west sides of the bridge at the final alignment over the freeway are labeled as east and west tie girders even though they were on the south and north sides of the bridge at the BSA, as shown in Figure 1-3.

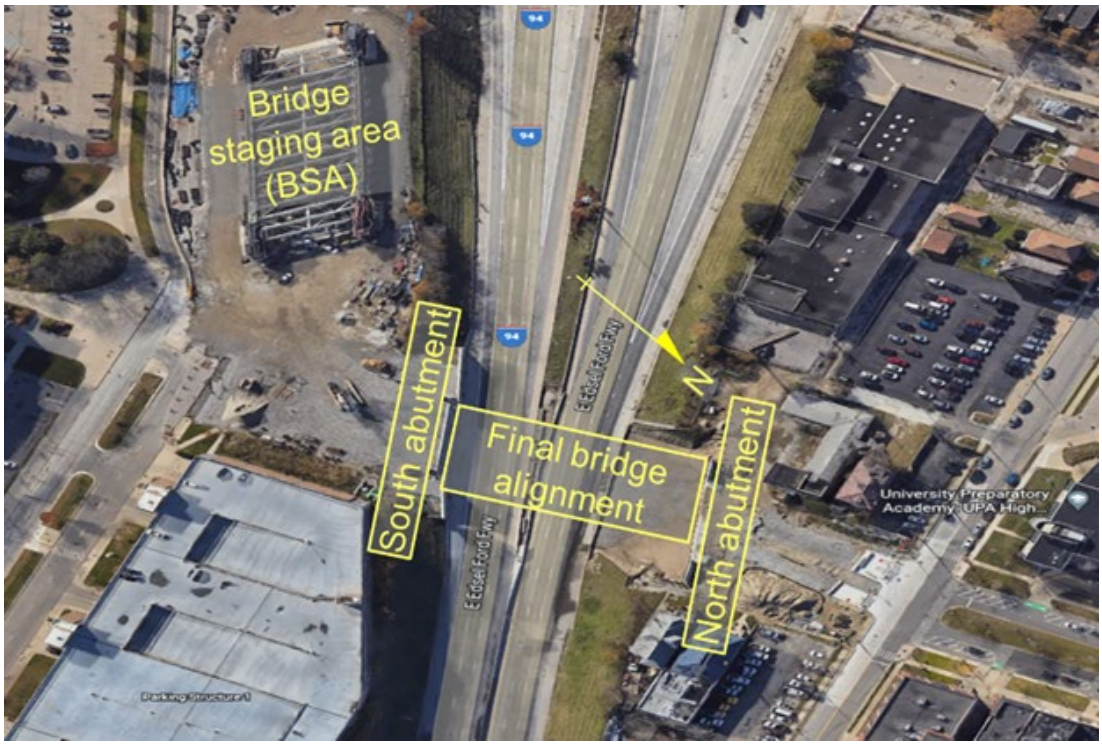

Figure 1-3. Aerial view of the bridge construction site.

Due to the complexity of the bridge construction procedure, three independent finite element models were developed by the Engineer of Record (EOR), the contractor's consultant, and a peer review engineer to evaluate stress, deflection, and the potential for arch rib buckling under each load case. Although some variations were observed between the results from the three models due to the modeling assumptions implemented in each, none of the load cases exceeded the design limits in any of the models. A consensus among the parties was reached, and any variations between models were documented in the project file before starting construction. Based on the observations from the above-mentioned finite element models and the subsequent discussions with MDOT, the EOR, and the peer reviewer, an instrumentation system was designed and installed in the 2nd Avenue bridge to (i) monitor and record strains in major structural elements during construction to determine the state of stress after construction, (ii) monitor and record the change in strains during service life to support bridge maintenance and load rating decisions, and (iii) collect adequate data to verify design assumptions.

Given the bridge's unique structural configuration, the implementation of accelerated bridge construction techniques (such as SPMTs and lateral launching), and the observed differences in structural responses among three independent finite element models, a research project was initiated to achieve the objectives listed in the following section.

1.2 OBJECTIVES AND TASKS

The objectives of this project are to: (i) evaluate structural performance during construction from the data acquired during construction, (ii) conduct load testing to establish an operational baseline for the structure, (iii) establish structural response under intrinsic and live loads, (iv) evaluate the performance of the structure during seasonal changes, and (v) identify instrumentation output envelopes within which the structure needs to be maintained.

The following tasks were completed to accomplish the objectives:

1. Develop an understanding of the structure by studying as-built drawings and making measurements.
2. Evaluate the performance of instrumentation.
3. Evaluate the data collected during construction.
4. Collect data from instruments for two years.
5. Store and evaluate seasonal trends in data.
6. Conduct load testing to establish an operational baseline for the structure.
7. Develop a refined finite element model of the bridge and calibrate it using load test data. Additionally, compare the assumptions of the research model with those of the EOR model.
8. Identify output envelopes from the measured data within which the structure can be maintained.
9. Develop a long-term data acquisition plan and transfer responsibility to MDOT for long-term monitoring of the structure.

1.3 REPORT ORGANIZATION

This report is organized into 10 chapters.

Chapter 1 includes the introduction and research project objectives and tasks.

Chapter 2 provides a state-of-the-art and practice review related to network-arch bridge design and construction, creep and shrinkage behavior of concrete with high doses of SCMs, and structural modeling and analysis.

Chapter 3 describes the construction activities, including the erection sequence, post-tensioning, bridge move, and placement on permanent bearings.

Chapter 4 details the instrumentation system, including the selection of monitoring locations, sensors, sensor configurations, and installation. Additionally, this chapter also describes the thermal control plan used to monitor and control curing temperature.

Chapter 5 documents the behavior of the structure during construction, focusing on strain development, elastic shortening, and time-dependent effects such as creep and shrinkage in post-tensioned elements.

Chapter 6 presents the response of the completed structure to seasonal temperature variations, analyzing two years of field-recorded data to establish correlations between temperature and strain behavior.

Chapter 7 explains the development of the finite element models in both LARSA 4D and Abaqus, outlining key modeling assumptions, material properties, and time-dependent behavior.

Chapter 8 describes load testing procedures, truck configurations, the design of truckload configurations for load testing, the load testing procedure, observations, and the analysis results.

Chapter 9 defines the operational limits of the structure, establishing stresses at the end of construction, compressive and tensile stress limits, and the change in stress due to thermal expansion and contraction using both analytical and measured results.

Chapter 10 presents the summary, conclusions, and recommendations, highlighting the principal findings, verification of design assumptions, establishment of operational baselines, and guidance for continued structural-health monitoring and future implementations.

2 STATE-OF-THE-ART AND PRACTICE

2.1 OVERVIEW

This chapter describes the behavior of tied network arch bridges, post-tensioning losses, creep and shrinkage behavior of concrete with high doses of SCMs, structural modeling of post-tensioned members, and finite element modeling practices.

2.2 NETWORK ARCH BRIDGES

Octavius F. Nielsen, a Norwegian engineer, introduced the concept of inclined hangers, replacing the conventional vertical hangers used for arch bridges (Per Tveit 2006, 2009). Nielsen patented the idea of arch bridges with inclined hangers in 1926. The bridges built as Nielsen bridges had a V-configuration for hangers. During the late 1950s, Dr. Per Tveit introduced the concept of inclined hangers with multiple crossings (network of hangers) on the plane of the arch. In 1963, the first two network arch bridges, the Steinkjer Bridge (spanning 262 ft) and the Bolstadstraumen Bridge (spanning 276 ft), were constructed. Both were designed by Dr. Per Tveit and built in Norway (Per Tveit 2006, 2009). The concept inspired several other network arches around the world with larger spans. The Fehrmrnsund bridge, built in Germany in 1963, has a span of 813 ft. The Blennerhassett Bridge, the first network arch in the US, has a span of 879 ft. The Brandanger bridge, built in Norway in 2010 with a span of 722 ft, is recorded as the world's slenderest arch bridge (Mato et al. 2011 and Varennes 2011).

A network arch bridge is classified as braced or unbraced. In a braced network arch bridge, the two arches are connected by lateral bracings to transmit lateral forces. The unbraced network arch bridge has two freestanding arches. Based on the available records, only four freestanding network arch bridges have been constructed in the US by the end of 2023. They are the Hastings bridge spanning over the Mississippi river in Hastings, Minnesota (Gastoni and Buckholdt 2014), the West 7th Street bridge spanning over the Clear Fork of the Trinity River in Fort Worth, Texas (Yousefpour et al. 2015), and the Ribbon of Light bridge over Los Angeles river in Los Angeles, California (sixthstreetviaduct.org n.d.), and the 2nd Avenue Bridge over I-94 freeway in Detroit, Michigan (Figure 1-1 and Figure 2-1).

(a) Hastings Bridge (Gastoni and Buckholdt 2014)

(b) West 7th Street Bridge (Sundt Construction 2023)

(c) Ribbon of Light Bridge (sixthstreetviaduct.org n.d.)

Figure 2-1. Three of the four unbraced network arch bridges in the US as of December 2023.

Figure 2-1a shows the Hastings bridge in Minnesota. In the Hastings bridge, the main span is 545 ft long, and the maximum height of the arch ribs is 94 ft. The steel box arch ribs are held in place by PT concrete knuckles and tie girders. The main span, comprising of arch ribs, floor beams, stringers, and temporary tie girders (made of steel), was erected on land and then transported on SPMTs to a flotilla of barges, where it was positioned in its final position over the river. Construction of the bridge began in August 2010 and was completed in June 2014. Figure 2-1b shows the West 7th Street bridge in Texas. This bridge replaced the original West 7th Street bridge in Fort Worth and is the world's first precast concrete network arch bridge. There are 12 precast and post-tensioned concrete arches, 102 precast floor beams, and 77, 499 ft^2 of stay-in-place deck panels (PCI 2023). The arch span is 163.5 ft, and the arch height is 24 ft. The 12 concrete arches were constructed off-site and transported to the site using SPMTs. The bridge construction began in January 2012 (off-site construction) and was completed in October 2013 (Yousefpour et al. 2015, Sundt Construction 2023). Figure 2-1c shows the Ribbon of Light bridge in California. This bridge replaced the Sixth Street Viaduct in Los Angeles. There are 10 pairs of canted concrete arches. The typical arch span is 300 ft, and arch heights vary as 60 ft (2 pairs), 40 ft (1 pair), and

30 ft (7 pairs). Each arch has a 9-degree outward cant. The bridge construction began in February 2015 and was completed in July 2022 (sixthstreetviaduct.org, n.d.).

2.3 TIED ARCH BRIDGE BEHAVIOR

A typical tied arch bridge consists of two arch ribs, tie girders, hangers, and a deck system. Uniform vertical loading on the deck is transferred to the arches through the hangers. This creates compression in the arches and is resisted by the tension in the tie girders. As a result, only the vertical reactions are transmitted to the foundation (Hall and Lawin 1985, Per Tveit 2006, Per Tveit 2009, and Mato et al. 2011). The typical structural response of a tied network arch bridge is shown in Figure 2-2. Because of the tie in tension and the arch in compression, this bridge is also called a bowstring bridge (da Costa 2013).

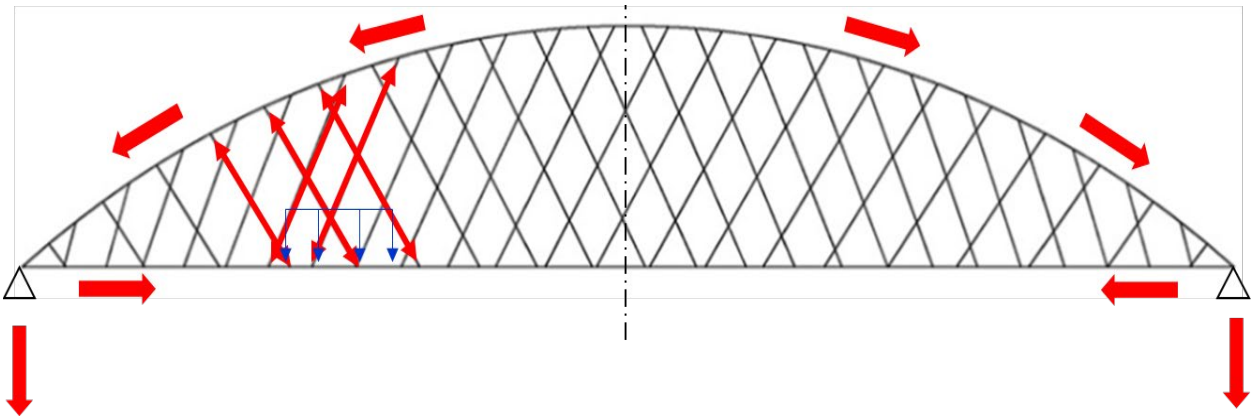

Figure 2-2. Typical response of a tied network arch bridge under uniform deck loading.

The structural response depends on the arrangement of the hangers (i.e., vertical or inclined) and vertical loading on the deck. Figure 2-3 shows the behavior of tied arch bridges with vertical hangers and a network of hangers under a nonsymmetric loading. As shown in the figure, the upper and lower chords of the tied arch bridge with vertical hangers deflect, resulting in larger moments in the arches and tie girders. But in a tied arch bridge with a network of hangers, the inclined hangers restrict these deflections, resulting in a minimal bending in the arch and tie girders (Per Tveit 2006, Per Tveit 2009, and Mato et al. 2011). The behavior of a network arch bridge is analogous to that of a simply supported beam; the arch, hangers, and the tie girder serve as the compression flange, the web, and the tension flange, respectively. Hence, most of the vertical shear forces are resisted by the vertical components of the compressive force in the arch, while the hangers carry the rest (Brunn and Schanack 2003).

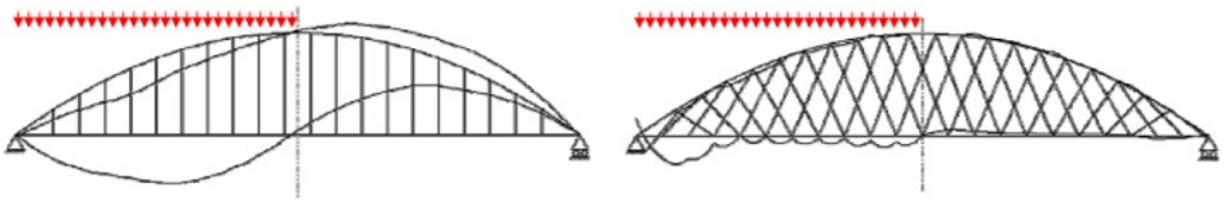

Figure 2-3. Bending moment comparison under uniform loading (Mato et al. 2011).

2.4 POST-TENSIONED (PT) MEMBERS IN NETWORK ARCH BRIDGES

The earliest network arch bridges with shorter spans used steel tie girders. To increase the efficiency of the network arch and accommodate longer spans, post-tensioned (PT) concrete tie girders are introduced. The PT tendons are kept bonded or unbonded with the surrounding concrete after being stressed. The tendons are bonded to the surrounding concrete by grouting the ducts. The unbonded tendons are generally coated with a grease containing corrosion inhibitors and are wrapped or encased in plastic. In bonded tendons, complete strain compatibility exists between the tendon and the concrete once the ducts are grouted (ACI 2016).

2.4.1 Stress Distribution in a PT Member

Figure 2-4 shows the stress distribution about the x-x axis for an eccentrically post-tensioned beam. The stress at any point in the cross-section (σ_{PT}) subjected to an eccentrically applied force, P, is calculated using Eq. 2-1.

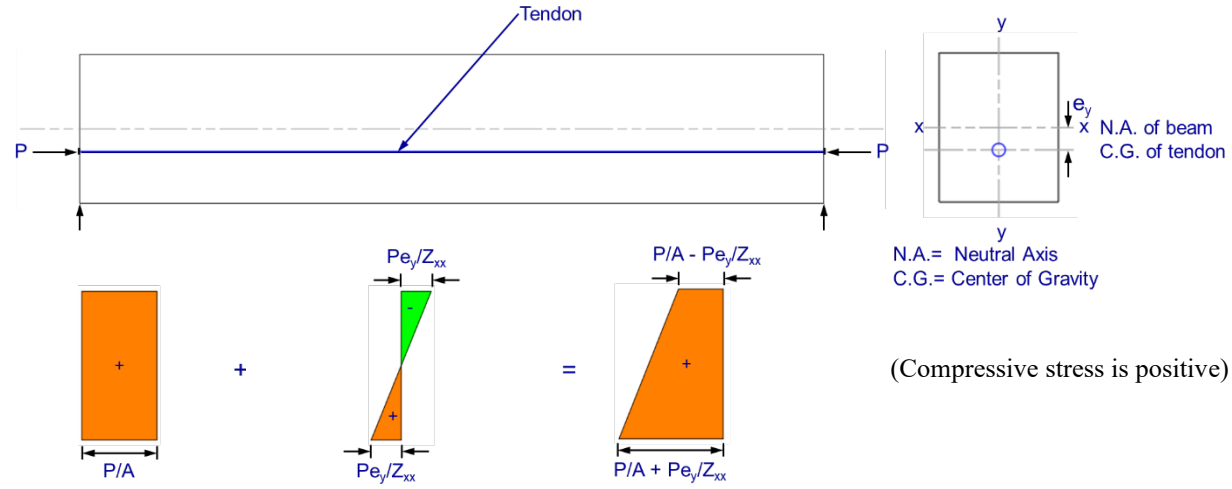

Figure 2-4. Stresses in a PT concrete beam.

$$\sigma_{PT} = \frac{P}{A} \pm \frac{Pe_y}{Z_{xx}}$$ Eq. 2-1

where,

A = beam cross-sectional area

e_y = eccentricity of the post-tensioning force along y-y axis

P = post-tensioning force

Z_{xx} = section modulus of the beam section about x-x axis

When a beam is post-tensioned eccentrically about both x-x and y-y axes, stress at any point in the cross-section is calculated using Eq. 2-2.

$$\sigma_{PT} = \frac{P}{A} \pm \frac{Pe_y}{Z_{xx}} \pm \frac{Pe_x}{Z_{yy}}$$ Eq. 2-2

where,

e_x = eccentricity of the post-tensioning force along x-x axis

Z_{yy} = section modulus of the beam section about y-y axis

The post-tensioning force in Eq. 2-1 and Eq. 2-2 is the effective post-tension after accounting for all the losses. Therefore, an accurate estimation of the prestress losses is necessary to evaluate the state of stress in PT members.

2.4.2 Losses in PT Members

Immediate losses (short-term losses) and time-dependent losses (long-term losses) are the two types of losses in PT members. Immediate losses occur between the time of tendon stressing and the time when force is transferred to the concrete at the anchorage. Friction between the tendon and the duct, anchorage set, and elastic shortening of the concrete member contribute to the immediate losses. The elastic shortening loss is zero if all the tendons are simultaneously stressed. When the tendons are sequentially stressed, the stresses in the already stressed tendons decrease due to elastic shortening as a result of the stressing of the subsequent tendons. Time-dependent losses occur throughout the service life of a concrete member and begin immediately after post-tensioning is applied. Concrete creep, concrete shrinkage, and steel relaxation contribute to time-dependent losses (PTI 2006). The total losses in PT members (Δf_{PT}) are calculated using Eq. 2-3.

$$\Delta f_{PT} = (\Delta f_{pF} + \Delta f_{pA}) + \Delta f_{pES} + (\Delta f_{pRE} + \Delta f_{pSH} + \Delta f_{pCR}) \quad \text{Eq. 2-3}$$

where,

Δf_{pA} = anchorage set losses

Δf_{pCR} = concrete creep losses

Δf_{pES} = elastic shortening losses

Δf_{pF} = friction losses

Δf_{pRE} = steel relaxation losses

Δf_{pSH} = concrete shrinkage losses

Figure 2-5 shows a typical variation of tendon stress in a PT member over time. A jacking stress of about 80% of the ultimate strength of the tendons (f_{pu}) is applied to the tendon. The tendon stress is reduced by about 10% of f_{pu} due to the combined effects of friction, anchorage set, and partial elastic shortening during the jacking and anchoring operations. Partial elastic shortening is due to the stress applied to subsequent tendons after the tendon under consideration is stressed and anchored. Over time, tendon stress is further reduced due to the combined effects of concrete shrinkage, concrete creep, and steel relaxation, resulting in an effective prestress (f_{pe}) of about 55% of f_{pu}. It should be noted that the stress values indicated in Figure 2-5 are approximate and do not represent all scenarios.

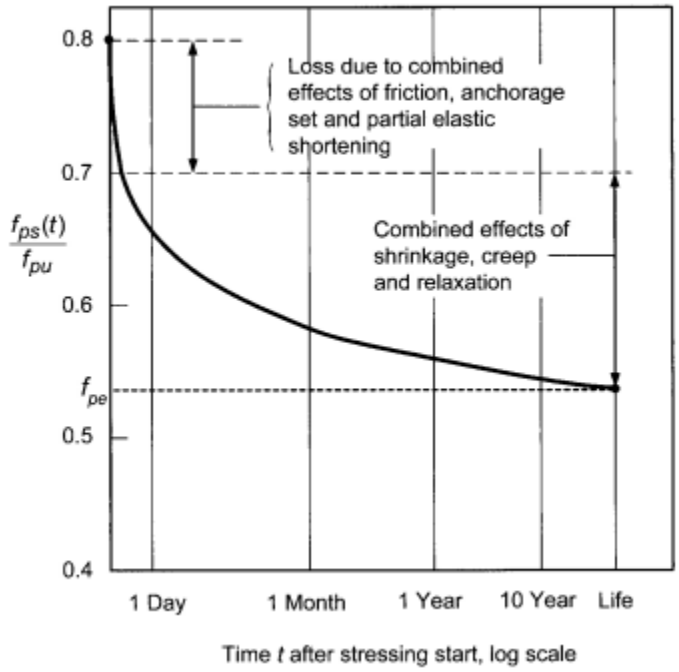

Figure 2-5. Typical variation of post-tension tendon stress with time (Naaman 2012).

The time-dependent losses and elastic shortening losses are estimated using approximate or refined methods. A lump sum estimate of the total time-dependent prestress losses is used in the approximate method. Typically, two approaches are followed for the refined methods. The first approach is to calculate the lump-sum value for each time-dependent prestress loss, then compute the cumulative effects to determine the total time-dependent loss. The second approach is to use the time-step method to accurately estimate each time-dependent prestress loss, accounting for the continuous change in stress within the system (ACI 2016). Compared with the approximate methods, the refined methods require a more extensive list of input information. The approximate lump-sum estimates of total prestress losses and the refined lump-sum estimates of individual prestress losses are commonly used in the design of structures. However, the time-step method is recommended for evaluating losses at each construction stage for special structures that require an accurate assessment of prestress losses, or for structures involving multiple construction stages or multiple prestressing stages (AASHTO 2020). For example, the implementation of the time-step method is required for the 2nd Avenue bridge because the bridge construction included multiple construction and post-tensioning stages.

2.4.3 Experimental Validation of Immediate Prestress Losses in PT Members

The majority of studies have evaluated the losses in PT tendons over time. Limited experimental studies have assessed the spatial variation of stress in PT tendons. Most of these experimental studies were relatively recent and used strands with sensors along the tendon length (Zhou et al. 2009, Cho et al. 2017, Tong et al. 2018, Kim et al. 2019, and Kim et al. 2022). A study by Cho et al. (2017) and Kim et al. (2022) investigated the losses during stressing and at transfer in a 65 ft (20 m) long full-scale PT beam (Figure 2-6a). The full-scale specimen had three smart prestressing tendons: Tendon #1 (curved), Tendon #2 (curved), and Tendon #3 (straight). The tendons were stressed from the left end in the order of Tendon #1, Tendon #2, and Tendon #3. The jacking force applied to each tendon was 40.5 kips (180 kN). Fiber optic sensors (FBG type) were embedded at various locations along the smart strands to measure strain (Figure 2-6b).

Figure 2-6c shows the measured strain in Tendon #1, when Tendon #1, Tendon #2, and Tendon #3 were stressed. At the end of stressing, the strain in Tendon #1 at the dead end is about 8.5% less than that at the stressed end. At the end of anchoring, the strain in Tendon #1 at the stressed end is reduced by about 10.9%. The elastic shortening losses in Tendon #1 varied from 50 - 150

με due to the stressing of Tendon #2. The elastic shortening losses in Tendon #1 ranged from 0 - 150 με due to the stressing of Tendon #3. Figure 2-6d shows the measured strain in Tendon #2, when Tendon #2 and Tendon #3 were stressed. At the end of stressing, the strain in Tendon #2 at the dead end is about 8.5% less than that at the stressed end. At the end of anchoring, the strain in Tendon #2 at the stressed end is reduced by about 10.9%. The elastic shortening losses in Tendon #2 vary from 100 - 230 με due to the stressing of Tendon #3. Figure 2-6e shows the measured strain in Tendon #3 when Tendon #3 was stressed and anchored. At the end of stressing, the strain in Tendon #3 at the dead end is about 2.9% less than that at the stressed end. At the end of anchoring, the strain in Tendon #3 at the stressed end is reduced by about 4.5%. The measured strains in Tendon #1 and Tendon #2 follow the theoretical strain behavior predicted for a tendon after friction and anchorage set losses.

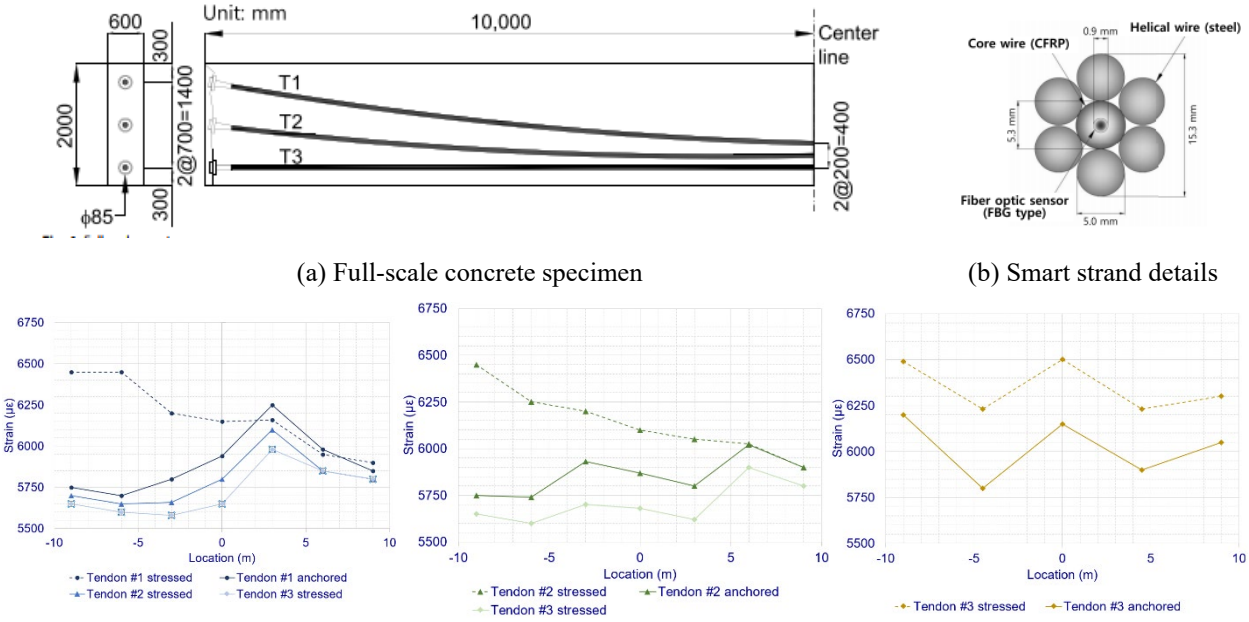

(a) Full-scale concrete specimen (b) Smart strand details

(c) Measured strain in Tendon #1 (d) Measured strain in Tendon #2 (e) Measured strain in Tendon #3

Figure 2-6. Tendon strain variation along the span during stressing and after anchoring (Cho et al. 2017 and Kim et al. 2022).

Figure 2-7 shows the comparison of the measured and calculated prestress force in Tendon #1. The prestress force in Tendon #1 reduces from 40.5 kips (180 kN) (jacking force) at the stressing end to about 35.3 kips (157 kN) at the dead end, after stressing. After anchoring, the jacking force of 40.5 kips (180 kN) is reduced to approximately 33.7 kips (150 kN) at the stressed end, indicating a loss in prestressing force at the stressing end due to the anchorage set of about 3.7 kips (16 kN). The maximum force in the tendon after accounting for friction losses and anchorage is

approximately 36.4 kips (162 kN), which is recorded at a distance of about 42.65 ft (13 m) from the stressed end. This maximum force in the tendon, after accounting for friction losses and anchorage set, is further reduced to approximately 35.7 kips (159 kN) due to elastic shortening. As shown in Figure 2-7, the measured prestress force does not precisely match the calculated force, possibly due to local wobble effects and entanglement of strands during construction and jacking operations (Kim et al. 2022).

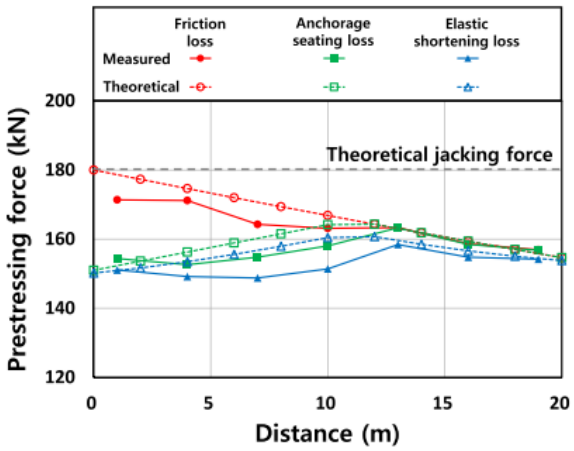

Figure 2-7. Measured and calculated tendon forces after accounting for the losses (Kim et al. 2022).

Kim et al. (2022) measured the variation in strand forces in a 197 ft (60 m) long concrete girder during post-tensioning. Figure 2-8a shows the strand arrangement. There were five strands: one smart strand and four regular strands. The smart strand is the top-most strand highlighted in Figure 2-8a. The strands were stressed from both ends. The smart strand was stressed before all the other strands. Seven Fiber Bragg grating sensors (FBG 1 to FBG 7) were installed along the smart strand (Figure 2-8b). Figure 2-8c shows the comparison of the measured and calculated force in the smart strand. The elastic shortening loss in the smart strand is due to the stressing of the four regular strands. As shown in Figure 2-8c, an exact symmetry in the prestress force distribution was not observed as predicted by the theoretical equations for a strand stressed from both ends. However, the current design equations for calculating prestress losses during stressing and transfer appear viable in the design of actual structures (Kim et al., 2022).

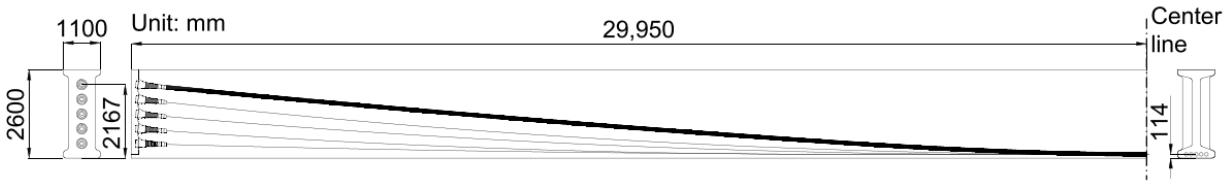

(a) Tendon arrangement of prestressed concrete bridge girder

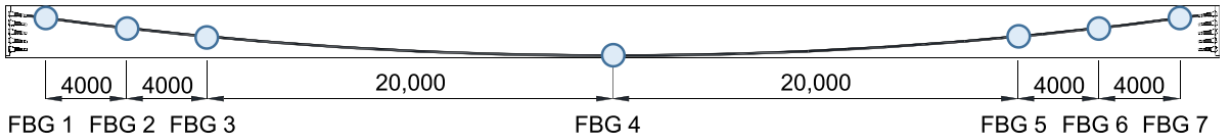

(b) Fiber Bragg gratings (FBG) sensor arrangement in the smart strand

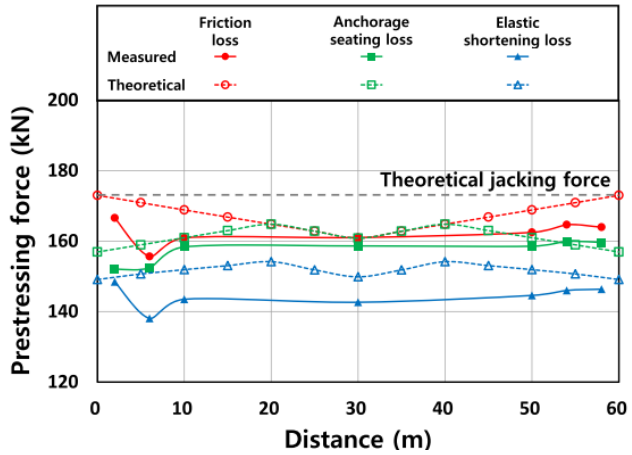

(c) Calculated and measured prestress force

Figure 2-8. Comparison of calculated and measured prestress force using a smart strand embedded in a prestressed concrete bridge girder (Kim et al. 2022).

2.4.4 Time-Dependent Prestress Losses

Creep is the volume change in concrete under a constant applied stress (ACI 2005). The volume change due to creep can be several times larger than the initial elastic strain caused by loading (Neville 1996). According to AASHTO (2020), depending on concrete maturity, creep shortening can be 0.4 to 0.5 times the initial elastic shortening under permanent loads. There are two types of creep: basic creep and drying creep. Basic creep results from crystalline flow in aggregates and hardened cement paste, plastic flow in cement paste, and the closure of internal voids. Drying creep is caused by moisture migration during drying. Therefore, basic creep depends on the viscoelastic properties of the concrete, while drying creep depends on both environmental exposure and component size (Gilbert and Ranzi 2011).

Creep is described in terms of the creep coefficient $\varphi(t,t_0)$ or the compliance function $J(t,t_0)$. The creep coefficient is the ratio of the time-dependent creep strain to the instantaneous elastic strain.

The compliance function represents the total strain as a function of time under unit stress (ACI 2008b). The relationship between the creep coefficient and the compliance function is given by Eq. 2-4.

$$J(t, t_0) = \frac{1+\varphi(t,t_0)}{E_c(t_0)} \qquad \text{Eq. 2-4}$$

where $E_c(t_0)$ is the concrete elastic modulus at the time of loading (t_0). The effect of concrete age on the creep strain is accounted for by both the creep coefficient, $\varphi(t,t_0)$, and the elastic modulus, $E_c(t_0)$.

For a concrete member subjected to a time-varying stress history, the principle of superposition is applied to find the resulting strain/deformation (Bažant 1988). For example, Figure 2-9 shows the creep and elastic deformations of a concrete member subjected to a stress history with two stress increments: $\Delta\sigma_c(\tau_0)$ and $\Delta\sigma_c(\tau_1)$ (Figure 2-9a). Figure 2-9b shows the creep coefficient, $\varphi(t, \tau)$, for each stress increment. Figure 2-9c shows the creep compliance function, $J(t, \tau)$, for each stress increment. The creep coefficient and the compliance function due to the stress increment $\Delta\sigma_c(\tau_0)$ occurring at time τ_0 are denoted as $\varphi(t, \tau_0)$ and $J(t, \tau_0)$, respectively. The creep coefficient and the compliance function due to the stress increment $\Delta\sigma_c(\tau_1)$ occurring at time τ_1 are denoted as $\varphi(t, \tau_1)$ and $J(t, \tau_1)$, respectively. Figure 2-9d shows the total elastic and creep strains in the structure using the principle of superposition. Figure 2-9e shows the total creep strain in the structure. The modulus of elasticity of concrete at time τ_0 and τ_1 is $E_c(\tau_0)$ and $E_c(\tau_1)$, respectively. The resulting creep strain curve due to the stress history is the sum of the creep curves produced by each stress increment.

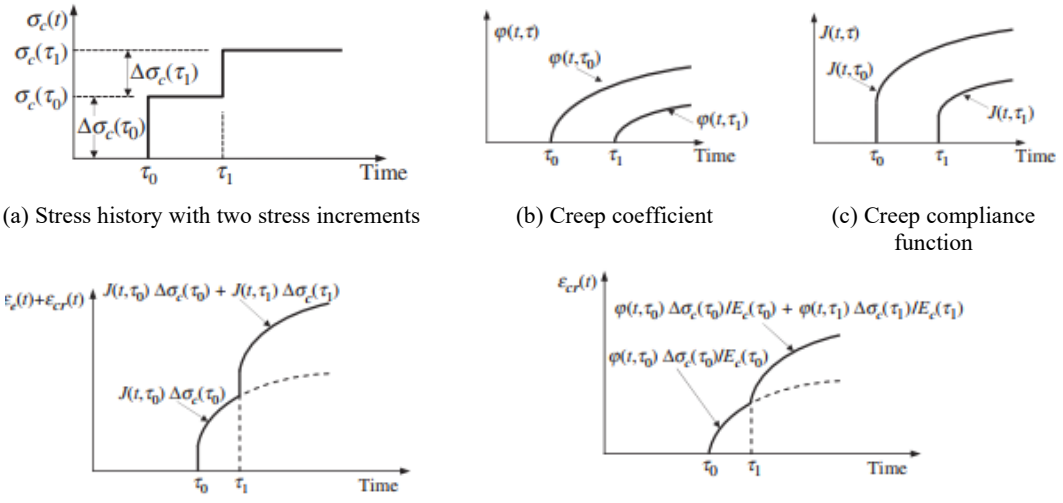

(a) Stress history with two stress increments

(b) Creep coefficient

(c) Creep compliance function

(d) Total elastic strain and creep strain

(e) Creep strain

Figure 2-9. Creep and elastic deformations due to a stress history (Gilbert and Ranzi 2011).

Shrinkage refers to the volume change in concrete, regardless of the applied load. There are two types of shrinkage: basic (autogenous) shrinkage and drying shrinkage. Basic shrinkage results from chemical processes during cement hydration. Drying shrinkage occurs when moisture migrates out of concrete during the drying process. In normal-strength concrete, the drying shrinkage is significant, but the autogenous shrinkage is negligible, accounting for approximately 10-20% of the long-term shrinkage. However, in high-strength concrete, autogenous shrinkage is significant due to its low water-to-cement (w/c) ratio (Tazawa et al. 1989, Sakata and Shimomura 2004). According to Tazawa (1999), the autogenous shrinkage of modern high-strength concrete with SCMs, admixtures, and low w/c contributes to 80 to 85% of the long-term shrinkage. As a result, high-strength concrete in large volume applications is more prone to cracking at early ages. Figure 2-10 shows this typical shrinkage behavior of a normal-strength concrete and a high-strength concrete (Sakata and Shimomura 2004).

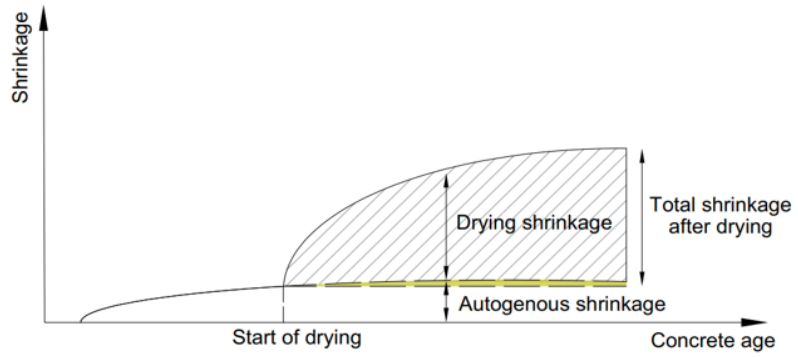

(a) For normal-strength concrete

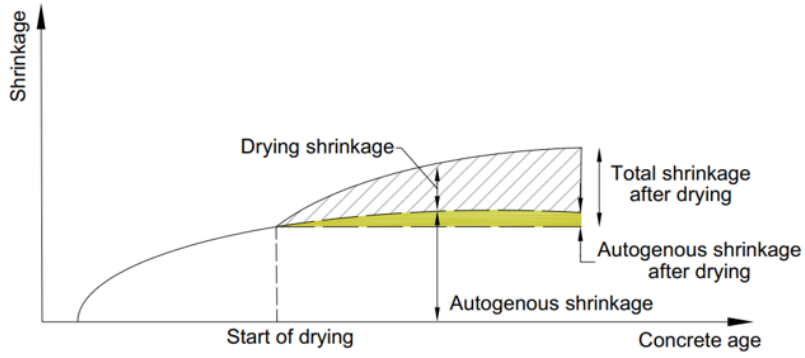

(b) For high-strength concrete

Figure 2-10. Shrinkage strain components in (a) normal-strength concrete and (b) high-strength concrete (Sakata and Shimomura 2004).

Within the service stress range of concrete structures (typically up to 40-45% of compressive strength), creep and shrinkage strains are considered independent and additive (Bažant 1988; ACI

2005). This principle of superposition allows total time-dependent strain to be calculated as the sum of individual components: elastic strain, creep strain, and shrinkage strain. Figure 2-11 illustrates this additive relationship and the temporal development of each strain component.

The temporal evolution of strain in a concrete member follows a characteristic sequence. From casting until the end of moist curing, the concrete undergoes autogenous shrinkage, which results from internal self-desiccation as hydration consumes water within the cement paste. If the member is cured by water immersion, slight swelling may occur due to moisture absorption, partially offsetting autogenous shrinkage. Once exposed to ambient conditions, the member experiences drying shrinkage in addition to ongoing autogenous shrinkage, with the combined effect termed total shrinkage.

Upon load application, an immediate elastic strain develops, with magnitude determined by the applied stress and the concrete's elastic modulus at that age. This instantaneous response is followed by time-dependent creep strain.

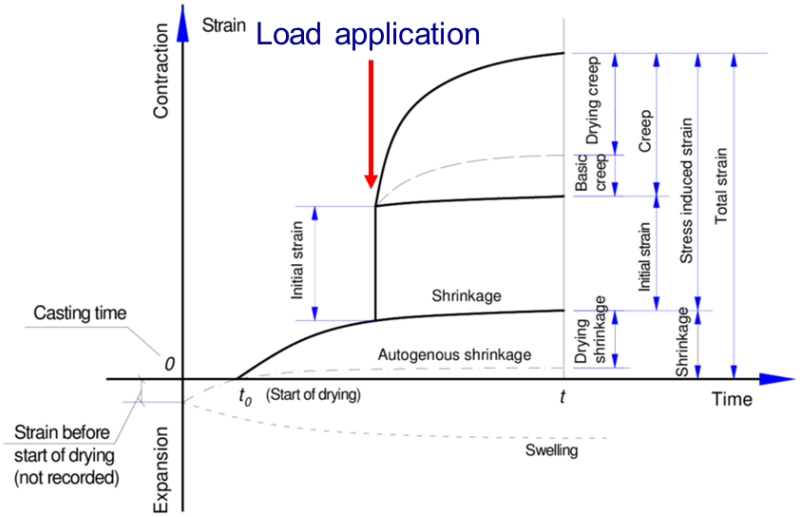

Figure 2-11. Time-dependent deformation components of concrete (ACI 2005).

2.4.4.1 Factors Affecting Concrete Creep and Shrinkage

Concrete creep and shrinkage are governed by intrinsic parameters (mix design properties) and extrinsic parameters (specimen geometry, loading conditions, environmental exposure) (Bažant 1988; ACI 2005). Neville (1996) summarizes the influence of these parameters based on published experimental data. The relative importance of each parameter varies with specific conditions including stress level, exposure environment, and time scale.

2.4.4.2 Concrete Creep and Shrinkage Models

The commonly used concrete creep and shrinkage models include ACI 209R-92 (ACI 2008a), AASHTO (AASHTO 2020), CEB-FIP 90 (CEB 1993), CEB-FIP 2010 (fib 2013), Bažant-Baweja B3 (Bažant and Baweja 1995), RILEM B4 (RILEM Technical Committee TC-242-MDC 2015), and GL 2000 (Gardener and Lockman 2001). Prior to CEB-FIP 90 and CEB-FIP 2010 models, there were CEB-FIP 1970 and CEB-FIP 1978 models (CEB 1993). Many of the models are empirical, with their parameters fitted to available experimental data, except the RILEM B4 model. The functions of the RILEM B4 model were derived from physical theory, while its parameters were fitted using an extensive experimental database (Hedegaard 2020). These models can be divided into two categories: asymptotic and logarithmic. In the asymptotic models, the ultimate creep strains or the ultimate shrinkage strains approach an asymptote with time. In logarithmic models, the long-term creep or shrinkage strains vary linearly with the logarithm of time and do not predict an ultimate creep or shrinkage strain, unlike asymptotic models (Bažant 1988). AASHTO, CEB-FIP 1978, CEB-FIP 90, CEB-FIP 2010, and ACI 209R-92 creep models are a few examples of asymptotic models. Bažant-Baweja B3, RILEM B4, and GL 2000 creep models are examples of logarithmic models (French et al. 2014). Unlike the creep behavior, shrinkage tends to achieve an ultimate value. Hence, all the shrinkage models are asymptotic (French et al. 2014). ACI 209R-92, AASHTO, CEB-FIP 90, and GL 2000 models calculate the total creep (the sum of basic creep and drying creep) and the total shrinkage (the sum of autogenous shrinkage and drying shrinkage). CEB-FIP 2010 and RILEM B4 models calculate the basic and drying components of creep and shrinkage separately. The Bažant-Baweja B3 model calculates basic creep and drying creep separately and ultimately computes the total shrinkage. Basnayake (2023) presents a summary of the parameters required to calculate creep and shrinkage of concrete using these seven models. For a particular concrete application, if the selected model for creep and shrinkage does not accurately describe the phenomena, extrapolation of the results could deviate significantly from reality (ACI 2008b).

Studies have evaluated the applicability of these empirical models in predicting the creep and shrinkage of selected concrete mixes (Meyerson et al. 2002, Mokarem et al. 2005, Al-Manaseer and Lam 2005, Videla and Aguilar 2005, Goel et al. 2007, and Al-Manaseer and Prado 2015). According to Meyerson et al. (2002), CEB-FIP 90 model best represented the creep of six high-strength concrete mixes used in prestressed concrete structures by the Virginia Department of

Transportation (VDOT) when compared to Sakata, GL 2000, ACI 209R-92, and Bažant-Baweja B3 models. The mixes had varying coarse aggregate types (gravel, diabase, and limestone) and SCMs (silica fume, class F fly ash, and slag). According to Mokarem et al. (2005), the drying shrinkage of mixes containing 20% fly ash or 40% slag as cement replacements was best represented by the GL 2000 model compared with the Bažant-Baweja B3 and CEB 90 models. The fly ash mix had a w/c of 0.41, and the slag mixes had a w/c varying between 0.39 and 0.43. Goel et al. (2007) evaluated the suitability of the ACI-209R-82 model, Bažant-Baweja B3 model, CEB-FIP 90 model, the Muller model, and GL 2000 model in predicting the creep and shrinkage of the concrete mix used in the construction of the Water Tower Place in Chicago. The concrete had a 28-day compressive strength ranging from 4700 psi (32.45 MPa) to 9100 psi (63.0 MPa). The creep and shrinkage strains were measured up to 5000 days using cylinders stored at 23^0 C and 5% relative humidity (RH). The GL 2000 model closely predicted the experimental results compared with the other models considered. Some studies have proposed new equations or modifications to existing models to predict the creep and shrinkage behavior of concrete (Huo et al. 2001, Sakata et al. 2001, and Tadros et al. 2003). Huo et al. (2001) proposed modifications to the ACI 209R-92 model based on the creep and shrinkage behavior of three high-performance concrete mixes used in bridge girders and deck slabs in Nebraska. The 56-day specified compressive strength of all three mixes was 12,000 psi, with w/c ratios of 0.24, 0.25, and 0.30. The fly ash content in these three mixes was 20%, 32% and 9%. The ACI 209R-92 model overestimated the actual shrinkage strains and creep coefficients for these mixes.

The first concrete creep and shrinkage database was created between 1976 and 1978 at Northwestern University (NU). In 1992, the RILEM committee TC107, chaired by Bažant, enhanced the database with new data to create the NU-RILEM-ACI Database, with the approval of both the RILEM and ACI-209 committees. Between 2010 and 2013, the database was extended, restructured, and introduced as the NU-ITI database. The database contains approximately 1,400 creep and 1,800 shrinkage curves. Approximately 800 creep and 1050 shrinkage curves contain admixtures (Hubler et al. 2015). Three Japanese technical committees developed the Japanese Society of Civil Engineers (JSCE) database using creep and shrinkage test data collected primarily from the papers published in Japan (Sakata et al., 2009). Sakata et al. (2001) proposed new models to predict concrete creep and shrinkage for a wide range of concrete strengths, based on regression analysis of data from the JSCE and RILEM databases. Several studies have used statistical

methods to compare and rank the existing creep and shrinkage models based on the data from these databases (Al-Manaseer and Lam 2005 and Jin et al. 2018). However, the data used for such evaluations exhibit bias, as pointed out by Bažant and Li (2008). The variability in concrete mix composition and other parameters, as well as the inclusion of data from concretes that are no longer in use, are among the reasons for this bias. Therefore, the different intrinsic and extrinsic assumptions and behavior needs to be carefully considered when choosing a model.

2.4.4.3 Creep and Shrinkage of Concrete with Slag and Fly Ash

The use of Ground Granulated Blast Furnace Slag (GGBFS) or slag and class F fly ash in mass concreting lowers the heat of hydration generated in the concrete, thereby minimizing the cracking potential (Kosmatka and Wilson 2011 and Basnayake et al. 2020). However, few studies have evaluated the properties of concrete blended with both slag and class F fly ash (Sakthivel et al. 2019). Brooks (1991), Hooton et al. (2004), Ghosh and Timusk (1981), and Saha (2018) have observed inconsistent concrete creep and shrinkage behaviors in the presence of slag. Autogenous shrinkage in slag and fly ash blended concretes is higher due to their fine pore structure that creates a high tensile stress at the water-to-air meniscus interface (Ma and Dehn 2017).

Ghosh and Timusk (1981) evaluated the creep and shrinkage of a high-strength concrete with a 28-day compressive strength of 8000 psi, a w/c of 0.34, and 16.7% cement replacement with fly ash. For this mix, an 11-13% shrinkage reduction was observed at 7 months of age. For the same mix, creep increased by 10-17% at the age of 7 months when loaded to a stress level equal to 25% of the compressive strength at the time of loading (28 days). Hooton et al. (2004) analyzed data from 16 studies for 62 concrete mixes with slag to identify the influence of slag on drying shrinkage. The 62 concrete mixes had (i) w/c ratios: 0.60 to 0.26, (ii) slag contents: 20 to 80%, (iii) calculated or estimated volumetric aggregate contents: 50 to 73%, (iv) drying time: 10 to 490 days, and (v) curing time before drying: 3 to 28 days (most commonly 7 days). The RH of the exposure environment was 50% and 65%. The results showed a 3% higher drying shrinkage compared to a similar concrete mix without slag. According to Saha (2018), the drying shrinkage was reduced by 8, 10, 16, and 75% for 10, 20, 30, and 40% fly ash replacements, respectively.

Brooks (1991) evaluated the effect of a temperature change on the basic creep of concrete with and without slag. Concrete specimens with three levels of cement replacement by slag (0%, 50%, and 70%) were subjected to varying temperatures. The specimens were initially stored at 40^0 C,

and then subjected to temperatures ranging from 40 to 65^0 C for concrete without slag, 40 to 61^0 C for concrete with 50% slag, and 40 to 53^0 C for concrete with 70% slag. The effect of temperature change on the basic creep of concrete in compression was negligible.

2.4.4.4 Creep and Shrinkage of Concrete with Shrinkage Reducing Admixtures (SRAs)

Chemical admixtures such as SRAs reduce shrinkage in high-strength concrete (Nmai et al. 1998, Folliard and Berke 1997, Rongbing and Jian 2005, D'Ambrosia et al. 2010, Saliba et al. 2011, Lopez et al. 2013, Kioumarsi et al. 2020, and Klausen and Kanstad 2021). SRAs reduce the surface tension of the capillary pore solution, thereby reducing both the autogenous and drying shrinkages in high-strength concrete (Nmai et al. 1998). According to Folliard and Berke (1997), the 28-day and 120-day drying shrinkage of a mix with a w/c of 0.35 and 1.5% SRA by cement weight were 35% and 29%, respectively, lower than those of the reference mix without SRA. Rongbing and Jian (2005) evaluated the effect of SRA dosage on the drying shrinkage of concrete with a w/c of 0.36. The reduction of drying shrinkage was 22%, 28%, and 44% for mixes with 1.0%, 2.0%, and 3% SRA by the cement weight, respectively. The shrinkage reduction was significant for lower w/c mixes (DAmbrosia et al. 2010). For a mix with 0.35 w/c and 1% SRA, the 7-day reduction in total shrinkage was about 75% while for a mix with w/c of 0.45 and 1% SRA, the 7-day shrinkage reduction was about 45%. According to Saliba (2011), the 7-day and 70-day drying shrinkage of a mix with a w/c of 0.43 and 1% of SRA by cement weight were 69% and 75%, respectively, lower than the reference mix without a SRA. The same SRA used in a concrete mix with a w/c of 0.65 reduced the 7-day and 70-day drying shrinkages by 44% and 67%, respectively. Klausen and Kanstad (2021) investigated the effect of fly ash and slag on a mix with a w/c of 0.4 and 1% SRA by cementitious material. The fly ash concrete had 17% of a siliceous fly ash, while the slag concrete had 68% slag by the weight of cement. The mixes also contained 5% silica fume by weight of cement. At the age of 2.5 years, the reductions in autogenous and total shrinkage for slag concrete with SRA were 23% and 32%, respectively. At the same age, the reductions in autogenous and total shrinkage for fly ash concrete with SRA were 23% and 20%, respectively (Klausen and Kanstad 2021).

2.4.4.5 Experimental Evaluation of the Concrete Creep and Shrinkage

ASTM C157 describes testing procedures for evaluating the shrinkage of mortar or concrete under laboratory conditions (ASTM 2017). According to ASTM C157, the change in length of mortar beams (1×1×11.25 in.) or concrete beams (4×4×11.25 in. or 3×3×11.25 in., depending on the aggregate sizes) exposed to controlled temperature and RH is measured to evaluate shrinkage. ASTM C512 describes procedures for assessing both concrete creep and shrinkage in the laboratory. Under ASTM C512, the load-induced time-dependent compressive strain is measured at selected ages for concrete loaded using creep frames under an arbitrary set of controlled environmental conditions (ASTM 2015). The creep specimens are loaded to no more than 40% of the compressive strength at the time of loading. Therefore, compressive strength tests are required at the ages of loading before testing for creep. Specimens similar to creep specimens (commonly known as companion specimens) are fabricated and exposed to curing environments identical to the creep specimens. The length change in these companion shrinkage specimens is measured at the same time intervals as in the creep specimens. The creep strain would be the difference between the total strain measured in a creep specimen and the strain measured in the companion shrinkage specimen.

ASTM C512 recommends the specimens to be evaluated at a temperature of 73.5 ± 3.5^0 F (23.0 ± 2.0^0 C) and a RH of 50 ± 4 % for the duration of testing. However, the laboratory measured shrinkage is not indicative of the actual shrinkage in an actual structure because of the effects of size, restraint, and exposure conditions. These standard room conditions may not represent the exposure conditions of an actual structure. These drawbacks were addressed in limited studies by testing the mixes under field conditions (Lee and Robertson 1995). Full-scale concrete bridge structures have been instrumented to monitor the concrete creep and shrinkage (Lee and Robertson 1995, Robertson and Li 2005, Huo et al. 2006, Sousa et al. 2014, French et al. 2014, and Ibrahim et al. 2015). Vibrating wire gage (VWG) sensors were the popular choice in measuring the strain developed in these structures (Geokon 2019).

2.4.4.6 Modeling Concrete Creep and Shrinkage

Finite element software commonly used in the design and analysis of structures, such as LARSA 4D, SAP 2000, LUSAS, and MIDAS Civil, includes built-in concrete creep and shrinkage models specified in design codes (MIDAS Information Technology 2019, LARSA 2021, LUSAS 2022,

and Computers and Structures 2023). However, finite element packages used for in-depth analysis and research, such as Abaqus and ANSYS, do not include built-in models for concrete creep and shrinkage. The user subroutines are used to model concrete creep and shrinkage behavior. The shrinkage is modeled as thermal strain increments in the user subroutine UEXPAN (Bažant et al. 2012, Faxiong et al. 2013, French et al. 2014, Li et al. 2018, Liu 2018, Ghabdian et al. 2019, Zhu et al. 2020, and Aval et al. 2022). The creep is modeled as thermal strain increments in the user subroutine UEXPAN (Li et al. 2018 and Zhu et al. 2020) or as inelastic strain increments in the user subroutine UMAT (Bažant et al 2012, French et al. 2014, Liu 2018, Ghabdian et al. 2019, and Aval et al. 2022). When modeling the creep, the utility subroutine GETVRM is used to capture the stress history required in the creep strain formulations (Faxiong et al. 2013). The subroutines are written in FORTRAN and are compiled into the finite element code upon job initialization. The subroutine UEXPAN is requested in the material data block of the input file using the keyword *Expansion, user. The subroutine UMAT is requested in the material data block of the input file using the statement *User material, user. The subroutine USDFLD is requested in the material data block of the input file using the statement *User defined field (Abaqus 2018).

2.4.5 Structural Modeling of PT Members

In the structural analysis of PT members, the tendon is modeled using two approaches: (1) as an applied loading or (2) as a load-resisting element. The load balancing method, the primary moment method, and the equivalent load through discretization of the tendon force method are three options when the tendon is modeled as an applied loading (Lin 1991, Aalami 1990, and 2000). Under these methods, the tendon is removed from its housing member and is replaced with the force it exerts on the housing member (PTI 2006). When the tendon is modeled as a load-resisting element, it is represented as a distinct element linked to its housing member. The load balancing method is a popular hand calculation tool used in the analysis of PT members. But this method cannot account for the variation of prestressing force along the tendon length (Aalami 2000). In this study, only the equivalent load obtained through the discretization of the tendon force method and the modeling of the tendon as a load-resisting element are discussed.

2.4.5.1 Equivalent Load Through Discretization of Tendon Forces

In this method, the tendons are discretized into smaller segments. The tendon forces are resolved locally within these segments and are applied to the joints of the housing member. Figure 2-12

shows this modeling approach for a two-span prestressed beam. The total tendon is discretized into a series of straight-line segments (Figure 2-12b). The tendon force components parallel and perpendicular to the centroidal axis of the beam (F_x and F_y) and moment due to eccentricity of F_x (M_i) are calculated at the discretized nodes (Figure 2-12c). These force components and the moments are applied to the centroid of the housing beam at the corresponding locations, as shown in Figure 2-12d.

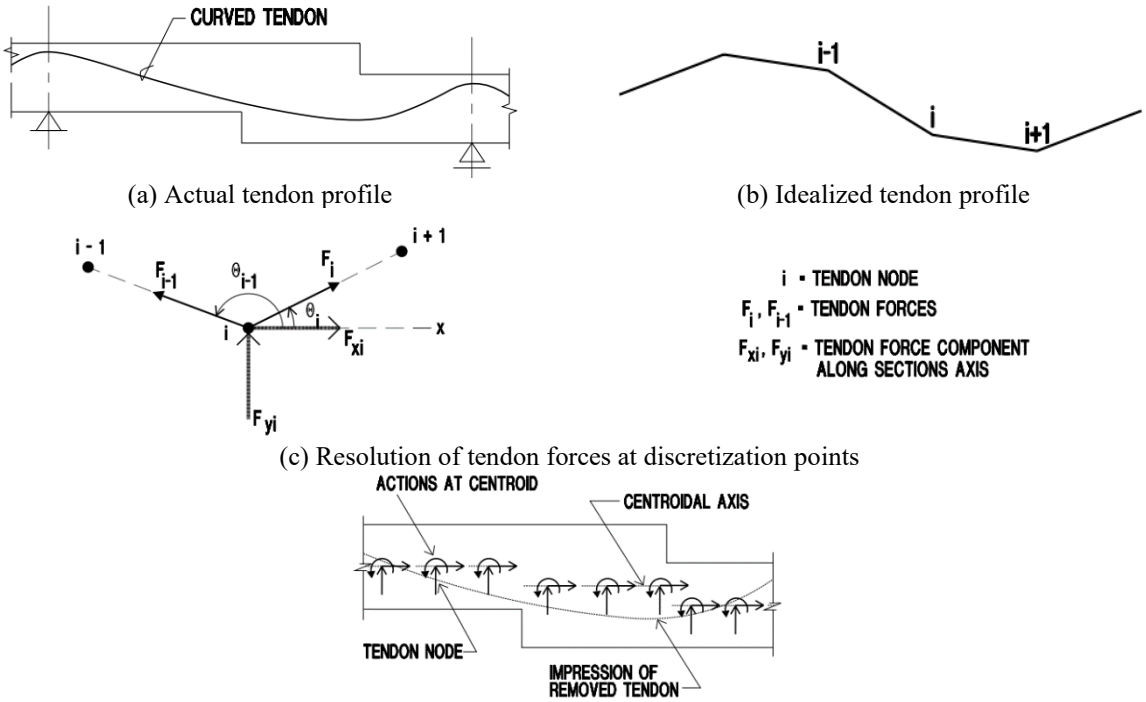

(a) Actual tendon profile

(b) Idealized tendon profile

(c) Resolution of tendon forces at discretization points

(d) Equivalent tendon actions exerted at the centroidal axis of the housing member

Figure 2-12. Equivalent load through the discretization of tendon forces method (Aalami 2000).

The equivalent load through the discretization of forces method can account for the varying tendon forces due to losses and non-prismatic geometry of the housing member. The long-term losses are calculated separately, and the tendon forces are updated. Since the losses are time-dependent, the tendon forces and moments are calculated at predefined time increments and applied to the beam. This modeling scheme is implemented in finite element software: LARSA 4D, LUSAS, and SAP 2000 (LARSA 2021, LUSAS 2022, and Computers and Structures 2023).

2.4.5.2 Discrete Modeling of Tendon as a Load-Resisting Element

The tendon is modeled as a discrete element connected to the housing concrete member. An initial prestress force, after friction and anchorage set losses, is applied to the tendon as a load. The prestress loss in the tendon due to creep, shrinkage, and elastic shortening does not need to be

separately calculated. Any deformation in the concrete member due to long-term losses and elastic shortening is implicitly accompanied by a corresponding displacement in the tendon element. This modeling scheme is implemented in more refined finite modeling, where the tendon is modeled as a beam, truss, plane stress, or a solid element (Ellobody and Bailey 2008, Bažant et al. 2012, Huang 2012, and French et al. 2014). This technique can be implemented in commercial finite element software such as Abaqus, ANSYS, SAP 2000, MIDAS FEA, and MIDAS Civil.

2.5 FINITE ELEMENT MODELING PRACTICES

2.5.1 Modeling Post-tensioning Procedures in Commercial Finite Element Programs

Two main challenges arise when modeling the post-tensioning procedure using finite element methods. The first challenge is the modeling of the interaction between concrete and tendon at different stages of post-tensioning. The second challenge is modeling the variation of prestress force along the length of the tendon.

2.5.1.1 Modeling the Interaction Between Concrete and Tendon

During post-tensioning, the tendons are unbonded to the surrounding concrete until grouting takes place. At this stage, the tendon force is transmitted to the concrete only at the anchorages. Once grouted, the tendons are fully bonded to the surrounding concrete, and forces are transferred from the tendons to the concrete through strain compatibility. Therefore, the contact defined between the tendon and the concrete should reflect the bonded and unbonded stages. Some studies have simply always assumed the perfect bonding between the tendon and the housing concrete member when modeling the post-tensioning procedure (Bažant et al. 2012, French et al. 2014, and Mohammed et al. 2017). This technique is valid once the ducts are grouted. But this assumption misrepresents the force transfer mechanism between the concrete and the tendon before grouting, and does not account for the effective cross-sectional area of the concrete member (the concrete gross cross-sectional area minus the post-tension duct area).

Mainly, three approaches have been used in the literature to model the unbonded stage between the tendon and the concrete member before grouting. The first approach is defining surface-to-surface contact between the tendon and the concrete as shown in Figure 2-13 (Ellobody and Bailey 2008, Huang et al. 2010, Huang 2012, Kang and Huang 2012, French et al. 2014, and Kang et al. 2015). The contact behavior in the tangential direction is assumed to be frictionless during post-tensioning. The tendons are free to slip along the tangential direction relative to the housing

concrete member during post-tensioning. The contact behavior in the tangential direction is changed from frictionless to hard contact at the grouting stage to model the perfect bonding between the concrete and the tendon. Ellobody and Bailey (2008) used the surface-to-surface contact approach in Abaqus to model the post-tensioning of unbonded tendons in a concrete slab. 3D solid elements were used to model the concrete slab, tendons, and anchorage blocks. Surface-to-surface contact elements were defined between the tendon and the surrounding concrete. The concrete surface surrounding the tendon was defined as the master surface, while the tendon surface in contact with the surrounding concrete was defined as the slave surface. The tangential property of the contact elements was defined as frictionless with small sliding. The normal property was defined as rough (forces are transmitted only when the two surfaces are in contact).

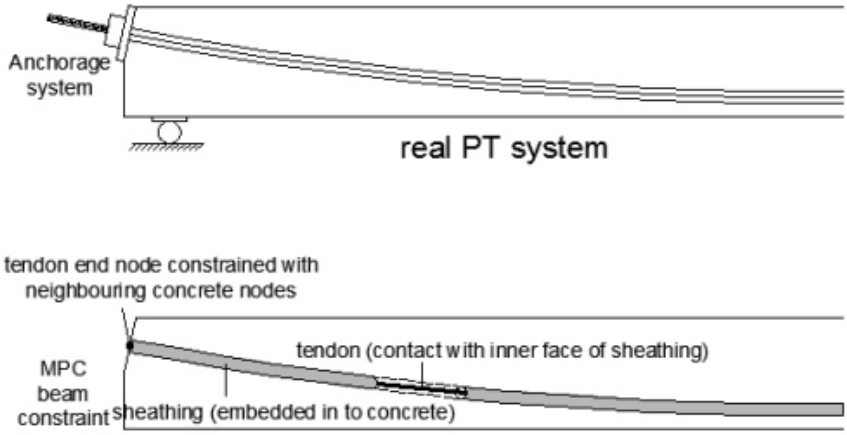

Figure 2-13. Modeling of tendons-concrete interface using surface-to-surface contact (Huang 2012).

The second approach is the use of tube-to-tube contact elements (ITT21 and ITT31 elements) in the Abaqus element library, as shown in Figure 2-14 (Huang et al. 2010, Huang 2012, and Kang and Huang 2012). The tube-to-tube contact elements are used to model the relative motion between two tubes representing the tendon and the duct along the line defined by the axis of one of the tubes (slide line). The tube-to-tube contact elements can be used with 2D or 3D beam, pipe, or truss elements (Abaqus 2018). The post-tension duct is modeled as the outer tube embedded in the housing concrete member. The tendon is modeled as the inner tube. The slide line is defined for the inner tube that represents the tendon. Frictional characteristics can be assigned to define the surface interaction between the surfaces. In Figure 2-14, frictionless contact is defined for the contact elements to model the finite sliding during post-tensioning.

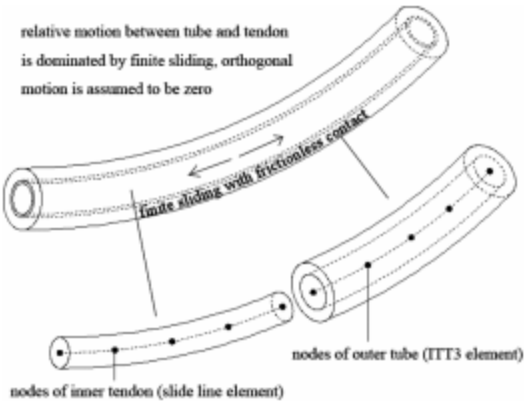

Figure 2-14. Modeling of unbonded post-tension tendons using tube-to-tube contact elements in Abaqus (Huang 2010).

The third approach is to use a spring system to model the unbonded stage between the tendon and concrete member that exists before grouting, as shown in Figure 2-15 (Huang et al. 2010). The unbonded tendon (introduced as the real tendon) is connected to a virtual tendon that is embedded in the concrete member using axially rigid spring elements at discrete locations. The virtual tendon is similar to the real tendon but has a lower elastic modulus. Both real and virtual tendons are modeled using the truss elements in Abaqus. The concrete member is modeled using 3D solid elements in Abaqus. The tendons are anchored to the housing concrete member at the ends using the multi-point constraints (MPCs) option in Abaqus, so that the prestress force is transferred to the concrete only at the anchorages. The springs between the real and virtual tendons were modeled using SPRINGA elements. Parametric studies by Huang et al. (2010) revealed that system behavior had negligible sensitivity to the number and length of spring elements used to model post-tensioning system. However, spring elements are necessary at locations where tendons change direction (deviation points) or where concentrated loads are applied to accurately capture local force transfer effects.

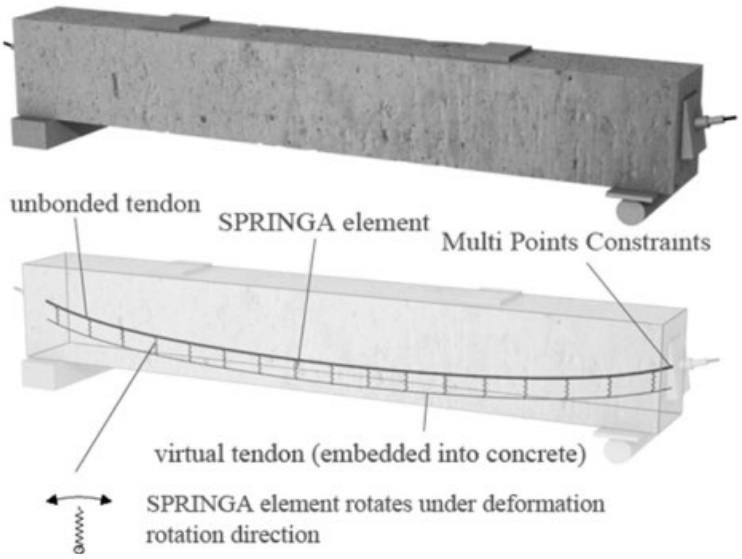

Figure 2-15. Modeling of unbonded post-tension tendons using springs (Huang 2010).

As shown in Figure 2-16, Brenkus (2016) and Brenkus et al. (2019) used springs, as introduced by Huang (2012), to model the unbonded post-tension tendons in a concrete I-girder. Instead of 3D solid elements, 2D beam elements were used to model the concrete I-girder. The I-girder cross-section was discretized into multiple sections. Each section was modeled using individual beam elements defined in layers, which were connected using tie constraints as shown in Figure 2-16c. The real and virtual tendons were modeled using 2D truss elements connected using SPRINGA elements. The virtual tendon was connected to the beam elements representing the concrete I-girder using MPCs. The real tendon was connected to the nearest beam element representing the concrete I-girder using rigid connectors at the girder ends, as shown in Figure 2-16d. The use of multiple beams to represent the girder cross-section correctly represented the tendon eccentricity with respect to the centroid of the girder, which is otherwise impossible if the complete girder were modeled using a single beam element representing the entire cross-section.

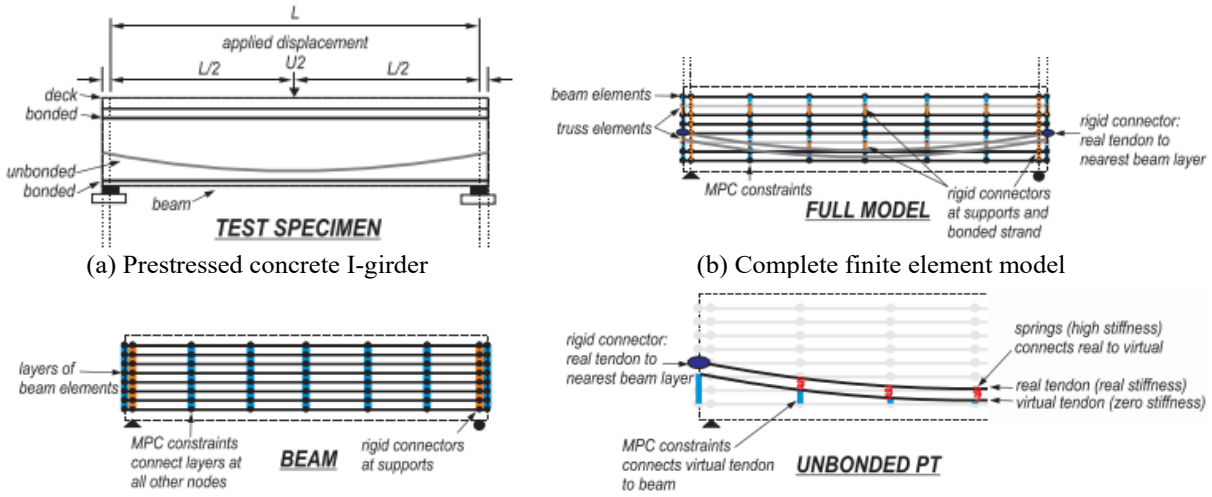

(a) Prestressed concrete I-girder (b) Complete finite element model

(c) Finite element model of the I-girder (d) Springs approach to model the unbonded tendons

Figure 2-16. Finite element model to represent the unbonded tendons in a concrete I-girder (Brenkus 2016).

2.5.1.2 Modeling Prestress Force in Tendons

As discussed in Section 2.4, the prestress force in the tendons varies along the tendon length and with time. The variation of the prestressing force with time due to concrete creep, concrete shrinkage, and elastic shortening is captured implicitly by the finite element model when the tendons are modeled as load-resisting elements. However, modeling the variation of the prestressing force along the tendon length after friction and anchorage set losses is challenging, particularly in 3D finite element modeling.

A few studies have modeled the friction and anchorage set losses in 2D finite element modeling (Vecchio et al. 2006, Huang 2012, and Huang and Kang 2018). Vecchio et al. (2006) used link elements to model friction losses in an unbonded tendon in a 2D reinforced concrete beam. Figure 2-17a shows the representation of the post-tension tendon in the concrete beam with the tendon ends attached to the anchorage block. The concrete beam was modeled using rectangular elements, and the post-tension tendon was modeled with truss elements. Link elements were used to establish the nodal connections between truss and solid elements. Figure 2-17b shows a bond-link element. The properties of the spring tangential to the truss elements (direction t) were defined with a bond slip model to describe the differential movement between the truss and solid elements. The spring normal to the truss elements (direction n) was defined with a high stiffness to restrict displacement in the normal direction. A differential temperature was applied to the anchorage block to simulate the extension and contraction of the tendon during jacking and anchoring operations.

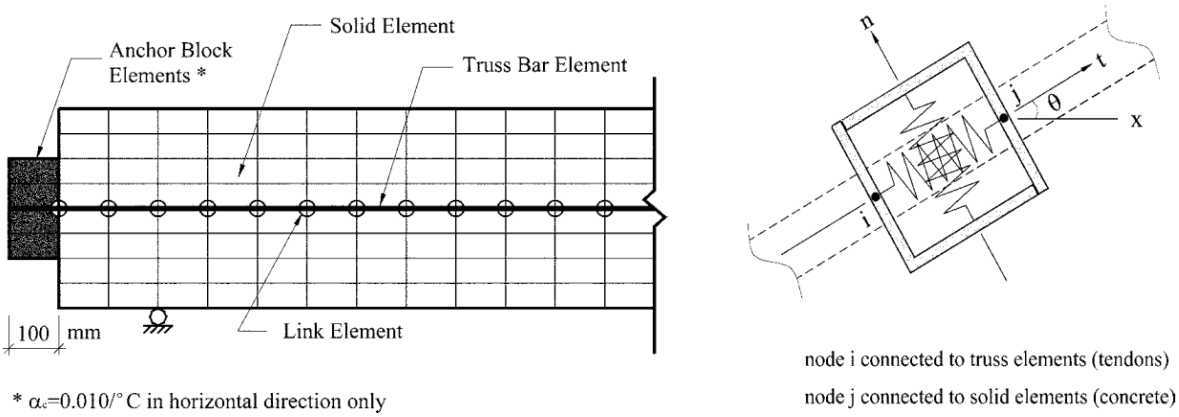

(a) Representation of unbonded tendons in the finite element model

(b) Bond-link element

Figure 2-17. 2D Finite element modeling of post-tension tendons using bond-link elements (Vecchio et al. 2006).

Huang (2012) and Huang and Kang (2018) proposed a two-dimensional nonlinear finite element formulation to model the variation of prestress force along the length of a post-tension tendon after friction and anchorage set losses. Figure 2-18b shows the finite element discretization of the post-tensioned member shown in Figure 2-18a. The tendon and the duct (termed as the sheathings in this study) are modeled using 2D linear truss elements, and the concrete member is modeled as 2D beam elements. The truss elements representing the sheathing are connected to the beam elements representing the concrete member via embedding elements, as shown in Figure 2-18b and Figure 2-18c. The embedding elements are 2-node Euler-Bernoulli beam elements with large axial and bending stiffnesses. The contact between the tendon and the duct is defined using node-to-segment contact elements, as shown in Figure 2-18c. The nodes in the tendon are slave nodes that are in contact with the master surface formed by the sheathing element nodes. A frictional contact formulation is defined in the tangential direction following Coulomb's friction law to model the friction behavior. The hard contact is used in the normal direction to model the complete bonding. As shown in Figure 2-18b and Figure 2-18d, special anchorage elements are introduced between the tendon elements and the embedding elements at the anchorage locations. The anchorage element is a rigid spring between the anchor point and the tendon end. Prescribed loads and displacements are applied to the nodes of the anchorage element that represent the tendon jacking force and anchorage set.

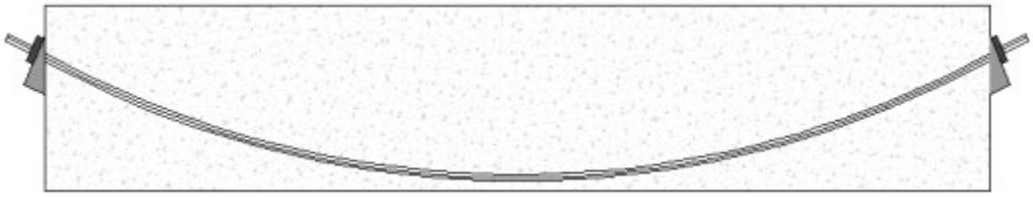

(a) Post-tensioned member

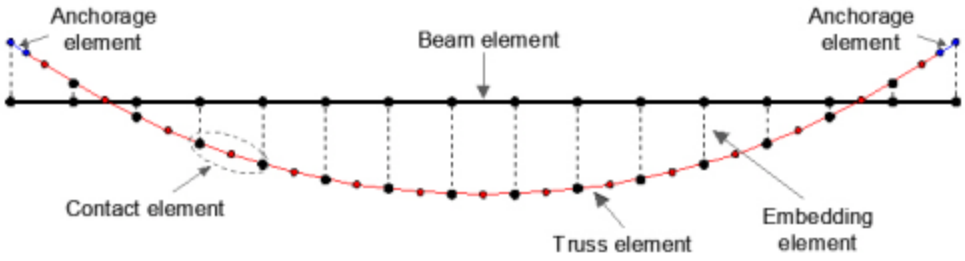

(b) Finite element discretization

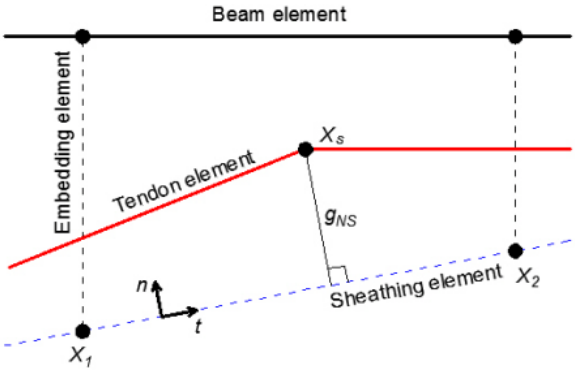

(c) Node-to-segment based contact element

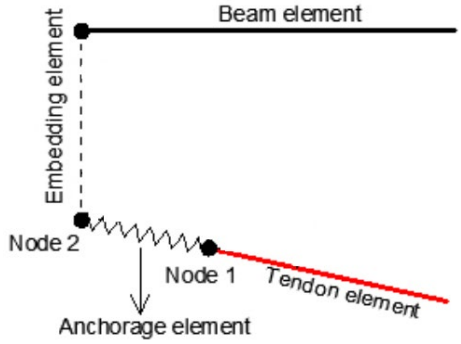

(d) Node-to-segment based contact element

Figure 2-18. Proposed finite element discretization scheme for a PT member (Huang 2012).

In contrast to 2D finite element modeling, there are no methods in the literature for modeling varying prestress force in 3D finite element modeling when solid elements are used to model the surrounding concrete and beam, truss, or solid elements are used to model the tendons. In the tube-to-tube contact element approach, a friction model can be assigned to model the friction between the tendon and the duct (Abaqus 2018). But to activate the friction component in the tangential direction, the tendon must contact the elements representing the duct to generate a normal force. The common approach in 3D finite element modeling is to represent prestressing force as a uniform force. Studies have followed different methods to calculate the magnitude of this uniform force to be applied. French et al. (2014) applied a stress equivalent to the jacking stress minus the friction losses averaged over the tendon length. Huang et al. (2010) applied an average stress after accounting for the prestress losses due to friction and anchorage set. The calculation method of the effective prestress and the average stress is not given in detail. The ADAPT-FELT software calculates an average initial stress, which is the average of the stress

distribution after friction and anchorage set losses (ADAPT 2017). Once the magnitude of the uniform force is established, the uniform force is applied as a predefined field of stress (Ellobody and Bailey 2008, French et al. 2014, Huang 2010, Bažant et al. 2012, and Mohammed et al. 2017) or the temperature field is manipulated to generate an equivalent prestressing force (Huang 2012 and Brenkus 2016). Mohammed et al. (2017) modeled a post-tensioned concrete one-way slab with bonded tendons using ANSYS. The concrete slab was modeled using SOLID65 elements while the tendons and reinforcement were modeled using 2-node discrete link elements (LINK8). Tendons were connected to the slab only at the end of the anchorages. The prestress force was applied as an initial stress. Abaqus also allows defining prestress as an initial stress using *Initial conditions, type = stress (Abaqus 2018). This option cannot be used if post-tensioning is modeled as a step in a construction-stage analysis. When the prestress force is applied to the tendon as a predefined stress or a temperature field, a loss of prestress force occurs due to the instant elastic shortening of the member. Therefore, several iterations are necessary until the desired post-tensioning force is generated in the tendon (Huang 2010).

3 CONSTRUCTION ACTIVITIES OF THE 2ND AVENUE BRIDGE

3.1 OVERVIEW

Construction activities of the 2nd Avenue Bridge were carefully planned and executed as part of the MDOT's ongoing I-94 modernization project. This project was notable for its use of ABC techniques to minimize traffic disruptions on one of Detroit's busiest freeway corridors. This chapter describes the primary construction activities associated with the bridge, organized into three major stages: (i) construction at the bridge staging area (BSA), (ii) the bridge move operation, and (iii) construction activities at the final alignment.

3.2 CONSTRUCTION AT THE BRIDGE STAGING AREA (BSA)

The bridge superstructure frame was fabricated in multiple stages at BSA, starting with the lower knuckles. As shown in Figure 3-1 and Figure 3-2, the fabrication was completed in seven stages before the frame was moved from the staging area to its final alignment over the freeway. These stages included multiple activities, as tabulated in Table 3-1 and Table 3-2 and shown in Figure 3-3 to Figure 3-6.

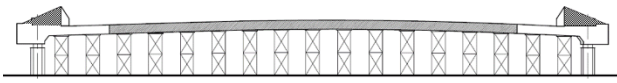

Stage 1: Fabricate concrete lower knuckles

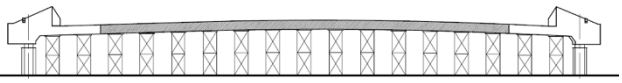

Stage 2: Fabricate concrete upper knuckles

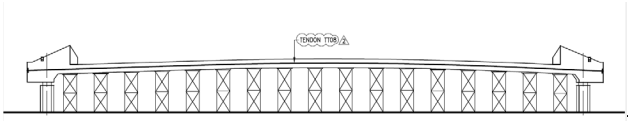

Stage 3: Fabricate tie girders and apply the required post-tension

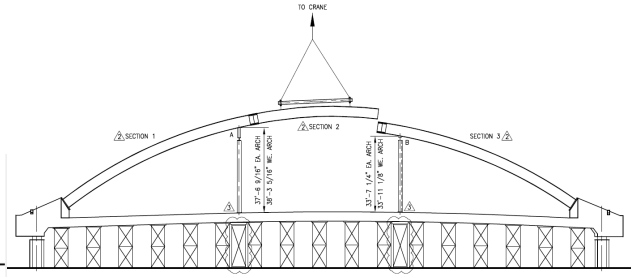

Stage 4: Erect arch ribs

Figure 3-1. Construction stages 1 to 4 at BSA.

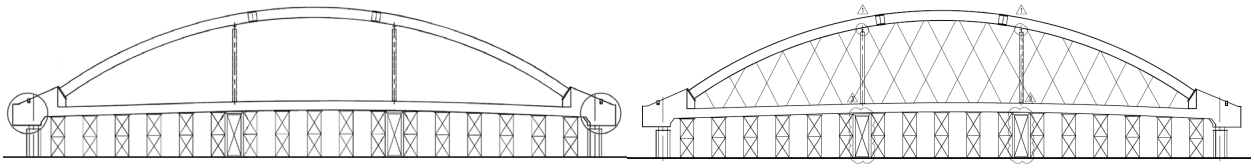

Stage 5: Fabricate and post-tension end diaphragms

Stage 6: Install and tension hangers

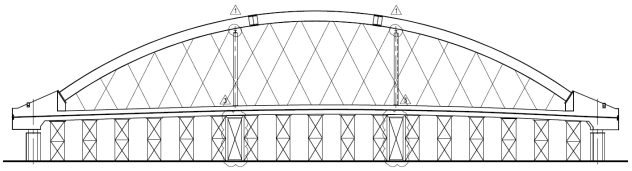

Stage 7: Apply required post-tension before bridge move

Figure 3-2. Construction stages 5 to 7 at BSA.

Table 3-1. Construction Activities at BSA: SE Lower Knuckle through North End Diaphragm Post-tensioning

Description	Date
Floorbeam erection (day 1: beams A to D; day 2: beams E to G; day 3: beams H, J, K, L, and M; day 4: beams N and P; and day 5: beams Q, R, and S)	7/22, 7/23, and 7/28 to 7/30/2020
SE lower knuckle fabrication	11/3/2021
SW lower knuckle fabrication	11/5/2021
NE lower knuckle fabrication	11/12/2021
NW lower knuckle fabrication	11/18/2021
SW upper knuckle fabrication	12/17/2021
SE upper knuckle fabrication	12/22/2021
West tie girder fabrication	12/23/2021
NE upper knuckle fabrication	1/5/2022
Upper and lower SE knuckle formwork removal	1/12/2022
Upper and lower SW knuckle formwork removal	1/12/2022
West tie girder formwork removal	1/12/2022
West tie girder formwork removal	1/13/2022
East tie girder fabrication	1/13/2022
West tie girder formwork removal	1/18/2022
NW upper knuckle fabrication	1/19/2022
Upper and lower NE knuckle formwork removal	1/19/2022
Upper and lower NE knuckle formwork removal	1/20/2022
East tie girder formwork removal	1/20 and 1/22/2022
Upper and lower NW knuckle formwork removal	1/28 and 2/4/2022
West tie girder Stage 1-1 (TT08) post-tensioning	2/21/2022
East tie girder Stage 1-1 (TT08) post-tensioning	3/14/2022
West arch rib erection at the SW knuckle	3/24/2022
West arch rib erection at the NW knuckle	3/25/2022
East arch rib erection at the NE knuckle	3/25/2022
East arch rib erection at the SE knuckle	3/28/2022
West arch rib middle section erection	3/29/2022
East arch rib middle section erection	3/29/2022
Arch rib splice installation	3/29/2022
South end diaphragm fabrication	4/12/2022
North end diaphragm fabrication	4/12/2022
North end diaphragm DT05, DT08, and DT11 post-tensioning	4/22/2022
South end diaphragm DT05, DT08, DT11, and DT04 post-tensioning	4/22/2022
North end diaphragm DT04, DT09, DT06, DT07, and DT01 post-tensioning	4/25/2022
South end diaphragm DT09, DT06, DT07, DT01, DT12, DT03, and DT10 post-tensioning	4/25/2022
North end diaphragm DT12, DT03, and DT10 post-tensioning	4/26/2022

Table 3-2. Construction Activities at BSA: Stage 1-1 Grouting of the East Tie Girder through the Grouting of Stage 1-2 Post-tensioning of the East Tie Girder

Description	Date
East tie girder Stage 1-1 PT duct grouting	5/2/2022
North end diaphragm PT duct grouting	5/2/2022
West tie girder Stage 1-1 PT duct grouting	5/4/2022
South end diaphragm PT duct grouting	5/4/2022
Arch rib-knuckle connection anchor bar post-tensioning	5/5/2022
North end diaphragm falsework removal	5/5/2022
South end diaphragm falsework removal	5/5/2022
Hanger installation	5/16 to 5/20/2022
Hanger tensioning	5/25 to 6/01/2022
West tie girder Stage 1-2 post-tensioning	6/8/2022
East tie girder Stage 1-2 post-tensioning	6/8/2022
East tie girder falsework removal	6/11/2022
West tie girder falsework removal	6/11/2022
West tie girder Stage 1-2 PT duct grouting	6/13/2022
East tie girder Stage 1-2 PT duct grouting	6/13/2022

(a) Floorbeam erection

(b) Southwest knuckle casting

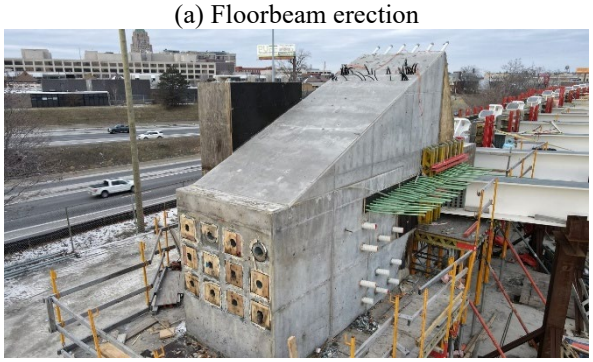

(c) Southwest knuckle

(d) Southwest knuckle

Figure 3-3. Construction activities at BSA (photo credit: Pat Sullivan, Z Contractors Inc.)

(a) Casting of the west tie girder

(b) Casting of the west tie girder

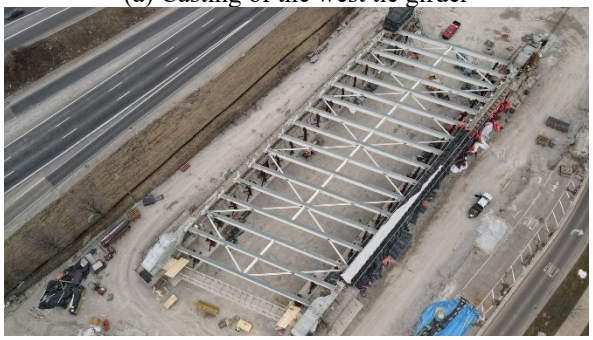

(c) Bird's eye view showing floor frame with tie girders and floorbeams

(d) South end knuckles and floor beams

(e) Tie girders on temporary supports

(f) Erection of temporary arch supports

(g) Erection of temporary arch supports

(h) Erection of arch ribs

Figure 3-4. Construction activities at BSA (photo credit: Pat Sullivan, Z Contractors Inc.)

(a) Erection of arch ribs

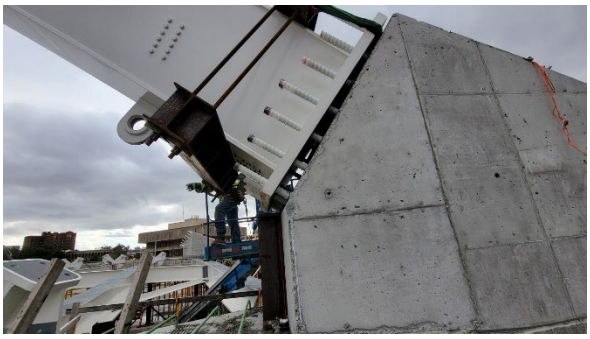

(b) Connecting an arch rib to a knuckle

(c) Arch rib supported on temporary supports

(d) Two arch rib sections between knuckles and temporary supports

(e) Erection of the arch center piece

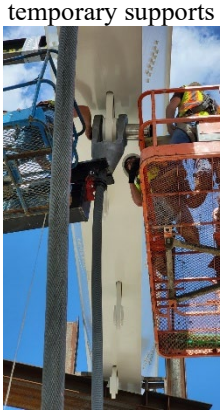

(f) Hanger connection

Figure 3-5. Construction activities at BSA (photo credit: Pat Sullivan, Z Contractors Inc.)

(a) Completed superstructure frame on temporary abutments and falsework

(b) Completed superstructure frame on temporary abutments

(c) Completed superstructure frame on SPMTs

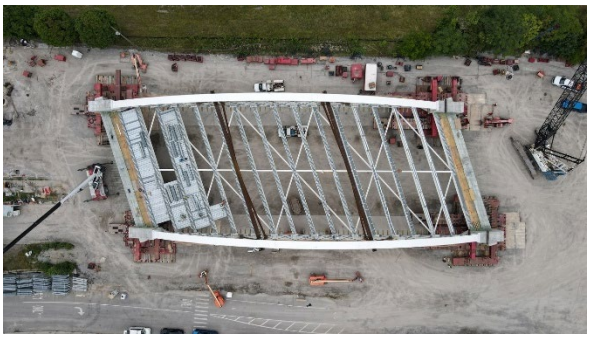

(d) Completed superstructure frame on SPMTs

Figure 3-6. Construction activities at BSA (photo credit: Pat Sullivan, Z Contractors Inc.)

3.3 BRIDGE MOVE OPERATION

Once the bridge superstructure frame was completed, it was moved into its final alignment using self-propelled modular transporters (SPMTs) (Figure 3-7 and Figure 3-8) and the lateral launching technique (Figure 3-9). The move operation involved several activities. First, the bridge was prepared for transport by jacking up the superstructure, removing temporary abutments, installing SPMTs underneath the knuckles, and loading the bridge onto the SPMTs. Next, the superstructure was moved toward the south abutment, and the north end was launched over the south abutment while the south end was simultaneously moved with SPMTs. The north end was then supported by SPMTs placed on I-94. Finally, the bridge was maneuvered using SPMTs located underneath both the north and south ends, slid over both abutments, loaded onto climbing jacks placed under the end diaphragms, lowered onto the bearings, and secured by welding the soleplates to the bearing assemblies. The timeline of major activities associated with the bridge move process is presented in Table 3-3.

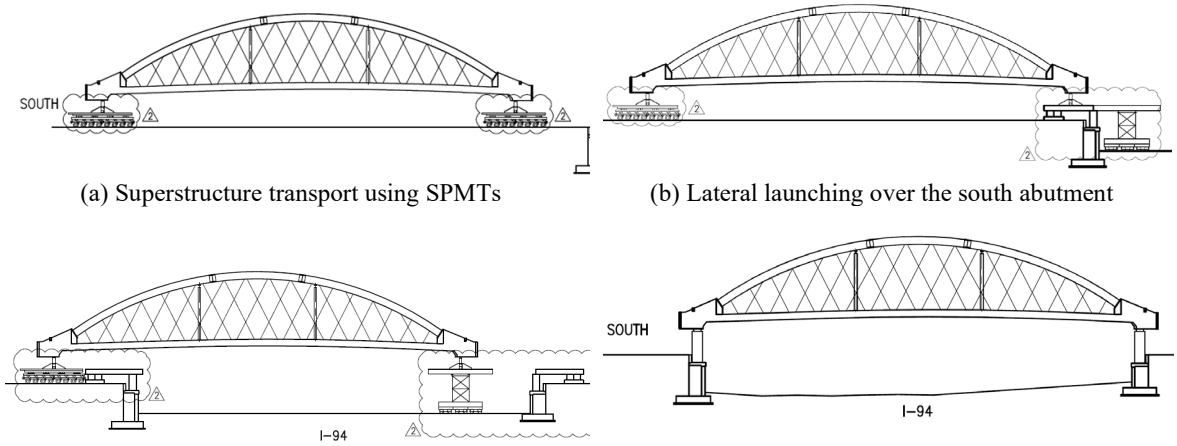

(a) Superstructure transport using SPMTs (b) Lateral launching over the south abutment

(c) Superstructure transport across I-94 using SPMTs (d) Lowering superstructure onto permanent bearings

Figure 3-7. Bridge move sequence.

Table 3-3. Construction Activities Associated with the Bridge Move Operation

Description	Date
Installing climbing jacks under each knuckle	7/11 to 7/13/2022
Lifting the superstructure frame using climbing jacks to provide adequate clearance for the removal of temporary abutments	7/14 and 7/15/2022
Removing temporary abutments	7/14/2022
Grinding sole plates under each knuckle	7/15/2022
Installing SPMTs underneath the knuckles (refer to Figure 3-8)	7/16 /2022
Performing bridge lift-off tests	7/18/2022
Installing skid rails at the south abutment	7/18/2022
Moving the bridge superstructure from BSA to the south abutment	7/19/2022
Launching the bridge superstructure over the south abutment (refer to Figure 3-9)	7/20/2022
Preparing the I-94 road surface and installing SPMTs on I-94 for the bridge move operation	7/20 to 7/23/2022
Supporting the north end of the superstructure on SPMTs installed on I-94 and moving the bridge towards the north abutment	7/24/2022
Launching bridge superstructure over both south and north abutments to its final alignment over the bearing, installing climbing jacks under the bridge, and supporting the bridge using support cylinders (refer to Figure 3-10)	7/25/2022
Lowering the bridge onto the permanent bearings	7/26 to 7/28/2022

Figure 3-8. Final SPMT arrangement at BSA.

Figure 3-9. Launching the bridge superstructure over the south abutment.

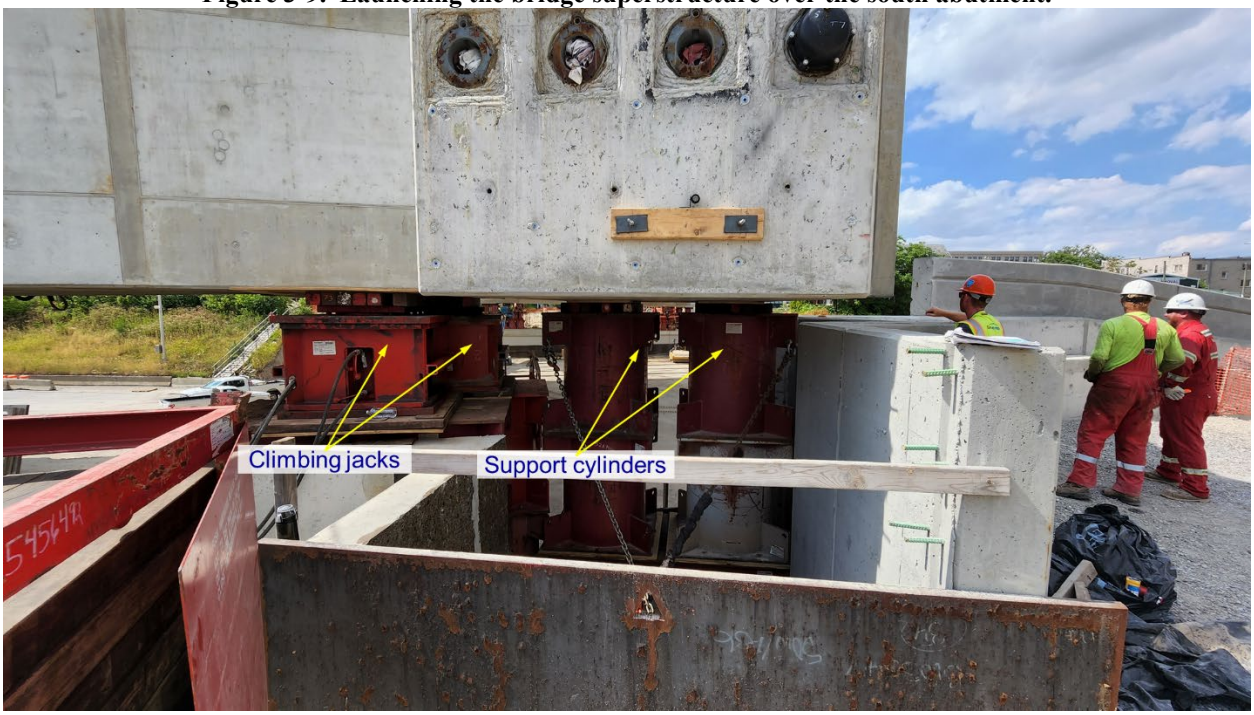

Figure 3-10. Support cylinders and climbing jacks placed underneath the southeast knuckle during the bridge lowering process.

3.4 CONSTRUCTION ACTIVITIES AT THE FINAL ALIGNMENT

The remaining construction activities were completed after the bridge was placed at its final alignment. These activities included deck construction, post-tensioning operations, structural finishing, and site amenities, as detailed in Table 3-4.

The deck pour diagram is shown in Figure 3-11. To maintain structural balance during construction, concrete placement followed a specific sequence centered on floorbeam J, located at the bridge midspan. Two concrete pumps, positioned at each end of the bridge, enabled simultaneous pour operations. The pour sequence was designed to maintain structural equilibrium by limiting the difference in pour length on either side of floorbeam J to a maximum of 5 ft at any time. Concrete placement began at floorbeam J and progressed toward each end while maintaining this balance requirement.

Deck pour E6 commenced at 8:40 p.m. on September 16, 2022, followed immediately by pour E5. Concrete placement started at floorbeam J and progressed toward both ends. Subsequently, pours E1 and E3 were completed concurrently, followed by pours E2 and E4 (Figure 3-12).

Stage 2 post-tensioning was applied to the tie girders on September 29, 2022, before placing pours D3, D4, D5, and D6. Following the removal of temporary arch supports, the remaining deck sections were completed. Figure 3-13 shows concrete placement in sections A1, A2, B1, B2, D1, D2, F, and G on October 15, 2022. All concrete was placed across the bridge width while maintaining the required balance about floorbeam J.

After deck completion, remaining activities included sidewalk construction, barrier railing installation, planter box construction, plinth installation, median construction, soil placement in planters and median, and final landscaping.

During Stage 2 post-tensioning, significant deformation of reinforcing bars was observed in deck sections where reinforcement had been installed but concrete had not yet been placed (Figure 3-14). This deformation resulted from the structural movements induced by post-tensioning. To prevent this issue in future projects, the construction sequence should ensure that all deck sections are either (a) fully concreted before post-tensioning operations, or (b) reinforcement is installed only after post-tensioning is complete. This sequencing issue should be further investigated and incorporated into construction specifications and scheduling for similar arch-tied bridge projects.

Table 3-4. Construction Activities Performed after Bridge Move

Description	Date
Concreting E1, E2, E3, E4, E5, and E6 sections	9/16/2022
Applying the tie girder Stage 2 post-tensioning	9/29/2022
Grouting Stage 2 PT ducts	9/30/2022
Removing lateral arch supports	10/1/2022
Concreting A1, A2, B1, B2, D1, and D2, F, and G sections (refer to Figure 3-13)	10/15/2022
Concreting D3, D4, D5, and D6 sections	10/18/2022
Concreting west sidewalk sections B, C, D, E, and S	10/27/2022
Concreting east sidewalk sections H, J, K, L, and T	10/28/2022
Concreting west sacrificial nosing - pour U	11/7/2022
Concreting east sacrificial nosing - pour U	11/15/2022
Concreting the west side safety barrier (not shown in the pour diagram, but presented in the structural drawings)	11/28/2022
Concreting west planter boxes - pour R	11/29/2022
Concreting the east side safety barrier (not shown in the pour diagram, but presented in the structural drawings)	12/2/2022
Concreting east planter boxes - pour R	12/7/2022
Concreting plinths on the east side – pour N	4/3/2023
Concreting plinths on the west side – pour N	4/26/2023
Concreting planter boxes at the median – pour R	5/3/2023
Filling soil into planter boxes along the sidewalks and the median	6/29/2023

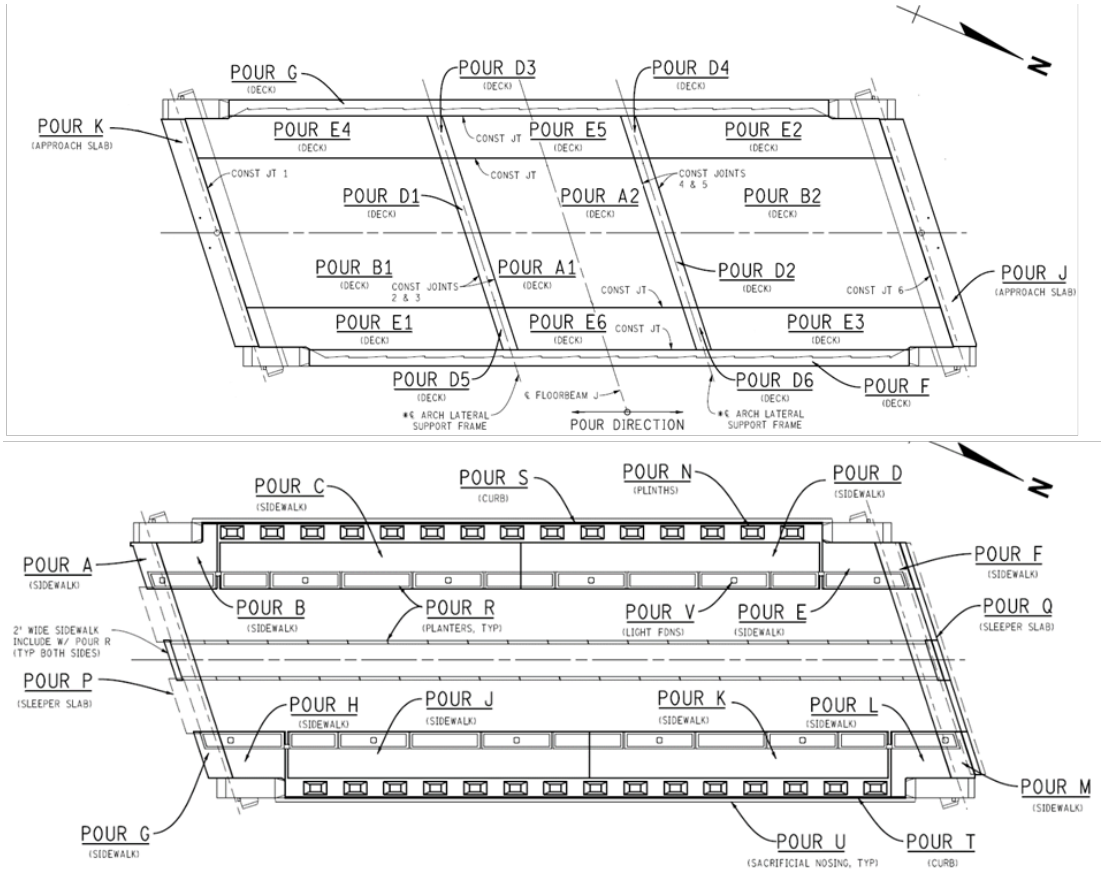

Figure 3-11. Deck pour diagram showing pour designations.

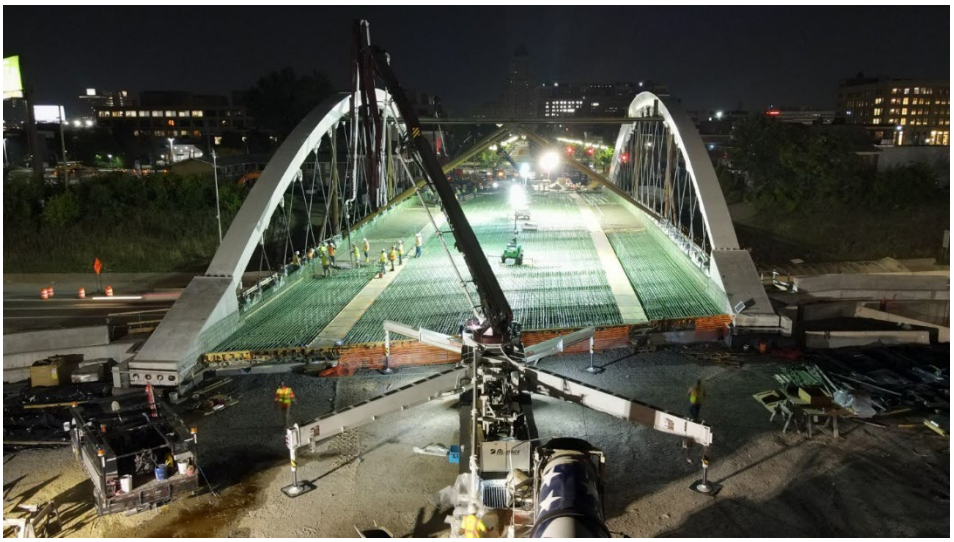

Figure 3-12. Concrete placement in progress for deck sections E2 and E4 (photo credit: Pat Sullivan, Z Contractors Inc.)

Figure 3-13. Concrete placement for deck sections A1, A2, B1, B2, D1, D2, F, and G, October 15, 2022.

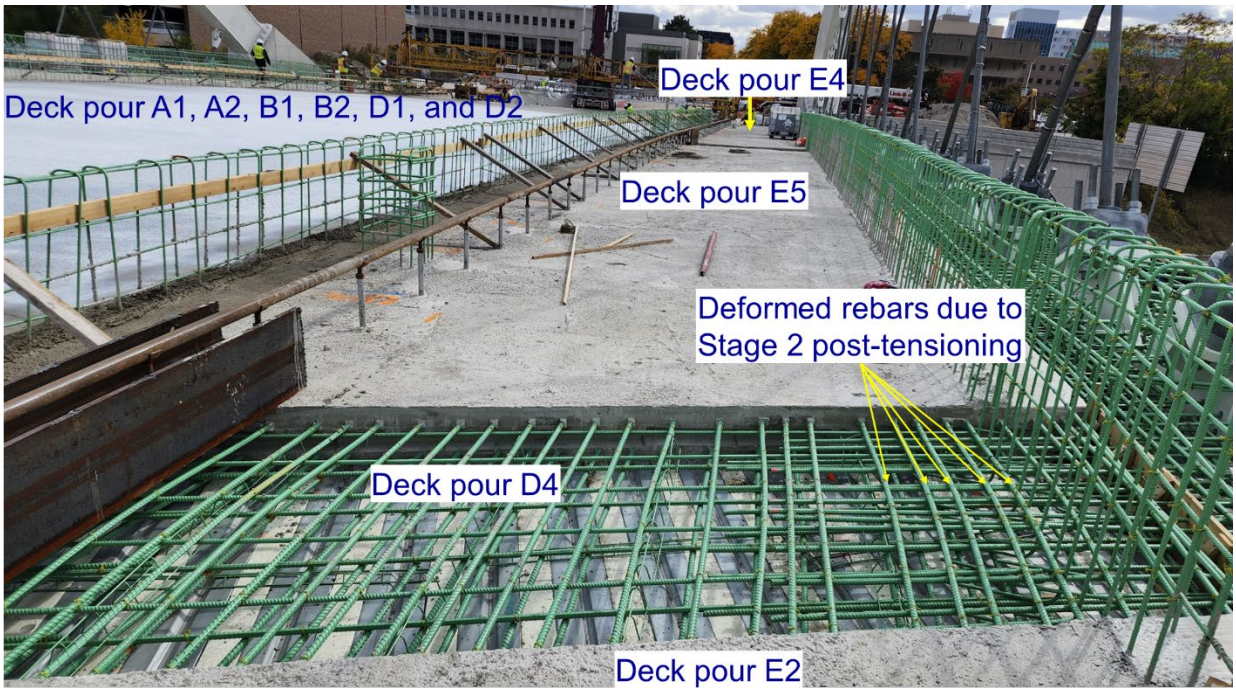

Figure 3-14. View of the deck after completing the deck pours on October 15, 2022.

Figure 3-15. Bird's-eye view of the completed superstructure before placing soil in the planter boxes and the raised median (photo credit: Pat Sullivan, Z Contractors Inc.).

4 INSTRUMENTATION OF PT MEMBERS AND HANGERS

4.1 OVERVIEW

Three instrumentation and monitoring systems were deployed at various stages of the construction process to support quality control, structural assessment, and long-term performance evaluation. The primary monitoring system consisted of 96 vibrating wire (VW) strain sensors and 16 strandmeters with thermistors. The VW strain sensors were embedded in the tie girders, knuckles, and end diaphragms. Strandmeters were mounted on the hangers. This system was activated on the first day of concrete placement and designed to serve two purposes: (i) assess the state of stress during construction and (ii) monitor strain changes during the bridge's service life to support maintenance and load rating decisions. A temperature monitoring system comprising 168 thermocouples was designed and implemented by a consultant hired by the contractor to track concrete temperatures during fabrication and manage the curing process of knuckles, tie girders, and end diaphragms. A third monitoring system, also designed and implemented by a consultant hired by the contractor specifically for the bridge move operation, utilized reflectors, a robotic total station, electrified string lines pulled diagonally between the structure's four corners, and linear variable differential transformers (LVDTs) to monitor superstructure deformations during the SPMT move and lateral launching operations. These systems served distinct but complementary roles in ensuring safety and construction quality while establishing baseline data for future structural assessment. This chapter describes the monitoring system with VW strain sensors and strandmeters, as well as the temperature monitoring system with 168 thermocouples.

4.2 MONITORING SYSTEM COMPONENTS

The monitoring system consists of 96 VW strain sensors and 16 VW strandmeters with thermistors to monitor strains and temperature in the PT concrete frame and the hangers during every stage of construction, thereby establishing the final state of stress in the structure. The VW strain sensors were embedded in PT tie girders, end diaphragms, and knuckles. Eight hangers in each frame were instrumented with strandmeters. The initial sensor settings were determined based on the EOR analysis model results and contractor submittals. All these sensors were connected to two sixty-four (64) channel data acquisition systems (DAQs). One of these DAQs was designated as the *master node,* and the communication between the *master* and *slave* nodes was established using a cross-communication cable. DAQs were installed on top of the south abutment wall and in front

of the end diaphragm. The interior layout of both DAQs is identical, except that the *master node* is equipped with a cellular modem to transfer data to a server for further analysis. Figure 4-1 shows the strain sensor locations in the PT concrete frame, instrumented hangers, and the locations of the DAQs.

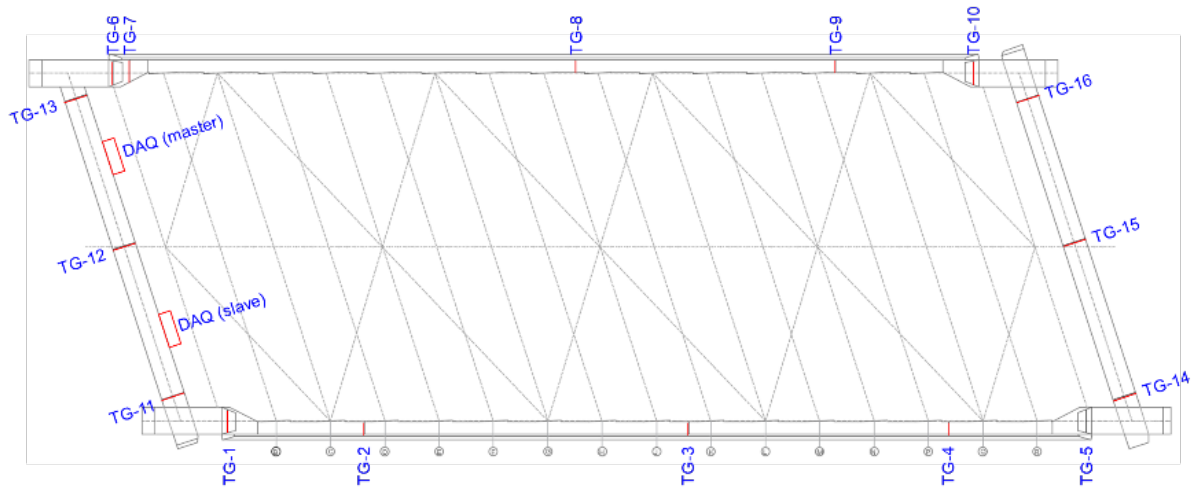

(a) Strain sensor locations in the PT concrete frame

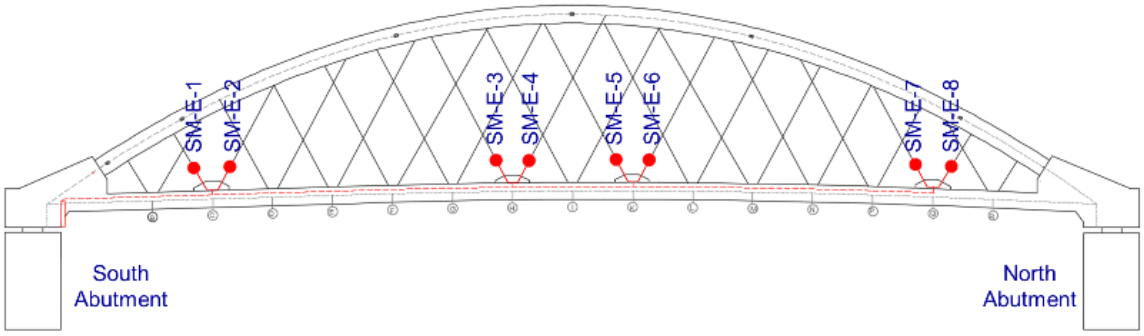

(b) Instrumented hangers at the east arch

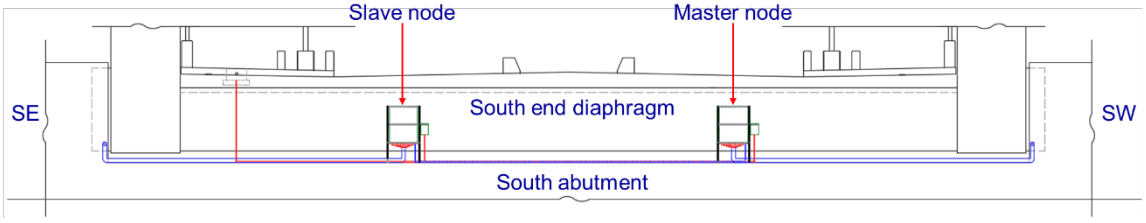

(c) Position of the DAQs on top of the abutment wall

Figure 4-1. VW sensor layout and the locations of the DAQ systems.

4.2.1 Strain Sensors

Three (3) different strain sensor arrangements were utilized based on the significance of the location. Eight (8) sensors are in sections TG-1, TG-3, TG-5, TG-6, TG-8, and TG-10. Six (6) sensors are in sections TG-2, TG-4, TG-7, and TG-9. Four (4) sensors are in sections TG-11 through TG-16. The sensors at TG-1, TG-5, TG-6, and TG-10 sections are located beneath the

arch ribs' baseplates to record strains due to the transfer of loads between the arch ribs and the knuckles. Although the original plan was to install sensors at TG-2, TG-4, TG-7, and TG-9 within the tapered section (i.e., the tie girder-knuckle transition zone), only the sensors at TG-7 could be installed there due to several challenges encountered during the construction and scheduling of this complex structure. The stability of arches is also a concern for these types of structures. However, considering the practical challenges of running sensor cables through the arch ribs and the need for future maintenance, sensors were not included in the arch ribs. Yet, this is not a limitation since any issues related to the global stability of the ribs can be evaluated using data from the VW strain gauges located under the arch base plates and the strandmeters mounted on the hangers. As per the construction schedule, many of these sensors were required to be attached to the rebar cage during the winter months with temperatures well below 0° F. To minimize time spent at the site, the sensors were prepared in the laboratory by attaching two 1-in. thick Styrofoam blocks to the ends of each sensor as spacers. The sensors were tied to rebars using ty-raps or rebar ties (Figure 4-2). Figure 4-3 presents the arrangement of VW sensors and the number of sensors in each section. All the sensors were oriented perpendicular to the cross-section at their respective locations.

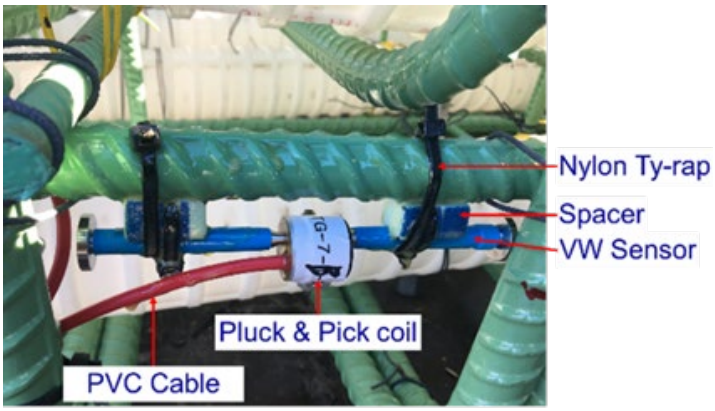

Figure 4-2. A VW strain sensor mounted on a rebar.

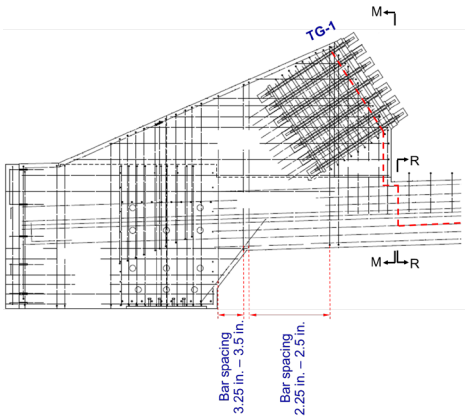

(a) Section below the arch rib baseplate

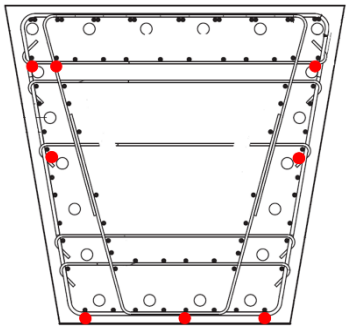

(b) Eight sensors at TG-1, -5, -6, and -10 sections

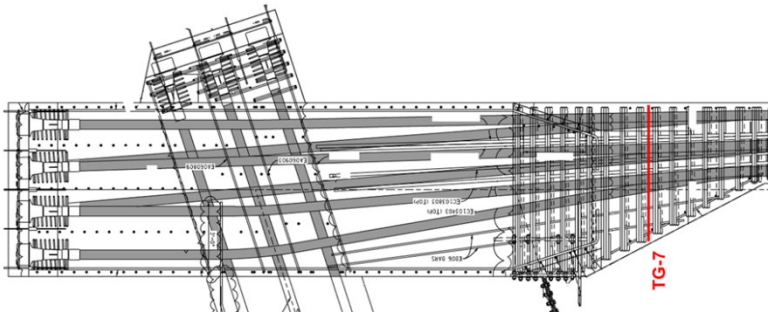

(c) Section TG-7 in the lower southwest knuckle

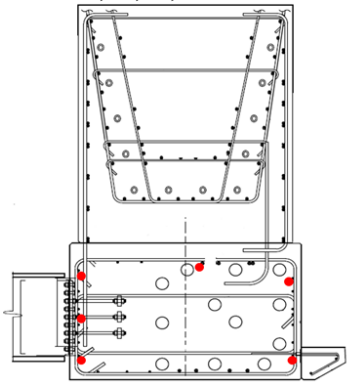

(d) Six sensors at the TG-7 section

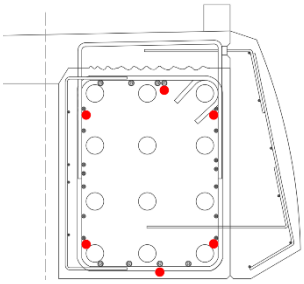

(e) Six sensors at TG-2, -4, and -9 sections

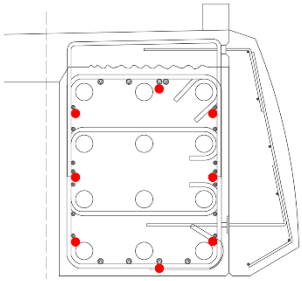

(f) Eight sensors at TG-3 and -8 sections

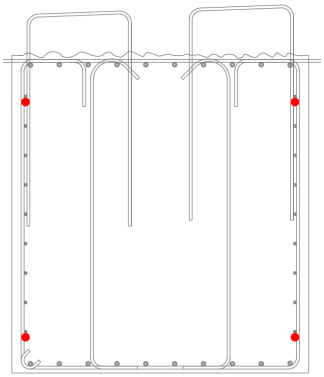

(g) Four sensors at TG-11 through 16 sections

Figure 4-3. VW strain sensor arrangements at selected cross-sections.

4.2.2 Strandmeters

The original erection plans required leaving an adequate space for the hydraulic jack arrangement to tension hangers and subsequently verify the hanger tension. This requirement did not leave adequate space to install strandmeters on the 1st and 2nd hangers, specifically those closer to the knuckles (i.e., WH1, WH2, WH29, WH30, EH1, EH2, EH29, and EH30), even though the forces in those hangers calculated from the two analysis models were significantly different. Therefore,

the strandmeters were installed on the 3rd and 4th hangers from the knuckles (i.e., WH3, WH4, WH27, WH28, EH3, EH4, EH27, and EH28). Additionally, four hangers at the midspan of each tie girder were instrumented (i.e., WH13, WH14, WH17, and WH18; EH13, EH14, EH17, and EH18). As illustrated in Figure 4-4, the strandmeters were mounted approximately 50 in. above the hanger plate using two hose clamps, leaving sufficient space for the hydraulic jack arrangement. An adhesive (Kearney Aqua Seal -0104742) was used between the hanger and the clamps to prevent galvanic corrosion. The exposed cable along the hangers was protected with liquid-tight, flexible, non-metallic PVC conduits.

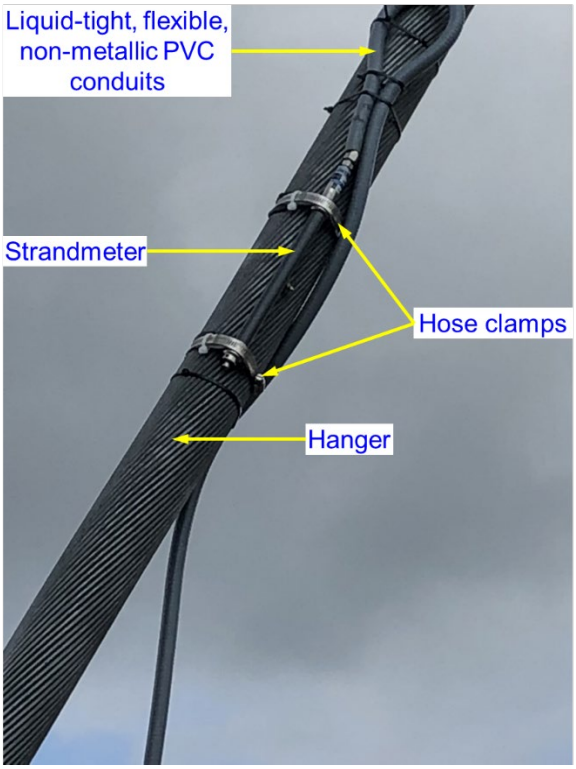

Figure 4-4. Strandmeter installation.

4.2.3 Data Acquisition Systems (DAQs)

The *master node* configuration is shown in Figure 4-5. The system consists of four 1-channel multiplexers, a datalogger, a power distribution circuit board, and a 12-volt lead-acid battery. Only the *master node* is equipped with a cellular modem, which facilitates remote access to the entire monitoring system. Figure 4-5b shows the bottom of the enclosure, featuring Ethernet and USB communication ports, a grounding terminal, a charging port, and an array of watertight cable entry terminals for sensor connections.

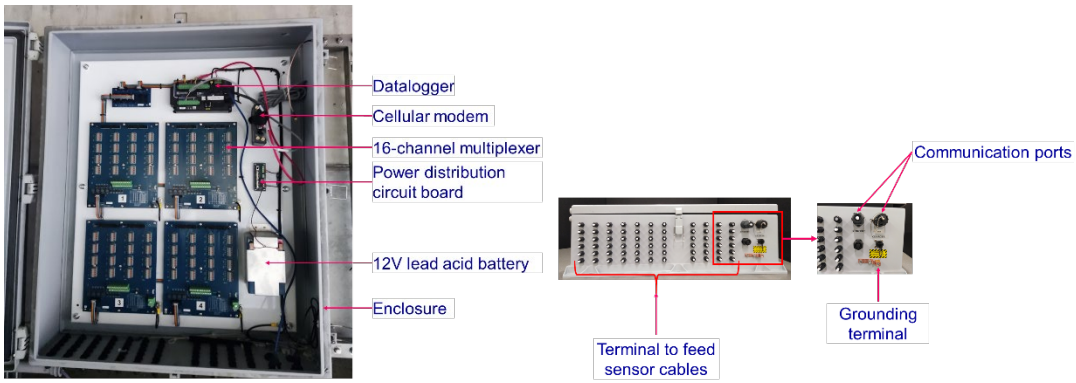

(a) Components of the *master node* (b) The bottom view of the enclosure

Figure 4-5. Components of the *master node*.

Figure 4-6 presents the multiplexer slot configuration. Each of the 4 multiplexers has 16 slots, providing a total of 64 sensor connections. Of these, 52 terminals are allocated for VW strain sensors (48 currently installed, 4 reserved for future expansion), and 10 terminals are allocated for VW strandmeters (8 currently installed, 2 reserved for future expansion). The remaining 2 terminals are left unprogrammed for potential future use. This configuration allows for modest system expansion without hardware modification.

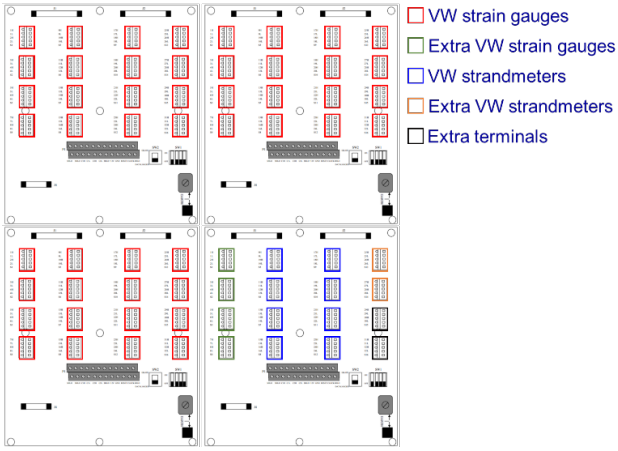

Figure 4-6. Multiplexer slot configuration.

4.2.4 Power Supply

Each monitoring node is powered by an internal 12-volt lead-acid battery, which requires continuous external charging. The monitoring system was connected to the grid on May 24, 2024. Prior to this connection, each node operated on a temporary solar power system consisting of a solar panel and two 88Ah deep-cycle marine batteries connected in parallel (Figure 4-7). This temporary configuration provided reliable power from the construction start date of November 3, 2021, until the permanent power connection was established—a period of approximately 30 months.

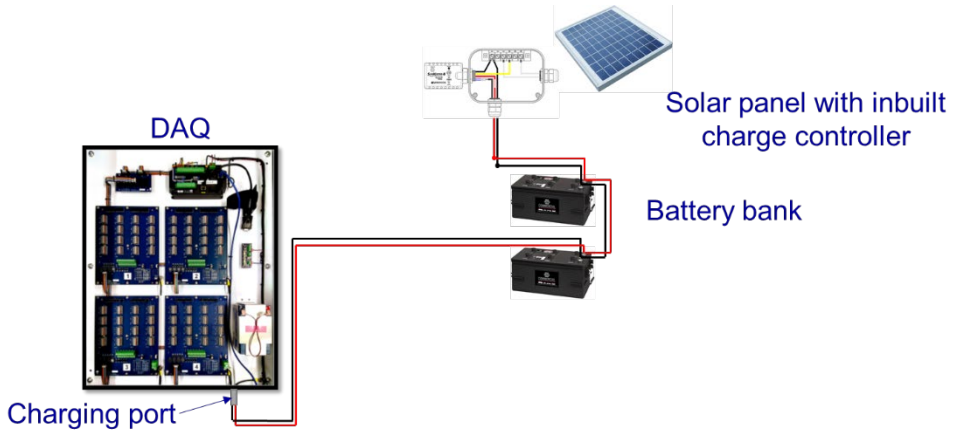

Figure 4-7. Basic components of the temporary power supply.

4.2.5 Cable Management

Power supply lines routed along the bridge superstructure for lighting systems (Figure 4-8) created potential electromagnetic interference (EMI) concerns for the monitoring system. EMI from power sources can contaminate sensor readings, and VW sensors are particularly susceptible due to their dual-coil design. In the absence of established industry standards for EMI spacing requirements, the design team consulted with the sensor manufacturer and established project-specific criteria based on similar installations and conservative engineering judgment. To minimize interference, sensor cables were positioned with at least 12 in. separation from 110/120 V AC power lines and routed through separate grounded metal conduits. Additional mitigation measures included electronic filtering (50/60 Hz noise rejection, common-mode filtering, and bandpass filtering) and adherence to standard wiring practices: minimizing cable lengths, avoiding cable coiling, maintaining perpendicular crossings with power lines, using high-quality shielded cables, and ensuring proper grounding of all components.

The permanent sensor cable layout is shown in Figure 4-9. Sensor cables are routed within the sacrificial nose sections, positioned outside the tie girders. At these locations, the nearest sensors and their associated cables are approximately 15.5 in. and 45.5 in. from parallel power cables, respectively—well exceeding the 12 in. minimum spacing requirement established for EMI mitigation. As shown in Figure 4-1c, sensor cables exiting the sacrificial nose are enclosed in PVC conduits and routed along the abutment wall to the DAQs. All sensors in the east and west arch frames, as well as those at the diaphragm ends, connect to the nearest *node* located atop the abutment wall. Sensors at TG-12 and TG-15 connect to the *slave* node and *master* node, respectively. Both DAQ nodes are electrically grounded to minimize electromagnetic interference.

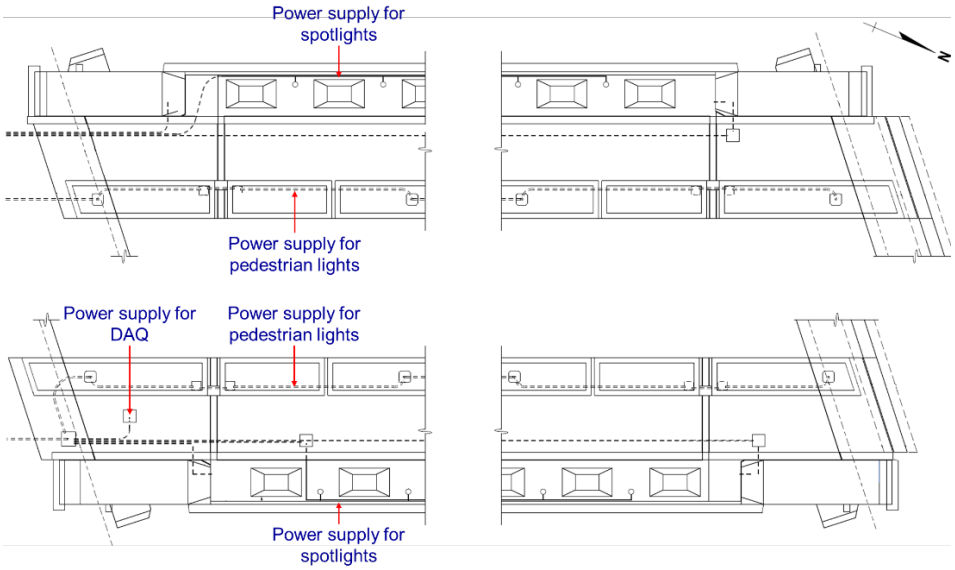

Figure 4-8. Electrical cable layout.

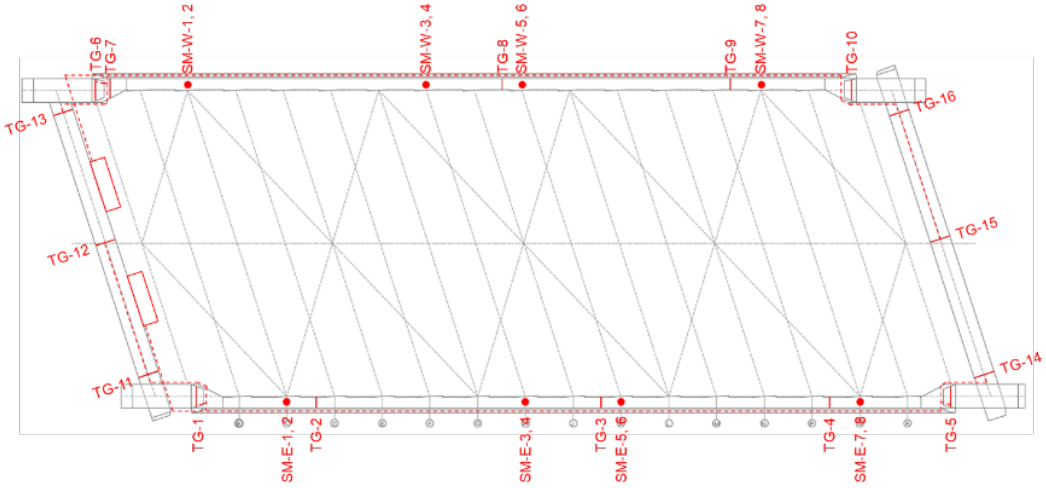

(a) Cable layout along the PT concrete frame

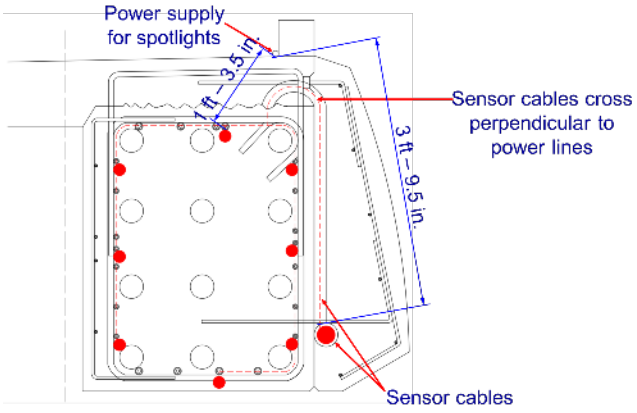

(b) Cable layout within the PT tie girder section

Figure 4-9. Cable layout.

4.3 THERMAL CONTROL PLAN

The project specifications required limiting the maximum temperature to 150° F and the maximum temperature difference between the interior and surface of the concrete elements to 35° F during hydration. To monitor compliance with these thermal control requirements, the contractor installed thermocouples throughout the PT frame to track concrete temperatures during the initial curing period. Figure 4-10 shows the locations of both the temporary thermocouples and the permanent VW strain sensors with integrated thermistors (described in Section 4.2.1).

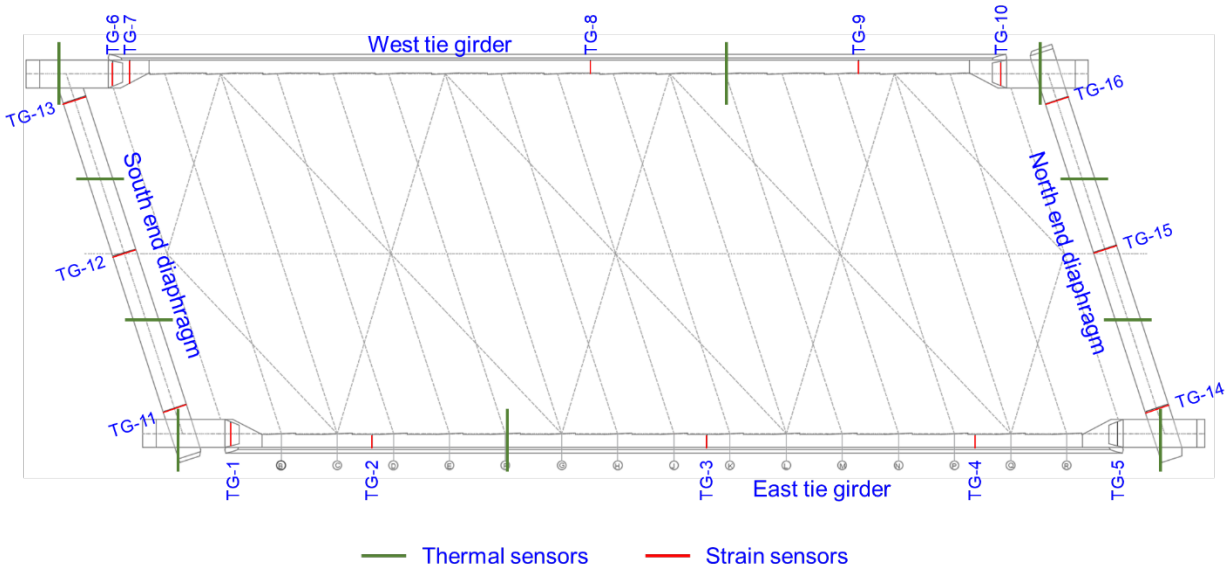

Figure 4-10. The locations of thermocouples and VW sensors with thermistors.

4.3.1 Thermocouple Locations in Lower and Upper Knuckles

Figure 4-11 shows the elevation and plan views of the lower knuckle and the thermocouple locations. Twelve thermocouples were placed in each lower knuckle. Out of these 12 sensors, 6 were backup sensors. Thermal monitoring of the lower SW, NW, SE, and NE knuckles continued for about 14, 19, 16, and 19 days, respectively.

Figure 4-12 shows the elevation and plan views of the upper knuckle and the thermocouple locations. Twelve thermocouples were placed in each upper knuckle. Out of these 12 sensors, 6 were backup sensors. Thermal monitoring of the upper SW, NW, SE, and NE knuckles continued for about 7, 9, 6, and 10 days, respectively.

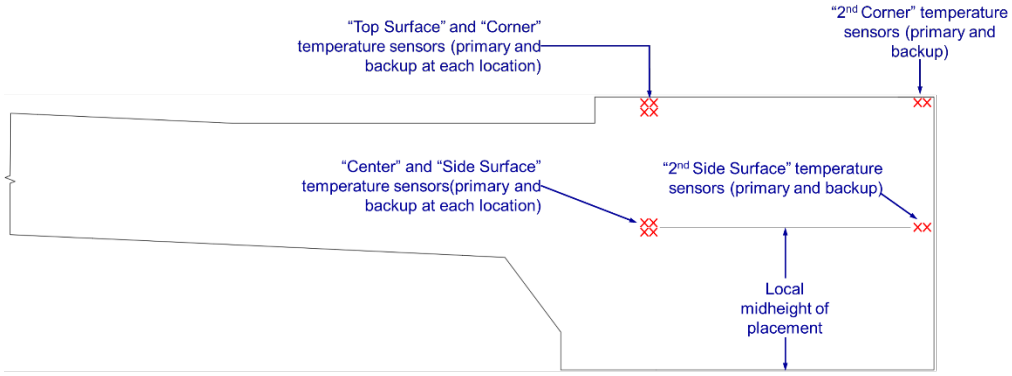

(a) Elevation view

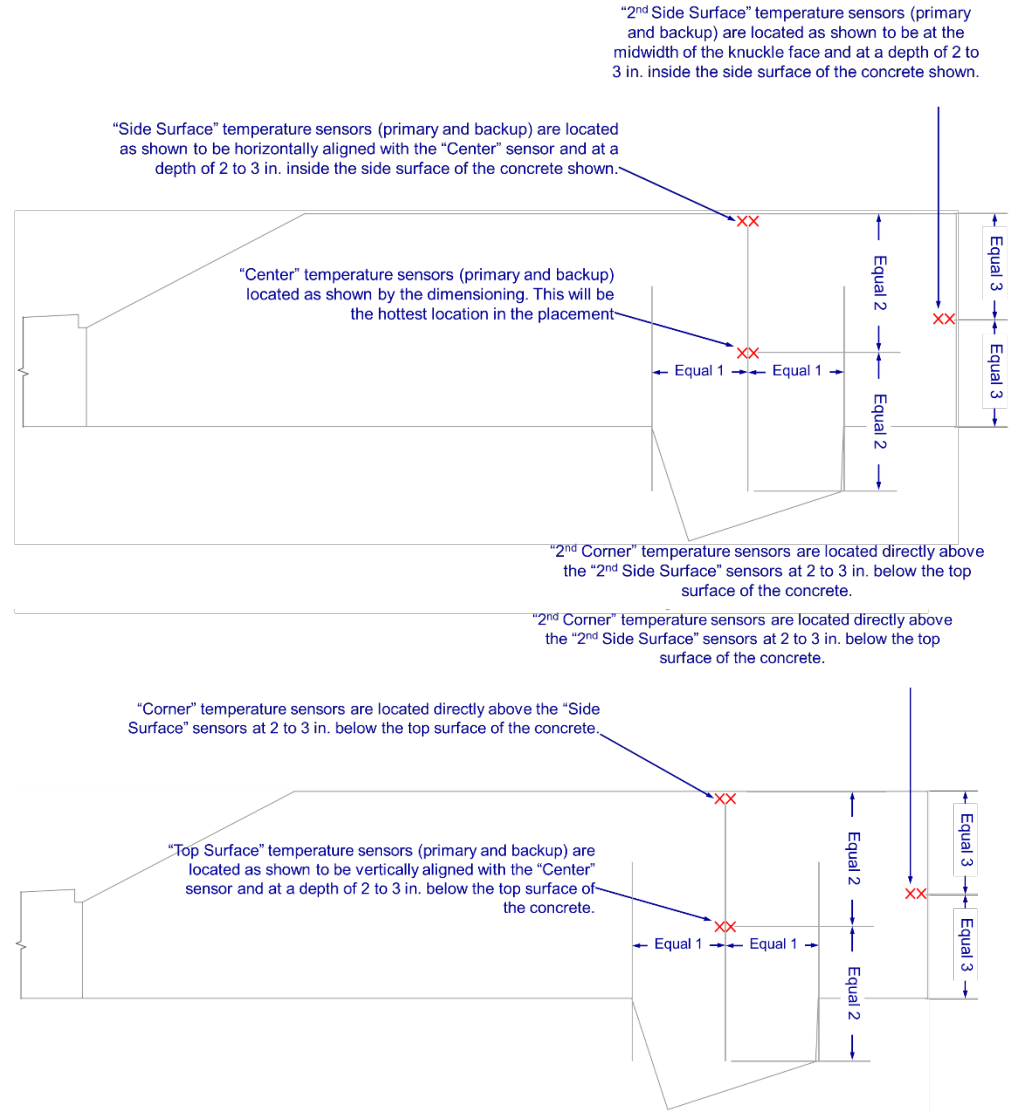

(b) Plan view showing temperature sensor locations at the midheight of the lower knuckle placements (SW/NE shown; SE/NW similar)

Figure 4-11. Thermocouple layout in the lower knuckles.

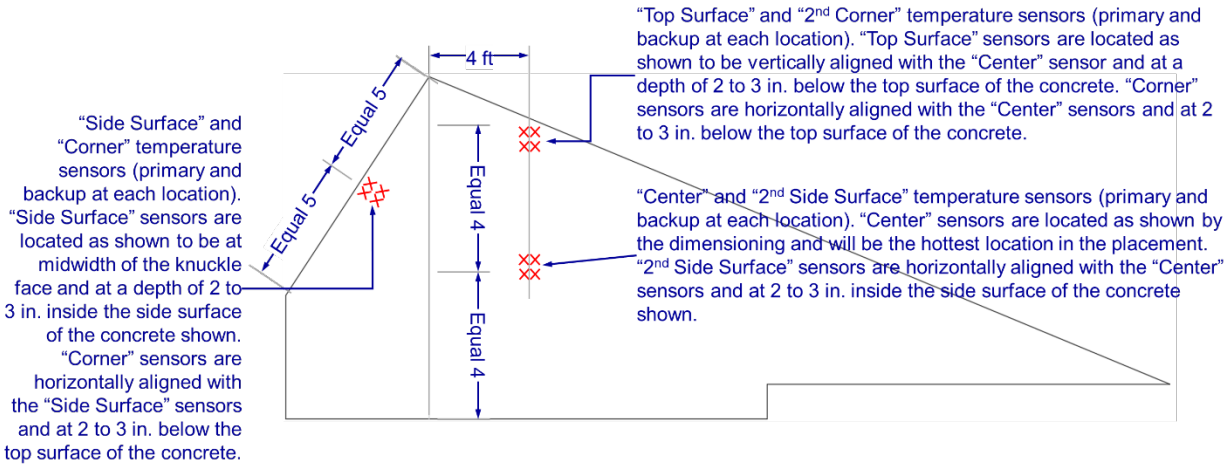

(a) Elevation view

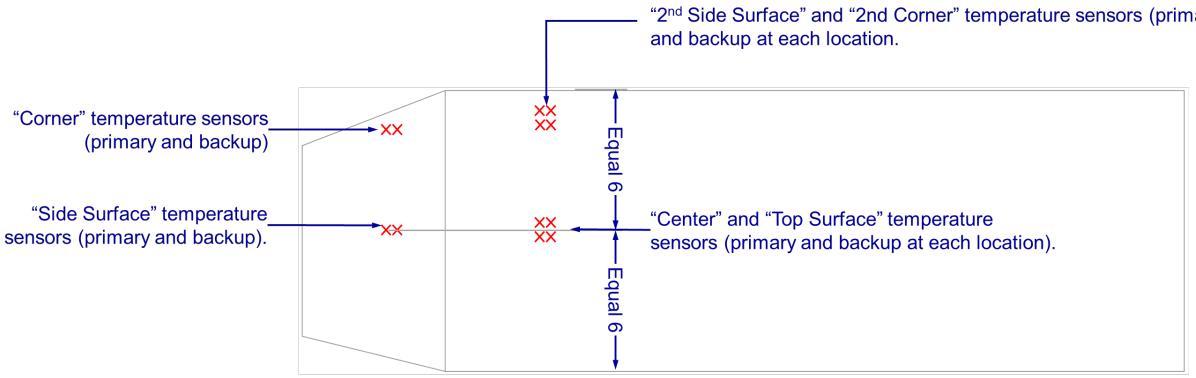

(b) Plan view

Figure 4-12. Thermocouple layout in the upper knuckles.

4.3.2 Thermocouple Locations in Tie Girders

As shown in Figure 4-10, thermocouples were installed in the west tie girder closer to the north end and in the east tie girder closer to the south end. A total of 12 thermocouples (primary and backup) were distributed within each girder cross-section. Figure 4-13 shows the primary thermocouple layout in the girder cross-section. Of the 12 sensors, six monitored temperature at the top, and the other six monitored temperature at the middle. The monitoring of the west tie girder continued for about 5 days, while the east tie girder monitoring continued for about 7 days.

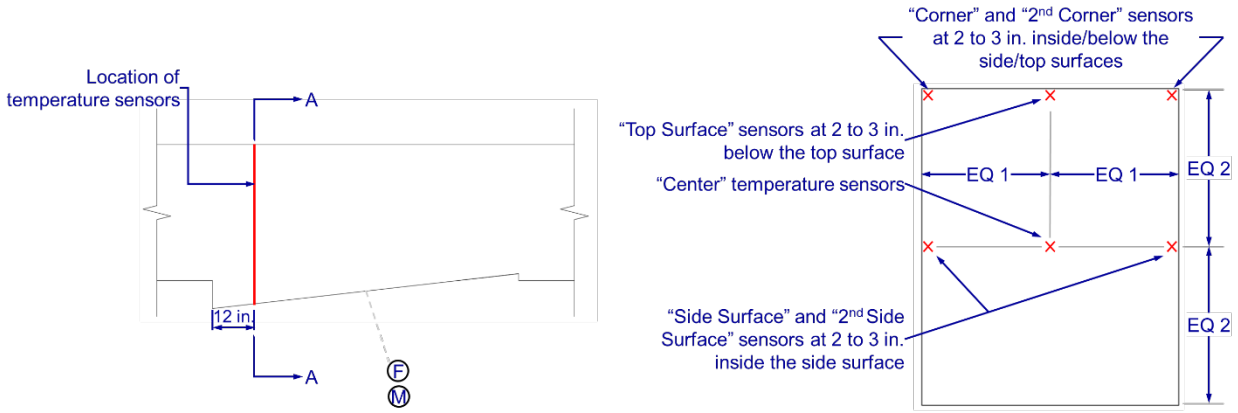

(a) Plan view (b) Section A-A

Figure 4-13. Thermocouple layout in the tie girders (Back-up sensors not shown).

4.3.3 Thermocouple Locations in End Diaphragms

As shown in Figure 4-10, thermocouples were installed at 1/3rd locations along the end diaphragms. A total of 12 thermocouples were distributed within each cross-section. Out of the 12 sensors, 6 were backup sensors. Figure 4-14 shows the thermocouple layout (primary) in the end diaphragm cross-section. Of the 12 sensors, six monitored temperature at the top, and the other six monitored temperature at the middle. Thermal monitoring of the end diaphragms was continued for about 7 days.

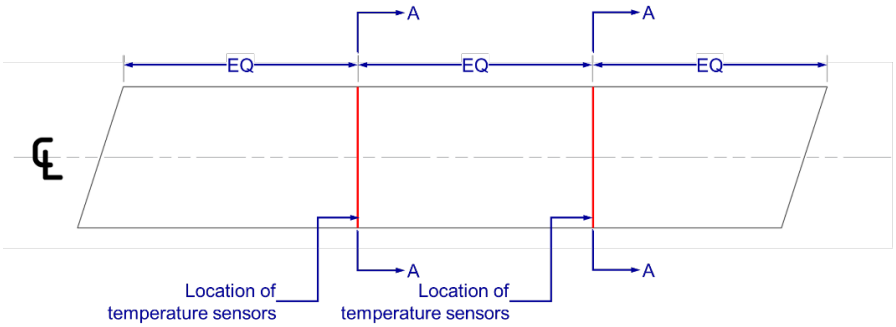

(a) Plan view

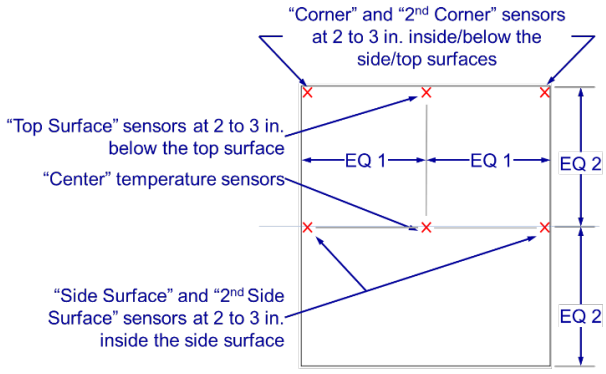

(b) Section A-A

Figure 4-14. Thermal sensor layout in the end diaphragms (Backup sensors not shown).

5 MONITORING DURING CONSTRUCTION

5.1 OVERVIEW

As described in Chapter 3 and detailed in Table 3-1 through Table 3-4, bridge construction was divided into three main stages: construction at BSA, the bridge move operation, and construction at the final alignment. The monitoring system was designed to capture strain variations resulting from construction activities, volume change effects, and in-service loads. Volume change effects include immediate elastic shortening due to post-tensioning, as well as time-dependent phenomena such as concrete shrinkage and creep, prestress relaxation, and thermal expansion and contraction due to ambient temperature variations. This chapter presents strain data from instrumented structural members during each construction stage.

5.2 STRAIN VARIATION IN TIE GIRDERS

Figure 5-1 and Figure 5-2 present strain variations in the west and east tie girders, respectively, from the start of construction through project completion on October 27, 2023. Each plot shows strains recorded by VW sensors at specific cross-sections, capturing the combined effects of temperature, concrete creep and shrinkage, post-tensioning, and applied loads. Negative strain values represent compression. The labels are provided to indicate the variation of strain during post-tensioning and deck concrete pours until the project was completed on October 27, 2023.

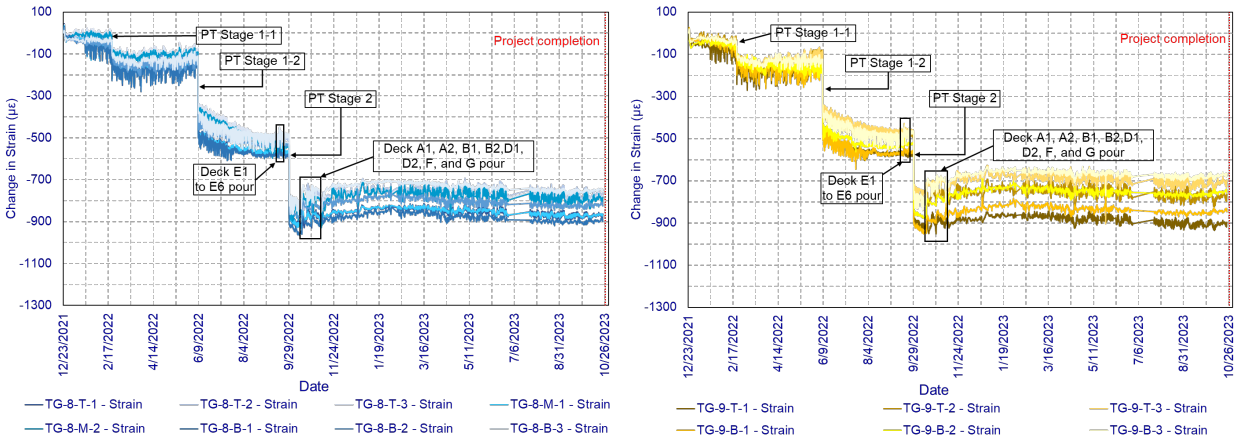

(a) At TG-8 (b) At TG-9

Figure 5-1. Strain variation at (a) TG-8 and (b) TG-9 during construction.

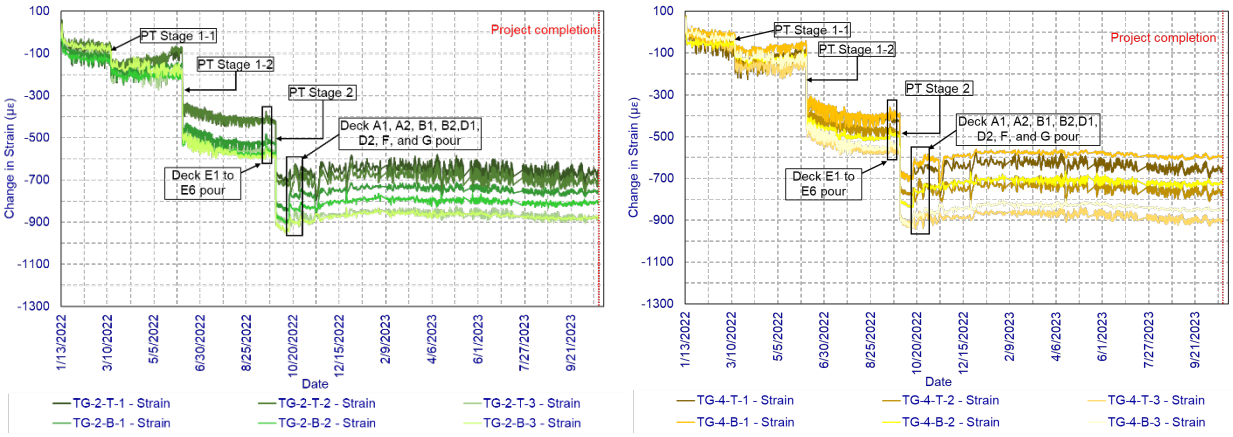

(a) At TG-2 (b) At TG-4

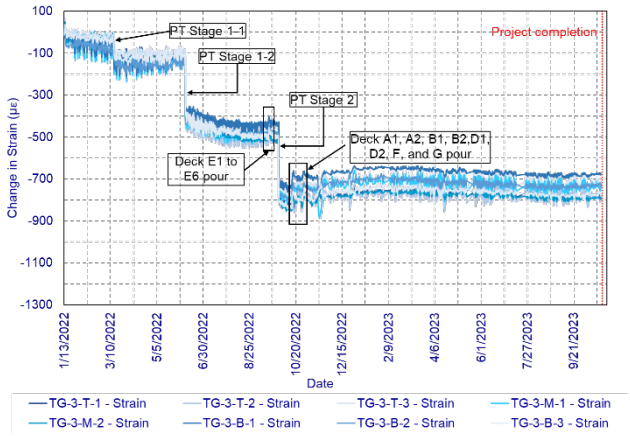

(c) At TG-3

Figure 5-2. Strain variation at (a) TG-2, (b) TG-4, and (c) TG-3 during construction.

Figure 5-3 shows the geometry and post-tension duct configuration of the west tie girder with two knuckles. Figure 5-3b shows the tendon layout at midspan. Figure 5-3c shows the tendon layout at the end of a knuckle. Each tie girder has 12 post-tension tendons (TT01 to TT12). Each tendon has 19 Grade 270 low-relaxation, 0.6 in. diameter 7-wire strands. The plan and elevation views of the tendon layout along the tie girder are shown in Appendix D.

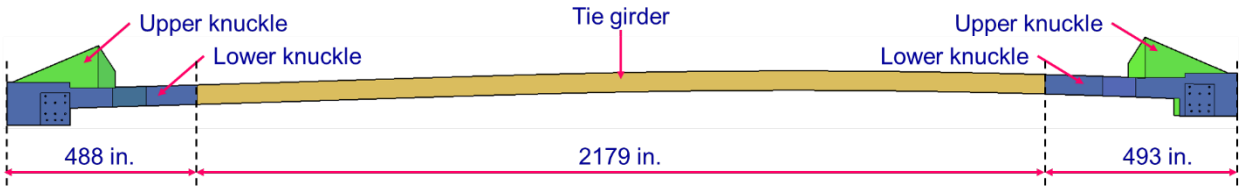

(a) Geometry of the west tie girder with end knuckles

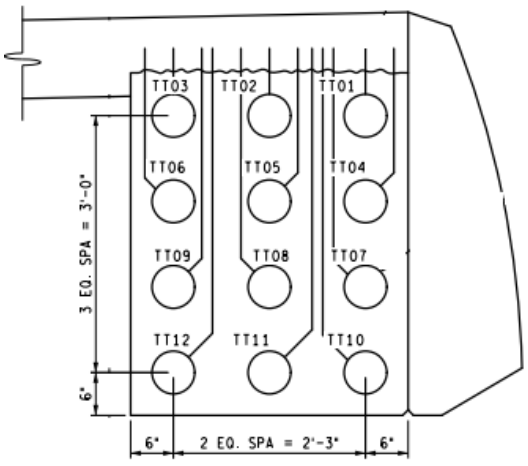

(b) Tendon layout at midspan

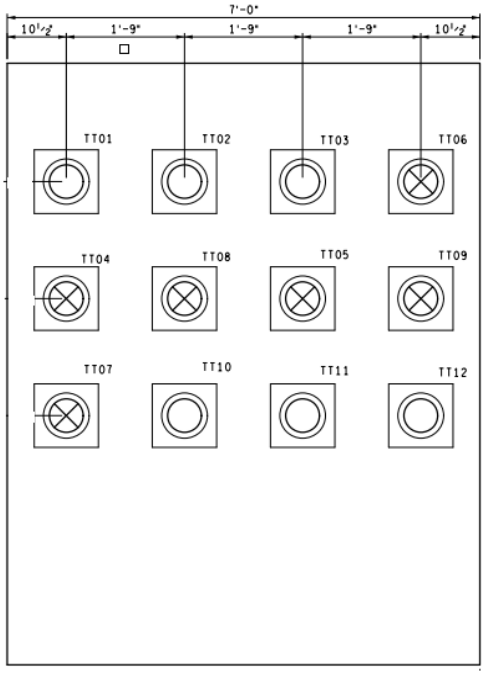

(c) Tendon layout at the knuckle end

Figure 5-3. Geometry and tendon layout of a post-tensioned tie girder; (a) tie girder geometry with knuckles, (b) tendon layout at midspan, and (c) tendon layout at knuckle end.

As described in Chapter 3, the tie girders were post-tensioned longitudinally in two stages. Stage 1 post-tensioning occurred at the BSA in two steps prior to the bridge move. During Stage 1-1, tendon TT08 was stressed. During Stage 1-2, five additional tendons were stressed sequentially in the following order: TT05, TT04, TT09, TT06, and TT07. Stage 2 post-tensioning was applied after the bridge was placed on permanent bearings at the final alignment and following partial deck placement. The remaining six tendons were stressed in the order: TT03, TT10, TT12, TT01, TT02, and TT11. The jacking force per tendon was 780 kips. The tendons in the west tie girder were stressed from the southwest (SW) end. The tendons in the east tie girder were stressed from the southeast (SE) end.

Table 5-1 lists the fabrication and post-tensioning schedule of tie girders. The west tie girder was fabricated 21 days before the east tie girder. The age of the west and east tie girders at Stage 1-1 post-tensioning was 60 days. The ages of the west and the east tie girders at Stage 1-2 post-

tensioning were 167 days and 146 days, respectively. The ages of the west and the east tie girders at Stage 2 post-tensioning were 280 days and 259 days, respectively. As shown in the table, the ducts were not immediately grouted after post-tensioning.

Table 5-1. Construction and Post-tensioning Schedule of Tie Girders

Component	Date of Fabrication	Post-tensioning Stage	Date of Post-tensioning	Date of Grouting	Time Between Post-tensioning and Grouting (days)	Age of Tie Girder at the Time of Post-tensioning (days)
West tie girder	12/23/21	Stage 1-1	2/21/22	5/4/22	72	60
		Stage 1-2	6/8/22	6/13/22	5	167
		Stage 2	9/29/22	9/30/22	1	280
East tie girder	1/13/22	Stage 1-1	3/14/22	5/2/22	49	60
		Stage 1-2	6/8/22	6/13/22	5	146
		Stage 2	9/29/22	9/30/22	1	259

As shown in Figure 5-1 and Figure 5-2, instantaneous compressive strain increases occurred during each post-tensioning stage, as expected. Following post-tensioning, gradual strain relaxation was observed due to the combined effects of concrete creep and shrinkage.

However, two deviations from this general trend were noted. First, strains increased from March 29, 2022, to June 8, 2022, during arch rib erection and hanger tensioning operations, indicating load transfer from the arch system to the tie girders. Second, intermittent strain increases coincided with deck concrete placement, reflecting the addition of dead load.

5.2.1 Static Modulus of Elasticity of Tie Girder Concrete

As discussed in Chapter 3, each tie girder remained an independent member during Stage 1-1 post-tensioning, since the arch was erected between Stage 1-1 and 1-2 post-tensioning, and the end diaphragms were fabricated after the arch was erected. Hence, the use of elastic shortening is a reasonable approach to estimate the modulus of elasticity (MOE) of tie girder concrete. Furthermore, the analysis of the tie girder with and without the arch revealed that the arch's impact on the tie girder's elastic deformation during Stage 1-2 post-tensioning was minimal. Additionally, the evaluation of end diaphragm strains during the Stage 1-2 post-tensioning of tie girders revealed negligible changes, indicating that the end diaphragm did not provide any resistance to tie girder deformation. For these reasons, using elastic shortening of tie girders during Stage 1-2 post-tensioning is a reasonable approach for estimating the MOE of tie girder concrete at that time.

Table 5-2 presents the MOE values calculated using strain data from the tie girders and from testing of 4×8 in. cylinders in the laboratory at the ages of post-tensioning. Appendix C presents the

prestress force estimated at the instrumented locations after accounting for friction and anchorage set loss. The MOE measured using cylinder specimens was higher than that calculated from the tie girder. However, the MOE estimated from measured strains is reasonable when compared with the typical values documented in literature for such mixes.

Table 5-2. Modulus of Elasticity of Tie Girder Concrete

PT Member	PT Stage	Average MOE (ksi)		Deviation of MOE in Girders from the Cylinders (%)
		Girder	Cylinder[1]	
West Tie Girder (at TG-8)	1-1 (60 days)	5094	5851	-12.9
	1-2 (167 days)	6224	6406	-2.8
East Tie Girder (at TG-9)	1-1 (60 days)	5488	6990	-21.5
	1-2 (146 days)	6725	7422	-9.4

[1]- The west tie girder MOE was compared with the MOE of Set 2 (Field) cylinders at 60 days and Set 1 (ASTM+Laboratory) cylinders at 167 days. The east tie girder MOE was compared with the MOE of Set 4 (Laboratory) cylinders at 60 and 146 days. Please refer to Appendix E for a description of the specimen labels and different curing conditions.

5.2.2 Shrinkage and Creep in Tie Girders

From the fabrication to the formwork removal, the measured strain in tie girders is primarily due to autogenous shrinkage. From formwork removal to the first load application (i.e., post-tensioning), autogenous and drying shrinkages contribute to the measured strain. The autogenous shrinkage, drying shrinkage, and total creep strain contribute to the strain recorded after post-tensioning. Figure 5-4 illustrates the temporal development of these components for the west tie girder. The recorded data before post-tensioning is used to calculate autogenous shrinkage and the total shrinkage. Since the strain due to creep cannot be isolated from drying shrinkage using data recorded after post-tensioning, only the measured strain up to post-tensioning is considered.

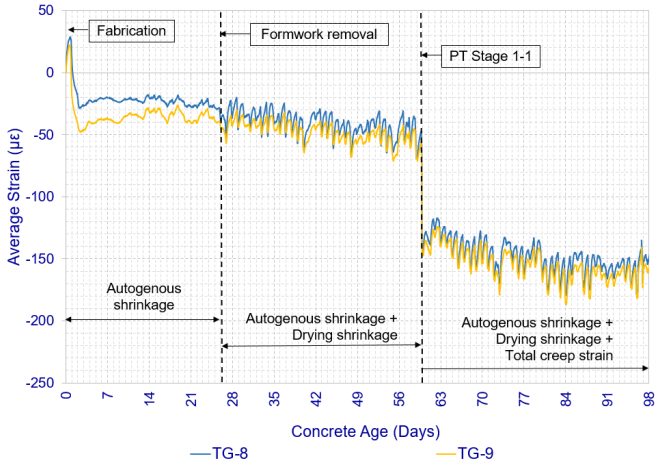

Figure 5-4. Strain variation in the west tie girder.

Figure 5-5 presents average strain evolution in both tie girders from fabrication through Stage 1-1 post-tensioning. By the time of formwork removal, the west tie girder exhibited average strains

of -30 to -40 με, while the east tie girder showed -42 to -70 με. These differences correlate with the timing of formwork removal: the west girder formwork was removed 26 days after fabrication, compared to only 9 days for the east girder.

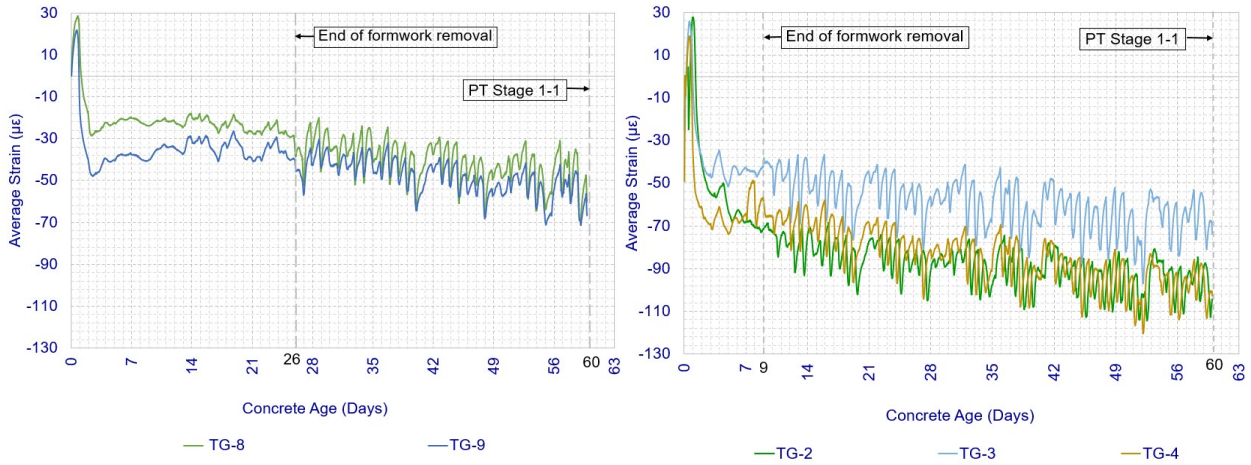

(a) West tie girder (b) East tie girder

Figure 5-5. Variation of shrinkage in the (a) west tie girder and (b) east tie girder.

At 60 days (i.e., just before Stage 1-1 post-tensioning), average strains reached approximately -60 με in the west tie girder and -70 to -100 με in the east tie girder. The incremental strain from formwork removal to post-tensioning averaged 25 με for the west girder [i.e., 60 – (30+40)/2] and 29 με for the east girder [i.e., (70+100)/2 – (42+70)/2]. These incremental strains represent primarily drying shrinkage, as the concrete was exposed to ambient conditions for 34 days (west) and 51 days (east) before post-tensioning. Based on this analysis, autogenous shrinkage accounts for approximately 60-65% of total shrinkage at the time of Stage 1-1 post-tensioning, with drying shrinkage comprising the remaining 35-40%.

Figure 5-6 shows temperature differentials between the center and surface of the tie girders during the first 5-7 days after fabrication. Thermocouples installed at six locations on the girder cross-section (outside face, center, inside corner, inside face, outside corner, and one additional location—see Section 4.3.2 for details) monitored thermal gradients to ensure compliance with the project specification limit of a maximum core-to-surface temperature differential of 35° F. Peak center temperatures were 84.2° F in the west tie girder and 100.4° F in the east tie girder, with minimum temperatures of 47.4° F and 51.8° F, respectively. All measured temperature differentials remained within the specified 35° F limit. The higher curing temperatures in the east tie girder likely contributed to its greater autogenous shrinkage, as higher temperatures accelerate early-age hydration and associated chemical shrinkage.

These early-age thermal and shrinkage effects posed no structural concerns because: (i) temperature differentials remained within specification limits, preventing thermal cracking; (ii) shrinkage strains developed before post-tensioning application, avoiding interaction with prestress; and (iii) the tie girders functioned as unrestrained independent members during this period, eliminating restraint-induced stresses.

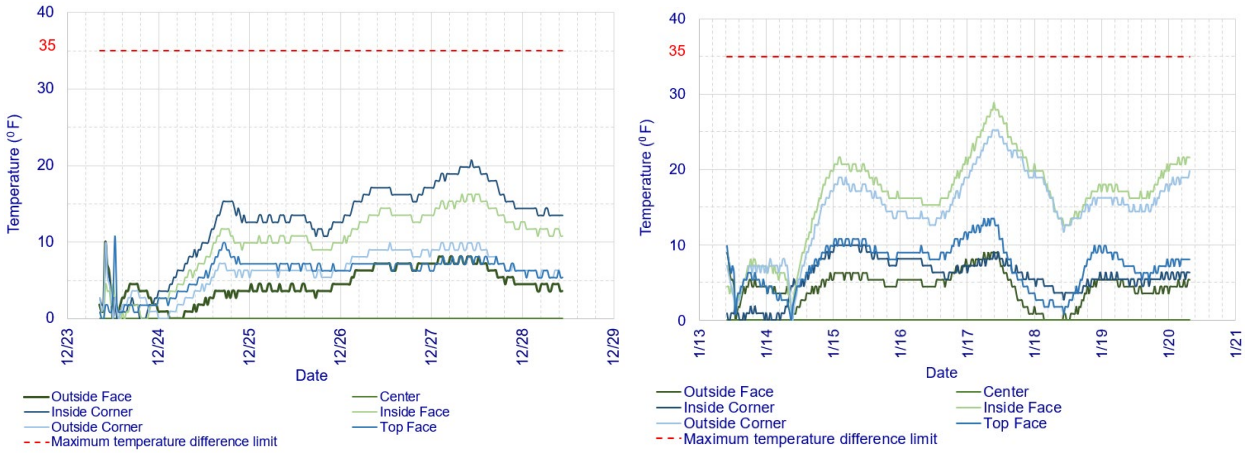

(a) For 5 days from the west tie girder fabrication (b) For 7 days from the east tie girder fabrication

Figure 5-6. The temperature difference observed in the tie girders: (a) for 5 days from the west tie girder fabrication and (b) for 7 days from the east tie girder fabrication.

5.3 STRAIN VARIATION WITHIN THE TAPERED SECTION OF THE SOUTHWEST LOWER KNUCKLE

Tapered sections of both tie girders have complex duct profiles. TG-7 is in the tapered section of the west tie girder, and the strains recorded in that section are shown in Figure 5-7. As explained in Section 4.2.1, 6 VW strain sensors are at TG-7. Due to their proximity to PT ducts, sensors TG-7-T-2, T-3, and B-3 clearly captured the increase in strain during post-tensioning. For example, the T-2 strain sensor shows a significant compression relative to T-3 and B-3 during PT Stage 1-2, whereas the readings at T-1, B-1, and B-2 remain unchanged. This indicates that the tapered section is not compressed as anticipated during the design stage.

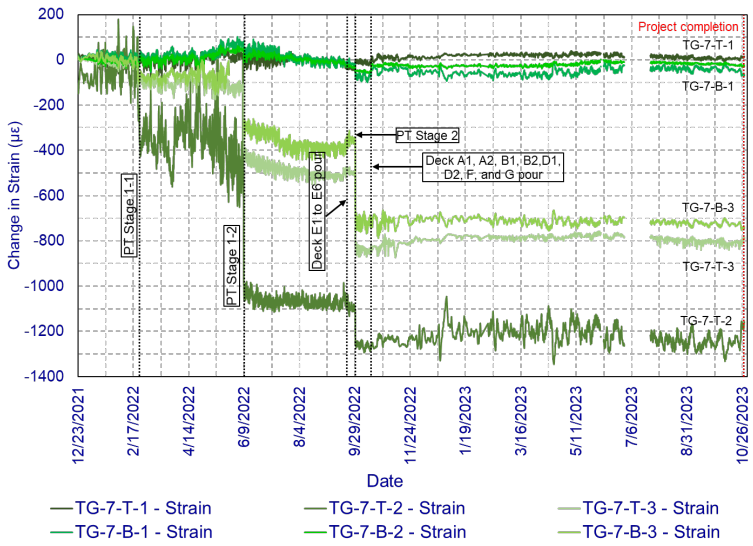

Figure 5-7. Variation of strain within the tapered section (TG-7).

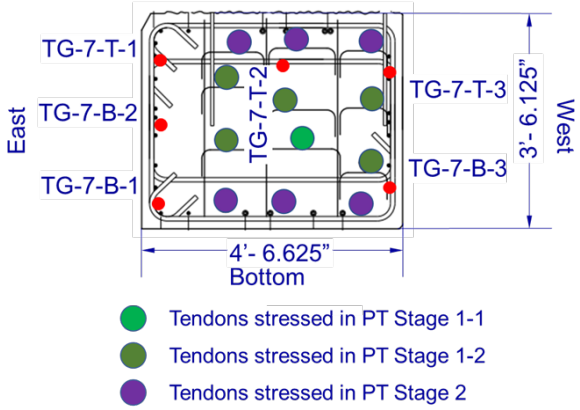

Figure 5-8. VW sensor arrangement at TG-7.

5.4 STRAIN VARIATION IN UPPER KNUCKLES

As described in Section 4.2.1, each upper knuckle contains 8 VW sensors installed under the arch rib baseplate. No external load was applied to the upper knuckles until the arch ribs were erected and the anchor rods were stressed. Figure 5-9 shows the strain recorded by the sensors at each instrumented location since fabrication. No significant change in strain was recorded until the anchor rods were stressed on May 5, 2022. An instantaneous increase in compressive strain was observed during post-tensioning of the anchor rods.

Additionally, a minimal increase in compression was observed during the Stage 1-2 post-tensioning of tie girders on June 8, 2022. A slight increase in tension was recorded on July 14, 2022, when the bridge was lifted to remove the temporary abutments under the knuckles in preparation for installing SPMTs for the bridge move. As construction progressed, a gradual

increase in compression was observed due to the additional loads imposed by the deck and other structural and non-structural components.

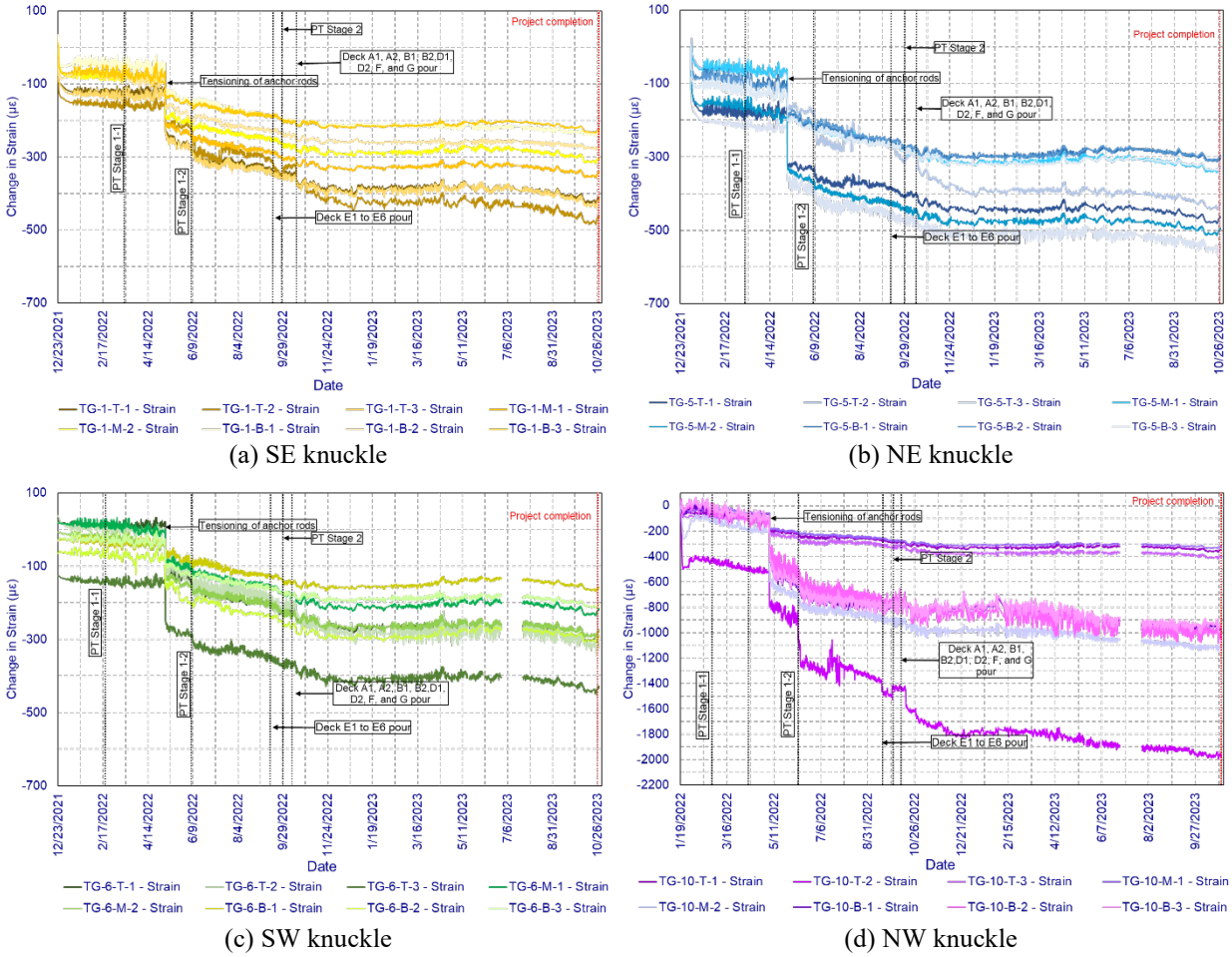

(a) SE knuckle (b) NE knuckle

(c) SW knuckle (d) NW knuckle

Figure 5-9. Strain variation in (a) SE, (b) NE, (c) SW, and (d) NW knuckles.

SW, SE, and NE knuckles were fabricated on 12/17/2021, 12/22/2021, and 01/05/2022, respectively. Figure 5-10 shows the variation of total strain in the SE, NE, and SW upper knuckles from fabrication to the post-tensioning of the anchor rods. The variation of shrinkage strain in the NW knuckle was not considered due to the high variability of the measured strain data. The age of concrete at formwork removal of SE, NE, and SW knuckles was 21, 15, and 28 days, respectively. Stage 1-1 PT was applied to the west and east tie girders on 02/21/2022 and 03/14/2022, respectively. The age of concrete at SE, NE, and SW knuckles at Stage 1-1 post-tensioning of the tie girders was 82, 68, and 68 days, respectively. The ages of concrete at SE, NE, and SW knuckles when tensioning the anchor rods of the knuckles were 134, 120, and 140 days, respectively. As observed in Figure 5-10, a significant strain change was not observed from

formwork removal to the tensioning of the anchor rod, i.e., the autogenous shrinkage contribution to the total shrinkage is substantial over the drying shrinkage.

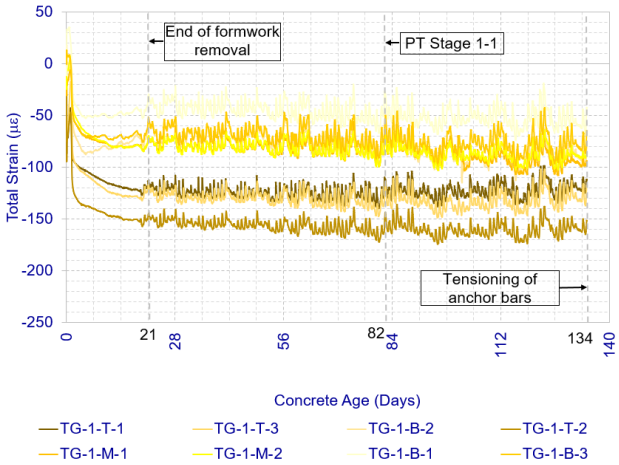

(a) SE knuckle

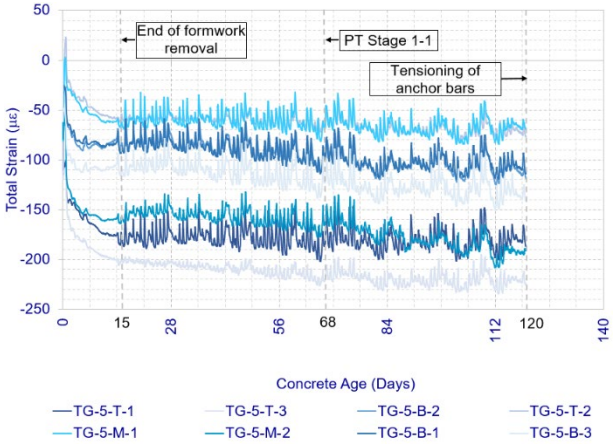

(b) NE knuckle

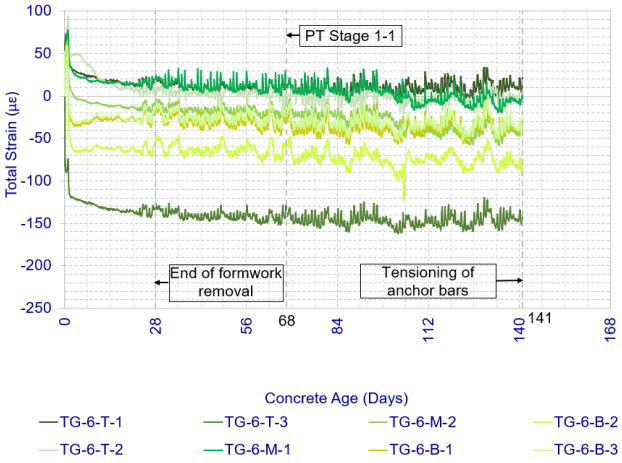

(c) SW knuckle

Figure 5-10. Shrinkage strain variation in (a) SE, (b) NE, and (c) SW knuckles.

5.5 STRAIN VARIATION IN END DIAPHRAGMS

Each end diaphragm has 11 post-tensioning ducts, with each duct containing 19-0.6 in. strands. Both end diaphragms were constructed simultaneously on April 12, 2022, and post-tensioned from April 22 to 26, 2022. The total strain developed in the south and north end diaphragms was measured from the day of fabrication (i.e., April 12, 2022) and shown in Figure 5-11 and Figure 5-12, respectively. Even though the end diaphragms were designed to be post-tensioned in a single stage, post-tensioning was carried out in several stages. The south end diaphragm was post-tensioned in two stages: Stage 1-1 on April 22, 2022 (DT05, DT08, DT11, and DT04), and Stage 1-2 on April 25, 2022 (DT09, DT06, DT07, DT01, DT12, DT03, and DT10). The north end diaphragm was post-tensioned in three stages: Stage 1-1 on April 22, 2022 (DT05, DT08, and

DT11), Stage 1-2 on April 25, 2022 (DT04, DT09, DT06, DT07, and DT01), and Stage 1-3 on April 26, 2022 (DT12, DT03, and DT10). The change in strain during post-tensioning is shown in Figure 5-13. An instantaneous change in strain was recorded during the post-tensioning process. A slight reduction in compression, caused by the combined effects of creep and shrinkage, continued until the bridge was lifted on July 18, 2022, to install SPMTs.

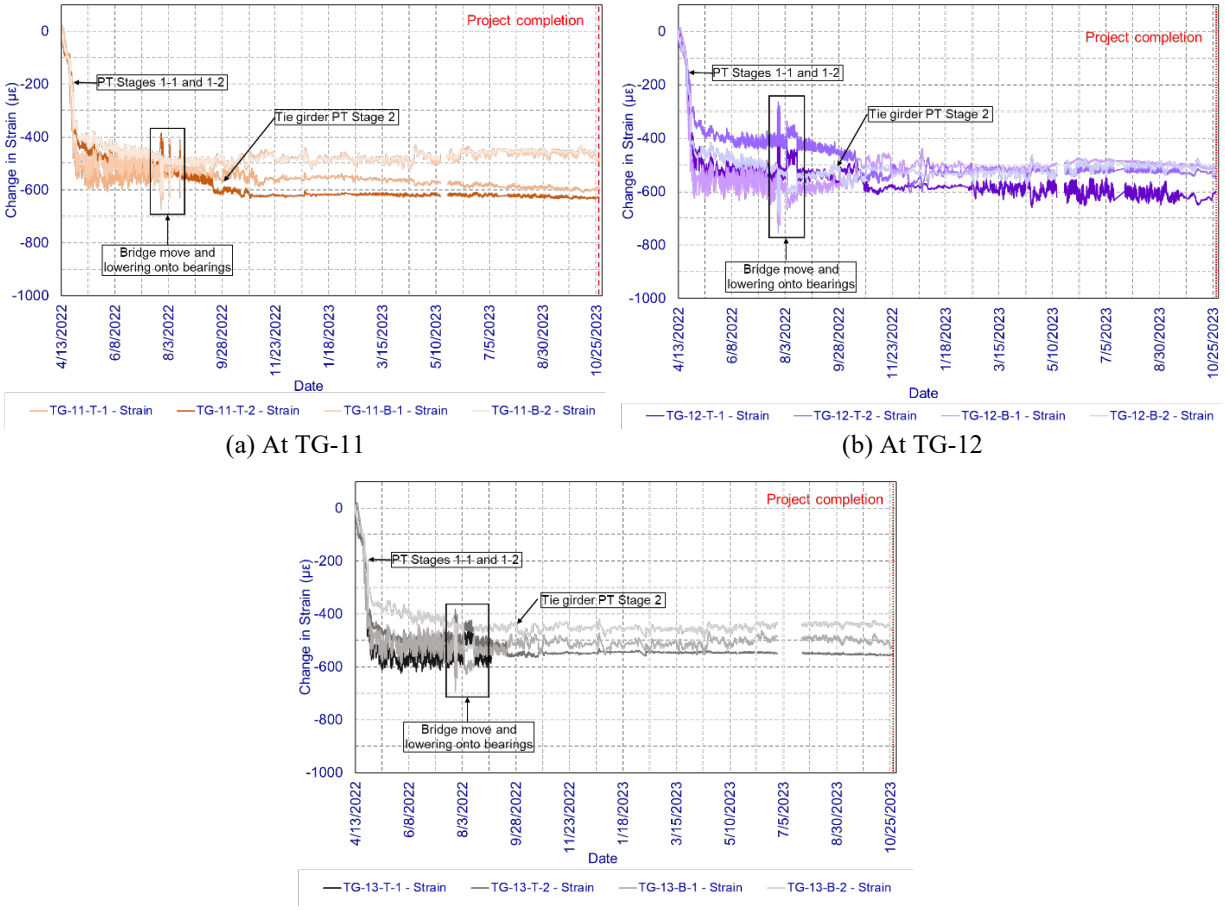

(a) At TG-11

(b) At TG-12

(c) At TG-13

Figure 5-11. Strain variation in the south end diaphragm at (a) TG-11, (b) TG-12, and (c) TG-13.

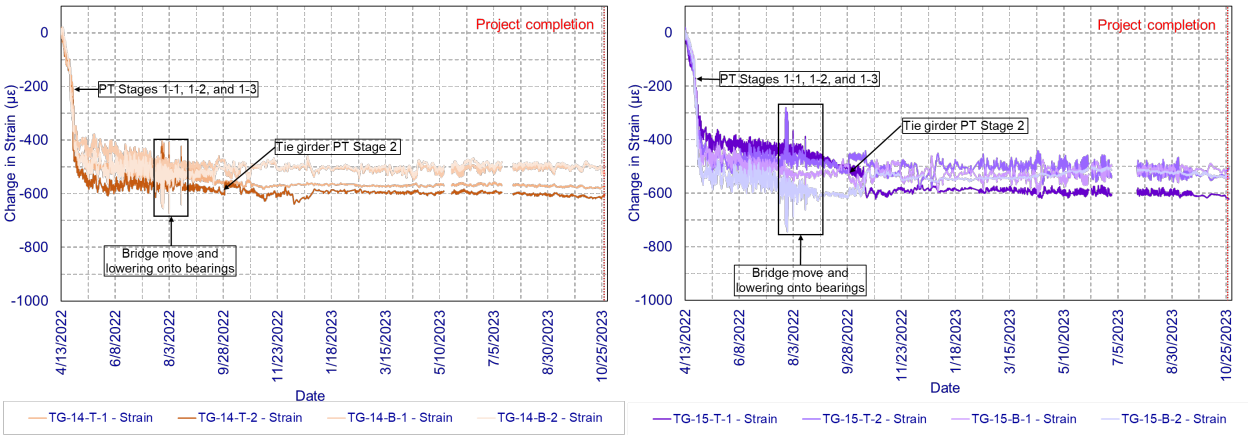

(a) At TG-14 (b) At TG-15

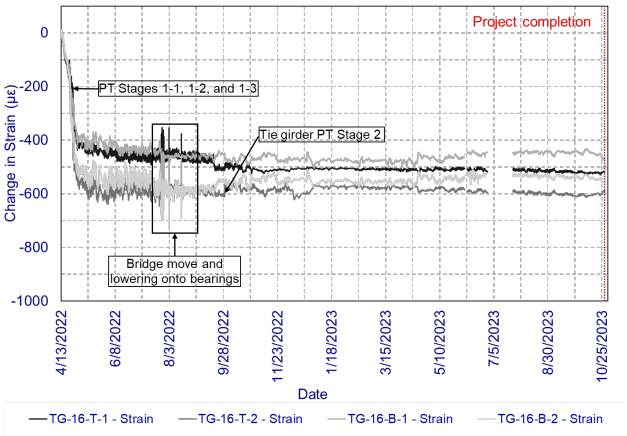

(c) At TG-16

Figure 5-12. Strain variation in the north end diaphragm at (a) TG-14, (b) TG-15, and (c) TG-16.

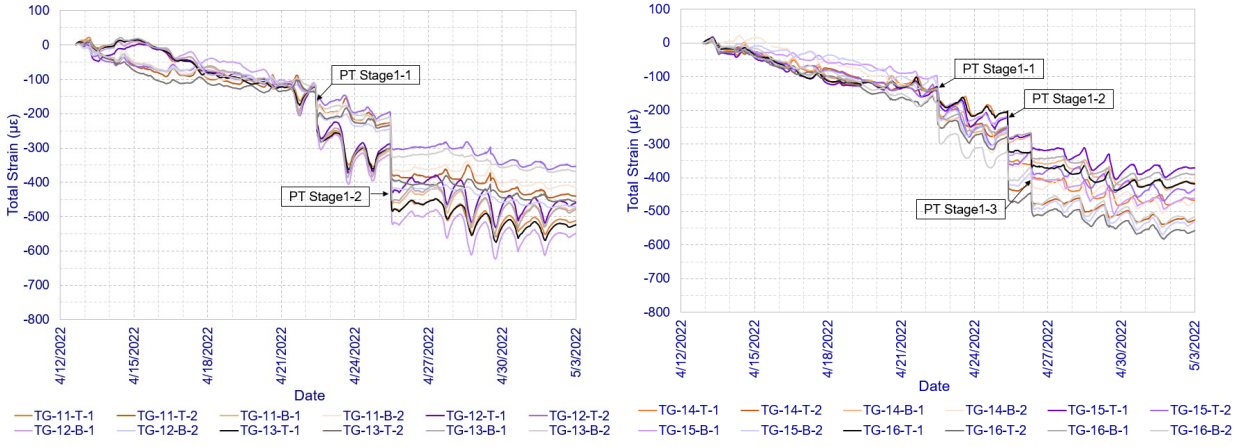

(a) South end diaphragm (b) North end diaphragm

Figure 5-13. Strain variation during post-tensioning:(a) south and (b) north end diaphragms.

During the last week of July 2022, the superstructure frame was moved from the BSA to its final alignment over I-94. Upon arrival, the frame was positioned on four climbing jacks located beneath the end diaphragms, 8 ft offset from each bearing centerline (Figure 5-14 and Figure 5-15).

This temporary support configuration, which transferred the arch frame self-weight through the end diaphragms rather than directly to the bearings, induced flexural stresses in the diaphragms that would not exist in the final supported condition.

The superstructure was lowered onto the permanent bearings in three incremental steps. At the completion of each step, the frame was temporarily supported on hydraulic cylinders positioned at the bearing locations (Figure 3-10). This staged lowering process created cyclic loading and unloading of the end diaphragms, producing the strain variations shown in Figure 5-16 and summarized in Table 5-3 and Table 5-4. Even though this process reduced compression by 218 με and increased compression by 180 με, the final strains remained within the design limits. Further, the strains returned to their original state, indicating elastic behavior of the structure.

After lowering the frame onto the permanent bearings, the soleplates were welded to the bearing assemblies. Although specifications were in place to control heat generated by welding, the process resulted in concrete delamination around the sole plates. This condition necessitated re-lifting the superstructure frame using the climbing jacks during the first two weeks of August 2022 to facilitate inspection and repair. Strain measurements during this re-lifting and subsequent lowering operation are shown in Figure 5-16 and exhibit similar elastic behavior to the initial lowering sequence.

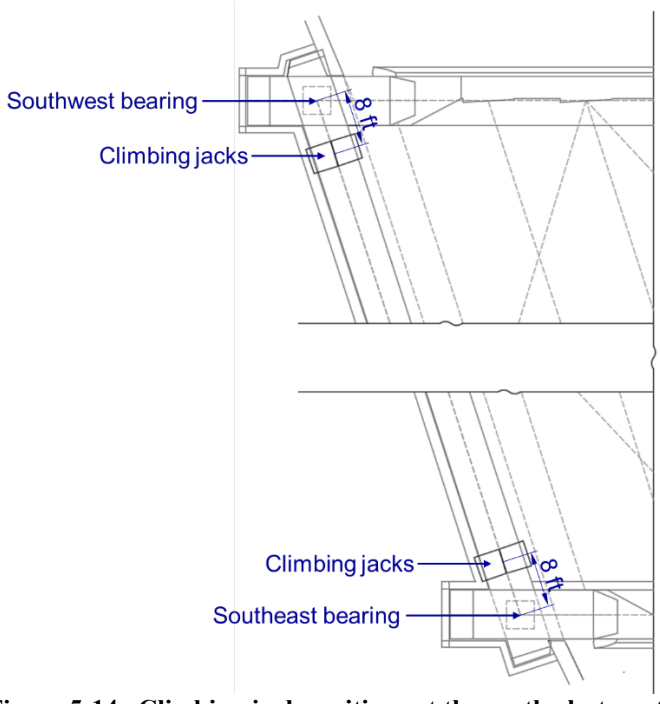

Figure 5-14. Climbing jack positions at the south abutment.

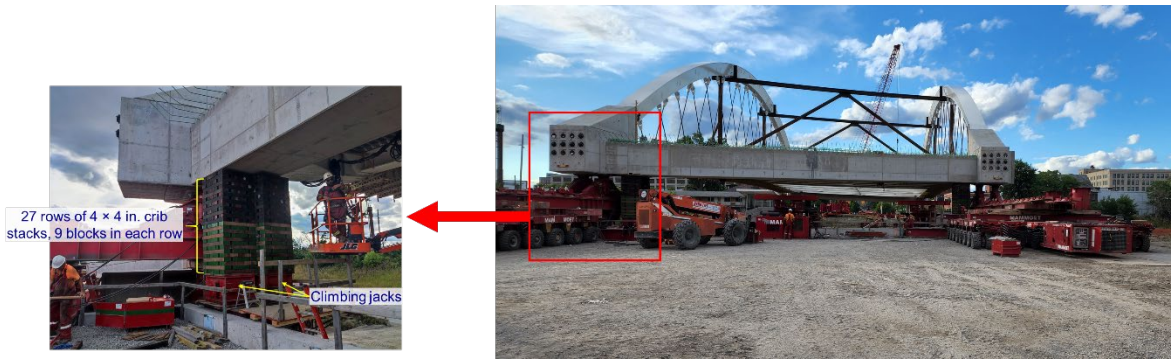

Figure 5-15. Climbing jack arrangement at the southwest bearing for stage 1 lowering.

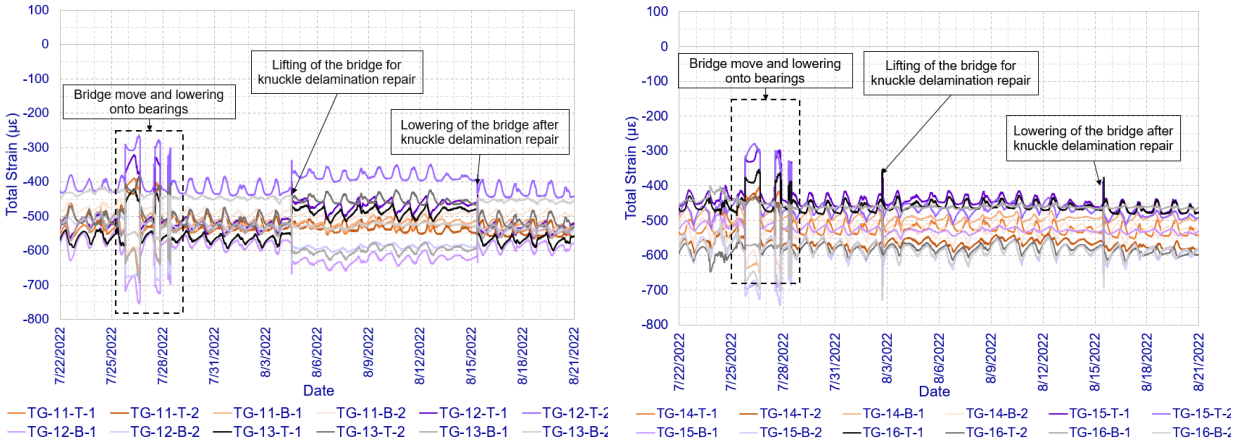

(a) South end diaphragm (b) North end diaphragm

Figure 5-16. Strain variation in (a) the south and (b) the north end diaphragms during bridge move, lowering onto bearings, and delamination repair.

Table 5-3. Strain Variations Developed in South End Diaphragm Sensor Locations During Bridge Lowering Process

Sensor Location	VW Strain Sensor	Recorded Strain (με)		Change in Strain (με)
		Before Lifting	After Lifting	
TG-11	TG-11-T-1	-430	-275	155
	TG-11-T-2	-402	-262	140
	TG-11-B-1	-365	-545	-180
	TG-11-B-2	-348	-485	-136
TG-12	TG-12-T-1	-424	-206	218
	TG-12-T-2	-307	-142	164
	TG-12-B-1	-476	-643	-167
	TG-12-B-2	-376	-546	-170
TG-13	TG-13-T-1	-459	-300	160
	TG-13-T-2	-395	-254	141
	TG-13-B-1	-396	-573	-177
	TG-13-B-2	-322	-459	-137

Table 5-4. Strain Variations Developed in North End Diaphragm Sensor Locations During Bridge Lowering Process

Sensor Location	VW Strain Sensor	Recorded Strain (με)		Change in Strain (με)
		Before Lifting	After Lifting	
TG-14	TG-14-T-1	-385	-261	124
	TG-14-T-2	-421	-290	131
	TG-14-B-1	-342	-502	-161
	TG-14-B-2	-368	-510	-142
TG-15	TG-15-T-1	-309	-152	156
	TG-15-T-2	-364	-158	206
	TG-15-B-1	-419	-597	-177
	TG-15-B-2	-467	-627	-161
TG-16	TG-16-T-1	-334	-212	122
	TG-16-T-2	-438	-277	162
	TG-16-B-1	-310	-451	-141
	TG-16-B-2	-396	-541	-146

5.5.1 Shrinkage and Creep in End Diaphragms

Figure 5-17 shows the variation of average strain in end diaphragms from fabrication to the Stage 1-1 post-tensioning.

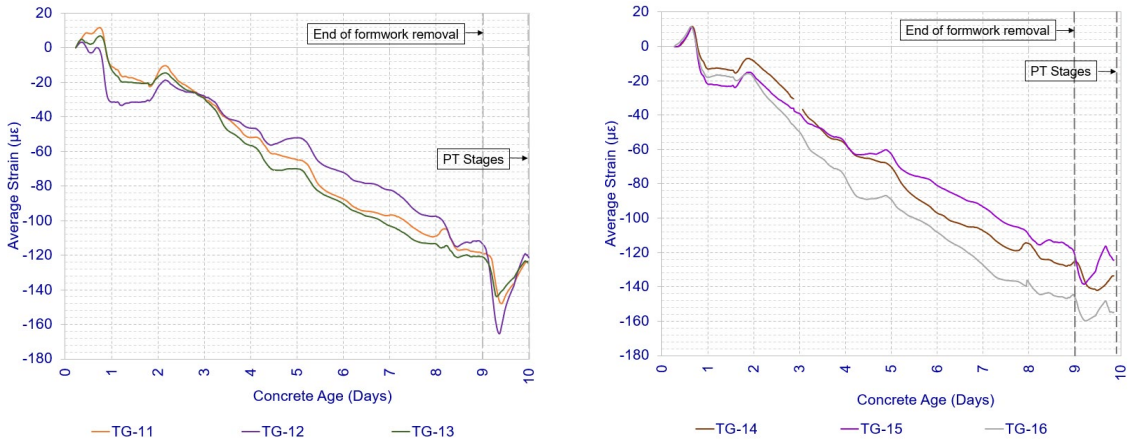

(a) South end diaphragm (b) North end diaphragm

Figure 5-17. Shrinkage in the (a) south and (b) north end diaphragms.

By the time of formwork removal, an average strain of -114 to -121 με was recorded in the south end diaphragm, while an average strain of -123 to -145 με was recorded in the north end diaphragm. The duration between the removal of formwork and the Stage 1-1 post-tensioning was only 1 day. Therefore, the period is inadequate to assess the magnitude of the drying shrinkage in the end diaphragms.

5.6 STRAIN VARIATION IN HANGERS

As mentioned in Section 3.2, the hangers were installed from May 16 to May 20, 2022, and were stressed from May 25 through June 01, 2022. Strandmeters were installed on eight hangers in each

arch frame after the hangers were stressed. Since hangers were released and re-tensioned multiple times during tension verification tests, a complete history of hanger forces could not be recorded. Figure 5-18 shows the seasonal variation of the hanger deformation.

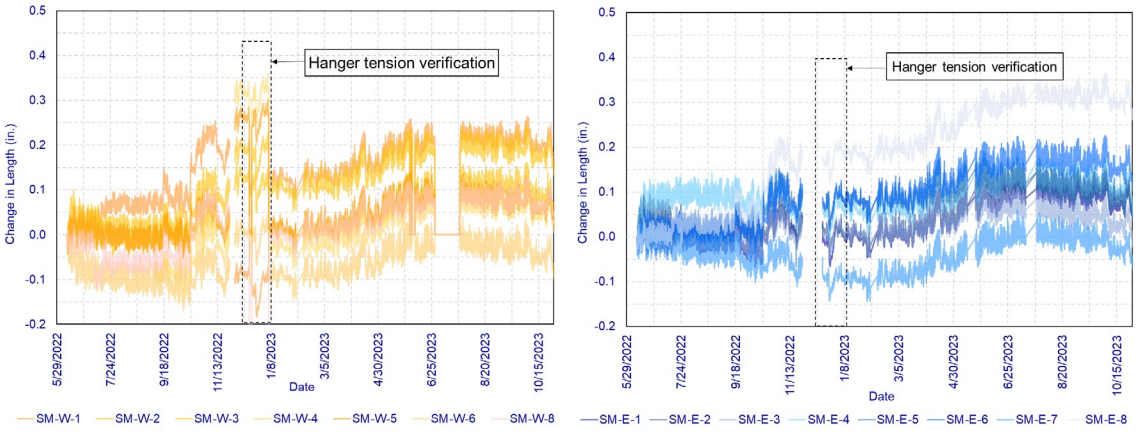

(a) West arch strandmeters (b) East arch strandmeters

Figure 5-18. Hanger deformation variation: hangers in the west and east frames.

5.7 THERMAL MONITORING DATA

As described in Section 4.3, the contractor followed a thermal control plan that included 168 temperature sensors installed at the upper and lower knuckles, tie girders, and end diaphragm to meet the project specifications; a maximum temperature limit of 150° F and a maximum temperature difference limit between the interior and surface of the concrete of 35° F. Additionally, VW sensors also record the temperature at their respective locations.

Both temperature sensors and VW sensors recorded similar temperature values, and the data show that the temperature of the PT members remained below the specified limits. For example, the temperature and temperature difference measured in the upper SW knuckle are presented in Figure 5-19. Please refer to Appendix G for additional temperature monitoring data.

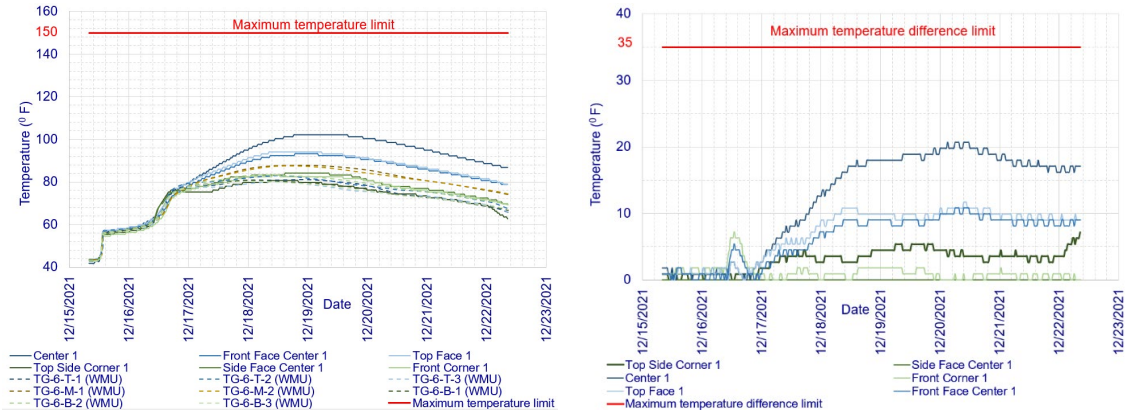

(a) Temperature (b) Temperature difference

Figure 5-19. (a) Temperature and (b) temperature difference in the upper SW knuckle.

6 STRUCTURAL RESPONSE DURING SEASONAL CHANGES

6.1 OVERVIEW

This chapter presents the seasonal variations in temperature and strain within the PT concrete frame. The plots display data spanning over two years, from September 28, 2023, to December 2, 2025. The strain variation during bridge construction and in service through December 2, 2025, is presented in Chapter 5. Although the bridge opened to traffic on December 22, 2022, construction was completed on September 27, 2023. Therefore, to show the seasonal strain variation in the completed structure, the strains recorded on September 28, 2023, at 12:00 a.m. were selected as the reference and set to zero. Correlation analyses were also performed between temperature and strain variations to explain the structural response to the seasonal temperature variation.

6.2 STRAIN AND TEMPERATURE VARIATION WITHIN TIE GIRDERS

Figures 6-1 and 6-2 present temperature and strain measurements from the east and west tie girders over a two-year monitoring period from September 28, 2023, to December 2, 2025. During this period, temperatures within the concrete frame ranged from -15°C (5°F) to 34°C (93°F), representing a total thermal range of 49°C (88°F).

Both temperature and strain exhibit seasonal cyclic patterns approximating sinusoidal functions. However, strain responses show a phase lag relative to temperature cycles. This phase shift results from the thermal mass of the concrete structure, which delays internal temperature response to ambient temperature changes.

To quantify the relationship between temperature and strain at each instrumented location, correlation coefficients were computed. Figure 6-3 presents the correlation matrix as a color-coded heatmap, where red indicates positive correlation (strain increases with temperature), purple indicates negative correlation (strain decreases with temperature), and intermediate colors represent weak or neutral correlations. The color scale ranges from +1.0 (perfect positive correlation, shown in red) to -1.0 (perfect negative correlation, shown in purple).

Accordingly, the temperature throughout the entire concrete frame varies in a similar pattern across seasonal changes. When strain variation within the tie girders (recorded at TG-2, TG-3, TG-4, TG-8, and TG-9) is considered, strains measured at the southeast and northeast ends of the bridge

(TG-2 and TG-4) show a slight positive correlation. In contrast, the strains developed at the midspan (TG-3 and TG-8) and towards the northwest end (TG-9) show a slightly increasing negative correlation. Primarily, the deformations at the northwest end of the bridge closely follow temperature cycles, with the tie girder developing tension as temperature decreases and vice versa. The correlation analysis results are primarily driven by patterns observed between January 2024 and August 2025. As shown in Chapter 5, strains are within the limits. However, multi-year datasets spanning 5-10 years are typically required to distinguish long-term trends from seasonal variations and to confirm the stability of observed structural behavior. Continued monitoring will enable validation of these preliminary findings and assessment of any progressive changes in thermal response.

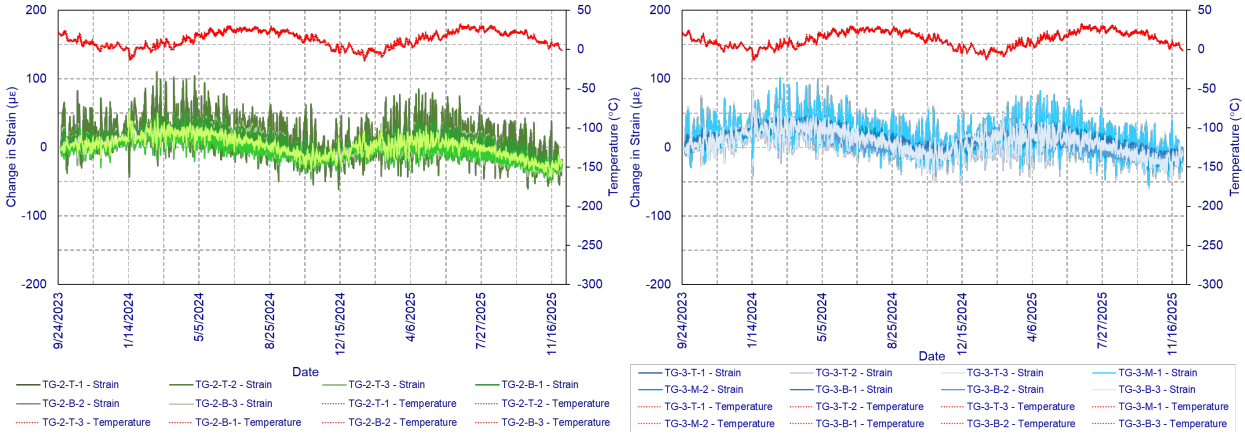

(a) TG-2 (b) TG-3

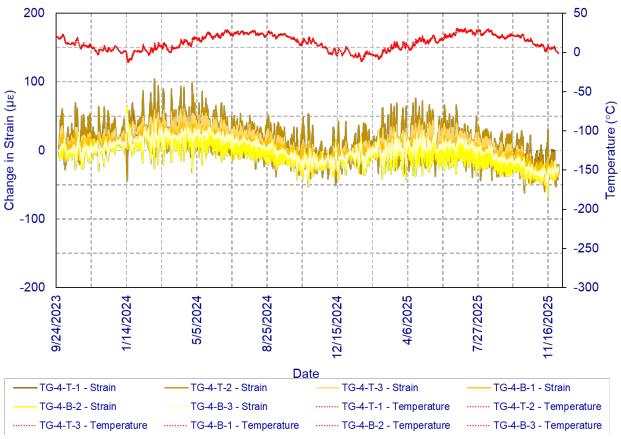

(c) TG-4

Figure 6-1. Seasonal strain and temperature variation within the east tie girder.

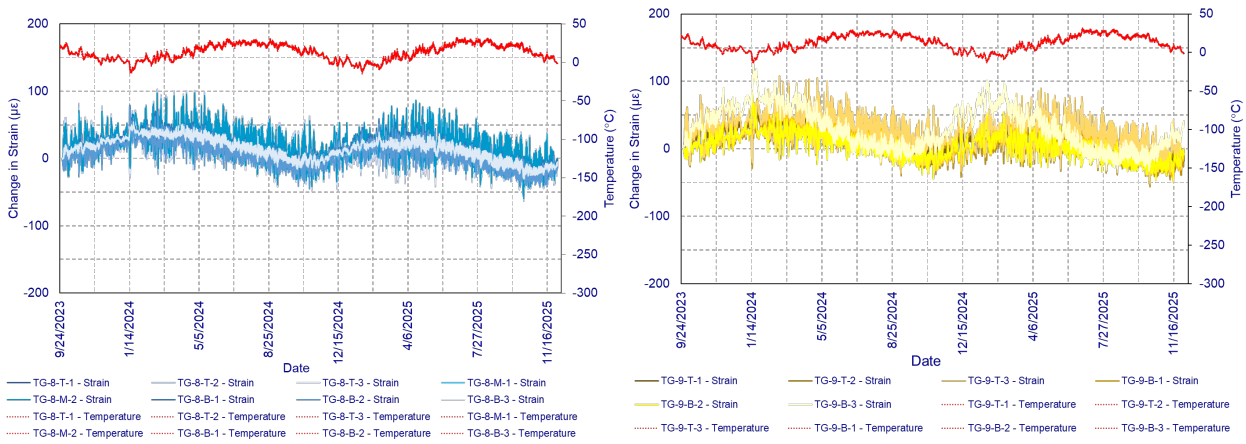

(a) TG-8 (b) TG-9

Figure 6-2. Seasonal strain and temperature variation within the west tie girder.

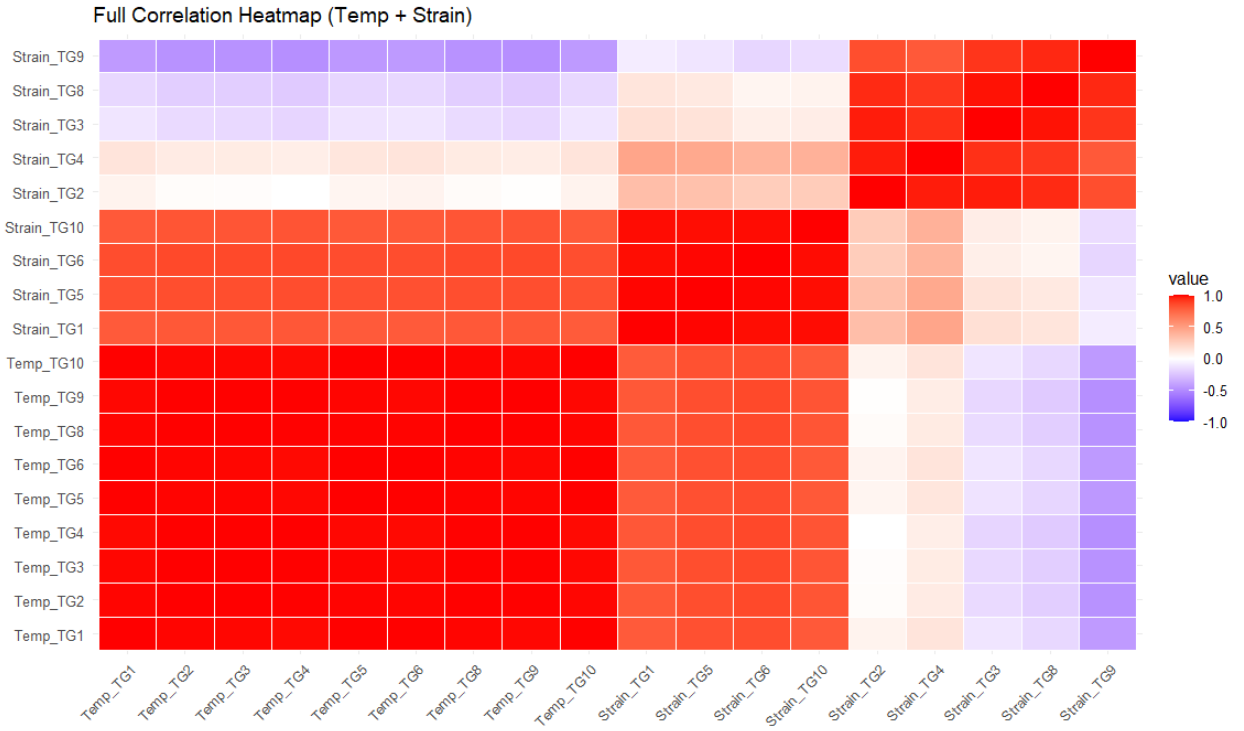

Figure 6-3. Correlation between the variation of temperature and strains within the concrete frame.

6.3 STRAIN AND TEMPERATURE VARIATION AT THE BASEPLATE – KNUCKLE CONNECTION

Figure 6-4 shows the seasonal temperature and strain variations recorded by the strain gauges at the baseplate–knuckle connections (i.e., at TG-1, TG-5, TG-6, and TG-10). During this period, the temperature ranged from -17° C (2° F) to 36° C (98° F). As shown in Figure 6-3, regardless of their location, the strains recorded by all sensors at TG-1, TG-5, and TG-6 exhibited a positive correlation with the temperature change. The positive correlation indicates similar variations in temperature and strains. As shown in Figure 6-4(a) to (c), the increase in temperature results in

tension at those three connections, and vice versa. However, as shown in Figure 6-4(d) and (e), TG-10 does not follow the same pattern. As shown in the figures, the strain measurements recorded by TG-10-T-1, TG-10-T-3, and TG-10-M-1 sensors exhibit a strong positive correlation with temperature, whereas the remaining five sensors (i.e., TG-10-T-2, TG-10-M-2, TG-10-B-1, TG-10-B-2, and TG-10-B-3) exhibit a negative correlation. As shown in Figure 6-3, TG-10 shows a strong positive correlation because the analysis used only the strains recorded by TG-10-T-1, TG-10-T-3, and TG-10-M-1. The TG-10 behavior is further discussed in Section 6.4.

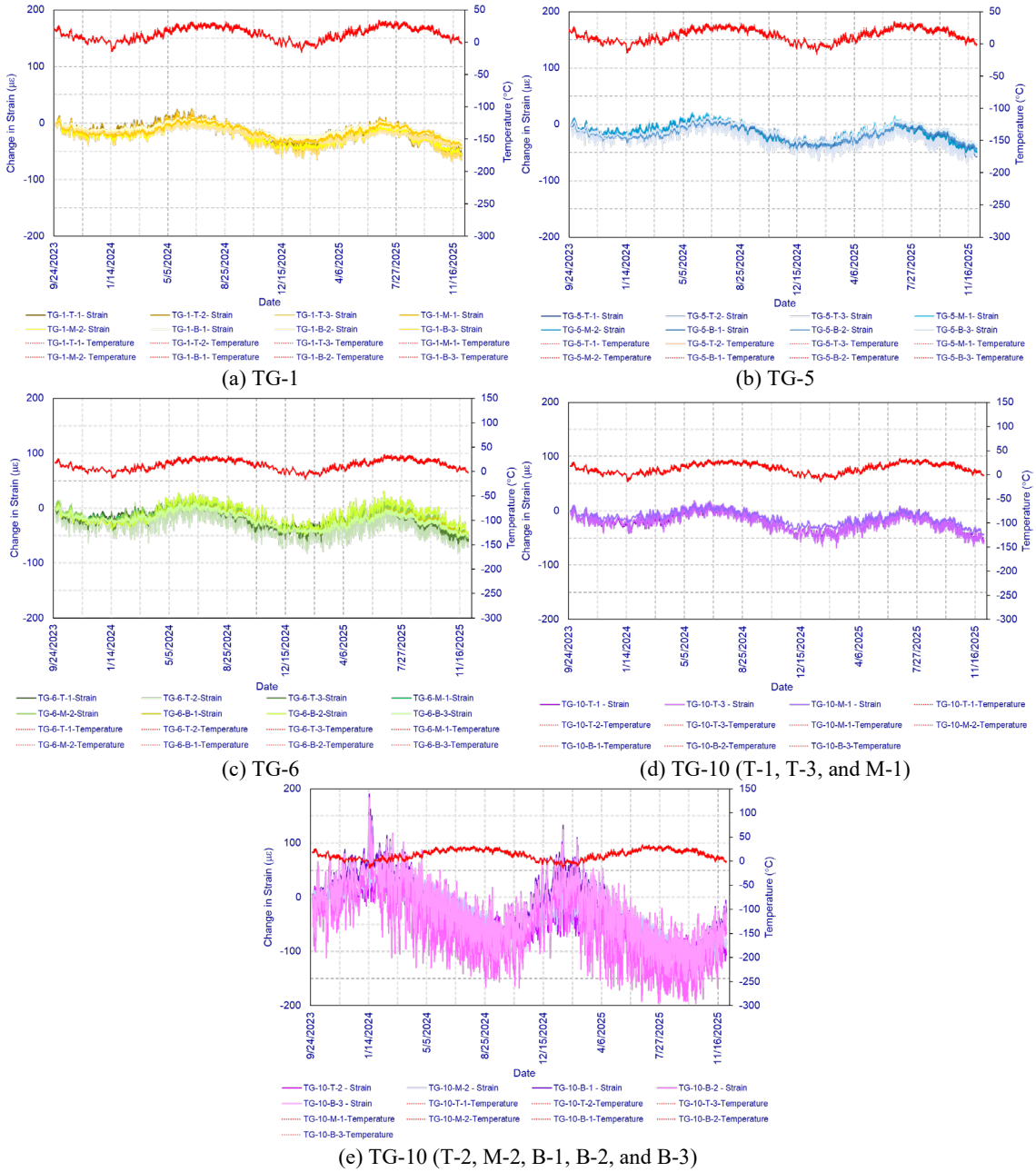

(a) TG-1

(b) TG-5

(c) TG-6

(d) TG-10 (T-1, T-3, and M-1)

(e) TG-10 (T-2, M-2, B-1, B-2, and B-3)

Figure 6-4. Seasonal strain and temperature variation at baseplate-knuckle connections.

6.4 STRAIN AND TEMPERATURE VARIATION WITHIN END DIAPHRAGMS

Figure 6-5 and Figure 6-6 present the seasonal strain and temperature variations within the south and the north end diaphragms. The data show that the seasonal strain variation in the south end diaphragm mirrors that of the north end diaphragm. For example, strain variations recorded by sensors TG-11 and TG-13 exhibit patterns similar to those of sensors TG-14 and TG-16, respectively. As shown in Figure 4-1(a), TG-11 and TG-16 are located near the obtuse corners of the bridge, whereas TG-13 and TG-14 sensors are positioned near the acute corners. These strain profiles indicate a slight twisting of the end diaphragms due to seasonal temperature changes. A similar twisting is observed at the baseplate-knuckle connection TG-10, rather than having an axial compression or tension as expected at a typical such connection. The data from the end diaphragms and TG-10 suggest conducting further studies to evaluate the impact of skew and the constraints imposed by the bearings on the structural response.

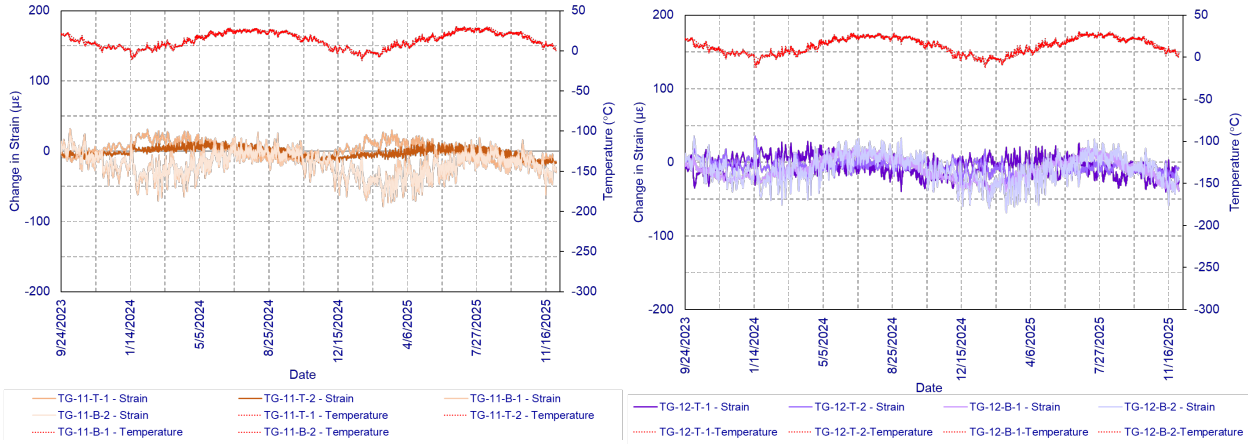

(a) TG-11 (b) TG-12

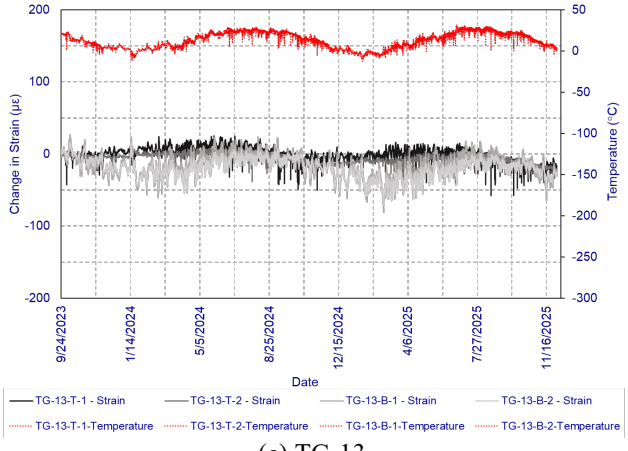

(c) TG-13

Figure 6-5. Seasonal strain and temperature variation within the south end diaphragm.

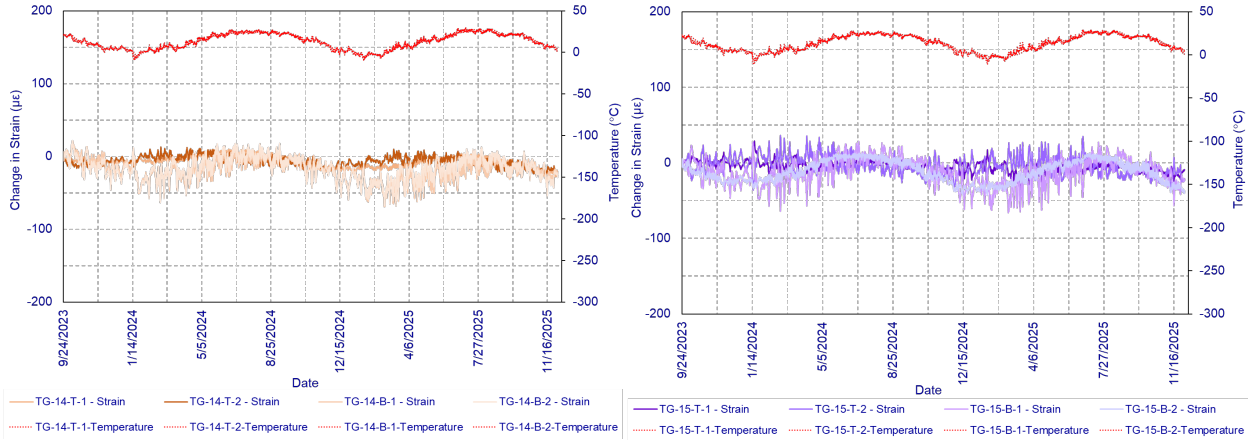

(a) TG-14 (b) TG-15

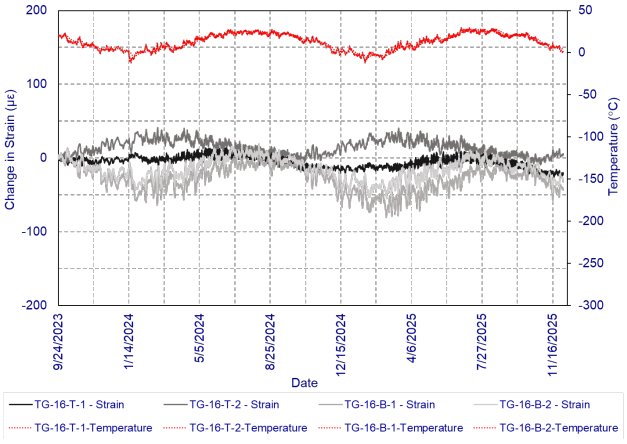

(c) TG-16

Figure 6-6. Seasonal strain and temperature variation within the north end diaphragm.

A full-scale model of the 2nd Avenue bridge was created in LARSA 4D to assess its behavior under seasonal changes. Please refer to Section 7.2 for detailed information about the model. The maximum and minimum temperatures the bridge experienced after opening to traffic were used to evaluate its response to seasonal temperature variations (see Section 7.2 for details on the temperature ranges selected for the analysis). Additionally, the impact of the skew was also evaluated.

Figure 6-7(a) shows the sensor arrangement in the end diaphragms. Figure 6-7(b) and (c) show the twisting of end diaphragm cross-sections at the sensor locations as the exposure temperature increases. Similar to the results documented earlier, the twist in the south end diaphragm mirrors that in the north end diaphragm. The figures show that the end diaphragms twist outward with the twist angle gradually increasing toward the acute corner of the bridge. For example, the twist angle is 0.017° at TG-11 and 0.029° at TG-13. This occurs due to skew, as the analysis of the straight bridge data shows a uniform twist of 0.029° along the end diaphragms.

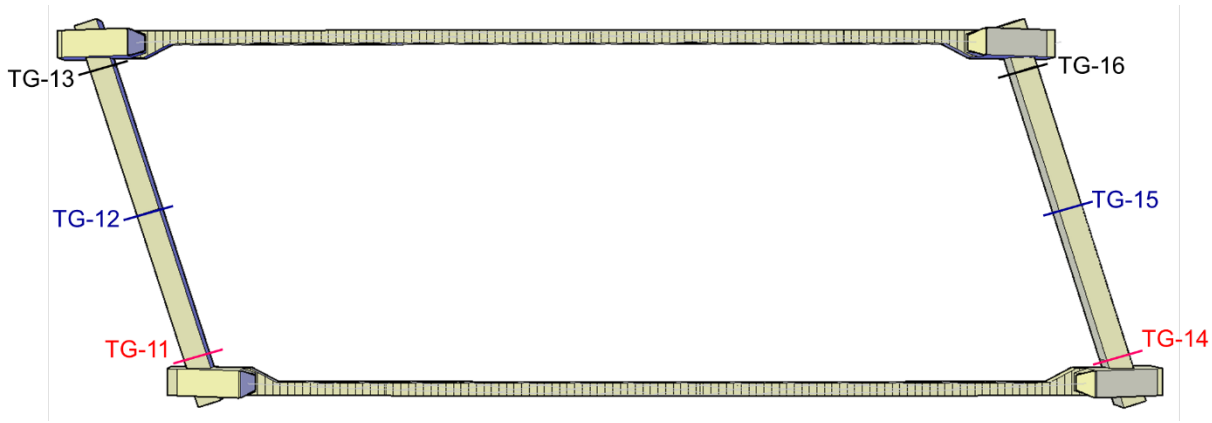

(a) Plan view of the bridge with sensor locations along the south and north diaphragms

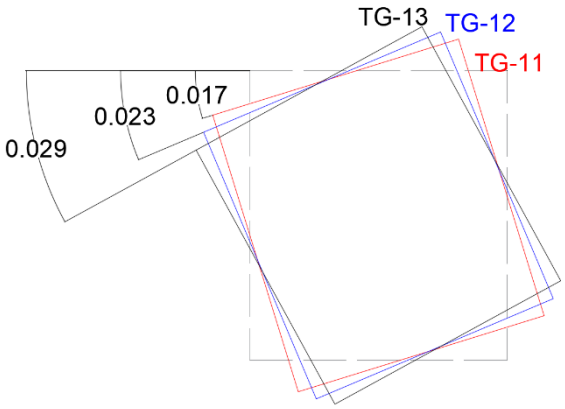

(b) Twist of sensor locations along the south end diaphragm when viewed from east to west.

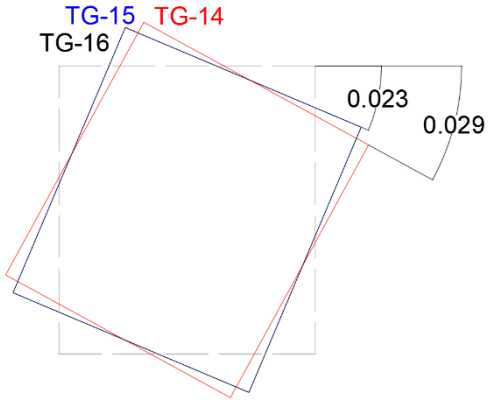

(c) Twist of sensor locations along the north end diaphragm when viewed from east to west.

Figure 6-7. The VW sensor arrangement in the end diaphragms and the twisting of the end diaphragms due to temperature increases.

6.5 HANGER DEFORMATIONS

Figure 6-8 shows the change in hanger length primarily due to the seasonal temperature variation. The change in length is positively correlated with temperature variation. As illustrated in the figure, the temperatures recorded for the east strandmeters ranged from -19° C (-3° F) to 37° C (99° F), while those for the west strandmeters ranged from -19° C (-3° F) to 45° C (113° F). Hanger elongation increases with rising temperatures and decreases with falling temperatures. In the east strandmeters, the elongation recorded ranges from -0.13 (about -16,620 με) to 0.11 inches (about 13,797 με), while in the west strandmeters, it ranges from -0.13 (around -15,994 με) to 0.12 inches (about 14,446 με).

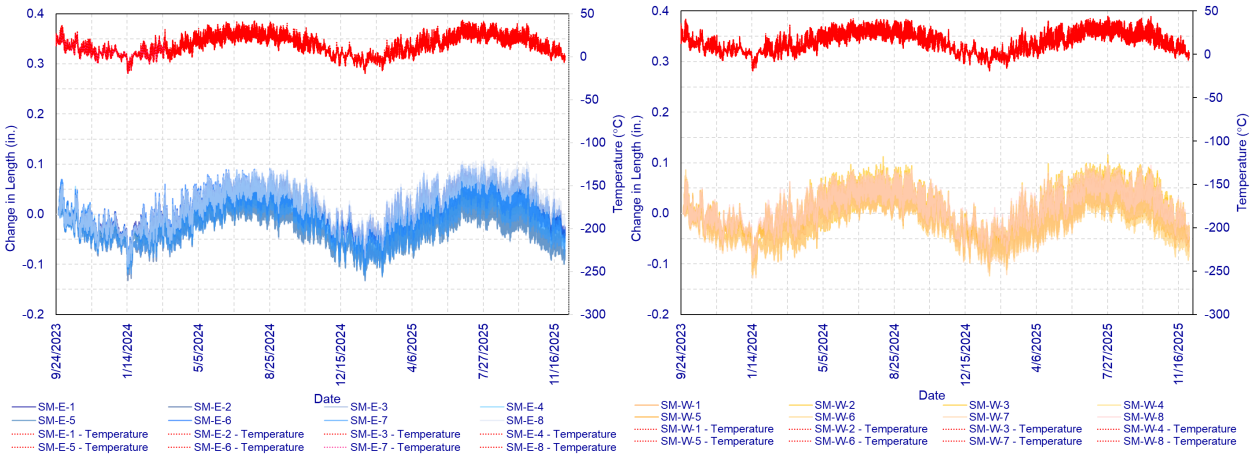

(a) East hangers (b) West hangers

Figure 6-8. Seasonal temperature and length variation of east and west hangers.

7 FINITE ELEMENT MODELING OF THE 2ND AVENUE BRIDGE

7.1 OVERVIEW

Due to the national significance of this project and the complexity of the bridge construction process, MDOT hired a peer review engineer to develop a finite element model and conduct an analysis in addition to the analyses performed by the Engineer of Record (EOR) and the contractor's consultant. This resulted in the development of three independent models to assess stress, deflection, and the potential for arch rib buckling under each load case. The models developed by the EOR and the contractor's consultant were reviewed as part of this project. Several modeling assumptions and simplifications used in these two models, primarily to represent the complex geometry of the knuckles and tapered sections, affected the stresses, forces, and moments in the members closer to the knuckles. For example, the upper knuckle in one of the models was divided into three segments along its length and modeled with beam elements with tapered cross-sections and concrete material properties. In contrast, the other model used beam elements with rigid material properties and applied an 84-kip downward concentrated load at the bearing centerline, representing the self-weight of the upper knuckle. Although some variations were observed across the three models due to their modeling assumptions, none of the load cases exceeded the design limits in any model. A consensus among the parties was reached, and any variations between models were documented in the project file before starting construction.

For this study, two refined finite element models were developed using LARSA 4D (Figure 7-1) and Altair HyperMesh (Figure 7-2). Due to the complexity of the bridge geometry, Altair HyperMesh (Altair 2025) was used to develop the Abaqus input files. All the bridge components were modeled in AutoCAD and imported to HyperMesh for preprocessing. The models encompassed all construction stages, complex post-tension duct profiles, variations in knuckle geometries, differential bearing elevations, diverse camber profiles in tie girders, distinct arch profiles, differences in end diaphragm profiles, and time-dependent concrete properties. A detailed discussion about these models is provided in the following sections.

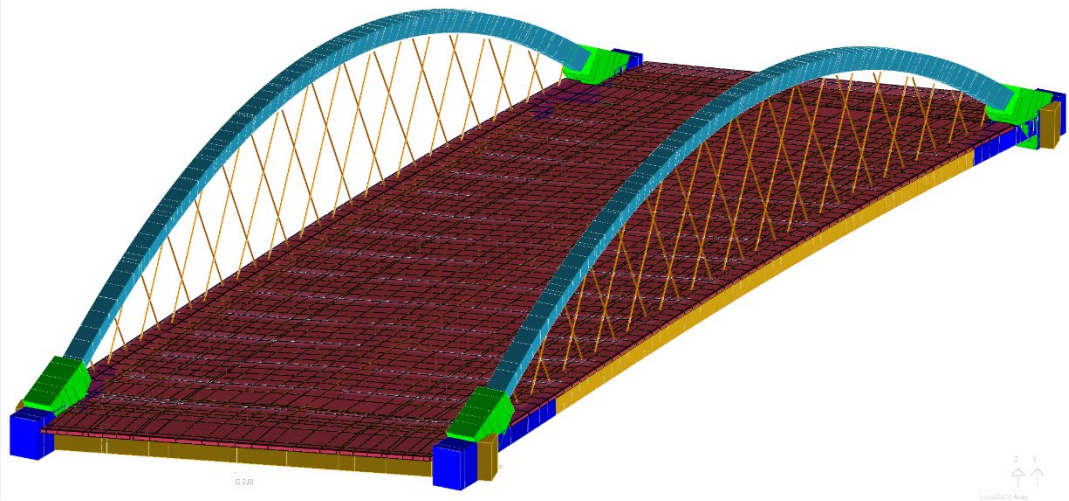

Figure 7-1. LARSA 4D model of the 2nd Avenue Bridge.

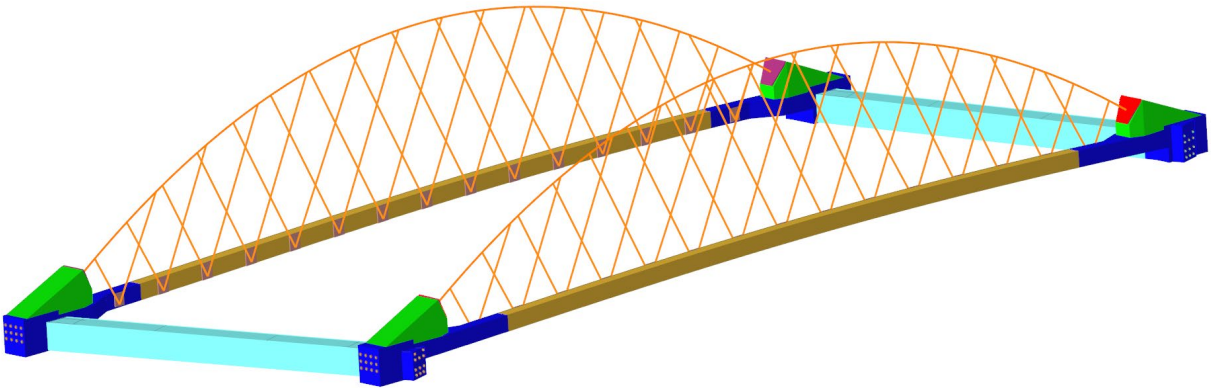

Figure 7-2. The 2nd Avenue Bridge model developed using HyperMesh.

7.2 LARSA 4D MODEL

As shown in Figure 7-3, all the bridge components, except the hangers and bridge deck, were modeled using beam elements. The hangers were modeled using cable elements, and the deck was modeled with shell elements. The following subsections outline the key assumptions used to develop the LARSA 4D model, including the modeling of the upper and lower knuckle geometries, bearings, and hangers.

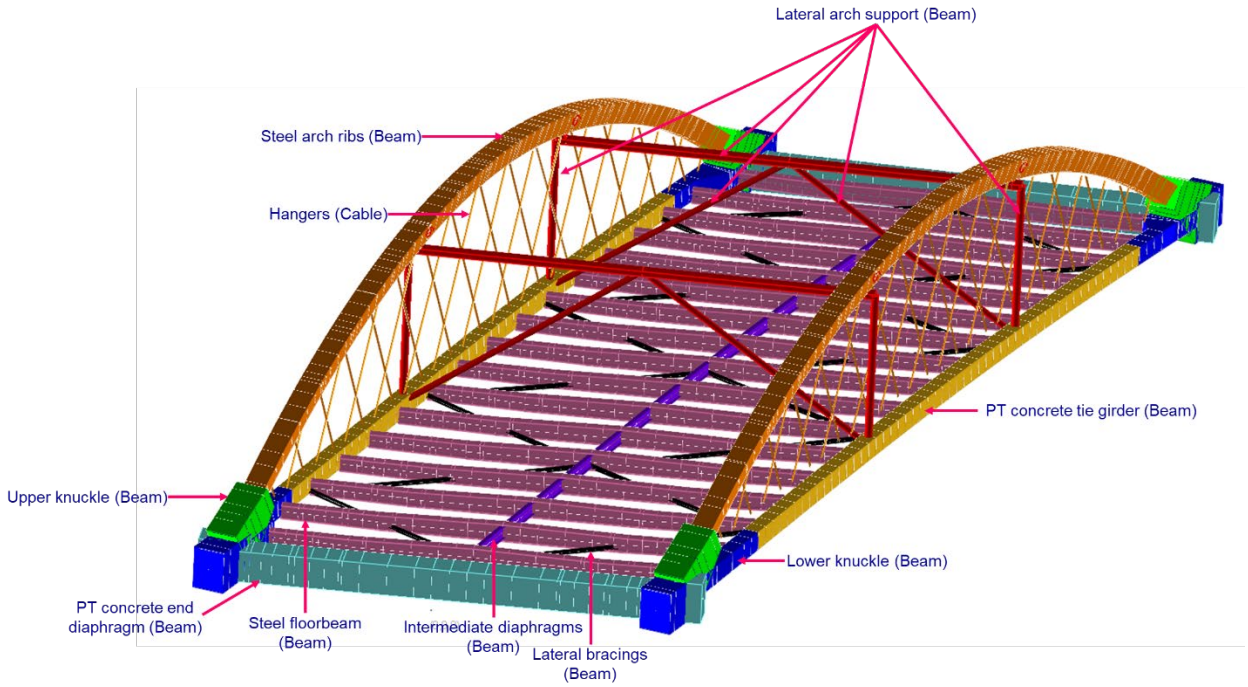

Figure 7-3. Structural elements used in the LARSA 4D model.

7.2.1 Modeling Upper and Lower Knuckle Geometries

Each knuckle has a slightly different geometry and a different bottom elevation. As shown in Figure 7-4, each knuckle extends either 41 ft-1 in. or 40 ft-8 in from each corner. Knuckle dimensions are provided in Table 7-1. The 1st two columns list the knuckle names and bottom elevations, while the remaining columns detail the respective dimensions.

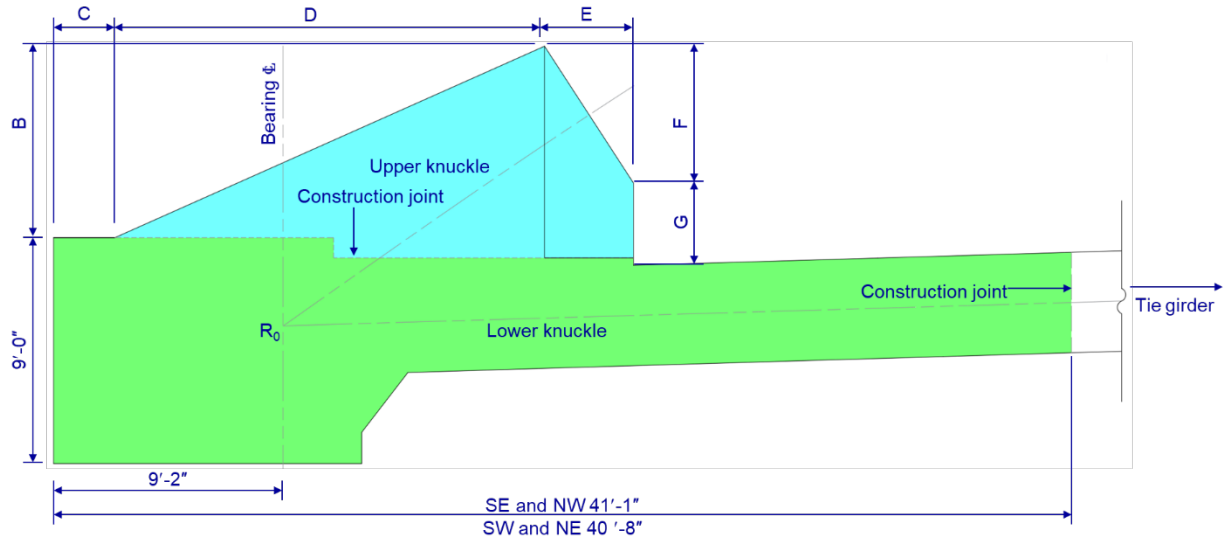

Figure 7-4. Knuckle geometry shown in construction drawings.

Table 7-1. Knuckle Dimensions

Knuckle	Elevation (ft)	B	C	D	E	F	G
Southwest (SW)	626.76	7′ - 8 ⅝″	1′ - 1 ⅝″	18′ - 4 ½″	3′ - 7 ¼″	5′ - 5″	6′ - 8″
Southeast (SE)	627.64	7′ - 7 ½″	2′ - 5 ⅜″	17′ - 2″	3′ - 6 ⅝″	5′ - 5 ⅜″	7′ - 3 ¾″
Northwest (NW)	628.75	7′ - 6 ⅝″	2′ - ⅜″	17′ - 8″	3′ - 6 ¼″	5′ - 5 ⅝″	7′ - 4″
Northeast (NE)	627.44	7′ - 7 ¾″	1′ - 2 ⅛″	18′ - 5″	3′ - 6 ¾″	5′ - 5 ¼″	6′ - 8 ⅛″

Due to the limitations in LARSA 4D, the knuckle geometry was simplified as shown in Figure 7-5. As illustrated in the figure, the upper and lower knuckles were divided into several sections based on their geometry. For example, the SW Lower Knuckle 1, SW Lower Knuckle 2, and PT Tie Girder sections were modeled using beam elements with uniform rectangular cross-sections of 84 × 108 in., 84 × 48 in., and 39 × 48 in., respectively. The tapered sections in the lower knuckle and upper knuckles were modeled using beam elements with varying cross-sections to match the geometry. However, due to software limitations, the gross cross-section of each component is used in the model. Although these simplifications enabled modeling the complex tendon geometry within the lower knuckle region, the forces in the knuckle area might not reflect the actual stresses because the moment of inertia differs between the simplified section and the as-built knuckle. Element end offset or beam elements with rigid material properties were used wherever needed to maintain the geometry.

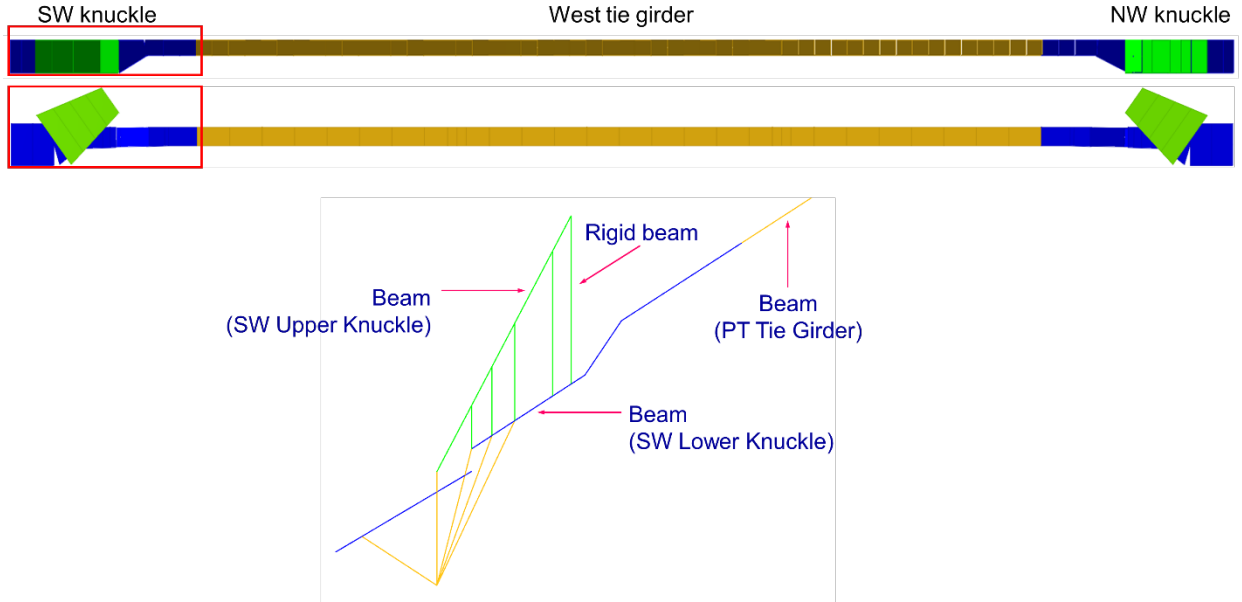

Figure 7-5. Upper and lower sections of the SW knuckle modeled in LARSA 4D.

7.2.2 Modeling Load Transfer Mechanism at Bearings

At least a 48 in. wide and 1¼ in. thick sole plate was embedded at the bottom of each knuckle. These plates cover approximately 23 to 30% of the knuckle's base area. Because of the height of the knuckle and the size of the bearing footprint, the load is transferred through a large area, as shown in Figure 7-6, rather than a single point typically used in an analysis model. To represent this load transfer mechanism, several rigid beam elements were used to connect beam elements representing the lower knuckle and located within the influence zone to the bearing node. The bearing node is located 65.75 in. below the beam elements that represent the lower knuckle (Figure 7-7).

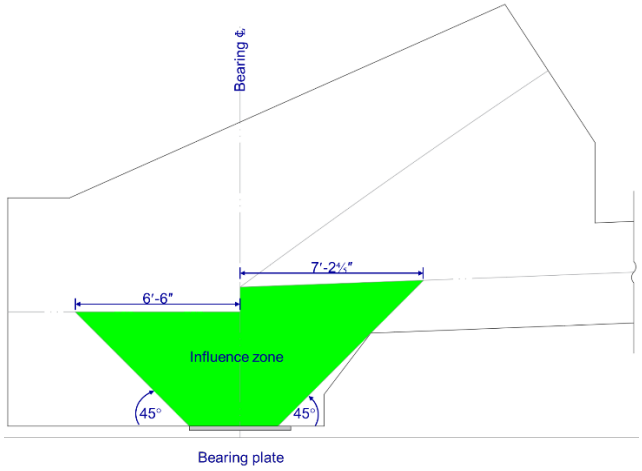

Figure 7-6. Influence zone of the bearing.

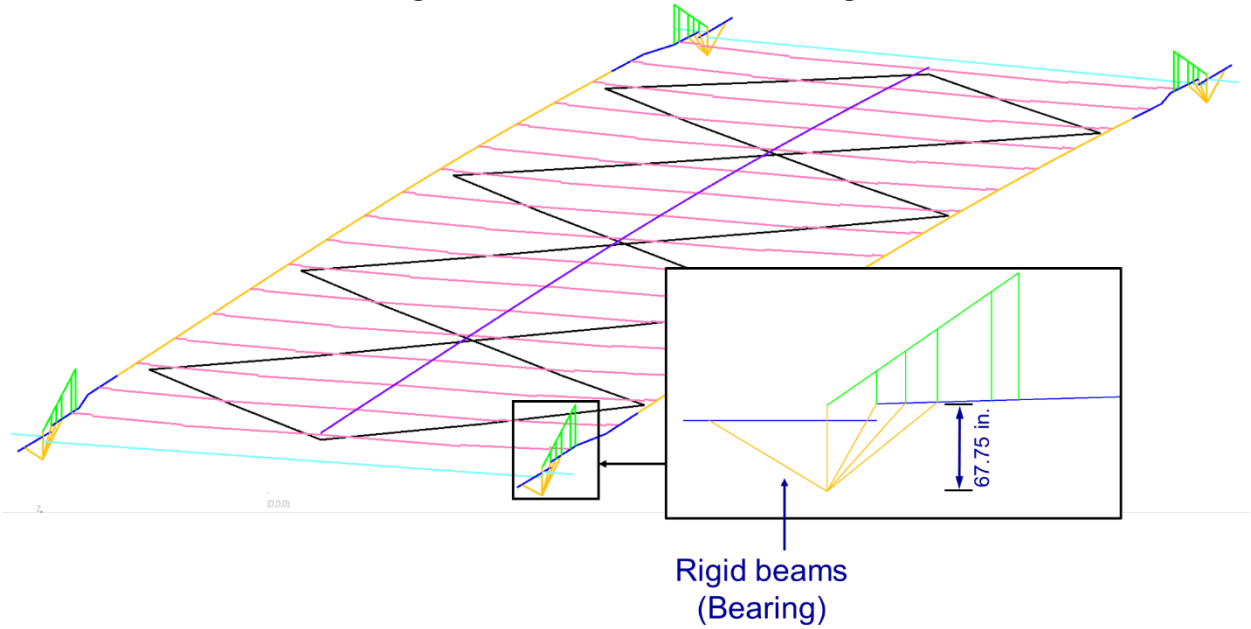

Figure 7-7. Modeling the load transfer mechanism at the bearing.

7.2.3 Modeling of Arches and Hangers

As shown in Figure 7-8, thirty (30) inclined hangers connect each arch rib to the respective tie girder to form the network arch. Figure 7-9a displays the elevation of the arch rib (only half) along with the field splice connections of the arch rib and the upper hanger connections. As shown in Figure 7-9b and Figure 7-9c, the arch rib has a hollow trapezoidal cross-section. The arch rib is offset by 22.5 in. from the centerline of the tie girder toward the interior of the bridge.

Figure 7-10 shows the hanger length and reference point definitions. There are two geometric parameters associated with the hanger: hanger length and working length. The working length is the straight-line distance between TH(n) (tie/hanger reference point at the intersection of hangers) and R(n) (arch rib reference point) (Figure 7-8). The hanger length is the straight-line distance between the upper pin and the top of the lower hanger base plate. For example, the working length and hanger length for hanger H1 of the west arch are 14.482 ft and 5.080 ft, respectively. As illustrated in Figure 7-10, the tie/hanger intersection (i.e., TH(n)) is located 17 in. below the tie girder reference point (i.e., T(n)).

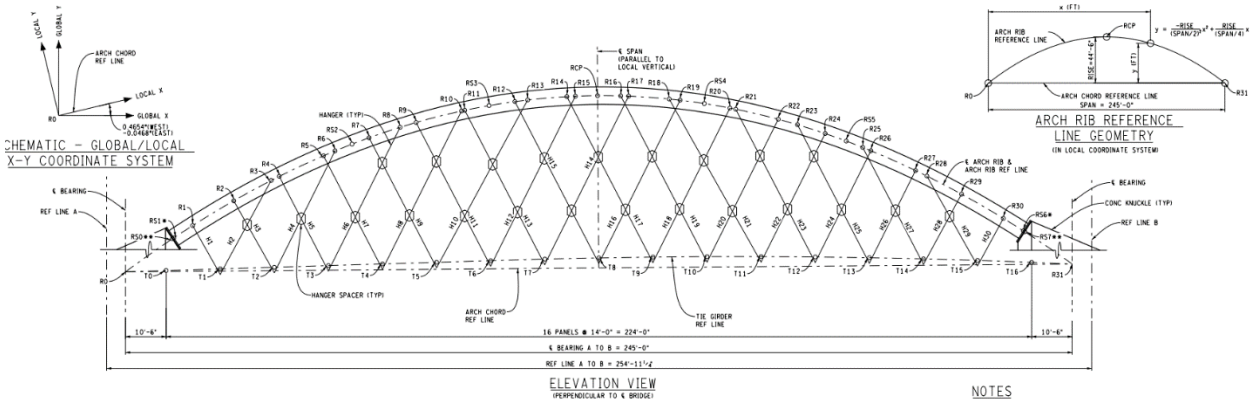

Figure 7-8. Arch with hanger elevation view.

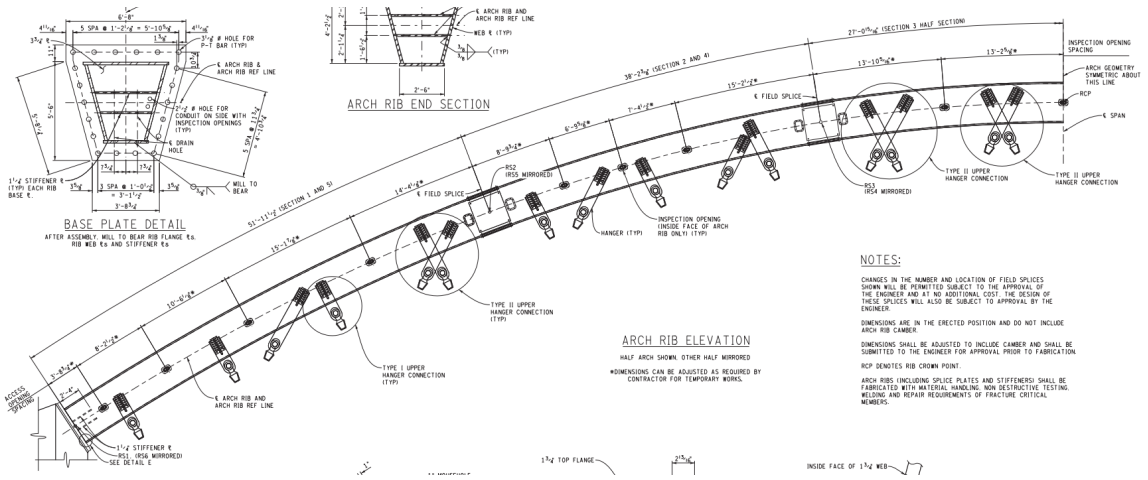

(a) Arch rib elevation view

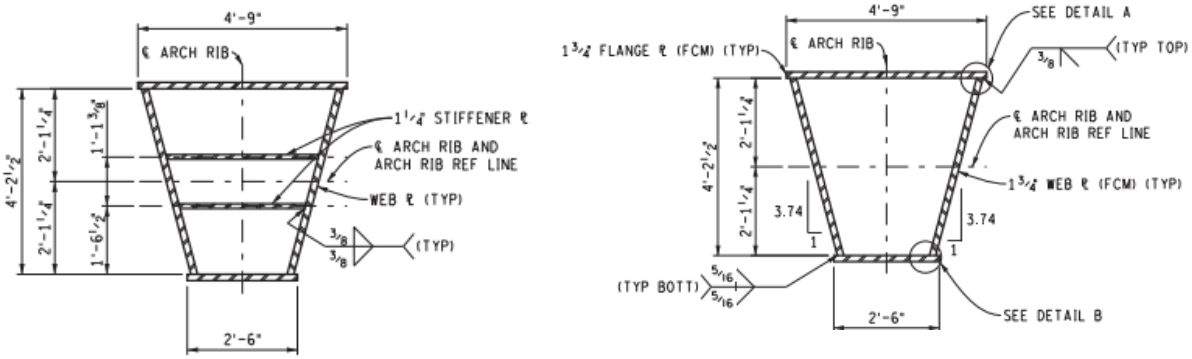

(b) End-section (c) Typical section

Figure 7-9. Arch-rib elevation and cross-sections.

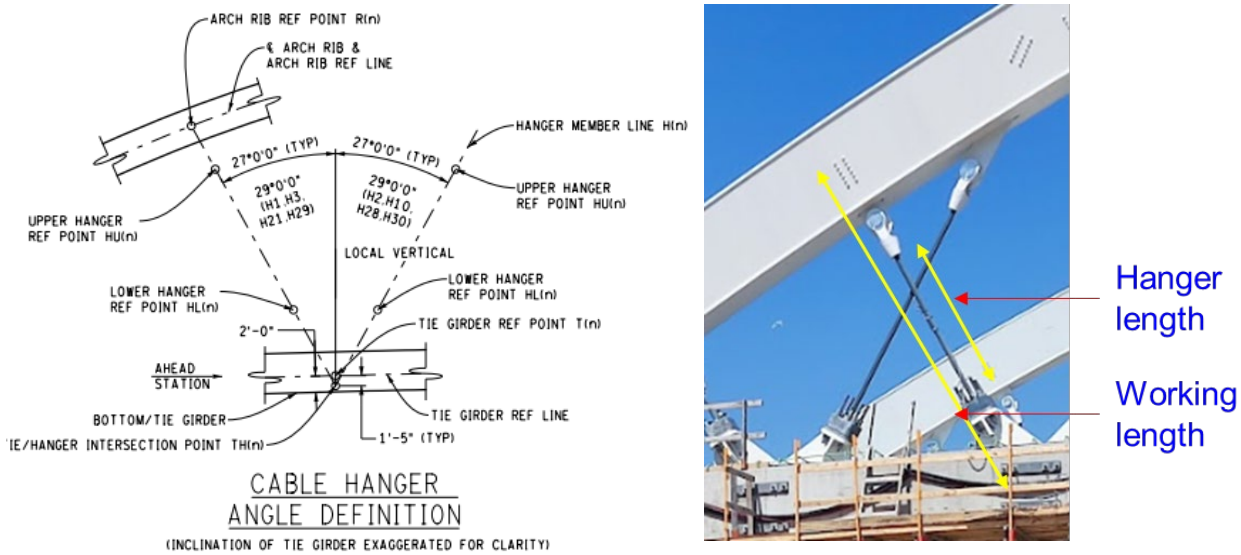

Figure 7-10. Hanger length and reference point definitions.

In the LARSA 4D model, the arch rib was modeled using beam elements with cross-section properties representing the actual trapezoidal geometry, excluding the stiffeners and base plates. The hangers were modeled using cable elements having an equivalent cross-sectional area. Only

the hanger length was modeled, and the ends of the hanger elements were offset to match the geometry. The nodes of the cable elements representing hangers and the beam elements representing arch ribs were connected at the upper hanger connections. Beam elements assigned with rigid properties (i.e., highlighted in red in Figure 7-11) were used to represent the eccentricity of the hangers at the tie girder and the tie/hanger intersection point from the tie girder reference line. The nodes of the cable elements, representing hangers, and the nodes of the beam elements, representing rigid connections, were connected at the lower hanger connections.

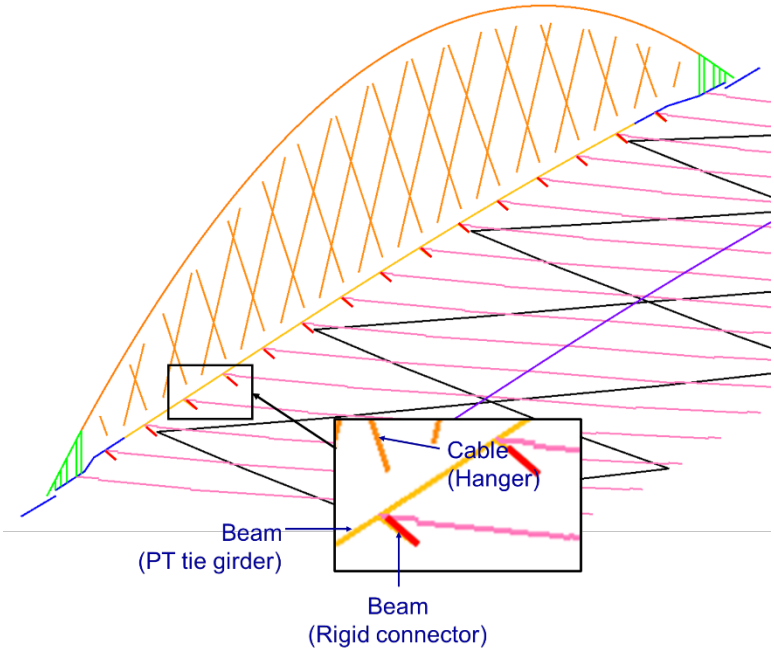

Figure 7-11. Hanger model in LARSA 4D.

Remaining bridge components, including PT end diaphragms, floorbeams, floorbeam diaphragms, and lateral bracings, were modeled using beam elements complying with the information provided in the as-built drawings. An appropriate offset was maintained at the beam ends to match the actual bridge geometry. The bridge deck was modeled with shell elements. Other non-structural components, including sidewalks, planter boxes, lower median barriers, barrier walls, plinths, and sacrificial nosing, were included as loads.

7.2.4 Modelling Tendon Geometry

Figure 7-12 and Figure 7-13 show the tendon layout of the end diaphragm and the tie girder, respectively. As shown in Figure 7-12, each end diaphragm contains 11 PT ducts numbered from DT01 and DT03 through DT12.

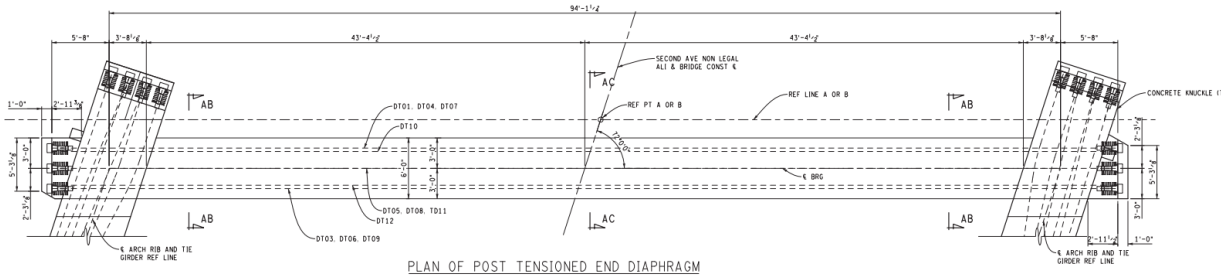

(a) Plan view

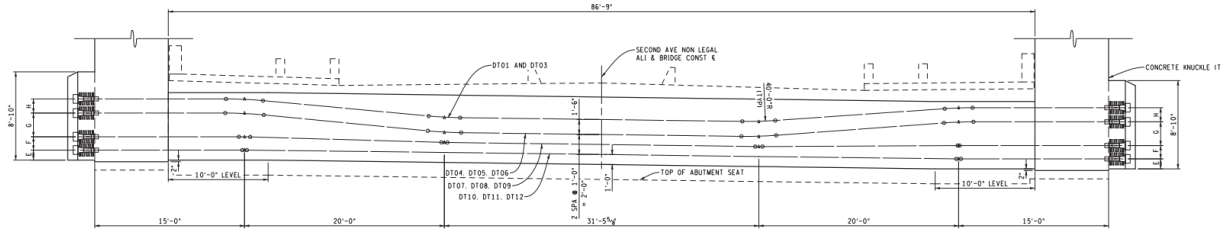

(b) Elevation view

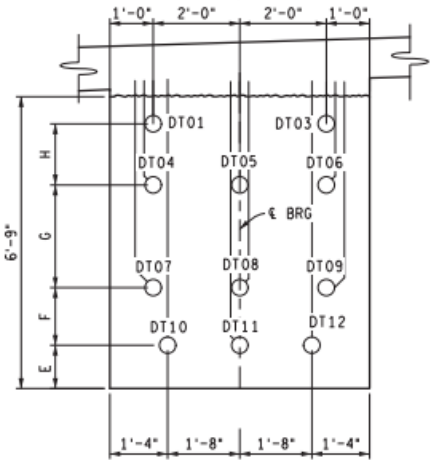

(c) Section AB-AB

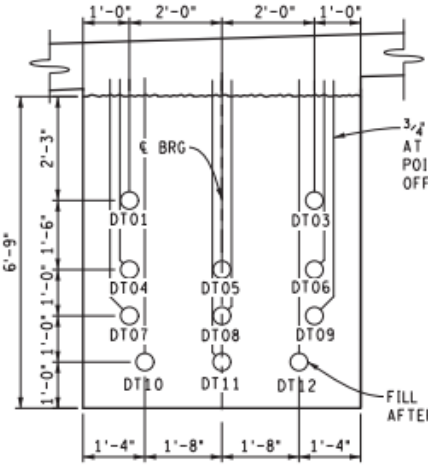

(d) Section AC-AC

Figure 7-12. End diaphragm PT tendon layout.

As shown in Figure 7-13, each tie girder consists of 12 PT ducts numbered from TT01 to TT12. The PT ducts in the tie girder follow a 4 × 3 pattern and are evenly distributed over a 36 × 27 in. grid. However, the PT duct profile inside the knuckle has a very complex geometry. As shown in Figure 7-13, the duct profile towards the end of the knuckle adopts a 3 × 4 pattern and shifts to a 4 × 3pattern towards the tie girder.

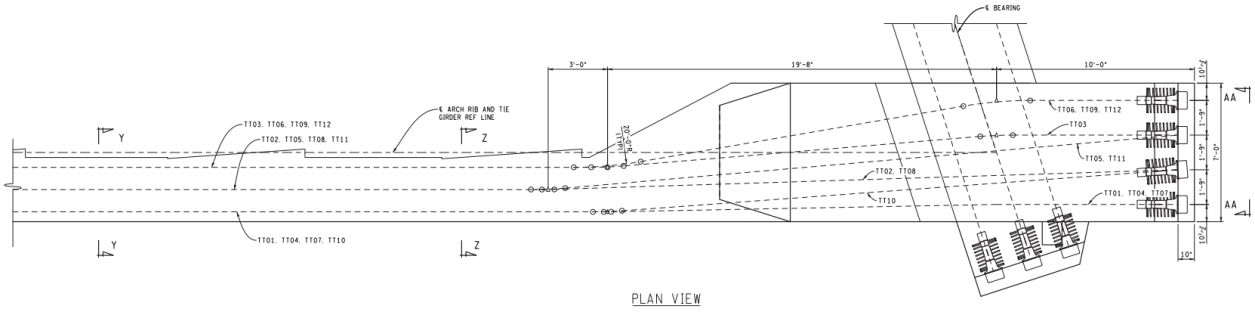

(a) Plan view

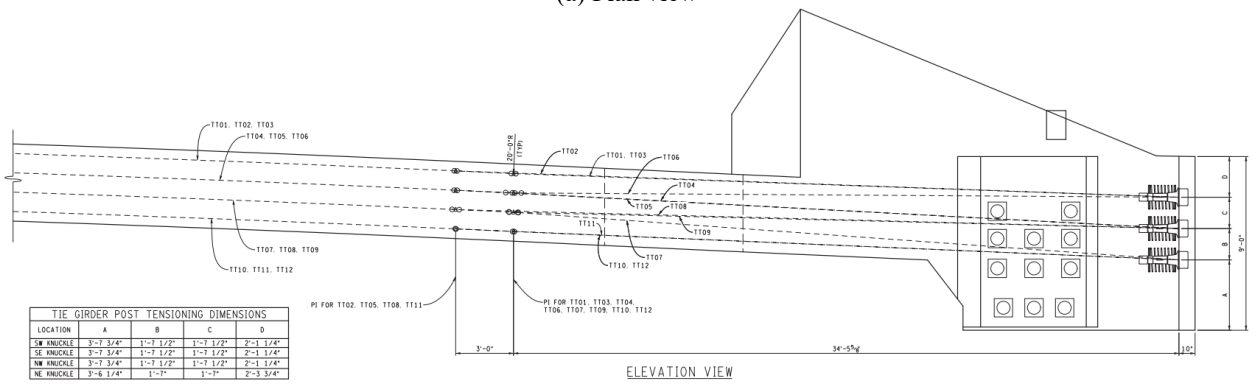

(b) Elevation view

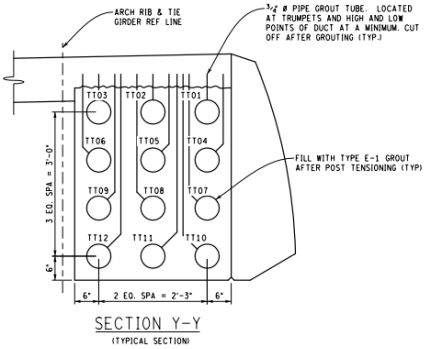

(c) Section Y-Y

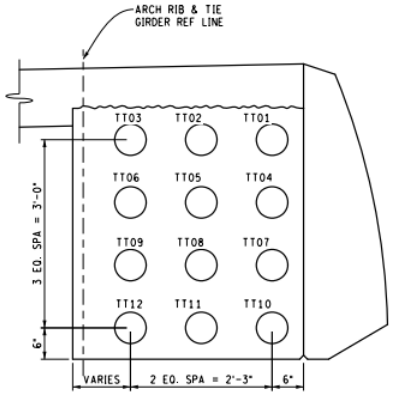

(d) Section Z-Z

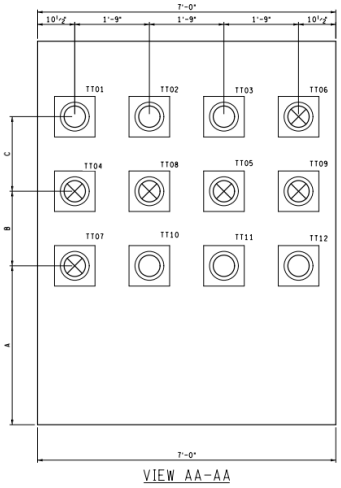

(e) Section A-A

Figure 7-13. Tendon layout in the tie girder.

The tendon paths were defined in accordance with the as-built drawing details (refer to Figure 7-14). Wobble and curvature friction coefficients were assigned as 0.003 rad/in. and 0.15/rad, respectively, based on the friction test results from the west tie girder tendon TT08.

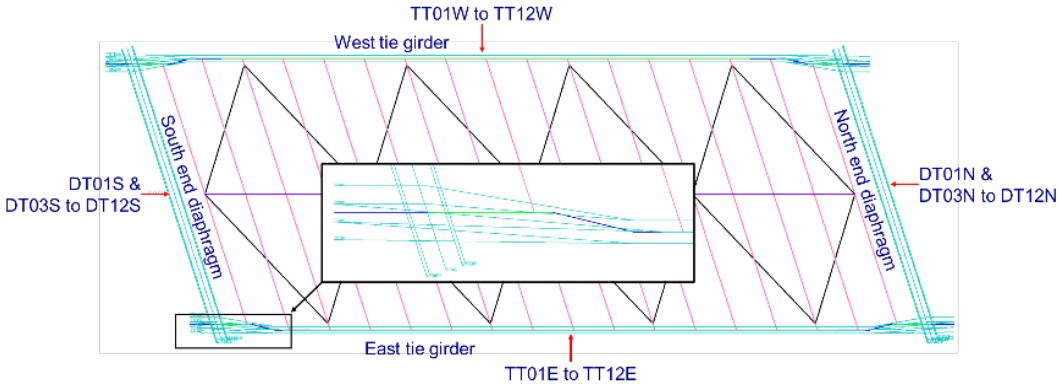

Figure 7-14. Tendon layout used in the LARSA 4D model.

7.2.5 The Impact of LARSA 4D Modeling Assumptions

Due to the complexity of the bridge construction procedure, three independent finite element models were developed by the Engineer of Record (EOR) (Figure 7-16), the contractor's consultant (Figure 7-16), and a peer review engineer to evaluate stress, deflection, and the potential for arch rib buckling under each load case. Among these three models, the results of two models, the EOR and the contractor's models, along with the new LARSA 4D model developed under this study, are presented in Figure 7-17.

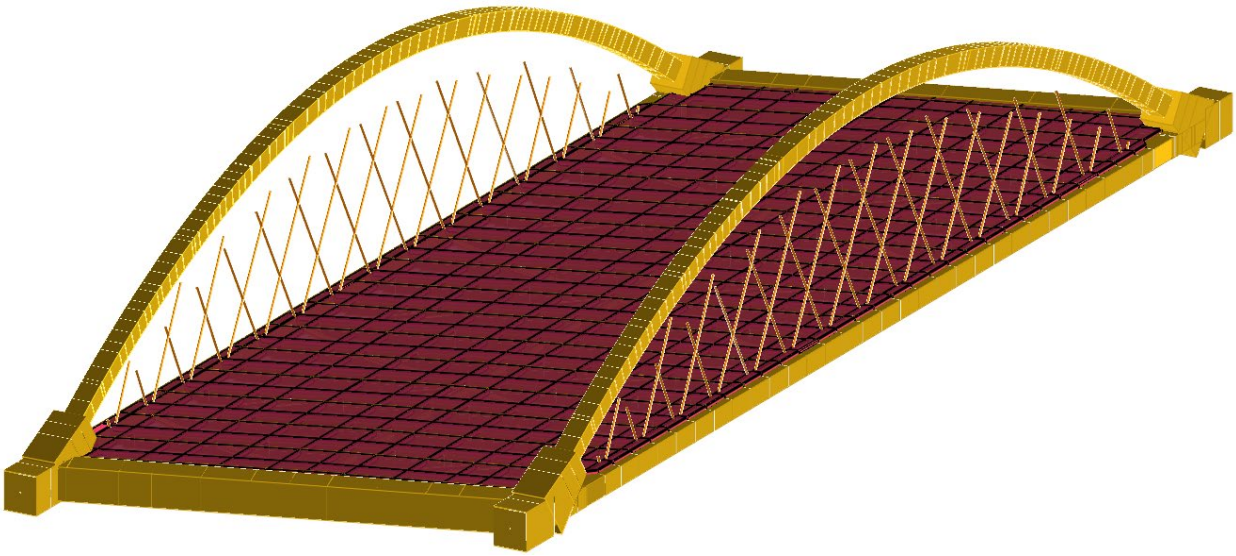

Figure 7-15. LARSA 4D models developed by the EOR.

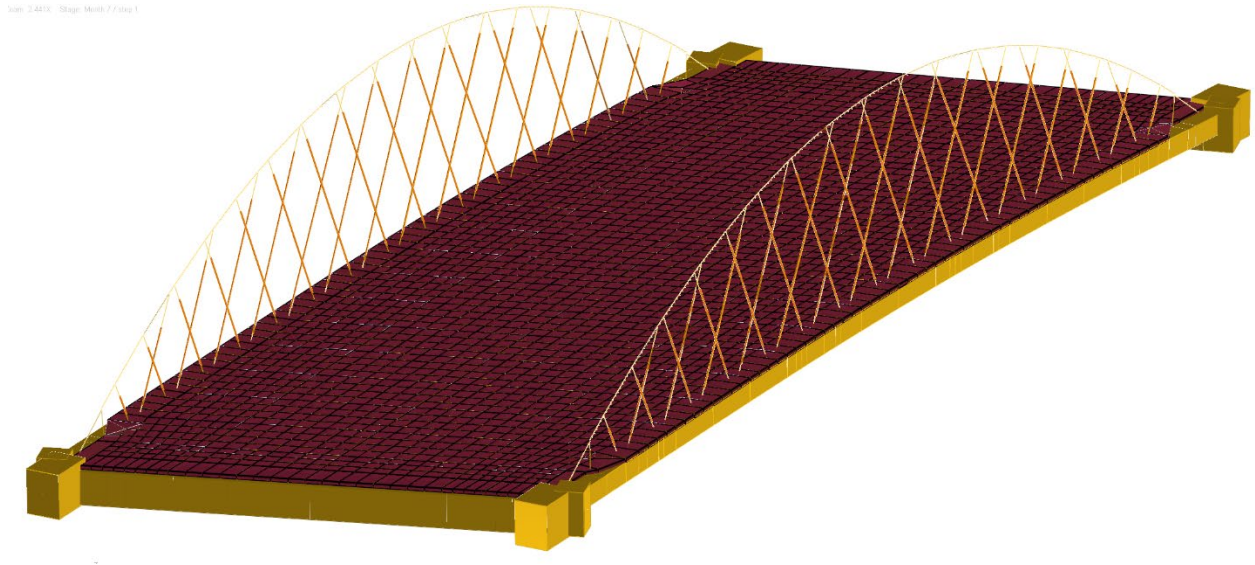

Figure 7-16. LARSA 4D models developed by the contractor's consultant.

Figure 7-17 presents the bending moment diagrams along the west and east tie girders under the dead load at the end of complete bridge construction. The plots also include sketches of arch and tie girders to use as geometric references for the horizontal axis. The different modeling assumptions and simplifications used in the two models to represent the knuckles and tapered sections affected the bending moments in the tapered sections. For example, the upper knuckle in the EOR model was divided into three segments along its length and represented with beam elements with tapered cross-sections and concrete material properties (refer to Figure 7-18a). In contrast, the contractor's model used beam elements with rigid material properties and applied an 84-kip downward concentrated load at the bearing centerline, representing the upper knuckle's self-weight (refer to Figure 7-18b). Additionally, in the EOR model, a cross-section (84 × 94 in.) different from the actual cross-section was assigned for Knuckle A. Furthermore, appropriate element offsets were not defined in the EOR model, thereby affecting the PT tendon geometry. Although these assumptions and deviations significantly influence the results along the length of the knuckle, their impacts on the tie girder behavior are not substantial (Figure 7-17). To explain the behavior of the knuckle and to develop design details, the EOR used refined finite element models and strut-and-tie modeling. As noted in the introduction, none of the load cases exceeded the design limits, even though some variations were observed across the three models due to their modeling assumptions. Therefore, a consensus among the parties was reached, and any variations between models were documented in the project file before starting construction.

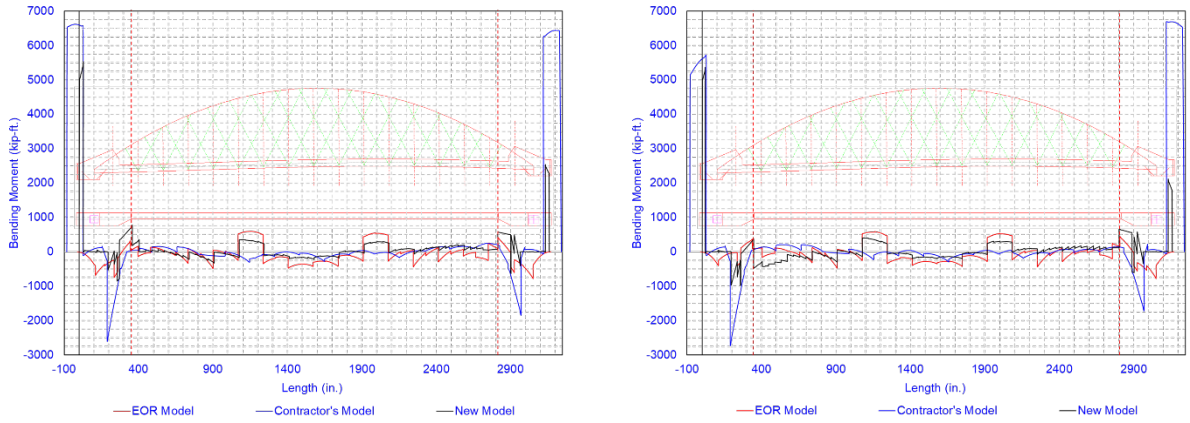

(a) East tie girder (b) West tie girder

Figure 7-17. Bending moment variation along the west and east tie girders at the end of construction.

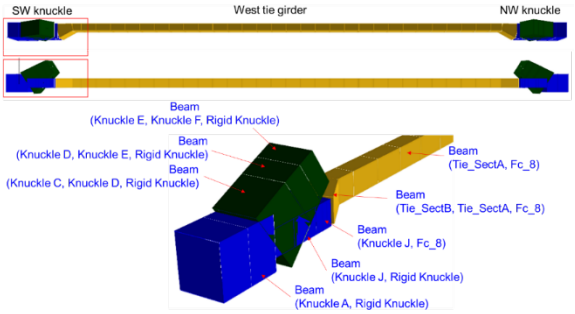

(a) Knuckle model in the EOR model

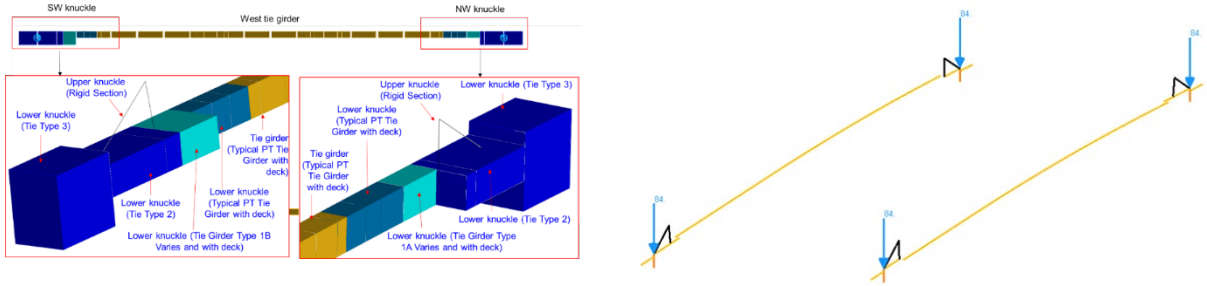

(b) Southwest (SW) and Northwest (NW) knuckles in the contractor's model

Figure 7-18. Knuckle geometries in EOR and contractor's models.

7.3 ABAQUS MODEL

A three-dimensional finite element model of the 2nd Avenue bridge was developed in HyperMesh to generate the input files for Abaqus, a general-purpose finite element software package. As illustrated in Figure 7-2, the model included components such as tie girders, knuckles, end diaphragms, arch ribs, hangers, PT tendons, bent plates, and wedge plates. Modeling bent plates was necessary because the hangers are connected to the bent plates rather than to the tie girder. The construction stages until the bridge move (i.e., until the end of construction at the BSA) were modeled, incorporating time-dependent concrete properties. Abaqus user subroutines were developed to incorporate CEB-FIP 2010 models and simulate the creep and shrinkage behavior of

concrete in PT members. The complex geometry of the bridge was modeled in AutoCAD and imported to HyperMesh for preprocessing. The modeling of individual components is described in the following sections.

7.3.1 West Tie Girder

As shown in Figure 7-19, the west tie girder has a 39 in. × 48 in. uniform rectangular cross-section and a unique camber profile. Twelve (12) 4.6 in. diameter ducts are located inside the girder. These ducts are grouted after the PT operation is completed.

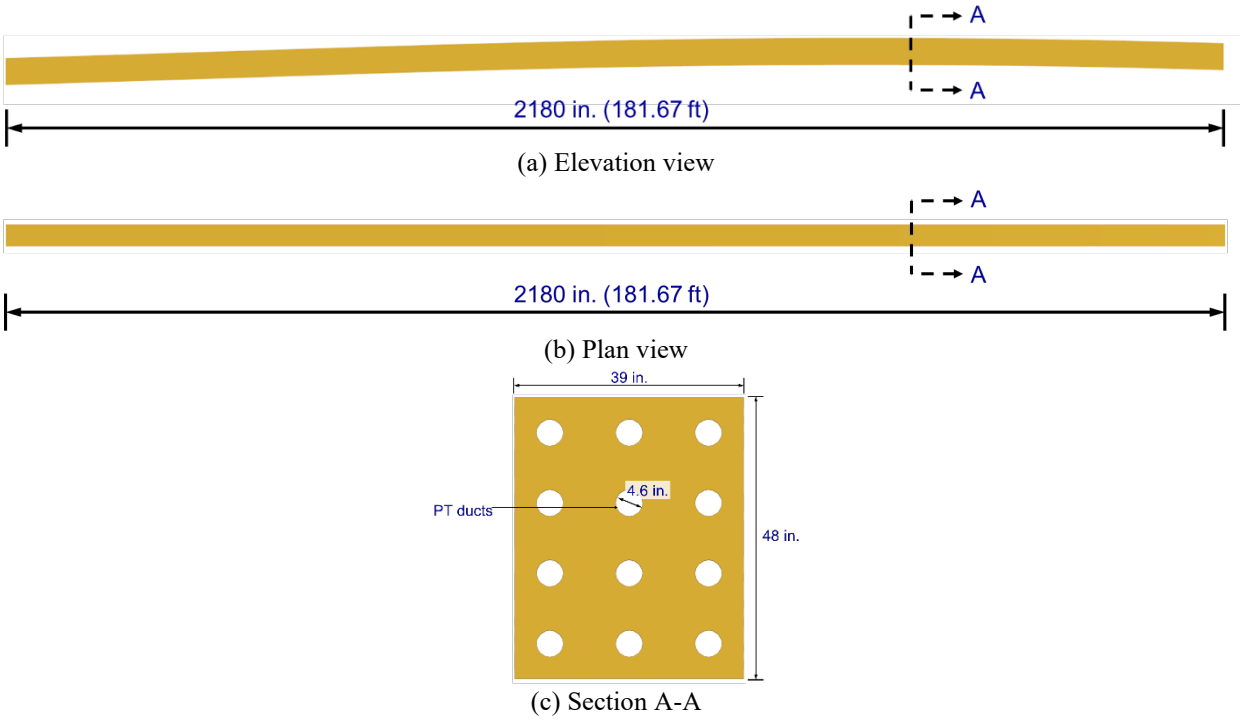

Figure 7-19. West tie girder: (a) elevation, (b) plan, and (c) section A-A.

7.3.2 Upper and Lower Knuckles

Figure 7-20 presents the geometry of the lower and upper knuckles. The geometry starts with a 39 in. × 48 in. rectangular cross-section (Section A-A) from the tie girder connection and ends with an 84 in. × 108 in. rectangular cross-section (Section C-C). The tapered section at the lower knuckle is the transition between the knuckle and tie girder geometries. The cross-section of the lower knuckle changes along the length to accommodate the PT duct profile.

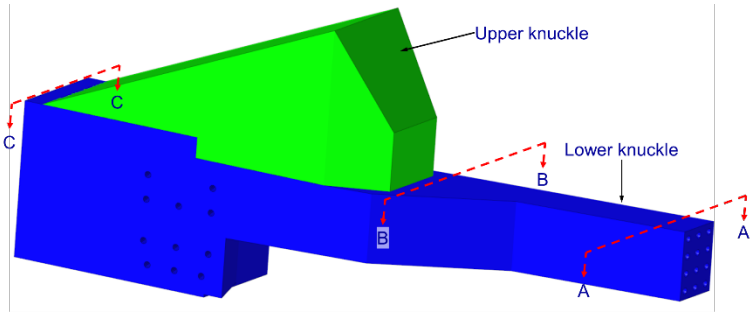

(a) Isometric view

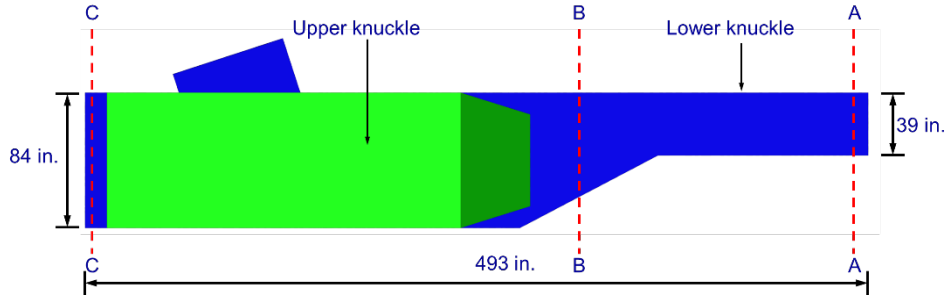

(b) Plan view

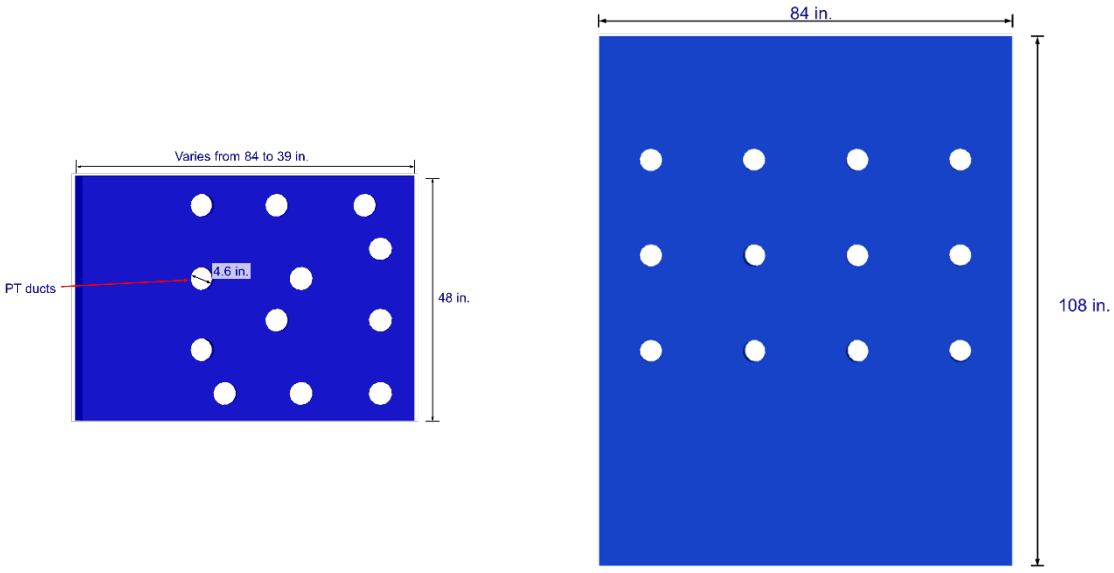

(c) Section B-B (d) Section C-C

Figure 7-20. Knuckle: (a) isometric view, (b) plan, (c) section B-B, and (d) section C-C.

7.3.3 Arch Rib, Hangers, and the Hanger Connections

The geometry of the arch rib was modeled using a 1D element with an equivalent cross-section representing the trapezoidal arch rib section shown in Figure 7-21a. In Abaqus, the arch rib cross-section is defined using an 'arbitrary shape' option, as shown in Figure 7-21b.

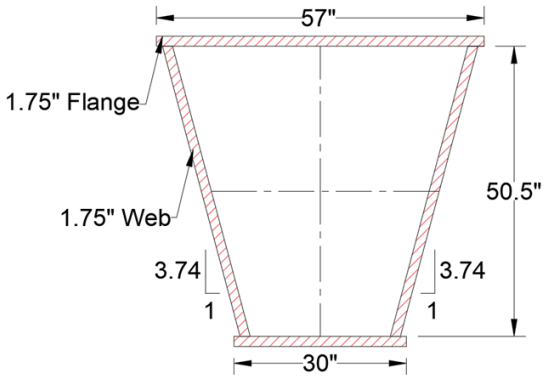

(a) Arch rib cross-section

```
*BEAM SECTION, ELSET=West_Arch_Rib, MATERIAL=ArchRib_Steel, poisson=0.15, temperature=GRADIENTS, SECTION=ARBITRARY
4, -12.8266  ,-26.125   ,12.8266   ,-26.125   ,1.75
26.7964   ,26.125    ,1.75
-26.7964  ,26.125    ,1.75
-12.8266  ,-26.125   ,1.75
0.,0.,1.
```

(b) Abaqus definition of arch rib geometry

Figure 7-21. Arch rib: (a) cross-section and (b) Abaqus definition.

Figure 7-22 shows the modeling of hangers and the connections. The working length of the hangers was modeled using 1D elements with an equivalent circular cross-section representing an area of 5.9 in^2. As illustrated in the figure, node-to-node connections were used to connect hangers to the arch rib at the top and the floorbeam bent plates at the bottom.

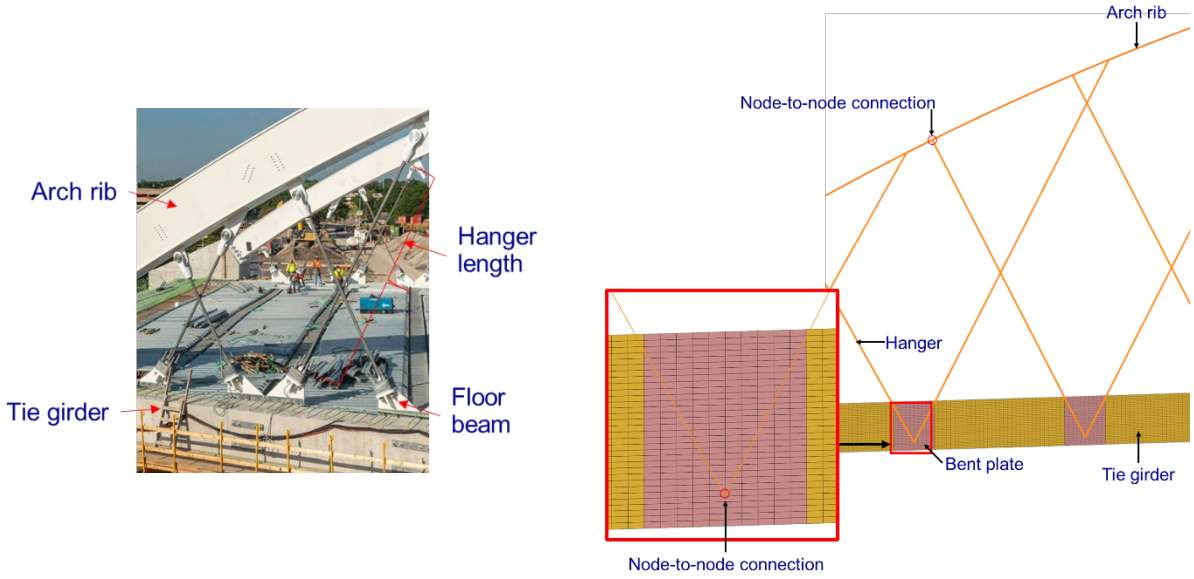

Figure 7-22. Modeling of hangers and the hanger connections.

7.3.4 Tendons, Grouted PT Ducts, and Anchorage Wedge Plates

The tendons were modeled using 1D elements with an equivalent circular cross-section with a radius of 1.146 in. to represent all 19 strands in a single duct (Figure 7-23(a) and (b)). The tendon layout was maintained as illustrated in Figure 7-24, similar to the tie girder. The elements within

a 7.5 × 7.0 in. area were selected, extruded to create the 1.75 in. wedge plate, and anchored the unbonded tendons (Figure 7-23c). The geometry of the grouted PT ducts consisted of circular cylinders with a diameter of 4.6 in. that followed the path of the tendon layout. Mild steel reinforcement was not included in the model.

(a) A single tendon with 19 7-wire strands

```
*Beam Section, elset=W_TT_01, material=PTSteel, temperature=GRADIENTS, section=CIRC
1.146
0.,0.,1.
```

(b) Equivalent circular section of a tendon

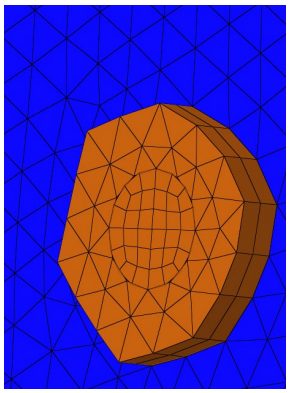

(c) Anchorage wedge plate

Figure 7-23. Geometry of the (a) tendon, (b) representation of the tendon as an equivalent circular section, and (c) the wedge plate.

.

(a) Plan view

(b) Elevation view

Figure 7-24. Tendon layout in the west tie girder: (a) plan view and (b) elevation view.

7.3.5 Elements and Mesh Generation

As mentioned earlier, HyperMesh was used to generate the mesh. Due to the complexity of the geometry, lower knuckles with empty PT ducts were meshed using 4-node linear tetrahedron

elements (C3D4). The upper knuckles were meshed using 6-node linear triangular prism (C3D6) and 8-node linear brick (hexahedral) (C3D8) elements. C3D8 elements were used to mesh tie girders with empty ducts, grout, and arch base plates. Floorbeam bent plates and wedge plates were modeled by extruding the representative areas of the tie girder and grout. Therefore, both wedge and bent plates included C3D6 and C3D8 elements. The arch ribs and PT tendons were modeled using 2-node linear beam elements (B31). Hangers were modeled with 2-node linear displacement truss (T3D2) elements as tension-only elements, with the no compression option enabled. Figure 7-25 shows the elevation view of the finite element model. An isometric view of the west tie girder, including element types used to develop the model, is shown in Figure 7-26.

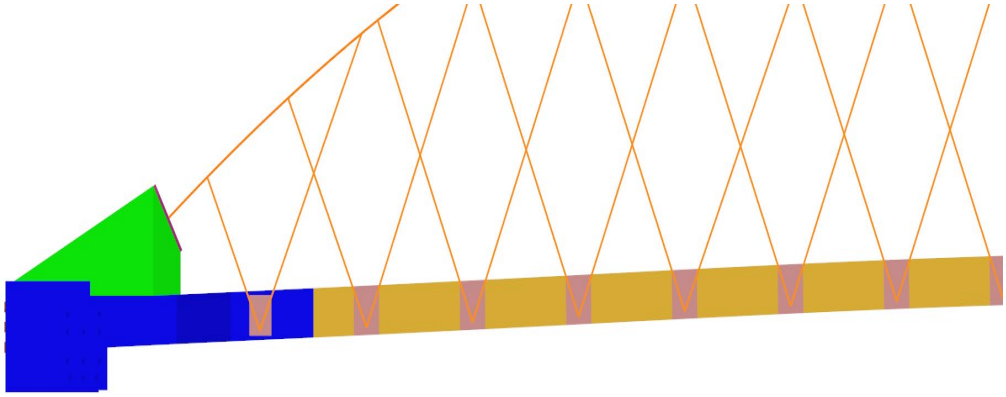

Figure 7-25. Elevation view of the finite element model (only half is shown).

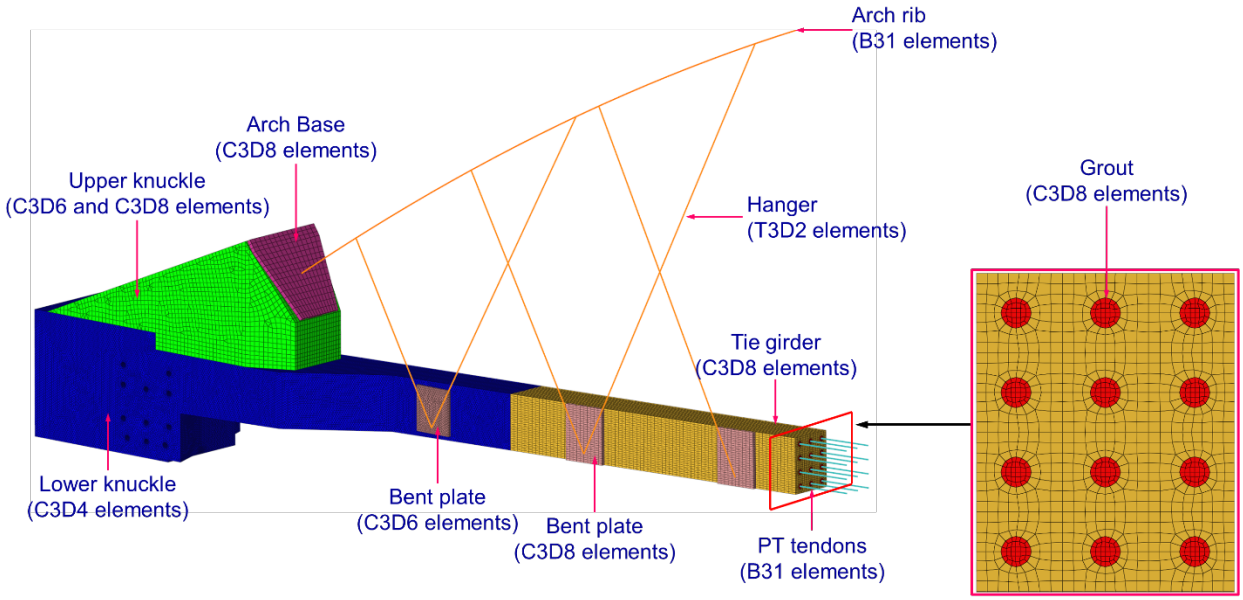

Figure 7-26. Finite element mesh of the tie girder and the knuckle.

Figure 7-27 shows the details of the mesh used to model the end diaphragms. As shown in the figure, each end diaphragm was divided into five segments based on the duct profile. The end

diaphragm sections with ducts parallel to the diaphragm profile were meshed using C3D8 elements, while the remaining sections were modeled using C3D4 elements. Grout and PT tendons within the diaphragms were modeled using C3D8 and B31 elements, respectively.

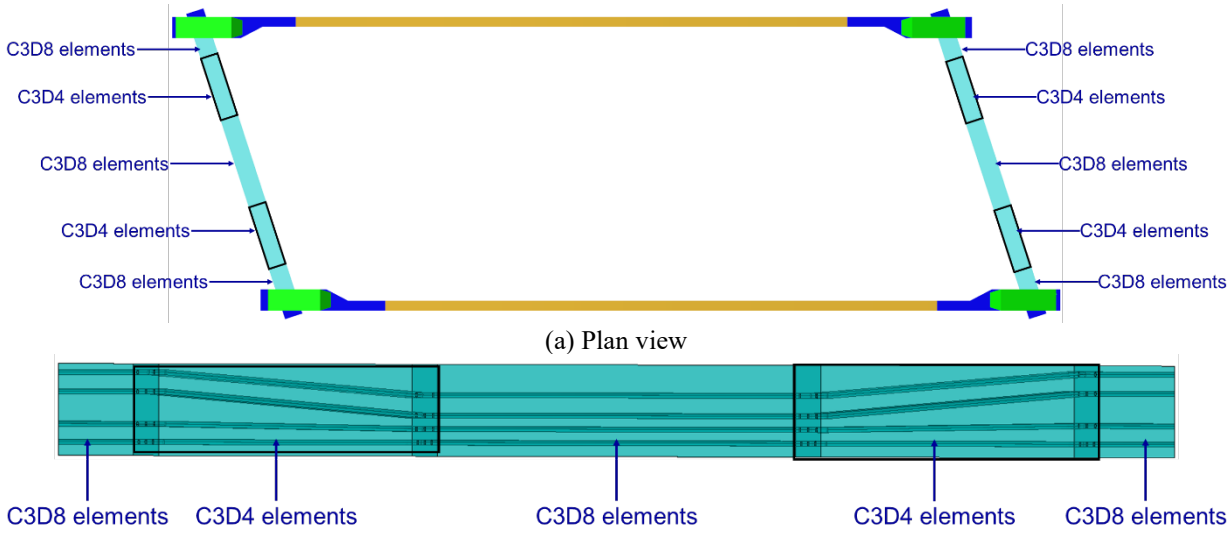

(a) Plan view

(b) Front elevation

Figure 7-27. Finite element model of end diaphragms.

To reduce computational time, node-to-node connections were maintained wherever possible. As shown in Figure 7-28, surface interaction was defined between upper knuckles and arch bases, lower knuckles and upper knuckles, lower knuckles and tie girders, lower knuckles and end diaphragms, end diaphragm sections with parallel and inclined duct profiles, and concrete and grout interfaces.

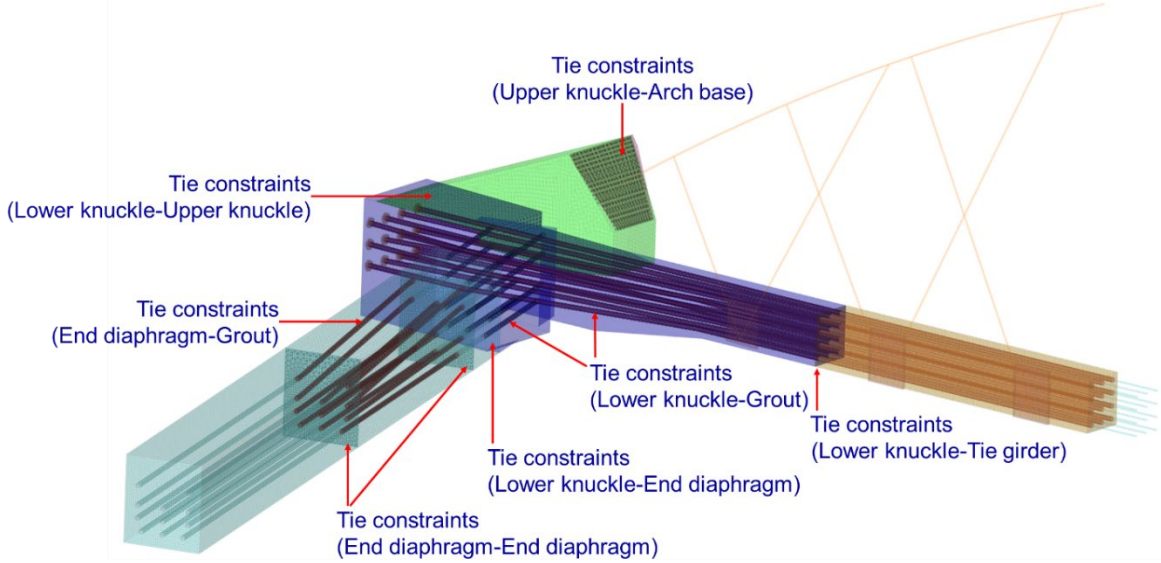

Figure 7-28. A few locations in the finite element model with contact interactions.

Mesh sensitivity analysis was not performed considering the refined mesh used in the model and its complexity due to multiple interactions and constraints. Instead, the mesh accuracy was verified in HyperMesh using the "Check Elements" option. Table 7-2 summarizes the mesh quality. A total of 16,181,413 elements were used in the model. Aspect ratio, Jacobian, minimum and maximum angles, and tetra collapse (i.e., applicable only for C3D4 elements) were utilized as quality control parameters. The aspect ratio was maintained at or below 5, and the Jacobian was kept at or above 0.8. The element angles were maintained between 45 and 135° for C3D8 elements and between 20 and 135° for C3D4 and C3D6 elements. As shown in the table, only 694,253 elements (i.e., 4% of the total elements) failed the aspect ratio; 565,691 elements failed the Jacobian; 173,287 elements failed the tetra collapse;1,497 elements failed the minimum angle for triangular faces, 368 elements failed the maximum angle for triangular faces, and zero elements failed the minimum and maximum angle for quad faces. Among these failed elements, most are in PT grouted ducts and are not expected to affect the analysis results.

Table 7-2. Quality of the Mesh in the Finite Element Model

Component	Element Type	Number of Elements	Number of Failed Elements				
			Aspect Ratio > 5	Jacobian < 0.8	Min Angle < 45° [1]	Max Angle > 135°	Tetra Collapse < 0.5
Tie girders	C3D8	837,120	30,741 (4%)	227,862 (27.2%)	0 (0%)	0 (0%)	NA[2]
Lower knuckles	C3D4	10,911,606	275 (0%)	0	1,155 (0%)	368 (0%)	72,853 (0.7%)
Upper knuckles	C3D6	6,498	0	0	0	0	NA
	C3D8	70,604	0	57 (0.1%)	0 (0%)	0 (0%)	NA
End diaphragms	C3D4	3,312,283	0	0	342 (0%)	0	100,434 (3%)
	C3D8	250,016	0	3,648 (1.5%)	0 (0%)	0 (0%)	NA
PT grouted ducts	C3D8	663,308	663,237 (100%)	331,916 (50%)	0	0	NA
Anchorage wedge plates	C3D6	5,056	0	0	0	0	NA
	C3D8	4,128	0	2,208 (53.5%)	0	0	NA
Floor beam bent plates	C3D6	7,984	0	0	0	0	NA
	C3D8	16,640	0	0	0	0	NA
Arch rib base plate	C3D8	896	0	0	0	0	NA
PT tendons	B31	23,821	NA				
Dummy PT elements		23,637	NA				
Hangers	T3D2	60	NA				
Arch rib	B31	390	NA				
Springs		47,366					

1. 20° for triangular faces and 45° for quad faces
2. Not applicable.

7.3.6 Post-tension Modeling

Unlike concrete shrinkage, concrete creep behavior is influenced by the stress history. Therefore, an accurate representation of the post-tensioning procedure is essential in modeling the creep. During post-tensioning, the load transfers to the concrete through the end anchorages. Figure 7-29 shows the approach used to model the post-tensioning at the end anchorages. Wedge plates were modeled at the end anchorages to transfer the force from the tendon to the concrete girder (Figure 7-23b). At the girder ends, node-to-node connections were used to anchor the tendon end nodes to the wedge plate. Node-to-node connections were used at the interface between the wedge plate and the lower knuckle.

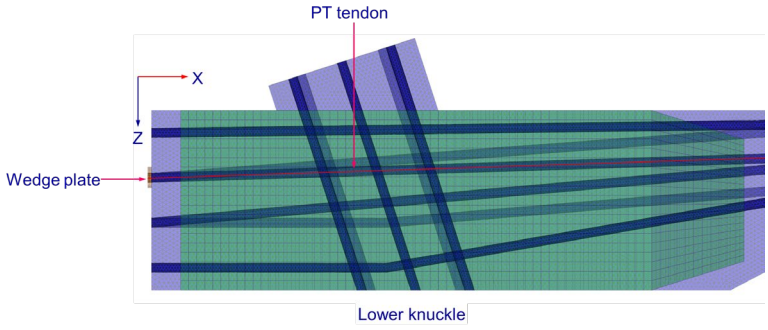

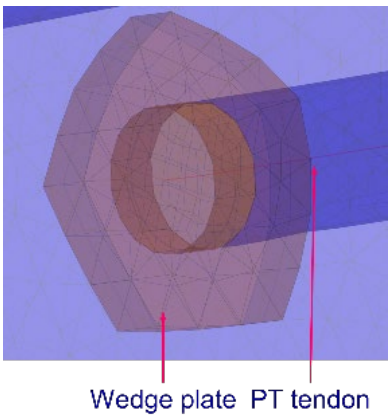

Node-to-node connection between the wedge plate and the tendon. Y- and Z-translations of the tendon are restrained.

Figure 7-29. Tendon anchorage at the girder end.

For accurate representation of the stress due to post-tensioning, the correct girder sectional geometry (area and section modulus), tendon eccentricity, and the force in the tendon need to be correctly modeled. The eccentricity of tendons along the plan and elevation profiles was controlled using spring elements, following the procedure described in Huang (2012). The PT tendon was connected to a virtual (i.e., dummy) tendon that was embedded in concrete. The virtual tendon was assigned a very low modulus to avoid any structural representation. The PT tendon and the virtual tendon were connected at selected locations along the length using Spring2 elements. The Spring2 elements were assigned very high stiffness in the Y- and Z-directions. Figure 7-30 shows the model.

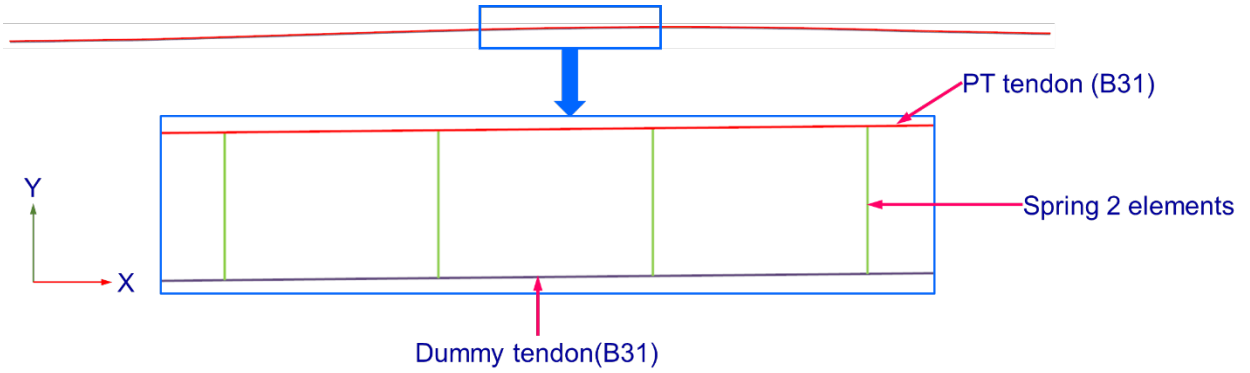

Figure 7-30. The modeling approach used to maintain the tendon profile.

In the Abaqus model developed in this study, the net area of the girder was modeled. The grouting was modeled by activating the corresponding grout elements in parallel to the grouting operations. After grouting the ducts, the virtual tendon is deactivated, allowing strain compatibility between the tendon and the concrete girder.

The variation of the tendon force along the profile due to friction and anchorage set losses cannot be explicitly modeled in Abaqus. Therefore, the average force in each tendon, after accounting for friction and anchorage set losses, was used. Appendix C presents the post-tension tendons stress calculations. Predefined temperature fields were assigned for each tendon such that the resultant force/stress in the tendon is equal to the average force/stress after friction and anchorage set losses. A thermal expansion coefficient of 0.000122/°C was assigned to the prestressing steel. However, when the average stress is applied to the tendon, the girder undergoes instant elastic shortening. This reduces the stress in the tendon from the expected value. This elastic shortening of the girder does not include the original elastic shortening during the jacking operation. Therefore, the exact stress value to be applied as a predefined field was determined after several preliminary analyses to ensure that the prestress in the tendon reached the expected level.

The stresses in the tendons were automatically updated to account for elastic shortening due to sequential stressing during multiple stages of post-tensioning, as well as long-term losses resulting from concrete creep and shrinkage. Before grouting, any change in the stress in the tie girder is transferred to the tendons from the end anchorages (wedge plates). After grouting, strain compatibility exists between the tendon and the surrounding concrete. Any change in stress (due to creep, shrinkage, and stressing sequence) is directly transferred to the tendon from the concrete.

7.4 MATERIAL PROPERTIES

7.4.1 Comparison of the Measured Total Shrinkage with Empirical Predictions

As discussed in Chapter 5, both tie girders were fabricated as independent components. Further, the formwork used for these girders had a very smooth surface. Therefore, the deformations of the tie girders due to shrinkage were not restrained, and the strains recorded by the embedded VW sensors represent the total shrinkage. Even though the end diaphragms were connected to the tie girders at the end of fabrication, the 18-degree skew is not sharp enough to provide any resistance to the deformation of the end diaphragm. Therefore, the strains recorded by the VW sensors embedded in the end diaphragm represent the autogenous and total shrinkage. The measured strain data are presented in Chapter 5. According to the literature, the CEB-FIP 2010 and RILEM B4 models are the most suitable for calculating total shrinkage in components fabricated with concrete mixes containing high dosages of supplementary cementitious materials. To select the most suitable model to represent the shrinkage behavior of the tie girders, end diaphragms, and knuckles, the measured shrinkage values were compared with the values calculated using CEB-FIP 2010 and RILEM B4 models, considering the geometries and the formwork removal times of the tie girders and end diaphragms.

7.4.1.1 Total Shrinkage in Tie Girders

Figure 7-31 and Figure 7-32 show the measured and calculated total shrinkage in the tie girders at the instrumented cross-sections. Table 7-3 shows the Residual Standard Error (RSE) of the measured and calculated total shrinkage strains in the tie girders. As observed in Figure 7-31, Figure 7-32, and Table 7-3, the CEB-FIP 2010 model provides better estimations of the total shrinkage in the tie girders, whereas the RILEM B4 model overestimates the total shrinkage.

Table 7-3. RSE of the Measured and Calculated Total Shrinkage in Tie Girders

Shrinkage Model	Residual Standard Error (RSE) of Total Shrinkage Strains				
	West Tie Girder		East Tie Girder		
	TG-8	TG-9	TG-2	TG-3	TG-4
CEB-FIP 2010	53	46	21	44	22
RILEM B4	305	298	257	285	262

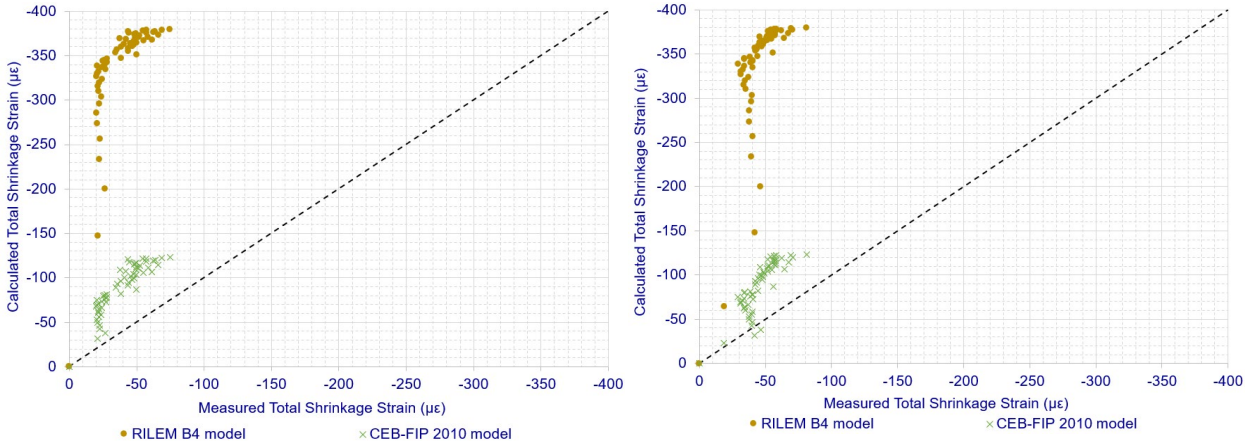

(a) West tie girder at TG-8 (b) West tie girder at TG-9

Figure 7-31. Measured and calculated total shrinkage strains in the west tie girder.

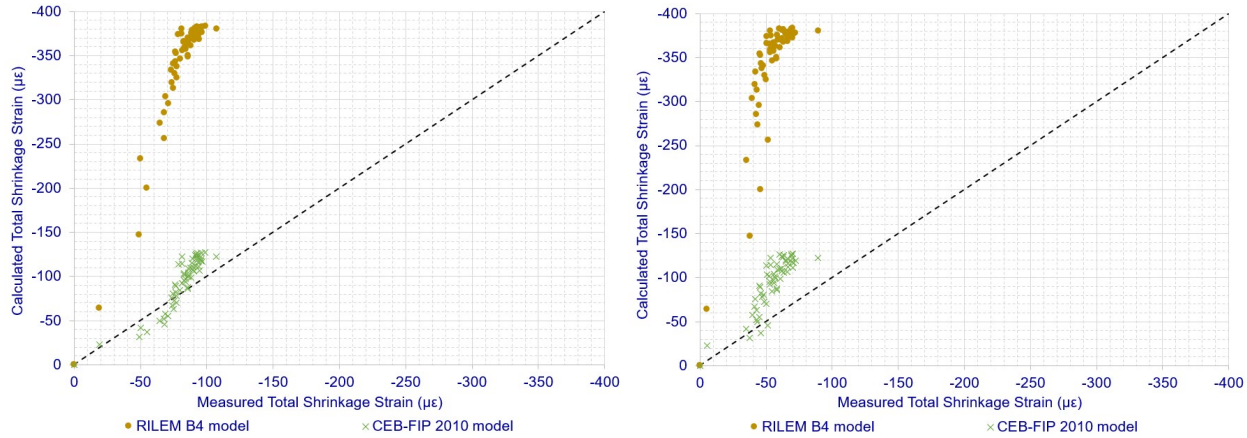

(a) East tie girder at TG-2 (b) East tie girder at TG-3

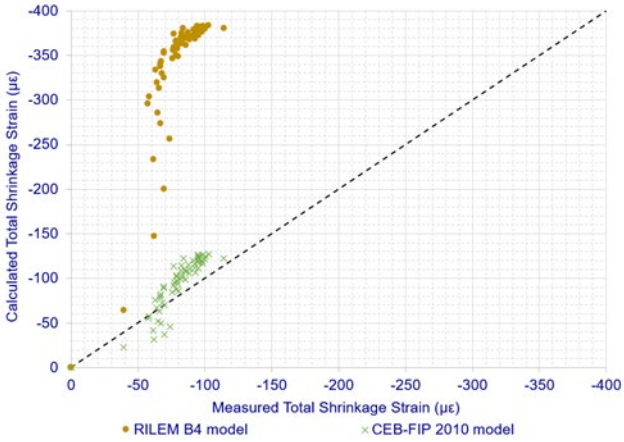

(c) East tie girder at TG-4

Figure 7-32. Measured and calculated total shrinkage strains in the east tie girder.

7.4.1.2 Total Shrinkage in End Diaphragms

Figure 7-33 depicts the measured and calculated total shrinkage in the end diaphragms at the instrumented locations. Table 7-4 shows the RSE of the measured and calculated total shrinkage

strains in the end diaphragms. As illustrated in Figure 7-33 and Table 7-4, the CEB-FIP 2010 model provides better estimations of the total shrinkage in the end diaphragms, whereas the RILEM B4 model overestimates the total shrinkage.

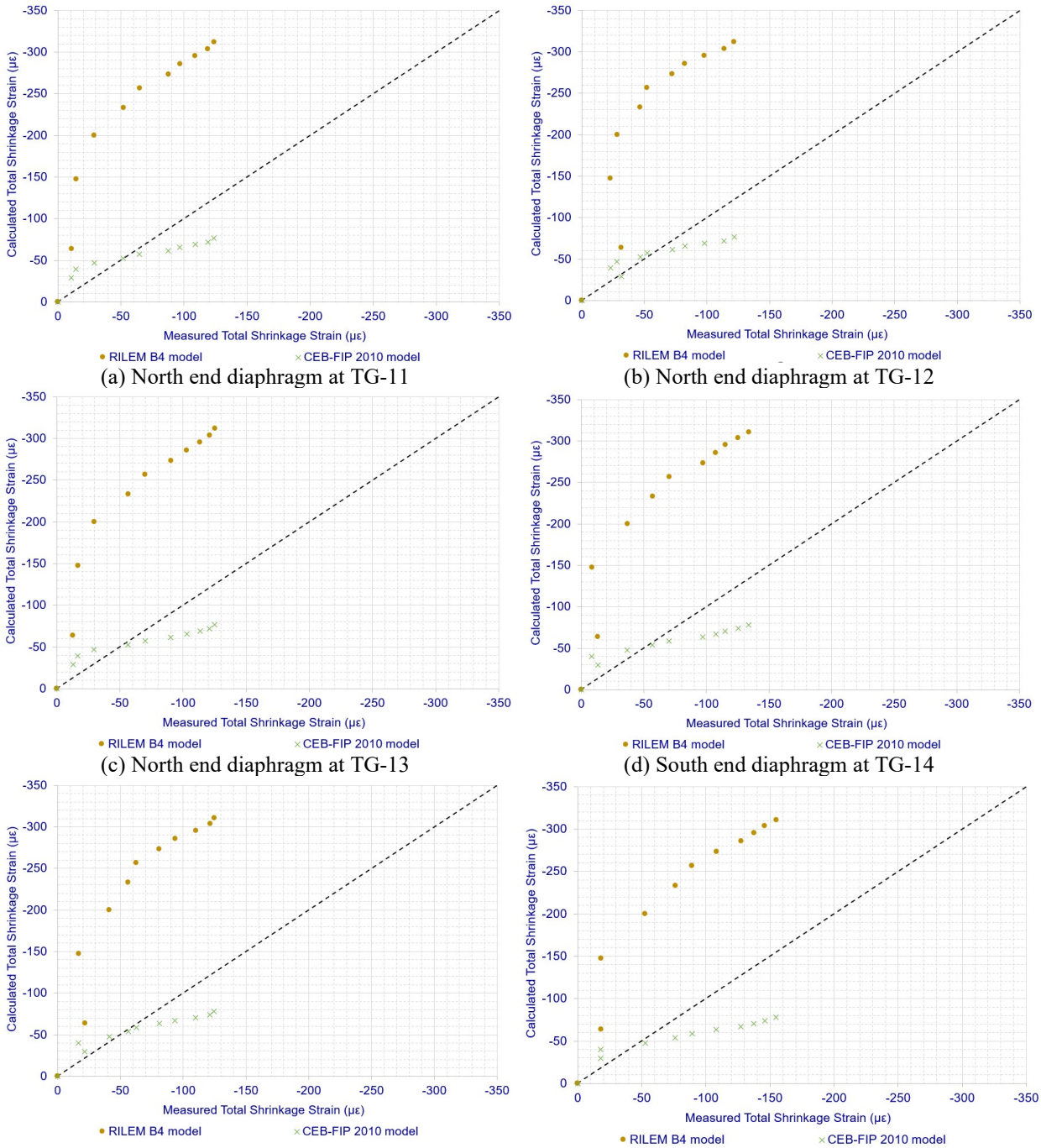

(a) North end diaphragm at TG-11

(b) North end diaphragm at TG-12

(c) North end diaphragm at TG-13

(d) South end diaphragm at TG-14

(e) South end diaphragm at TG-15

(f) South end diaphragm at TG-16

Figure 7-33. Measured and calculated total shrinkage strains in the end diaphragms.

Table 7-4. RES of the Measured and Calculated Total Shrinkage in End Diaphragms

Shrinkage Model	Residual Standard Error (RSE) of Total Shrinkage Strains					
	North End Diaphragm			South End Diaphragm		
	TG-11	TG-12	TG-13	TG-14	TG-15	TG-16
CEB-FIP 2010	29	23	30	33	26	46
RILEM B4	181	187	177	174	179	156

7.4.2 Comparison of the Measured Creep Coefficients with Empirical Predictions

Basnayake (2023) conducted an extensive laboratory study to assess the creep coefficient of the concrete mix used in the 2nd Avenue Bridge. Ten concrete prisms (4×4×24 in.) were fabricated at the bridge site in two batches (Batch 1 and Batch 2). Batch 1 specimens were fabricated simultaneously with the west tie girder on 12/23/2021. Batch 2 specimens were fabricated simultaneously with the east tie girder on 1/13/2022 (i.e., 21 days after Batch 1). Specimens were cured under four different conditions as described in Table 7-5.

Table 7-5. Exposure Before Demolding of Concrete Specimens and Curing Conditions

Batch	Exposure Before Demolding	Curing Type	Curing Conditions	Specimen Set
Batch 1	Specimens were left at the bridge site for 36-48 hours after fabrication, then transported to WMU and demolded.	ASTM + Laboratory cured	The specimens were submerged in lime-saturated water at 73.5 ± 3.5° F (23.0 ±2.0° C) until concrete reached 7 days of age. Then, the specimens were stored at 73.5 ± 3.5° F (23.0 ±2.0° C) and 50 ± 4% relative humidity until testing.	Set 1 (ASTM + Laboratory)
	Specimens were left at the bridge site, transported to WMU at the time of testing, and demolded before testing.	On-site cured[1]	The specimens were cured under the field conditions at the bridge site in their molds and wrapped in plastic until the time of testing. During testing, specimens were stored at 73.5 ± 3.5° F (23.0 ±2.0° C) and 50 ± 4% relative humidity.	Set 2 (Field)
Batch 2	Specimens were transported to WMU after fabrication at the bridge site. Specimens were wrapped in plastic and demolded at the time of testing.	Laboratory cured	The specimens were stored at 73.5 ± 3.5° F (23.0 ±2.0° C) and 50 ± 4% relative humidity until the end of testing.	Set 4 (Laboratory)

WMU – Western Michigan University

[1]- The west tie girder was cured inside an enclosure prepared with insulation blankets. The temperature inside the enclosure was maintained by supplying heated air. The concrete specimens were stored at the ground level directly below the west tie girder and protected with the same insulation blankets.

Three sets of concrete prisms were used for the laboratory experimental program: Set 1 (ASTM + Laboratory), Set 2 (Field), and Set 4 (Laboratory). Set 1 (ASTM + Laboratory) prisms were transported to the lab after keeping them at the site for about 2 days, removed from the molds, cured in lime-saturated water at 73.5 ± 3.5° F (23.0 ±2.0° C) until concrete reached 7 days, and then stored inside an enclosure built in the lab with controlled temperature and humidity

conditions. Set 4 (Laboratory) prisms, protected with plastic wrapping, were stored in the enclosure until testing. Set 2 (Field) prisms were protected with plastic wrap and stored at the bridge site until testing. Specimens were brought to the lab, removed from plastic wrapping, and then stored inside the enclosure. The specimens were loaded at 7 and 28 days of concrete age and at the time of post-tensioning of the tie girders, following ASTM C512 (2015).

The purpose of curing specimens under the conditions stipulated in the ASTM C31 was to compare the results with published data. The purpose of curing specimens under typical laboratory conditions was to evaluate the impact of lower RH conditions on concrete properties. The purpose of on-site curing was to assess properties of concrete exposed to conditions similar to those of the west and east tie girders. The use of these different exposure conditions helped establish upper and lower bounds to the measured properties and evaluate the significance of curing conditions on the behavior of this unique mix.

The specimens subjected to creep at 7 and 28 days of concrete age were loaded to a value close to 40% of their compressive strength at the respective concrete ages and maintained the load throughout testing. The creep specimens that were loaded synchronously with the tie girder post-tensioning were subjected to multi-stage loading, representing the stress state of the tie girder. The west tie girder was post-tensioned in three stages at 60, 167, and 280 days of age. The east tie girder was post-tensioned in three stages at 60, 146, and 259 days of age. Set 1 and Set 2 creep specimens were loaded synchronously with the west tie girder post-tensioning. Set 4 creep specimens were loaded synchronously with the east tie girder post-tensioning.

7.4.2.1 Comparison of the Measured and Calculated Creep Coefficients

The measured creep coefficients were compared with the calculated ones using seven creep models: ACI 209R-92, AASHTO, CEB-FIP 90, CEB-FIP 2010, Bażant B3, RILEM B4, and GL 2000. Figure 7-34 shows the relationship between the measured and calculated creep coefficients for Set 1 specimens loaded at 7 and 28 days of concrete age.

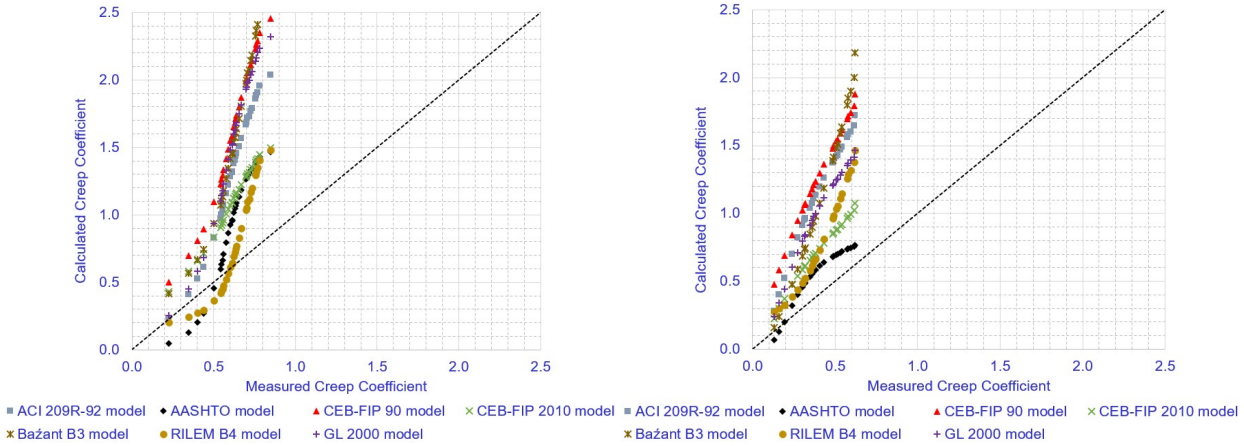

(a) Loaded at 7 days (b) Loaded at 28 days

Figure 7-34. Measured and calculated creep coefficients from Set 1 specimens loaded at (a) 7 and (b) 28 days.

Figure 7-35 shows the relationship between the measured and calculated creep coefficients for Set 1, Set 2, and Set 4 specimens loaded at post-tensioning ages.

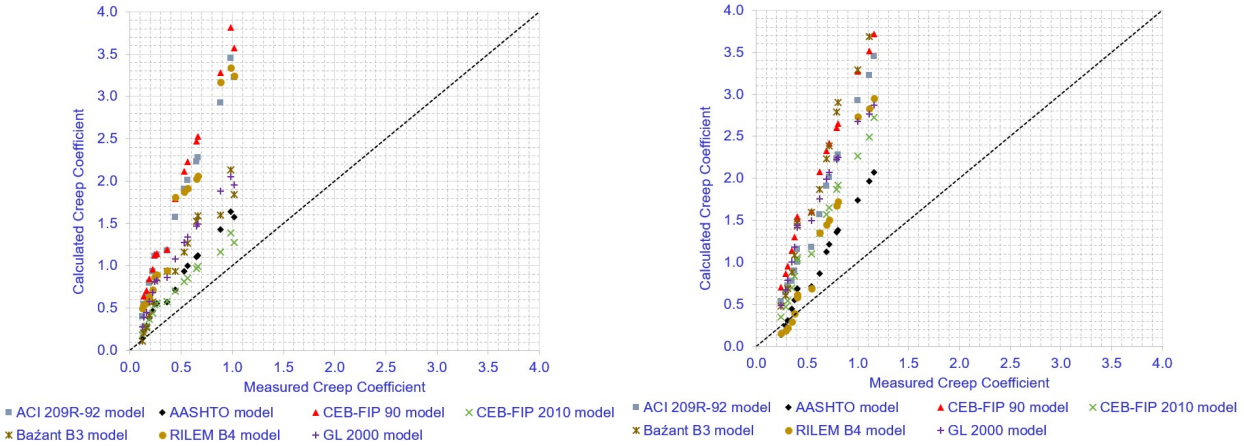

(a) For Set 1 (ASTM + Laboratory) specimens (b) For Set 2 (Field) specimens

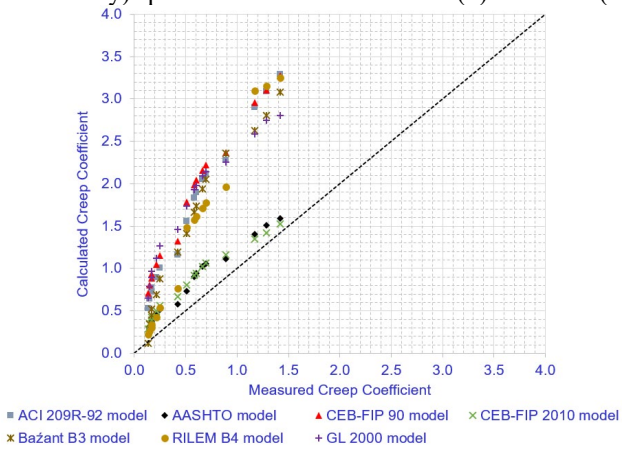

(c) For Set 4 (Laboratory) specimens

Figure 7-35. Measured and calculated creep coefficients for (a) Set 1, (b) Set 2, and (c) Set 4 specimens loaded at post-tensioning ages.

In general, all the creep models overestimated the creep coefficient for this mix. The dense microstructure developed in this concrete mix at later ages, due to the presence of slag and fly ash, could be the reason for the measured lower creep coefficients.

Table 7-6 shows the residual standard error (RSE) of the measured and calculated creep coefficients. The grey-highlighted cells indicate the lowest RSE for each set of specimens. There is no single model that represents the creep behavior of this mix. The CEB-FIP 90 model could not yield the least RSE for any of the specimens, thus invalidating the assumptions made during the design stage. The AASHTO model yielded the lowest RSE for specimens in Sets 2 and 4, which were cured similarly to the tie girders and loaded at post-tensioning ages. Although the AASHTO model provided the lowest RSE for Set 2 and Set 4 specimens, the input parameters used in the creep calculations are basic. Therefore, the CEB-FIP 2010 model, which yielded the second-lowest RSE for specimens in Sets 2 and 4, is selected to represent the creep behavior of this mix.

Table 7-6. RSE of the Measured and Calculated Creep Coefficient

Creep Model	Residual Standard Error (RSE) of Creep Coefficient				
	Set 1 (ASTM+ Laboratory) loaded at		Loaded at post-tensioning ages		
	7 days	28 days	Set 1 (ASTM+ Laboratory)	Set 2 (Field)	Set 4 (Laboratory)
ACI 209R-92	0.830	0.825	1.441	1.309	1.229
AASHTO	0.453	**0.173**	0.398	**0.501**	**0.253**
CEB-FIP 90	1.136	0.949	1.651	1.650	1.330
CEB-FIP 2010	0.522	0.346	**0.278**	0.930	0.275
Bażant B3	1.115	0.886	0.680	1.697	1.082
RILEM B4	**0.319**	0.480	1.391	0.951	1.071
GL 2000	1.052	0.662	0.726	1.253	1.212

7.4.3 LARSA 4D Model

The material properties used in the LARSA 4D model are documented in Table 7-7. Accordingly, MOE, Poisson's ratio, shear modulus, unit weight, and thermal expansion coefficient were defined for each component. Relaxation properties were assigned to PT strands, while time-dependent material properties were assigned to concrete components (including upper and lower knuckles, tie girders, end diaphragms, and the deck). The fib MC2010/CEB-FIP 2010 model was used to represent creep and shrinkage behavior. One major limitation of LARSA 4D is that the program does not calculate concrete drying shrinkage until 3 days after the casting date (LARSA 2022).

Table 7-7. Material Properties Defined in LARSA 4D Model

Component	MOE (kip/in.^{2})	Poisson's Ratio	Shear Modulus (G) (kip/in.^{2})	Unit Weight (kip/in.^{3})	Thermal Expansion (1/°F × 10^{-6})
Upper knuckles	5,852	0.21	2,418	0.0001	5.5
Lower knuckles					
Tie girders					
End diaphragms					
Deck	3,605	0.21	1,541	0[1]	5.5
Arch rib	28,500	0.30	10,962	0.0003	6.5
Floorbeams					
Intermediate diaphragms					
Lateral bracings					
Lateral arch support					
Hangers	23,000	0.30	8,846	0.0003	6.5
PT strands	28,500	0.30	10,962	0.0003	6.5
Rigid material	2,900,000	0.30	1,115,385	0	0

[1] Only the deck stiffness was considered. Deck load was modeled as a uniformly distributed load acting on the floor beams.

7.4.4 Abaqus Model

The time-dependent material properties were defined for concrete, assuming material isotropy. The time-dependent variation of the concrete MOE was defined using the field variables option in Abaqus. Based on the laboratory tests, the MOE was defined as 5851.159 ksi, 6406.190 ksi, and 6541.918 ksi at 60, 168, and 280 days of concrete age, respectively. A time-independent Poisson's ratio of 0.21 was used for concrete, based on the laboratory tests. The unit weight of concrete used in the PT members was 150 lbs/ft^3 for the purpose of applying gravity loading. The same concrete properties were also used for grouts. The MOE and a Poisson's ratio of 28,500 ksi and 0.3 were used for the prestressing steel, arch rib, and wedge plates. The MOE and Poisson's ratio of hangers were 23,000 ksi and 0.3, respectively. Hangers were defined as tension-only members. Only the linear-elastic properties were used. The self-weight of hangers and prestressing steel was not included in the model. Thermal expansion coefficients stated in Table 7-7 were used in the Abaqus model. The CEB-FIP 2010 model was used to represent creep and shrinkage behavior in concrete components through a user subroutine.

8 LOAD TESTING

8.1 OVERVIEW

This diagnostic static load testing was conducted to assess the real-time response of the 2nd Avenue bridge, particularly in terms of strain, under specified loads, and to verify design assumptions. The load testing was conducted on August 7, 2024, 10 months after the bridge was officially opened for traffic. This chapter describes the truck configurations, the design of truckload configurations for load testing, the load testing procedure, observations, and the analysis results.

8.2 TRUCK CONFIGURATIONS AND PLACEMENT

8.2.1 Truck Configurations

The bridge was loaded using eight tandem trucks. The truck configuration and labels for each wheel are shown in Figure 8-1. As shown in the figure, wheels are labeled as Front Left (FL), Front Right (FR), Rear Front Left (RFL), Rear Front Right (RFR), Rear Rear Left (RRL), and Rear Rear Right (RRR).

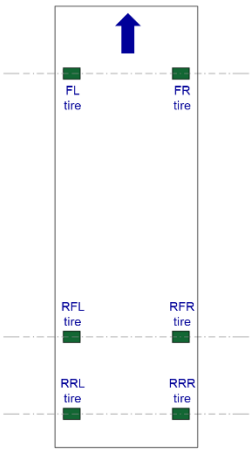

Figure 8-1. Truck configuration and wheel labels.

The axle spacing and wheel loads of each truck are measured and documented in Figure 8-2 and Table 8-1. As depicted in Figure 8-2, the spacing between the Front and Rear Front axles varies between 182 in. and 187 in., except for Truck 04-4116. The spacing between the Rear Front and Rear Rear axles varies between 53 in. and 56 in. The spacing between the Front and Rear Front axles of Truck 04-4116 is 200 in. The distance from the front axle to the truck in front of it varied due to the snowplow attachment (Figure 8-3).

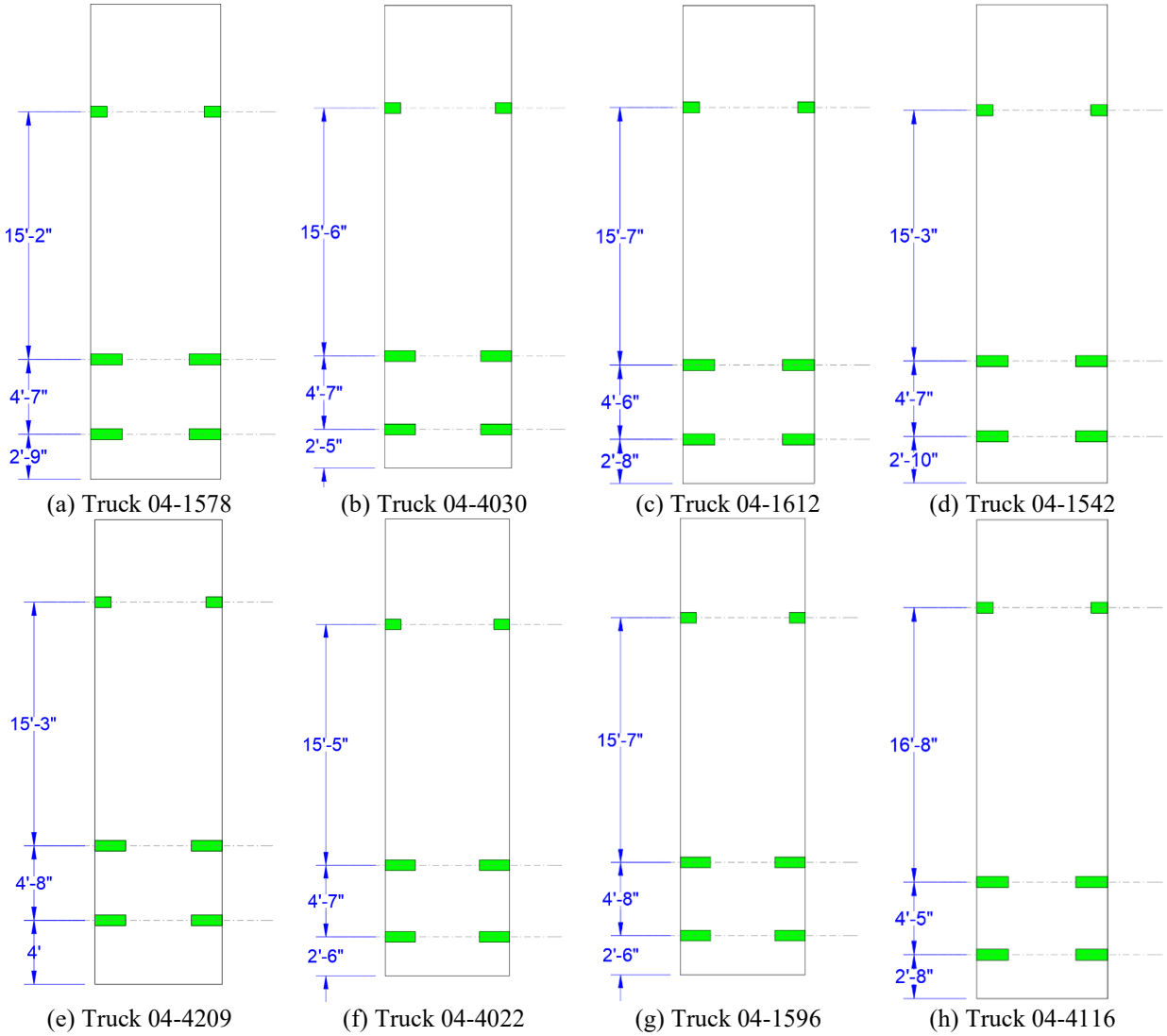

(a) Truck 04-1578 (b) Truck 04-4030 (c) Truck 04-1612 (d) Truck 04-1542

(e) Truck 04-4209 (f) Truck 04-4022 (g) Truck 04-1596 (h) Truck 04-4116

Figure 8-2. Truck configurations.

Figure 8-3. A truck with a snow plow attachment.

Table 8-1. Wheel Loads and Gross Vehicle Weight

Truck No.	Wheel Load (lbs)						GVW (lbs)
	Front Left (FL)	Front Right (FR)	Rear Front Left (RFL)	Rear Front Right (RFR)	Rear Rear Left (RRL)	Rear Rear Right (RRR)	
Truck 04-1578	7,150	7,600	7,650	6,200	7,400	6,550	42,550
Truck 04-4030	8,650	9,350	9,300	9,800	9,200	9,850	56,150
Truck 04-1612	8,200	8,350	8,700	8,750	8,750	8,750	51,500
Truck 04-1542	8,350	8,100	8,300	8,850	8,400	7,590	49,590
Truck 04-4209	8,600	8,750	9,050	10,150	8,800	10,150	55,500
Truck 04-4022	8,800	9,000	8,750	8,500	8,100	8,550	51,700
Truck 04-1596	8,350	8,900	8,150	9,100	8,350	8,750	51,600
Truck 04-4116	8,600	9,100	10,200	9,850	10,250	9,400	57,400

8.2.2 Load Testing Procedure

The bridge was closed to traffic during load testing. Six different truckload configurations were developed, as shown in Appendix F, to position them on the bridge and maximize the strains at selected instrumented cross-sections or members. For example, Figure 8-4 shows the placement of *Truckload Configuration 1* to induce maximum strains at the sensor location TG-8. To induce the maximum strains at sensor locations TG-1, TG-3, TG-7, and TG-8, different truck load configurations were used, and the bridge was completely unloaded before reloading. Truckloads were also placed to induce maximum strains at 14 other sensor locations, including TG-2, -3, -4, -6, -8, -9, and -10; EM-SM-2 and -7; and WH-SM-2, -4, -6, -7, and -8. To minimize the bridge closure and complete load testing within the allotted time, these locations were loaded by rearranging trucks without entirely unloading the bridge.

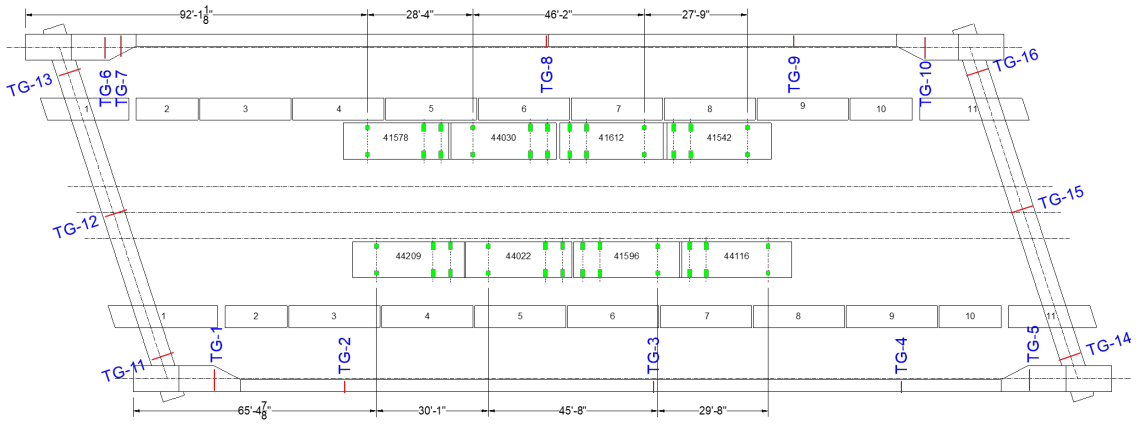

Figure 8-4. *Truckload Configuration 1* placed over a designated area to maximize strains at TG-8.

8.3 OBSERVATIONS

Figure 8-5 presents the total strain variation at TG-03 in the east tie girder and TG-08 in the west tie girder. Two vertical red lines included in the plots indicate the dates of bridge opening and

load testing. As shown in the figure, no significant change in strains was observed during load testing. The bridge's response to 8 trucks with a total load of 416 kips (i.e., 50% of the HL-93 Mod design load) highlights its minimal sensitivity to live loads, owing to the very rigid structural system. Figure 8-6 shows the change in strains during load testing as recorded by the sensors installed along the tie girders. The load test began around 9:20 a.m. on August 7, 2024, and the change in strain was calculated relative to the strain values recorded at the start of the load testing. As shown in the figure, the observed maximum strain variation during the test was approximately 20 με. A gradual increase in strain was also recorded between the tests due to diurnal temperature variation (i.e., the temperature recorded by the sensors ranged from 69° F to 78° F). The load test data were used to validate the finite element models, as discussed in the subsequent sections.

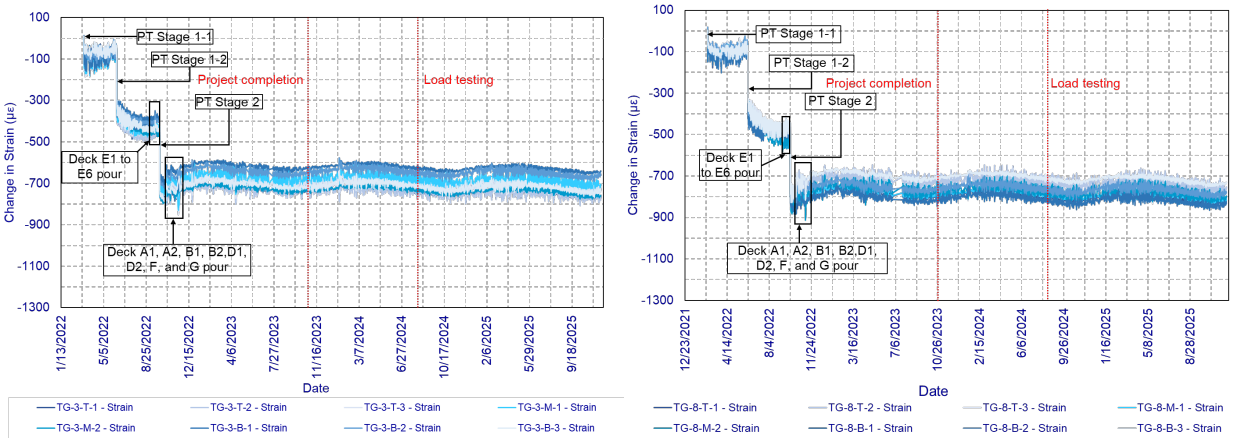

(a) TG-03 (b) TG-08

Figure 8-5. Total strain variation starting from the 1st day of construction.

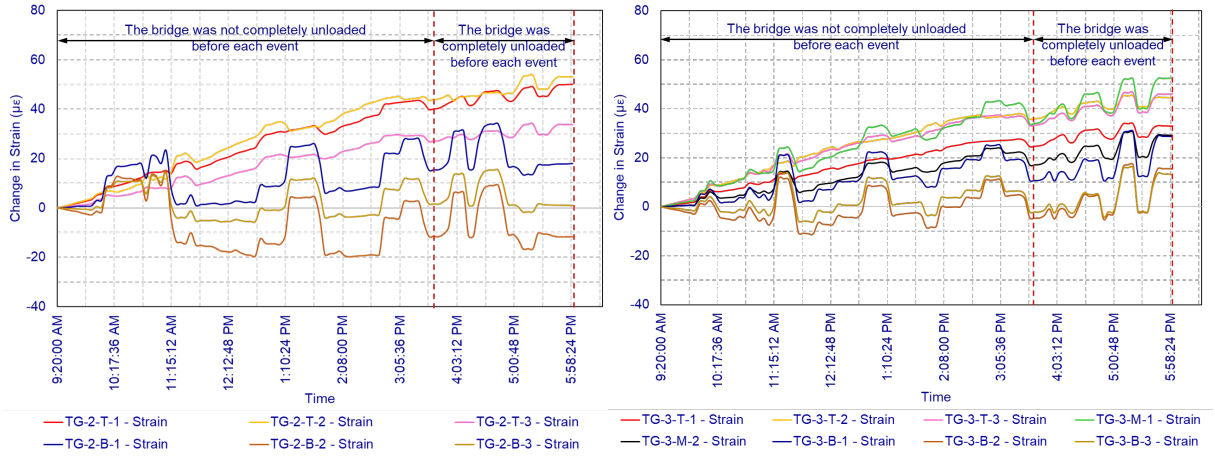

(a) at TG-2

(b) at TG-3

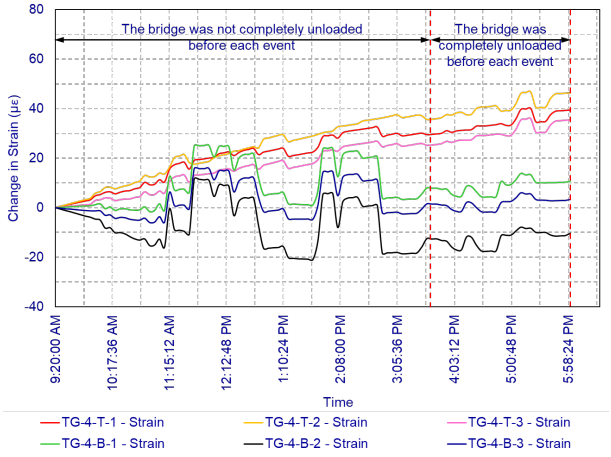

(c) at TG-4

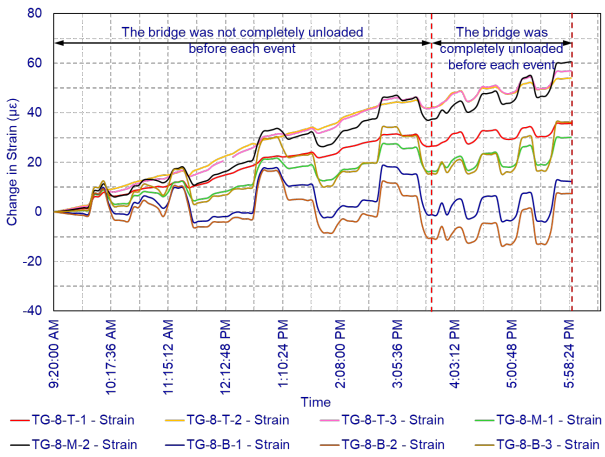

(d) at TG-8

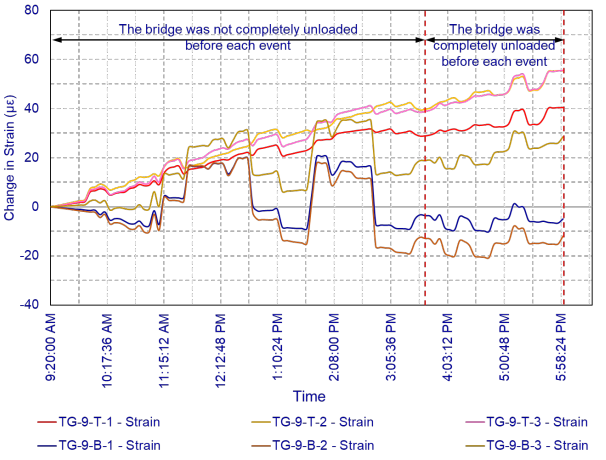

(e) at TG-9

Figure 8-6. Variation of strains at specific cross-sections along the tie girders during load testing.

8.4 LARSA 4D MODEL VALIDATION

The strain change at each sensor location during each load case was calculated using the recorded sensor readings shown in Figure 8-6. These strain values were then used to determine the axial force, bending moments around the major axes, eccentricity, and the equation and orientation of

the neutral axis. Since multiple sensors were installed at each cross-section, the best-fit curve for the neutral axis at each location was computed from the strain values using the following method.

If the beam is subjected to an eccentric loading about both the x-x and y-y axes, strain at any point in the cross-section can be calculated using Eq. 8-1.

$$\boldsymbol{\varepsilon} = \frac{\mathbf{1}}{\boldsymbol{E}}\left[\frac{\boldsymbol{F}}{\boldsymbol{A}} \pm \frac{\boldsymbol{F e_y}}{\boldsymbol{Z_{xx}}} \pm \frac{\boldsymbol{F e_x}}{\boldsymbol{Z_{yy}}}\right] \qquad \text{Eq. 8-1}$$

where,

F = axial force
e_x = eccentricity of the axial force along x-x axis
e_y = eccentricity of the axial force along y-y axis
E = modulus of elasticity (MOE)
Z_{xx} = section modulus of the beam section about x-x axis
Z_{yy} = section modulus of the beam section about y-y axis

Eq. 8-1 can be rearranged as shown in Eq. 8-2.

$$\boldsymbol{\varepsilon} = \boldsymbol{a} + \boldsymbol{b e_x} + \boldsymbol{c e_y} \qquad \text{Eq. 8-2}$$

where,

$$a = \frac{F}{AE}$$

$$b = \frac{F}{Z_{yy} \, . E}$$

$$c = \frac{F}{Z_{xx} . E}$$

For a series of sensors within a single cross-section, like in TG-8, Eq. 8-2 can be modified and represented in matrix form, as shown in Eq. 8-3.

$$[\boldsymbol{\varepsilon}] = [\boldsymbol{e}] . [\boldsymbol{A}] \qquad \text{Eq. 8-3}$$

where,

$$[\varepsilon] = \begin{bmatrix} \varepsilon_{T-1} \\ \varepsilon_{T-2} \\ \varepsilon_{T-3} \\ \varepsilon_{M-1} \\ \varepsilon_{M-2} \\ \varepsilon_{B-1} \\ \varepsilon_{B-2} \\ \varepsilon_{B-3} \end{bmatrix}$$

$$[e] = \begin{bmatrix} 1 & e_{x-T-1} & e_{y-T-1} \\ 1 & e_{x-T-2} & e_{y-T-2} \\ 1 & e_{x-T-3} & e_{y-T-3} \\ 1 & e_{x-M-1} & e_{y-M-1} \\ 1 & e_{x-M-2} & e_{y-M-2} \\ 1 & e_{x-B-1} & e_{y-B-1} \\ 1 & e_{x-B-2} & e_{y-B-2} \\ 1 & e_{x-B-3} & e_{y-B-3} \end{bmatrix}$$

$$[A] = \begin{bmatrix} a \\ b \\ c \end{bmatrix}$$

The values of a, b, and c can be determined using Eq. 8-4.

$$[\boldsymbol{A}]^{\boldsymbol{T}} = [\boldsymbol{e}]^{\boldsymbol{T}}.[\boldsymbol{e}]^{-\boldsymbol{1}}.[\boldsymbol{e}]^{\boldsymbol{T}}.[\boldsymbol{\varepsilon}] \quad \text{Eq. 8-4}$$

At the neutral axis ε = 0, and Eq. 8-2 can be written as follows:

$$\boldsymbol{a} + \boldsymbol{b}\boldsymbol{e}_{\boldsymbol{x}} + \boldsymbol{c}\boldsymbol{e}_{\boldsymbol{y}} = \boldsymbol{0} \quad \text{Eq. 8-5}$$

Eq. 8-5 represents the equation of a line and can be rearranged as shown in Eq. 8-6.

$$\boldsymbol{e}_{\boldsymbol{y}} = -\frac{\boldsymbol{a}}{\boldsymbol{c}} - \frac{\boldsymbol{b}}{\boldsymbol{c}}\boldsymbol{e}_{\boldsymbol{x}} \quad \text{Eq. 8-6}$$

Eq. 8-7 through Eq. 8-9 can be used to calculate the axial force and moments.

$$\boldsymbol{F} = \boldsymbol{E}.\boldsymbol{A}.\boldsymbol{a} \quad \text{Eq. 8-7}$$

$$\boldsymbol{M}_{\boldsymbol{xx}} = \boldsymbol{E}.\boldsymbol{I}_{\boldsymbol{xx}}.\boldsymbol{c} \quad \text{Eq. 8-8}$$

$$\boldsymbol{M}_{\boldsymbol{yy}} = -\boldsymbol{E}.\boldsymbol{I}_{\boldsymbol{yy}}.\boldsymbol{b} \quad \text{Eq. 8-9}$$

where,

I_{xx} = moment of inertia of the beam section about x-x axis
I_{yy} = moment of inertia of the beam section about y-y axis

For example, Table 8-2 shows how the strain change recorded by each sensor at five cross-sections along the tie girders when the trucks were arranged as shown in Figure 8-4 to maximize the strains at TG-8.

Table 8-2. Change in Strain Recorded by Each Sensor in Tie Girders when the Loads are Placed to Maximize Strains at TG-8

Sensor Location	Change in Strain (με)							
	T-1	T-2	T-3	M-1	M-2	B-1	B-2	B-3
TG-2	4.607	4.847	3.978	-[1]	-	0.485	-1.024	-0.201
TG-3	4.344	3.565	7.144	11.982	8.698	15.983	17.690	15.243
TG-4	4.451	5.658	4.781	-	-	0.218	-1.239	-0.064
TG-8	5.193	4.141	6.808	10.825	13.334	16.236	20.188	19.480
TG-9	6.742	7.788	7.314	-	-	-0.372	-0.192	2.107

[1.] No sensors are installed at the respective locations.

The corresponding e_x and e_y values for the TG-08 sensor location are listed in Table 8-3.

Table 8-3. Eccentricities Calculated w.r.t. Each Sensor at TG-8

Sensor Label	e (in.)	e (in.)
T-1	-16.75	13.5
T-2	2.5	19
T-3	16.75	13.5
M-1	-16.75	-0.75
M-2	16.75	-0.75
B-1	-16.75	-16.625
B-2	2.5	-21.5
B-3	16.75	-16.625

Using Eq. 8-3 through Eq. 8-9 and the information provided in Table 8-2 and Table 8-3, the axial force, bending moments around the major axes, the equation and orientation of the neutral axis, and the eccentricity of the centroid w.r.t. the neutral axis were calculated for the section at TG-08. Figure 8-7 shows the neutral axis and the centroid of the section. Accordingly, it was found that the axial force, bending moments around the x and y axes acting on the TG-08 cross-section were 133.69 kips, -73.55 kip-ft, and -9.03 kip-ft, respectively.

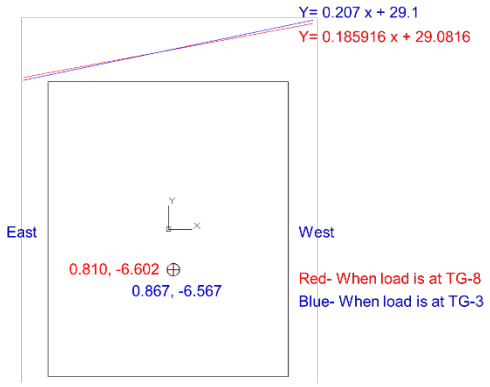

Figure 8-7. Orientation of the neutral axis at TG-08 for the load arrangement presented in Figure 8-4.

Axial forces and moments were calculated at five instrumented cross-sections along the tie girders using sensor data and the LARSA 4D model for the same truckload configuration, as shown in Table 8-4.

Table 8-4. Axial Forces and Moments at Selected Cross-Sections Calculated Using Sensor Data and LARSA 4D for the Truckload Configuration Shown in Figure 8-4

Sensor location	F (kips)		M_x (kip-ft)		M_Y (kip-ft)	
	Sensor data	LARSA 4D	Sensor data	LARSA 4D	Sensor data	LARSA 4D
TG-2	26.86	67.38	31.00	32.80	3.79	11.59
TG-3	130.00	159.40	-69.03	-62.18	-1.63	6.37
TG-4	30.23	111.28	35.12	16.55	0.98	16.36
TG-8	133.69	161.70	-73.55	-84.05	-9.03	-7.28
TG-9	48.65	78.87	37.96	33.17	-4.63	-12.84

The axial forces and moments about the horizontal axis (x-axis) are reasonably accurate for a majority of the sections, except TG-4, obtained from the LARSA 4D model. TG-4 is the furthest point from the loaded area and is located closer to the acute corner. Small strains measured at such locations could influence the resultant forces and moments calculated from sensor data. The LARSA 4D model predicts higher axial forces, but the moments about the x-axis are very close to the measured data. The observed differences are most likely due to small strain values recorded by the embedded sensors, and to the LARSA 4D model not accounting for the stiffness of non-structural components such as sidewalks, planter boxes, plinths, and sacrificial nosing. The model is considered to be accurate within the limitations of the software.

When half of the bridge length is loaded, the tie girder is expected to develop larger moments closer to the support, with moments gradually decreasing towards the midspan, and moments beyond the midspan having opposite signs to those at the loaded area. This load configuration and the moment variation are depicted in Figure 2-3. The loading configuration shown in Figure 8-8 resembles the loading pattern described in Figure 2-3, even though it was placed to maximize the strains at TG-1.

The strain changes observed at each sensor location along the east tie girder are listed in Table 8-5. Table 8-6 shows the calculated axial forces and bending moments resulting from this loading. Accordingly, the moments about the horizontal axis at the TG-2, TG-3, and TG-4 sensor cross-sections are -92.22, -13.24, and 47.17 kip-ft, respectively. This moment pattern resembles the behavior of a typical tie girder in a tied network arch bridge, as reported by Mato et al. (2011) and shown in Figure 2-3.

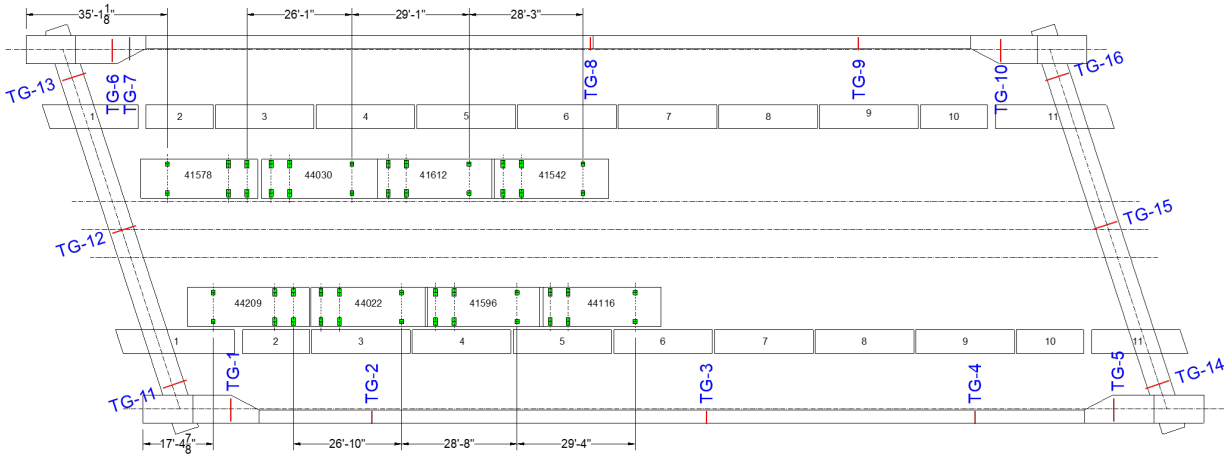

Figure 8-8. Truck positions to maximize the strain at the TG-1 sensor location.

Table 8-5. Strain Changes Recorded at Selected Cross-Sections along the East Tie Girder for the Truckload Configuration Shown in Figure 8-8

Sensor location	Change in Strain (με)							
	T-1	T-2	T-3	M-1	M-2	B-1	B-2	B-3
TG-2	5.735	1.520	3.286	-[1]	-	17.917	20.373	13.857
TG-3	5.189	4.875	5.887	9.960	6.350	7.455	8.401	6.967
TG-4	2.148	3.604	2.406	-	-	-4.132	-5.522	-3.685

[1.] No sensors are installed at the respective locations.

Table 8-6. Axial Forces and Moments About the Major Axes at Selected Cross-Sections along the East Tie Girder for the Truckload Configuration Shown in Figure 8-8

Sensor location	F (kips)	M_x (kip-ft)	M_Y (kip-ft)	e_x (in.)	e_Y (in.)
TG-2	126.82	-92.22	-8.32	-0.788	8.726
TG-3	85.26	-13.24	-3.87	-0.545	1.863
TG-4	-8.94	47.17	-0.147	0.197	63.35

9 OPERATIONAL LIMITS FOR THE BRIDGE

9.1 OVERVIEW

This chapter establishes the operational limits of the 2nd Avenue Network Arch Bridge based on measured field data, material properties, and analytical modeling. The objective is to define stress and strain thresholds that represent safe operating conditions under all realistic combinations of temperature, shrinkage, creep, and service loading. The chapter integrates results from the instrumentation program, construction-stage monitoring, and numerical simulations developed using LARSA 4D and Abaqus models. These results are used to quantify the stresses and strains developed in key structural components, including the post-tensioned tie girders, end diaphragms, and concrete knuckles, during construction and service.

9.2 DESIGN LIMITS FOR PT TIE GIRDERS AND END DIAPHRAGMS

Table 9-1 presents the design and measured compressive strengths of the tie girder and end diaphragm concrete. A concrete with an 8000-psi compressive strength was specified for the upper and lower knuckles and tie girders. A concrete with a 6500-psi compressive strength was specified for the end diaphragms. However, during construction, the same 8000-psi concrete was used for the end diaphragms.

Table 9-1. Compressive Strength of Concrete Used in Tie Girders and End Diaphragms

Bridge Component	Specified Compressive Strength (psi)	Measured Compressive Strength at 56 Days (psi)
East tie girder	8,000	11,823
West tie girder		11,957
South end diaphragm		14,777
North end diaphragm		15,113

Table 9-2 lists the limiting compressive and tensile stresses for tie girders and end diaphragms calculated using the equations in AASHTO Table 5.9.4.2.1-1 (AASHTO 2020), the specified design strength, and the measured strength from specimens fabricated during construction.

Table 9-2. Compressive and Tensile Stress Limits for Tie Girders and End Diaphragms

Bridge Component	Compressive Stress Limit[1] (psi)		Tensile Stress Limit[2] (psi)	
	Specified Strength	Measured Strength	Specified Strength	Measured Strength
East tie girder	4,800	7,174	678	825
West tie girder		7,094		830
South end diaphragm		8,866		923
North end diaphragm		9,068		933

[1] Compressive stress limit = $0.6 f_c'$
[2] Tensile stress limit = $0.24 \sqrt{f_c'}$

9.3 STRESSES IN THE PT FRAME AT THE END OF CONSTRUCTION

Figure 9-1 through Figure 9-3show strain variation in the west tie girder (TG-8), the SW concrete knuckle (TG-6), and the south end diaphragm (TG-12), respectively. The negative strain values represent compression. Similar trends were observed at other instrumented sections, except at the NW knuckle (TG-10). Each plot presents the actual strains recorded by the VW sensors at the respective cross-sections due to temperature effects, concrete creep and shrinkage, and applied loads. Because each component underwent free contraction during shrinkage, it was not expected to develop a structurally significant level of stress until it was subjected to post-tensioning. Hence, the strains recorded at 07:00 a.m. on the date of initial post-tensioning were used as the reference (zero) strain for the graphs. For example, the graphs shown in Figure 9-1 for the TG-8 sensor location were developed with reference to the strains recorded at 7:00 a.m. on February 21, 2022, the day of Stage 1-1 post-tension application. Similarly, the strains recorded at 7:00 a.m. on May 5, 2022 (the day of anchor rods tensioning) and April 22, 2022 (the day of Stage 1-1 post-tension application) were used as the reference strains for the SW knuckle and end diaphragms, respectively.

Figure 9-4 shows the strain variations at the NW knuckle (TG-10). As shown in the figure, sensors TG-10-T-1, TG-10-T-3, and TG-10-M-1 exhibit strain patterns consistent with those observed at the other knuckles. The remaining five sensors (TG-10-T-2, TG-10-M-2, TG-10-B-1, TG-10-B-2, and TG-10-B-3) recorded higher strain levels than the other sensors during anchor bar tensioning. Notably, sensor TG-10-T-2 exhibited increased sensitivity to Stage 1-2 post-tensioning of the tie girder and subsequent construction activities. Following completion of construction, this sensor exhibited a strain pattern similar to those of the other four sensors (refer to Figure 6-4).

Figure 9-5 shows the arch rib anchorage details at a knuckle. The anchor bars are connected to a 1.75-in. thick anchor plate mounted within the knuckle. The inspector's daily records indicate that no issues occurred during anchor bar stressing, and all anchor bars exhibited the same elongation of 0.32 in. Although the cause of the observed differences in sensor readings requires further investigation, construction records and post-construction inspections did not indicate any concerns regarding structural integrity.

The stresses due to known static loads, such as post-tensioning and dead loads, were calculated using the measured strain changes during each construction activity and the MOE of the relevant component. Strain changes associated with each construction activity were calculated at each sensor location and are documented in Appendix H.

According to the laboratory investigation conducted by Basnayake (2023), the MOE of the west tie girder was 5851, 6406, and 6542 ksi at Stage 1-1, Stage 1-2, and Stage 2 post-tensioning, respectively. The corresponding MOE values of the east tie girder at Stage 1-1, Stage 1-2, and Stage 2 post-tensioning were 6990, 7422, and 7338 ksi, respectively. However, because the MOE at a given age should not be less than that at a previous age, the value of 7,338 ksi was excluded from further consideration. Therefore, an MOE of 7,422 ksi was used as the final MOE for the east tie girder. Using these values, the stresses developed within each superstructure member during each construction activity were computed by multiplying the strain values reported in Appendix H by the corresponding MOE for the applicable age.

For example, Table 9-3 summarizes the construction activities that contributed to strain changes at the TG-8 sensor location on the west tie girder. As shown in Figure 9-4, stresses due to Stage 1-1 post-tensioning were calculated using a modulus of elasticity (MOE) of 5,851 ksi. Stresses resulting from Stage 1-2 post-tensioning and the dead loads associated with deck pours E1 through E6 were calculated using an MOE of 6,406 ksi. Stresses due to subsequent loading were calculated using an MOE of 6,542 ksi, which was the final MOE determined for this component. However, as shown in Figure 9-2 and Figure 9-3, no significant strain changes were observed at the knuckles and end diaphragms during construction activities, except during anchor rod tensioning at the knuckles and post-tensioning of the end diaphragms, respectively. Therefore, the strains measured at the end of construction were taken to represent the final strains for each VW sensor at the knuckles and end diaphragms. The corresponding stresses at these sensor locations were calculated using an MOE of 5,851 ksi for the knuckles and 6,990 ksi for the end diaphragms during anchor rod tensioning and post-tensioning, respectively.

The stresses developed at the SW knuckle and the south end diaphragm at the end of construction were computed using MOE values of 6,542 ksi and 7,422 ksi, respectively. Following a similar procedure, the stresses developed at the end of construction were calculated and summarized in Table 9-5 through Table 9-7.

Using the compressive and tensile stress limits provided in Table 9-2 and the stress values listed in Table 9-5 through Table 9-7, the residual tensile and compressive stress capacities at the end of construction were determined. For example, Table 9-6 indicates a maximum compressive stress of 2,834 psi at TG-8-B-1 and a minimum compressive stress of 1,856 psi at TG-8-T-2. Table 9-2 lists compressive and tensile stress limits of 7,094 psi and 830 psi, respectively, for the west tie girder. Accordingly, the residual tensile and compressive stress capacities at TG-8 are approximately 2,686 psi (i.e., 830 + 1,856) and 4,260 psi (i.e., 7,094 - 2,834), respectively.

Among the tie girders and end diaphragms, the tie girders exhibit the lowest residual compressive and tensile stress capacities, approximately 2,800 psi and 2,686 psi, respectively. However, among all concrete components, the upper knuckles exhibit the lowest residual compressive and tensile stress capacities.

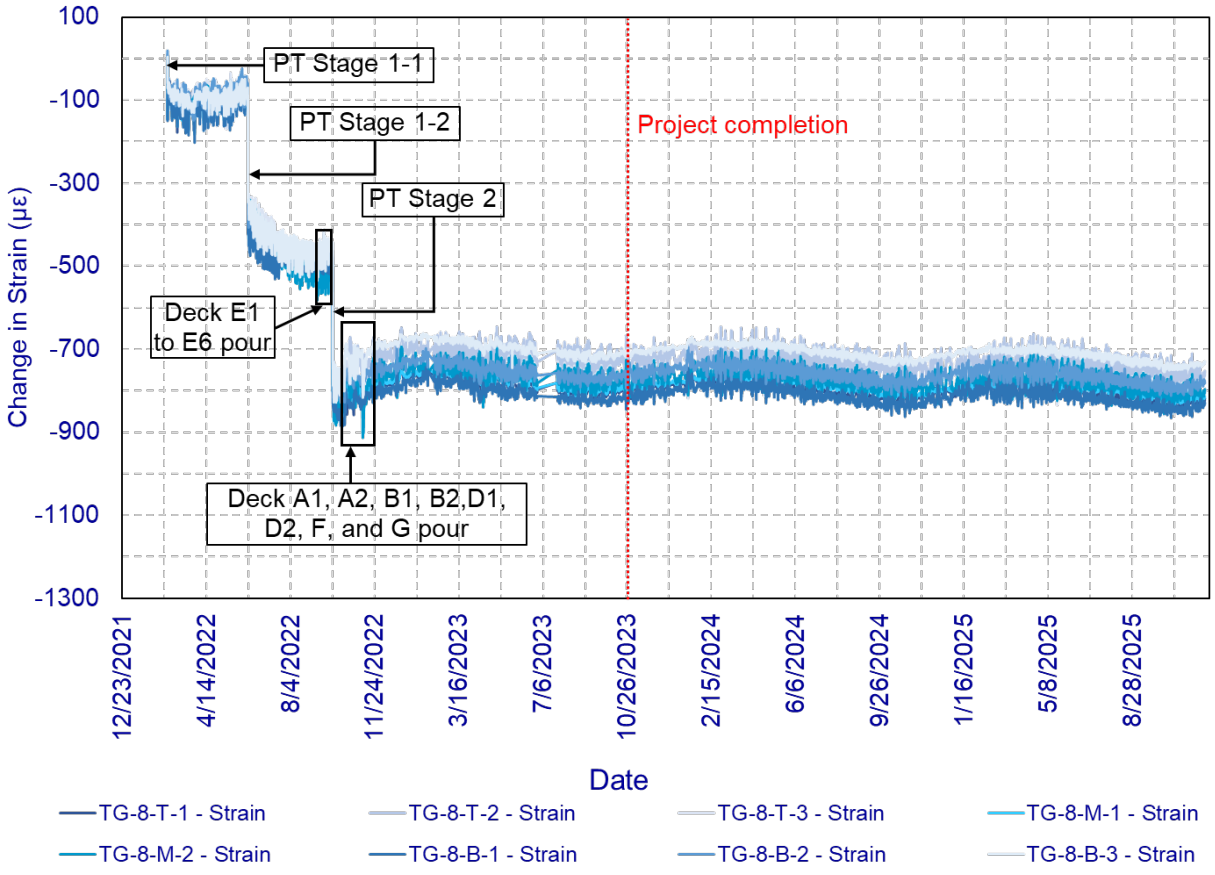

Figure 9-1. Strain variation in the west tie girder at TG-8, starting from Stage 1-1 post-tensioning (February 21, 2022) until December 02, 2025.

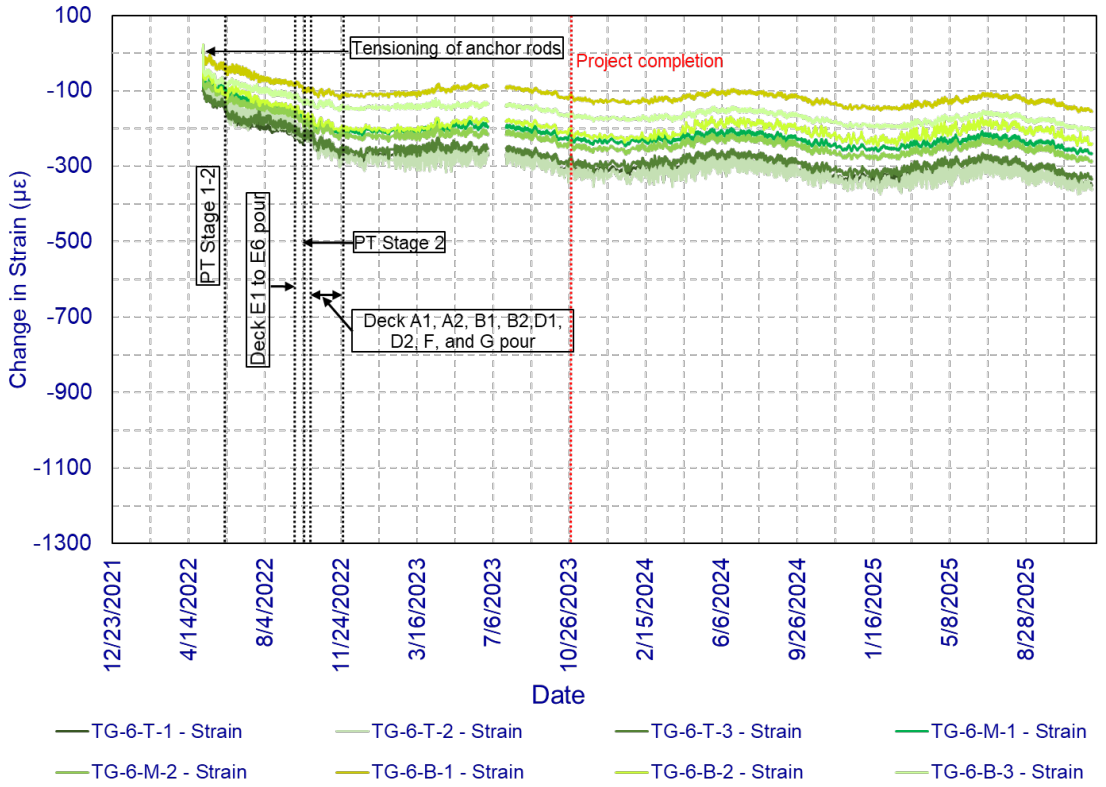

Figure 9-2. Strain variation in the SW knuckle, starting from anchor bar tensioning (May 05, 2022) until December 02, 2025.

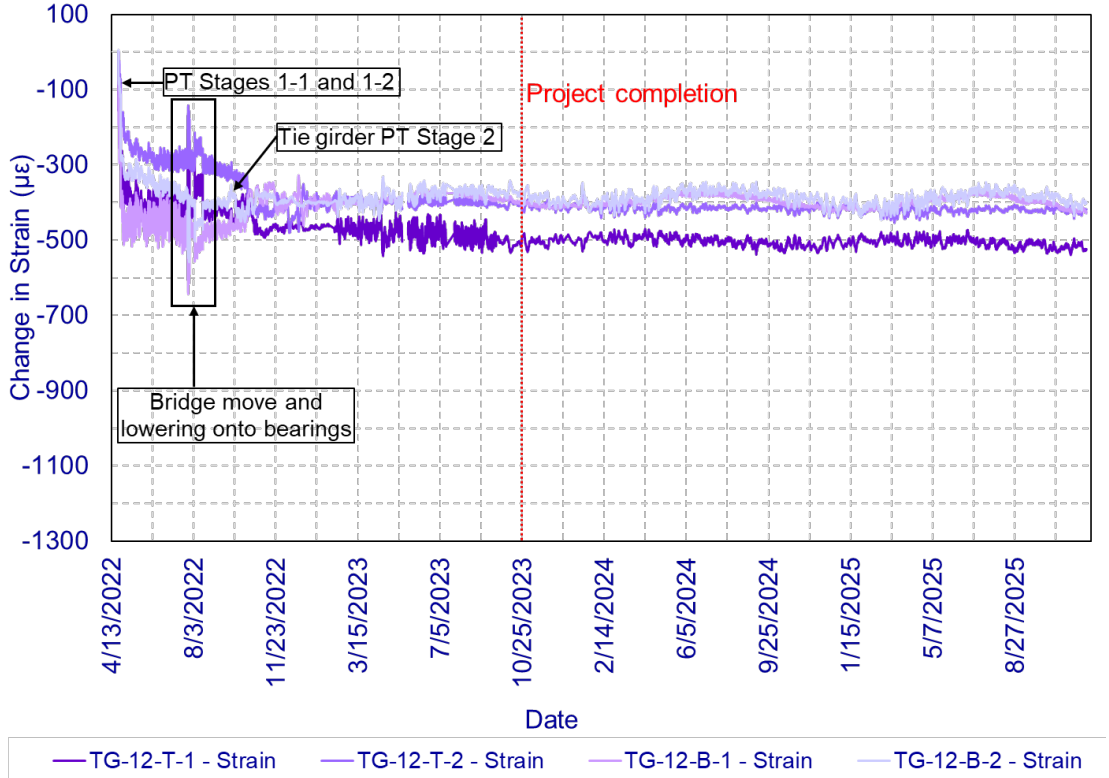

Figure 9-3. Variation of strain in the south end diaphragm at TG-12, starting from post-tensioning (April 22, 2022) until December 02, 2025.

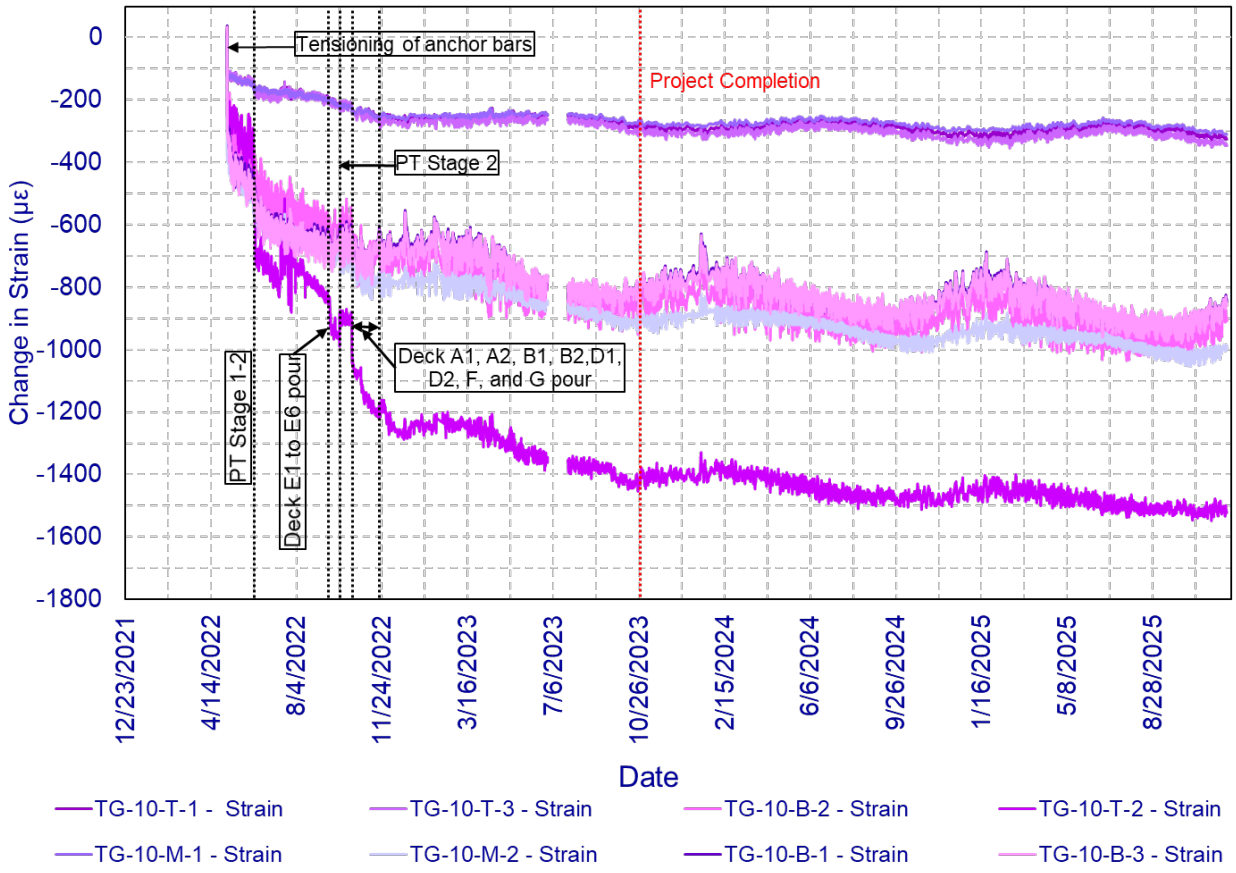

Figure 9-4. Strain variation in the NW knuckle, starting from anchor bar tensioning (May 05, 2022) until December 02, 2025.

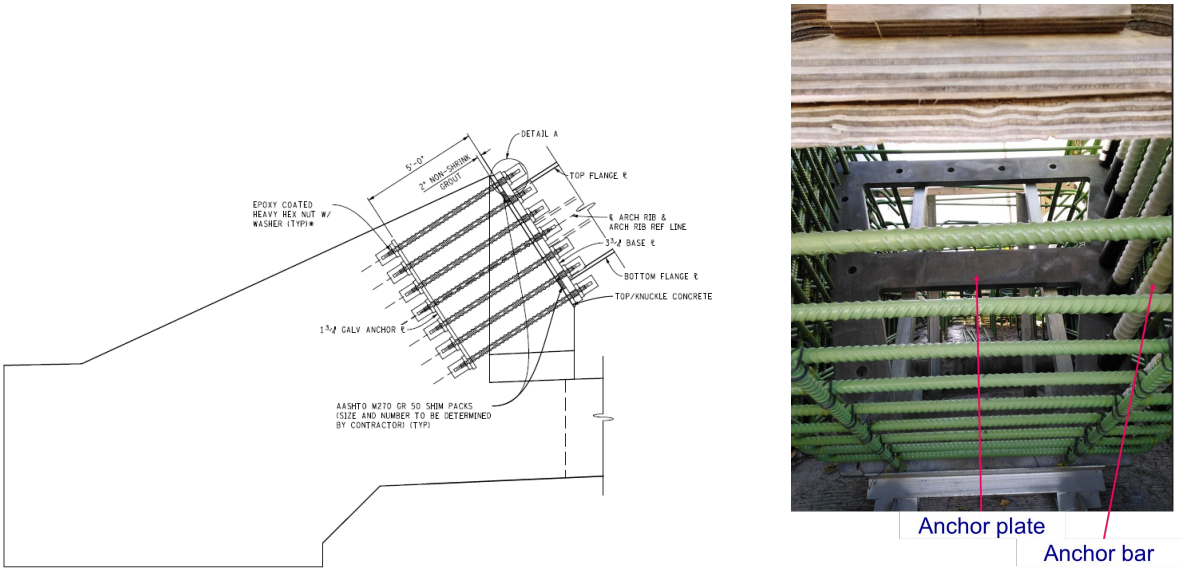

Figure 9-5. Arch rib anchorage details.

Table 9-3. Change in Strain at TG-8 Sensor Location Due to Static Loads

Activity	Strain Change (με)							
	TG-8-T-1	TG-8-T-2	TG-8-T-3	TG-8-M-1	TG-8-M-2	TG-8-B-1	TG-8-B-2	TG-8-B-3
Stage 1-1 post-tensioning	-144.749	-107.040	-98.593	-145.095	-78.199	-148.964	-63.099	-72.134
Stage 1-2 post-tensioning	-339.126	-316.819	-289.314	-309.239	-273.984	-316.297	-313.165	-276.597
Deck pour E1, E2, E3, E4, E5, and E6	55.941	43.100	61.106	52.710	75.894	53.957	43.711	94.179
Stage 2 post-tensioning	-309.484	-277.107	-289.441	-318.165	-319.937	-337.076	-315.669	-344.697
Deck pour A1, A2, B1, B2, D1, and D2	70.830	54.804	49.446	79.277	71.132	86.786	81.812	80.604
Deck pour D3, D4, D5, and D6	18.501	23.245	7.967	7.039	9.747	6.076	7.158	11.792
West sidewalk- pour B, C, D, E, and S	56.041	57.084	29.287	41.597	65.831	32.977	34.633	78.702
East sidewalk- pour H, J, K, L, and T	36.934	45.719	51.626	18.773	70.550	13.399	13.660	78.846
West sacrificial nosing- pour U	46.582	-51.896	-125.485	43.346	-141.124	49.089	28.611	-116.201
East sacrificial nosing- pour U	5.128	5.855	5.904	6.254	8.064	7.212	7.517	8.876
West side barrier railing construction	8.681	13.092	13.205	9.253	13.385	13.595	14.920	14.573
West planter boxes- pour R	12.000	24.509	22.821	11.018	23.886	16.584	13.149	14.714
East side barrier railing construction	13.275	38.691	38.853	6.796	37.531	18.853	21.702	8.845
East planter boxes- pour R	4.440	8.081	7.945	5.130	7.703	8.860	5.810	7.228
Plinths on the east side	20.451	45.548	45.267	9.562	40.730	26.410	30.734	12.384
Plinths on the west side	33.280	49.326	47.287	25.000	47.485	7.379	14.096	22.985
Low-profile center median construction	26.831	43.075	38.364	17.888	39.679	6.762	10.746	13.874

Table 9-4. Stresses at TG-8 Sensor Location Due to Static Loads

Activity	MOE (ksi)	Stress Developed at TG-8 Cross Section Due to Construction Activity (psi)							
		TG-8-T-1	TG-8-T-2	TG-8-T-3	TG-8-M-1	TG-8-M-2	TG-8-B-1	TG-8-B-2	TG-8-B-3
Stage 1-1 post-tensioning	5851	-847	-626	-577	-849	-458	-872	-369	-422
Stage 1-2 post-tensioning	6406	-2172	-2030	-1853	-1981	-1755	-2026	-2006	-1772
Deck pour E1, E2, E3, E4, E5, and E6		358	276	391	338	486	346	280	603
Stage 2 post-tensioning	6542	-2025	-1813	-1894	-2081	-2093	-2205	-2065	-2255
Deck pour A1, A2, B1, B2, D1, and D2		463	359	323	519	465	568	535	527
Deck pour D3, D4, D5, and D6		121	152	52	46	64	40	47	77
West sidewalk- pour B, C, D, E, and S		367	373	192	272	431	216	227	515
East sidewalk- pour H, J, K, L, and T		242	299	338	123	462	88	89	516
West sacrificial nosing- pour U		305	-340	-821	284	-923	321	187	-760
East sacrificial nosing- pour U		34	38	39	41	53	47	49	58
West side barrier railing construction		57	86	86	61	88	89	98	95
West planter boxes- pour R		79	160	149	72	156	108	86	96
East side barrier railing construction		87	253	254	44	246	123	142	58
East planter boxes- pour R		29	53	52	34	50	58	38	47
Plinths on the east side		134	298	296	63	266	173	201	81
Plinths on the west side		218	323	309	164	311	48	92	150
Low-profile center median construction		176	282	251	117	260	44	70	91
Total Stress at the end of Construction		**-2377**	**-1856**	**-2411**	**-2736**	**-1892**	**-2834**	**-2299**	**-2294**

Table 9-5. Stresses Developed at the End of Construction and Residual Compressive and Tensile Stress Capacities of the Knuckles

Bridge Component	Sensor Location	Sensor Label	Stress at the End of Construction (psi)	Residual Compressive Stress Capacity(psi)	Residual Tensile Stress Capacity (psi)
SE Knuckle	TG-1	TG-1-T-1	-1777	5397	2602
		TG-1-T-2	-1904	5270	2729
		TG-1-T-3	-1739	5435	2564
		TG-1-M-1	-1529	5645	2354
		TG-1-M-2	-1314	5860	2139
		TG-1-B-1	-1058	6116	1883
		TG-1-B-2	-1097	6077	1922
		TG-1-B-3	-874	6300	1699
NE Knuckle	TG-5	TG-5-T-1	-1719	5455	2544
		TG-5-T-2	-2240	4934	3065
		TG-5-T-3	-1962	5212	2787
		TG-5-M-1	-1602	5572	2427
		TG-5-M-2	-1887	5287	2712
		TG-5-B-1	-1198	5976	2023
		TG-5-B-2	-1115	6059	1940
		TG-5-B-3	-1178	5996	2003
SW Knuckle	TG-6	TG-6-T-1	-2145	4949	2975
		TG-6-T-2[1]	-	-	-
		TG-6-T-3	-2010	5084	2840
		TG-6-M-1	-1550	5544	2380
		TG-6-M-2	-1706	5388	2536
		TG-6-B-1	-819	6275	**1649**
		TG-6-B-2	-1435	5659	2265
		TG-6-B-3	-1166	5928	1996
NW Knuckle	TG-10	TG-10-T-1	-1980	5114	2810
		TG-10-T-2[2]	-	-	-
		TG-10-T-3	-2101	4993	2931
		TG-10-M-1	-1880	5214	2710
		TG-10-M-2	-6584	**510**	7414
		TG-10-B-1	-6116	978	6946
		TG-10-B-2	-6497	597	7327
		TG-10-B-3	-6125	969	6955

[1.] TG-6-T-2 was not installed.
[2.] Significant drift in the data is observed.

Table 9-6. Stresses Developed at the End of Construction and Residual Compressive and Tensile Stress Capacities of the East and West Tie Girders

Bridge Component	Sensor Location	Sensor Label	Stress at the End of Construction (psi)	Residual Compressive Stress Capacity(psi)	Residual Tensile Stress Capacity (psi)
East tie girder	TG-2	TG-2-T-1	-3348	3826	4173
		TG-2-T-2	-2602	4572	3427
		TG-2-T-3	-3340	3834	4165
		TG-2-B-1	-4043	3131	4868
		TG-2-B-2	-2932	4242	3757
		TG-2-B-3	-3969	3205	4794
	TG-3	TG-3-T-1	-2899	4275	3724
		TG-3-T-2	-3273	3901	4098
		TG-3-T-3	-4374	**2800**	5199
		TG-3-M-1	-4225	2949	5050
		TG-3-M-2	-3226	3948	4051
		TG-3-B-1	-4358	2816	5183
		TG-3-B-2	-2813	4361	3638
		TG-3-B-3	-3143	4031	3968
	TG-4	TG-4-T-1	-3959	3215	4784
		TG-4-T-2	-2928	4246	3753
		TG-4-T-3	-3456	3718	4281
		TG-4-B-1	-4100	3074	4925
		TG-4-B-2	-2849	4325	3674
		TG-4-B-3	-3981	3193	4806
West tie girder	TG-8	TG-8-T-1	-2377	4717	3207
		TG-8-T-2	-1856	5238	**2686**
		TG-8-T-3	-2411	4683	3241
		TG-8-M-1	-2736	4358	3566
		TG-8-M-2	-1892	5202	2722
		TG-8-B-1	-2834	4260	3664
		TG-8-B-2	-2299	4795	3129
		TG-8-B-3	-2294	4800	3124
	TG-9	TG-9-T-1	-2564	4530	3394
		TG-9-T-2	-2123	4971	2953
		TG-9-T-3	-2298	4796	3128
		TG-9-B-1	-2747	4347	3577
		TG-9-B-2	-2250	4844	3080
		TG-9-B-3	-2009	5085	2839

Table 9-7. Stresses Developed at the End of Construction and Residual Compressive and Tensile Stress Capacities of the South and North End Diaphragms

Bridge Component	Sensor Location	Sensor Label	Stress at the End of Construction (psi)	Residual Compressive Stress Capacity(psi)	Residual Tensile Stress Capacity (psi)
South end diaphragm	TG-11	TG-11-T-1	-3343	5523	4266
		TG-11-T-2	-3552	**5314**	4475
		TG-11-B-1	-2372	6494	3295
		TG-11-B-2	-2315	6551	3238
	TG-12	TG-12-T-1	-3525	5341	4448
		TG-12-T-2	-2949	5917	3872
		TG-12-B-1	-2670	6196	3593
		TG-12-B-2	-2660	6206	3583
	TG-13	TG-13-T-1	-3302	5564	4225
		TG-13-T-2	-2964	5902	3887
		TG-13-B-1	-2657	6209	3580
		TG-13-B-2	-2302	6564	3225
North end diaphragm	TG-14	TG-14-T-1	-3016	6052	3949
		TG-14-T-2	-3304	5764	4237
		TG-14-B-1	-2535	6533	3468
		TG-14-B-2	-2604	6464	3537
	TG-15	TG-15-T-1	-3366	5702	4299
		TG-15-T-2	-2858	6210	3791
		TG-15-B-1	-2875	6193	3808
		TG-15-B-2	-2952	6116	3885
	TG-16	TG-16-T-1	-2681	6387	3614
		TG-16-T-2	-3152	5916	4085
		TG-16-B-1	-2155	6913	**3088**
		TG-16-B-2	-2689	6379	3622

9.4 EVALUATION OF STRAINS WITHIN THE TAPERED SECTION

The refined finite element model of the PT frame with arches and hangers, described in Section 7.3, with the material models discussed in Section 7.4, was used to simulate the construction process, including Stage 1-1 and Stage 1-2 post-tensioning. The simulation encompassed all construction activities up to Stage 2 post-tensioning, excluding the bridge move. Time-dependent strains were extracted from the VW strain sensors at the TG-8 and TG-9 locations on the west tie girder and compared with the corresponding finite element analysis results.

Figure 9-6 shows the measured and simulated total strains in the west tie girder. The simulated strains at the TG-8 and TG-9 locations closely match the measured strain profiles. Although the simulation results slightly overestimate the measured strains, the overall agreement is reasonable, thereby validating the refined finite element model for subsequent analyses.

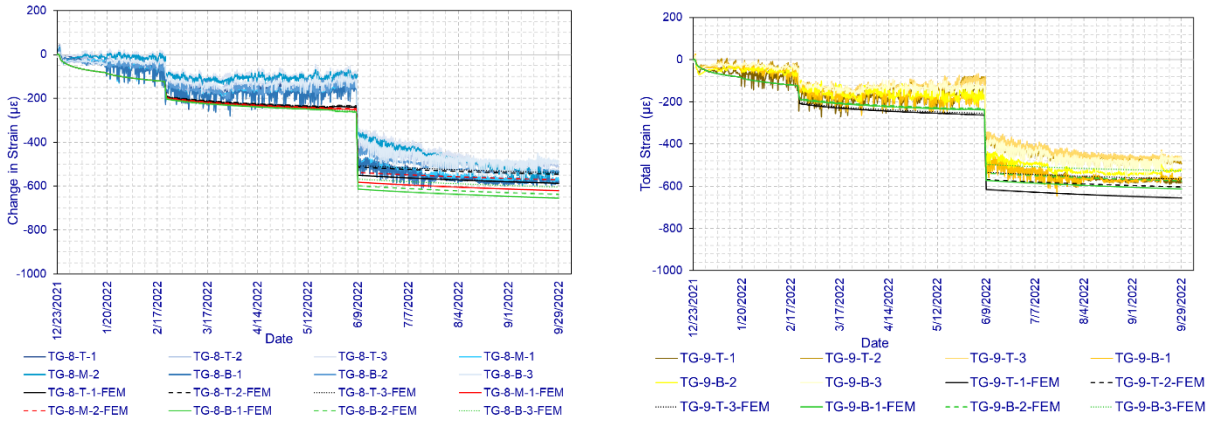

(a) At the girder midspan (TG-8) (b) At the girder end (TG-9)

Figure 9-6. The comparison of measured and simulated total strains in the west tie girder sections at (a) TG-8 and (b) TG-9.

Figure 9-7 shows the measured and simulated strains in the tapered section of the SW lower knuckle at sensor location TG-7 up to the bridge move, which commenced on July 15, 2022, when the west tie girder was 204 days old. The strain data from sensor TG-7-T-2 were excluded from the analysis due to significant variability in the recorded readings (see Figure 5-7). Measured strain changes at sensors TG-7-T-3 and TG-7-B-3 were more pronounced during PT Stage 1-1 and PT Stage 1-2 than those recorded at TG-7-T-1, TG-7-B-1, and TG-7-B-2. A similar trend is observed in the simulated strain results. However, the simulated strains at TG-7-T-1, TG-7-B-1, and TG-7-B-2 are higher than the corresponding measured strains.

Within the tapered section, only sensors TG-7-T-2, TG-7-T-3, and TG-7-B-3 are located closer to the PT ducts. The localized stress distribution resulting from the eccentricity of the PT ducts may have contributed to the higher strains observed at these locations compared with those farther from the ducts. In addition, the presence of floor beam connections on the east face of the tie girder may have influenced the compression developed in these regions during post-tensioning. These factors should be considered in future design evaluations.

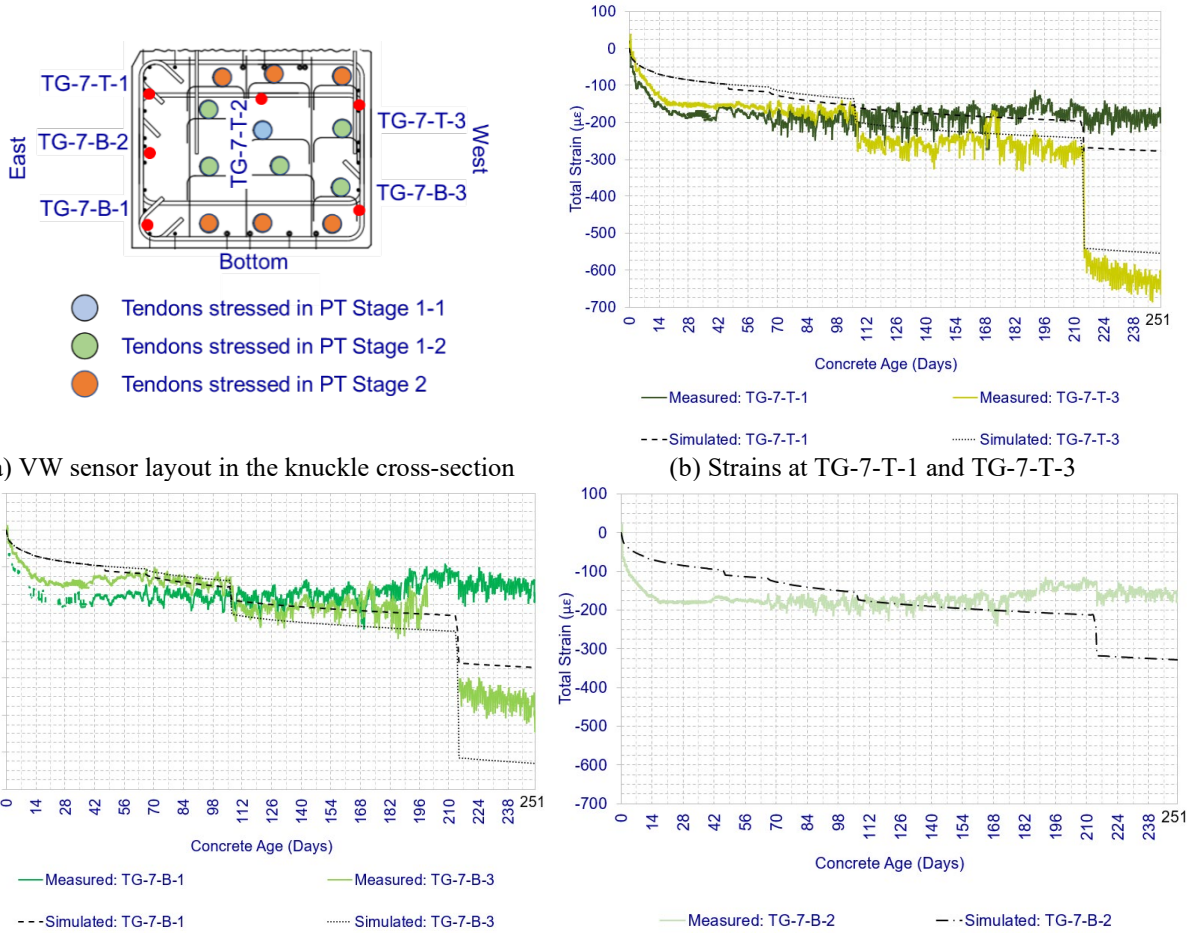

(a) VW sensor layout in the knuckle cross-section

(b) Strains at TG-7-T-1 and TG-7-T-3

(c) Strains at TG-7-B-1 and TG-7-B-3

(d) Strains at TG-7-B-2

Figure 9-7. (a) VW strain sensors at TG-7 and strains at (b) T-1 and T-3, (c) B-1 and B-3, and (d) B-2.

9.5 OPERATIONAL LIMITS FOR THE BRIDGE

As described in Chapter 8, the bridge response observed during load testing demonstrates minimal sensitivity to live loads, owing to the rigidity and indeterminate nature of the structural system. Accordingly, as discussed in Chapter 6, bridge deformations are governed primarily by temperature loads.

Strains resulting from known static loads, such as post-tensioning, can be converted to stresses using the modulus of elasticity of the corresponding concrete components. In contrast, recorded strains associated with volume-change effects, including temperature, creep, and shrinkage, are not directly proportional to the stresses developed in this indeterminate structure and therefore cannot be directly expressed in terms of stress. Moreover, stresses induced by restrained shrinkage are not captured by the embedded strain sensors. Consequently, a refined finite element analysis was performed using the maximum and minimum design temperatures determined in accordance

with AASHTO LRFD (2024), Procedure B. The results of this analysis were used to evaluate the stresses developed in the structural components and to compare them with limiting stresses based on concrete strength, thereby establishing the operational limits of the bridge.

On August 15, 2022, at approximately 12:20 p.m., the bridge was placed on permanent bearings following completion of patch repairs around the sole plates. The average temperature of each instrumented member at that time was taken as the reference temperature for determining the temperature range used to calculate bridge expansion and contraction. The minimum and maximum temperatures were recorded on January 22, 2025, and June 24, 2025, respectively. Table 9-8 documents the average reference temperature and the recorded average minimum and maximum temperatures for each bridge component. Based on these data, a base temperature of 74° F was selected as the reference temperature to determine expansion and contraction temperature ranges.

Table 9-8. Temperature Recorded by Instrumentation and the Selected Range for Analysis

Bridge component	Recorded Temperature (° F)		
	Reference Temperature Recoded on August 15, 2022	Minimum Temperature Recorded on January 22, 2025	Maximum Temperature Recorded on June 24, 2025
Upper knuckles	73	5	92
Tie girders	74	9	89
End diaphragms	74	16	84
West hangers	81	-2	112
East hangers	81	-3	105

Following Section 3.12.2 of AASHTO LRFD (2024), Procedure B, a design temperature range of −10° F to 105° F was selected for this structure. This temperature range exceeds the minimum and maximum temperatures recorded by sensors embedded in the concrete elements. The concrete MOE values listed in Section 9.3 were used for this evaluation.

Stress values calculated at the embedded sensor locations are listed in Appendix H and are graphically presented as increases or decreases in compression relative to the stresses calculated at the end of construction. As shown in Figure 9-8, the vertical lines indicate the range of stress variation. For example, the stress at sensor TG-6-B-2 at the end of construction is −1,435 psi. When the temperature decreases from 74° F to −10° F, the compressive stress reduces to −665 psi. Conversely, when the temperature increases from 74° F to 105° F, the compressive stress increases to −1,681 psi.

Figure 9-9 and Figure 9-10 present the corresponding results for the tie girders and end diaphragms, respectively. These results indicate that the arch rib–knuckle connections are more sensitive to temperature variations, whereas the end diaphragms are the least sensitive. While the tie girders and end diaphragms provide more than 2,000 psi residual capacity towards compression and tension, certain locations at the top of the knuckles have less than 600 psi residual capacity under thermal contraction beyond −10° F exposure. Therefore, the temperatures recorded by the embedded VW sensors should be closely monitored to ensure that concrete temperatures do not fall below −10° F for extended periods.

Although the arch rib–knuckle connections at TG-1, TG-5, and TG-6 exhibit similar behavior, the TG-10 connection shows markedly different behavior (Figure 9-8). This difference is evident in the monitoring data presented in Figure 6-4 and Figure 9-4. *However, the refined finite element analysis results show similar behavior across all four arch rib-knuckle connections*.

Due to the unique response of the bridge superstructure to thermal expansion and contraction, measured strains do not directly reflect the stresses developed within the system. However, temperature and strain measurements can be used to verify whether each sensor continues to follow the characteristic strain patterns identified from the available monitoring data. Deviations from these patterns should trigger an engineering review to assess potential causes and determine appropriate actions until future studies establish damage signatures that can be correlated with sensor data and used to automate the monitoring process.

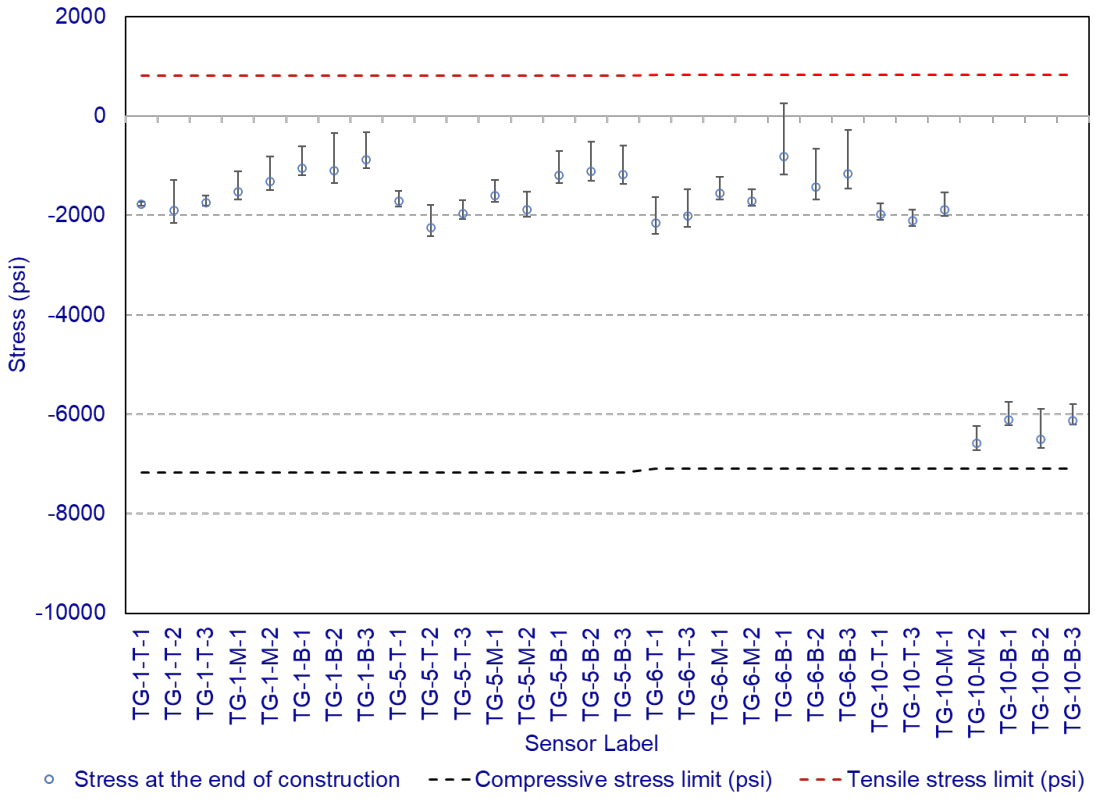

Figure 9-8. Stress change at the top of the upper knuckles when the bridge is subjected to the design temperature range.

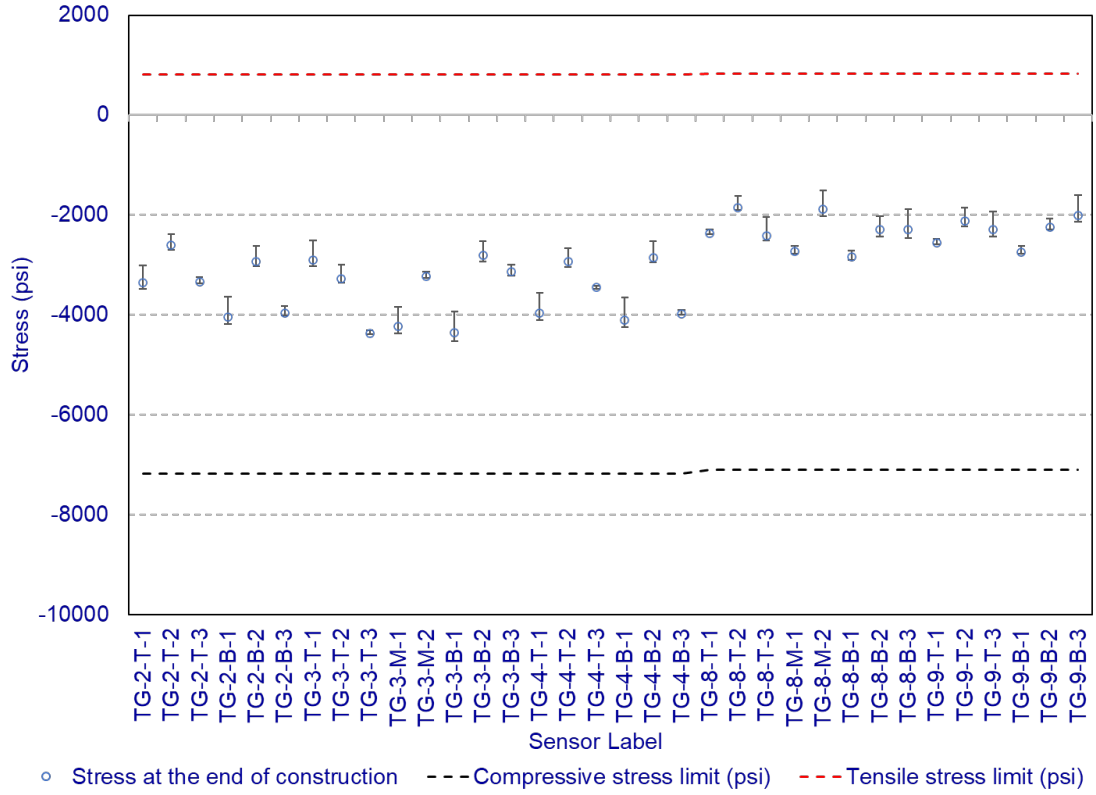

Figure 9-9. Stress change within the tie girders when the bridge is subjected to the design temperature range.

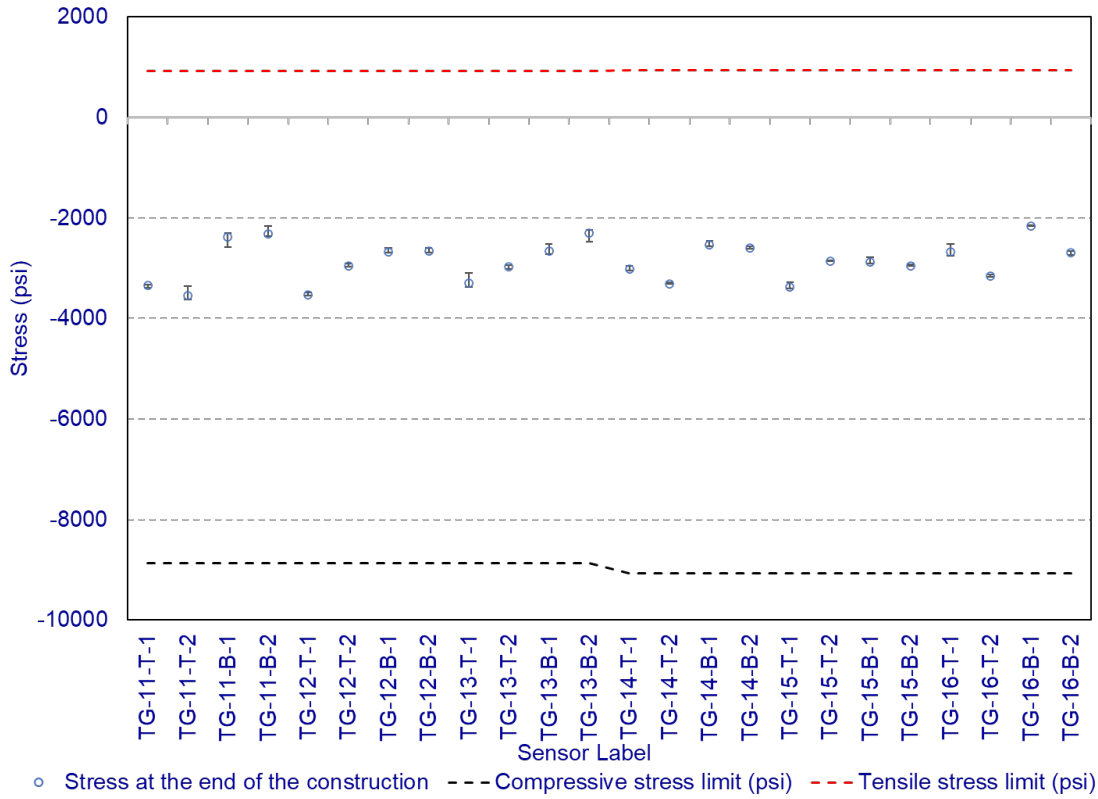

Figure 9-10. Stress change within the end diaphragm when the bridge is subjected to the design temperature range.

10 SUMMARY, CONCLUSIONS, AND RECOMMENDATIONS

10.1 SUMMARY

This research project investigated the structural performance of the 2nd Avenue Bridge in Detroit, Michigan - the first skewed, unbraced network tied-arch bridge in the United States. The bridge was constructed using accelerated bridge construction (ABC) techniques, including off-site fabrication at a bridge staging area (BSA) and installation via self-propelled modular transporters (SPMTs) and lateral launching.

A unique high-performance concrete mix with a water-to-cement ratio of 0.30 and supplementary cementitious materials (47% slag and 20% Class F fly ash) was used for the post-tensioned tie girders, knuckles, and end diaphragms. Due to the project's national significance and structural complexity, three independent finite element models were developed during design by the Engineer of Record, the contractor's consultant, and a peer review engineer.

A comprehensive instrumentation system was installed, comprising 96 vibrating wire strain sensors embedded in concrete members and 16 strandmeters on hangers. This system monitored the structure from initial concrete placement on November 3, 2021, through construction completion on October 27, 2023, and continues to collect data during service life.

The research evaluated structural performance during construction, conducted diagnostic load testing in August 2024, developed refined finite element models using LARSA 4D and Abaqus, and analyzed monitoring data collected from the first day of construction. Key findings include successful thermal control during early-age curing, validation of ABC techniques, characterization of seasonal thermal response, and establishment of operational stress limits for ongoing structural health monitoring.

10.2 CONCLUSIONS

10.2.1 Construction Performance

- **Thermal Control Success:** All monitored concrete components remained within specified temperature limits during curing. Maximum temperatures reached 84.2° F (west tie girder) and 100.4° F (east tie girder), with core-to-surface temperature differentials remaining below the 35° F specification limit, successfully preventing thermal cracking.

- **Shrinkage Behavior:** High-performance concrete with low w/c ratio exhibited autogenous shrinkage as the dominant mechanism, contributing 60 - 65% of total shrinkage at 60 days. This behavior differs significantly from that of conventional concrete and underscores the need for explicit consideration of autogenous shrinkage in similar high-performance concrete applications.
- **Modulus of Elasticity:** Field-estimated MOE values from elastic shortening measurements (5,851 - 7,422 ksi at various ages) were 13 - 21% lower than laboratory cylinder values but remained within expected ranges for the concrete mix.
- **ABC Technique Validation:** The bridge move operation and placement on permanent bearings proceeded successfully. Cyclic strain variations during the staged lowering process (maximum changes of 218 με) remained within design limits, and the structure exhibited full elastic recovery, confirming the adequacy of the construction methodology.
- **Construction Sequencing Issue:** Rebar deformation was observed in deck sections during Stage 2 post-tensioning, where reinforcement had been installed, but concrete had not yet been placed. This finding indicates the need for modified construction sequencing in future projects to prevent similar occurrences.

10.2.2 Structural Performance

- **Live Load Response:** Diagnostic load testing with eight tandem trucks (total 416 kips, 50% of HL-93 Mod design load) produced maximum strain variations of only approximately 20 με, demonstrating minimal sensitivity to live loads due to the structure's high rigidity and load distribution efficiency through the network arch system.
- **Thermal Dominance:** Seasonal temperature variations (5° F to 93° F) govern structural deformations far more significantly than live loads.
- **Skew Effects:** The 18-degree skew produces twisting of end diaphragms during seasonal temperature changes, with twist angles increasing toward acute corners (0.017° at obtuse corners to 0.029° at acute corners). This behavior differs from straight bridges and requires consideration in future skewed tied-arch bridge designs.
- **Tapered Section Behavior:** Strain measurements at the tapered tie girder-knuckle transition (TG-7) revealed localized stress concentrations near post-tensioning ducts rather than uniform

distribution assumed in plane-section analysis. Sensors near ducts registered significant compression during post-tensioning, while sensors farther from ducts showed minimal changes.

- **NW Knuckle Anomaly:** According to the recorded data, the northwest knuckle (TG-10) exhibits a different thermal response compared to other knuckles, showing twisting behavior rather than uniform compression/tension. Five of eight sensors displayed unusual patterns. However, all four knuckles showed a similar behavior when the refined finite element analysis was performed under uniform thermal loads.

10.2.3 Analytical Validation

- **Finite Element Model Accuracy:** The LARSA 4D model demonstrated reasonable agreement with measured strains and forces during load testing, with axial forces and moments about the horizontal axis matching field measurements within acceptable tolerances for most locations. Model limitations include simplified knuckle geometry and exclusion of non-structural component stiffness.
- **Shrinkage and Creep Modeling:** The CEB-FIP 2010 model provided superior predictions of shrinkage behavior compared to RILEM B4 and other empirical models for this high-performance concrete mix. For creep behavior, the AASHTO and CEB-FIP 2010 models yielded the lowest residual standard errors for field-cured specimens loaded at post-tensioning ages.
- **Material Model Selection:** Time-dependent behavior of the unique concrete mix required careful model selection. Standard design models did not provide optimal predictions. The dense microstructure from high SCM content led to lower creep coefficients than anticipated, underscoring the importance of material-specific testing for innovative concrete mixes.

10.2.4 Operational Performance

- **Stress State Assessment:** At the end of construction, stresses in all concrete components remain within the design limits. For example, the minimum residual capacities of tie girders are approximately 2,800 psi and 2,686 psi for compression and tension, respectively. The upper knuckles exhibited lower residual capacities, with a minimum of 510 psi (at TG-10-M-2) and 576 psi (at TG-6-B-1) for compression and tension, respectively. The need for continuous

monitoring is highlighted by the marginal residual capacities observed at the upper knuckles and the inconsistent sensor readings at TG-10.

- **Temperature-Induced Stress Ranges:** Under the design temperature range (-10° F to 105° F per AASHTO LRFD Procedure B), stress variations remain within the design limits. However, at certain locations in the knuckles, the residual capacities under thermal loads approach the design limits, leaving a margin of approximately 500 psi, necessitating vigilant temperature monitoring throughout the service life.
- **Electromagnetic Interference Mitigation:** Sensor cable separation of 12 inches minimum from 120V power lines, combined with separate grounded conduits and electronic filtering (50/60 Hz noise rejection), successfully minimized EMI effects on monitoring system performance.
- **Long-term Monitoring Viability:** The instrumentation system has functioned reliably for over four years (November 2021 to December 2025), surviving construction activities, bridge move operations, and environmental exposure. Solar power adequately supported the system for 30 months until grid connection in May 2024.

10.3 RECOMMENDATIONS

10.3.1 Immediate Actions

- **Temperature Monitoring Protocol:** Establish alert thresholds for embedded sensor temperatures approaching -10° F. During extreme cold events, increase monitoring frequency and implement visual inspections if temperatures remain below -10° F for extended periods.
- **NW Knuckle Investigation:** Conduct a detailed forensic investigation of the northwest knuckle (TG-10) using advanced techniques (ground-penetrating radar, ultrasonic testing) to verify structural integrity and understand the cause of anomalous sensor behavior.
- **Sensor Data Validation:** Implement automated data quality checks to identify sensor drift or malfunction. Develop characteristic strain pattern signatures for each sensor location to enable early detection of deviations that may indicate structural changes or instrumentation issues.
- **Load Rating:** Load rate the bridge using validated finite element models and measured structural response data. The demonstrated high stiffness and load distribution efficiency may support increased load capacity beyond initial conservative assumptions.

10.4 FUTURE DESIGN IMPROVEMENTS

- **Construction Sequencing Specifications:** For future tied-arch bridges with post-tensioning, specify that deck reinforcement installation must occur either: (a) after all post-tensioning operations are complete, or (b) only in sections that will be concreted before post-tensioning. Include this requirement explicitly in construction specifications and scheduling documents.
- **Tapered Section Design Refinement:** For future projects with tapered sections and complex duct profiles, employ three-dimensional finite element analysis rather than conventional plane-section analysis. Evaluate the impact of all local constraints and geometric irregularities to optimize the post-tension duct configuration and improve stress distribution.
- **Skewed Bridge Thermal Considerations:** For skewed tied-arch bridges, explicitly evaluate thermal-induced twisting of end diaphragms and differential bearing restraint effects during design.
- **EMI Spacing Standards:** Advocate for the development of industry standards for sensor-to-power cable separation distances based on voltage levels and sensor types. Document project-specific spacing criteria as a reference for future instrumented structures.

10.5 LONG-TERM MONITORING STRATEGY

- **Extended Monitoring Duration:** Continue data collection for a minimum of 5 - 10 years to establish long-term trends, distinguish seasonal variations from progressive changes, and validate predicted time-dependent behavior. This extended dataset will be invaluable for calibrating service life prediction models.
- **Seasonal Baseline Updates:** Annually update characteristic seasonal response patterns for each sensor location. Establish statistical control limits for temperature-strain relationships to enable automated anomaly detection.
- **Periodic Load Testing:** Conduct diagnostic load testing every 5 years to track changes in structural stiffness and load distribution characteristics. Compare results with baseline testing to identify any deterioration or change in structural behavior.
- **Data Management and Accessibility:** Develop a comprehensive database management system for long-term data storage, retrieval, and analysis. Ensure data accessibility for future

researchers and maintain detailed metadata documenting sensor locations, calibration factors, and known anomalies.

10.6 RESEARCH AND KNOWLEDGE TRANSFER

- **Damage Signature Development:** Conduct research to establish damage-sensitive features in monitoring data that can reliably indicate structural degradation, concrete cracking, prestress loss, or bearing malfunction. Develop machine learning algorithms for automated damage detection based on these signatures.
- **Comparative Studies:** As additional network arch bridges are constructed and instrumented in the United States, establish a comparative database to identify common behavioral characteristics and project-specific anomalies.
- **Design Guide Development:** Work with AASHTO and FHWA to develop supplemental design guidance for unbraced network arch bridges addressing thermal analysis requirements for skewed configurations, refined analysis methods for tapered sections, construction sequencing for deck-post-tensioning interaction, and instrumentation recommendations for similar future projects.
- **High-Performance Concrete Guidelines:** Disseminate findings on autogenous shrinkage dominance, early-age thermal control, and time-dependent behavior to the concrete materials research community. Advocate for explicit consideration of autogenous shrinkage in design codes when $w/c < 0.35$ and SCM content > 50%.
- **Technology Transfer:** Conduct workshops and webinars for bridge owners, designers, and contractors on lessons learned from this project, including: ABC technique implementation, instrumentation system design and installation, thermal control procedures, and long-term monitoring strategies.
- **Undergraduate and Graduate Education:** Develop case study materials for civil engineering education, highlighting innovative aspects of this project: accelerated construction methods, network arch structural systems, high-performance concrete behavior, structural health monitoring implementation, and finite element model validation. This first-of-its-kind bridge provides exceptional educational opportunities.

11 REFERENCE

1. Aalami, B. O. (1990) “Load Balancing - A Comprehensive Solution to Post-Tensioning.” *ACI Struct. J.,* 87(6), pp. 662 - 670.
2. Aalami, B. O. (2000). “Structural Modeling of Post-tensioned Members”. *Journal of Structural Engineering*, 126 (2).
3. AASHTO. (2020). *AASHTO LRFD Bridge Design Specifications*, 9th Edition, American Association of State Highway and Transportation Officials, Washington DC
4. AASHTO. (2024). *AASHTO LRFD Bridge Design Specifications*, 10th Edition, American Association of State Highway and Transportation Officials, Washington DC
5. Abaqus. (2018). Abaqus/CAE User's Guide. SIMULIA User Assistance 2018.
6. ACI (2005). *ACI 209.1R-05: Report on Factors Affecting Shrinkage and Creep of Hardened Concrete*, ACI Committee 209, Farmington Hills, Michigan.
7. ACI (2008a). *ACI 209R-92: Prediction of Creep, Shrinkage, and Temperature Effects in Concrete Structures*, ACI Committee 209, Farmington Hills, Michigan.
8. ACI (2008b). *ACI 209.2R-08: Guide for Modeling and Calculating Shrinkage and Creep in Hardened Concrete*, ACI Committee 209, Farmington Hills, Michigan.
9. ACI. (2010). *ACI 363R-10: Report on High-Strength Concrete*, American Concrete Institute (ACI), Farmington Hills, Michigan.
10. ACI. (2016). *ACI 423.10R-16: Guide to Estimating Prestress Loss,* Joint ACI-ASCE Committee 423, Farmington Hills, Michigan.
11. ADAPT Corporation. (2017). *ADAPT-FELT 2017 User Manual*, ADAPT Corporation, Redwood City, California.
12. Al-Manaseer, A. and Lam, J. P. (2005). “Statistical Evaluation of Shrinkage and Creep Models.” *ACI Materials Journal*, 102 (3), pp. 170 - 176.
13. Al-Manaseer, A. and Armando, P. (2015). “Statistical Comparisons of Creep and Shrinkage Prediction Models Using RILEM and NU-ITI Databases.” *ACI Materials Journal*, 112 (1), pp. 125 - 136.
14. ASTM. (2014). *ASTM C469 / C469M-14 - Standard Test Method for Static Modulus of Elasticity and Poisson’s Ratio of Concrete in Compression*, ASTM International, West Conshohocken, Pennsylvania.
15. ASTM. (2015). A*STM C512/ C512M-15 - Standard Test Method for Creep of Concrete in Compression*, ASTM International, West Conshohocken, Pennsylvania.
16. ASTM. (2017). *ASTM C157/ C157M-17 - Standard Test Method for Length Change of Hardened Hydraulic-Cement Mortar and Concrete*, ASTM International, West Conshohocken, Pennsylvania.
17. ASTM. (2021a). *ASTM C39 / C39M-21 - Standard Test Method for Compressive Strength of Cylindrical Concrete Specimens*, ASTM International, West Conshohocken, Pennsylvania.
18. ASTM. (2021b). *ASTM C31 / C31M-21 - Standard Practice for Making and Curing Concrete Specimens in the Field*, ASTM International, West Conshohocken, Pennsylvania.
19. Aval, S. B. B., Ghabdian, M., Noori, M., and Altabey, W. A. (2022). “Simultaneous Effect of Temperature, Shrinkage, and Self-Weight Creep on RC Beams: A Case Study.” *Journal of Materials: Design and Applications*, 236(5), pp. 1020 - 1036.

20. Basnayake, K. (2023). *Development and Validation of Simulation Protocols for Assessing Stresses in a Network Tied Arch with a Posttensioned Tie Girder*, Ph.D. Dissertation, Western Michigan University, 1903, W Michigan Ave, Kalamazoo, Michigan.
21. Basnayake, K., Mazumdar, A. F., Attanayake, U., and Berke, N. S. (2020). "Assessment of Concrete Curing Duration using Bulk Electrical Conductivity and Porosity." *Transportation Research Record*, 2674(10), pp. 1 - 8.
22. Bažant, Z. P. (1988). "Chapter 2 - Material Models for Structural Analysis." Mathematical Modeling of Creep and Shrinkage, John Wiley & Sons Ltd, New York, pp. 99 - 211.
23. Bažant, Z. P. and Baweja, S. (1995). "Creep and Shrinkage Prediction for Analysis and Design of Concrete Structures - Model B3." ACI SP–194, *Adam Neville Symposium: Creep and Shrinkage—Structural Design Effects,* A. Al-Manaseer ed., American Concrete Institute, Farmington Hills, Michigan, pp. 1 - 83.
24. Bažant, Z. P. and Li, G. H. (2008). "Unbiased Statistical Comparison of Creep and Shrinkage Prediction Models." *ACI Materials Journal*, 105 (6), pp. 610 - 621.
25. Bažant, Z. K. P., Qiang, Y., and Guang-Hua, L. (2012). "Excessive Long-Time Deflections of Prestressed Box Girders. II: Numerical Analysis and Lessons Learned." *Journal of Structural Engineering*, 138 (6), pp. 687 - 696.
26. Brenkus, N. R. (2016). *Ultimate Strength of Post-tensioned Girders with Mixed Bonded and Unbonded Prestressing*, PhD. Dissertation, University of Florida, Florida.
27. Brenkus, N. R., Tatar, J., Hamilton, H. R., and Consolazio, G. R. (2019). "Simplified Finite Element Modeling of Post-Tensioned Concrete Members with Mixed Bonded and Unbonded Tendons." *Engineering Structures*, 179, pp. 387 - 397.
28. Brooks, J. J., Wainwright, P. J., and Al-Kaisi, A. F. (1991). "Compressive and Tensile Creep of Heat-Cured Ordinary Portland and Slag Cement Concretes." *Magazine of Concrete Research,* 43(154).
29. Brunn, B. and Schanack, F. (2003). *Calculation of a Double Track Railway Network Arch Bridge Applying the European Standards*, Dresden University of Technology.
30. Comite Euro-International Du Beton (CEB). (1993). *CEB-FIP 90 Model Code 1990: Design Code*, Thomas Telford Services Ltd, Heron Quay, London.
31. Cho, K., Kim, S. T., Cho, J. R., and Park, Y. H. (2017). "Estimation of Tendon Force Distribution in Prestressed Concrete Girders Using Smart Strand." *Applied Sciences,* 7 (12), pp. 1319.
32. Computers and Structures. (2023). "Tendon implementation in SAP2000." CSI Knowledge Base, <https://wiki.csiamerica.com/display/kb/Tendon+implementation+in+SAP2000> (Accessed on: 5-18-2023 at 5:43 pm).
33. Da Costa, B. M. (2013). *Design and Analysis of a Network Arch Bridge*, MSc Thesis, University of Lisbon, Portugal.
34. D'Ambrosia, M. D., Altoubat, S., and Lange, D. A. (2010). "Early Age Tensile Creep and Shrinkage of Concrete with Shrinkage Reducing Admixtures." *Jordan Journal of Civil Engineering*, 4(3).
35. Ellobody, E. and Bailey, C. G. (2008). "Behavior of Unbonded Post-Tensioned One-way Concrete Slabs." *Advances in Structural Engineering*, 11(1), pp 107 - 120.
36. Faxiong, L., Jia, G., Houqing, H., and Qian, L. (2013). "Concrete Creep and Shrinkage Effect Analysis Program Development." *Applied Mechanics and Materials*, pp. 405 – 408, pp. 850 - 855.

37. Folliard, K. J. and Berke, N. S. (1997). "Properties of High-Performance Concrete Containing Shrinkage Reducing Admixtures." *Cement and Concrete Research*, 27 (9), pp. 1357 - 1364.
38. French, C. E. W., Shield, C. K., and Hedegaard, B. D. (2014). *Modeling and Monitoring the Long-Term Behavior of Post-Tensioned Concrete Bridges*, Report no MN/RC 2014-39, Minnesota Department of Transportation, Research Services & Library, St. Paul, Minnesota.
39. Gardner, N. J. and Lockman M. J. (2001) "Comparison of Prediction Provisions for Drying Shrinkage and Creep of Normal Strength Concretes." *ACI Materials*, March-April, pp. 159 - 167.
40. Gastoni, V. T. and Buckholdt, M. (2014). "Innovative Steel Arches Over the Mississippi Utilizing ABC Technology." *Proceedings of World Steel Bridge Symposium (WSBS)*, March 26 – 29, 2014, Metro Toronto Convention Centre, Toronto, Canada.
41. Geokon. (2019). *Model 4200 Series: Vibrating Wire Strain Gauges Instruction Manual,* Geokon, Lebanon, New Hampshire.
42. Ghabdian, M., Beheshti, A. S. B., and Vafai, A. (2019). "Effect of Creep on High-Order Shear Deformable Beams." *Scientia Iranica - Transactions A: Civil Engineering*, 26(4), pp. 2187 - 2202.
43. Ghosh, R. S. and Timusk, J. (1981). "Creep of Fly Ash Concrete." *Journal of the American Concrete Institute*, 78 (5), pp. 351 - 357.
44. Gilbert, R. I. and Ranzi, G. (2011). *Time-Dependent Behavior of Concrete Structures*, 1st Edition, Taylor & Francis e-Library.
45. Goel, R., Kumar, R., and Paul, D. K. (2007). "Comparative Study of Various Creep and Shrinkage Prediction Models for Concrete." *Journal of Materials in Civil Engineering*, 19(3), pp. 249 - 260.
46. Hall, D. H. and Lawin, A. R. (1985). *Design of Steel Tied Arch Bridges: An Alternative*, Bridge Software Development International Ltd, Coopersburg, Pennsylvania.
47. Hedegaard, B. (2020). "Creep and Shrinkage Modeling of Concrete Using Solidification Theory." *Journal of Materials in Civil Engineering*, 32(7).
48. Hooton, D., Stanish, K., and Prusinski, J. (2004). "The Effect of Ground, Granulated Blast Furnace Slag (Slag Cement) on the Drying Shrinkage of Concrete – A Critical Review of the Literature." *Proceedings of 8th International Conference on Fly Ash, Silica Fume, Slag and Natural Pozzolans in Concrete*, 2004.
49. Huang, Y., Kang, T. H., K., Ramseyer, C., and Rha, C. (2010). "Background to Multi-Scale Modeling of Unbonded Post-Tensioned Concrete Structures." *International Journal of Theoretical and Applied Multiscale Mechanics*, 1(3), pp. 219 - 235.
50. Huang, Y. (2012). *Finite Element Method for Post-tensioned Prestressed Concrete Structures*, PhD. Thesis, University of Oklahoma, Oklahoma.
51. Huang, Y. and Kang, T. H. K. (2018). "Modeling of Sliding Behavior of Unbonded Tendons in Post-Tensioned Concrete Members." *ACI Structural Journal*, 115(4), pp. 1153 – 1164.
52. Hubler, M. H., Wendner, R., and Bažant, Z. P. (2015). "Comprehensive Database for Concrete Creep and Shrinkage: Analysis and Recommendations for Testing and Recording." *ACI Materials Journal*, 112(4), pp. 547 - 558.
53. Huo, X. S. O., Al-Omaishi, N., and Tadros, M. K. (2001). "Creep, Shrinkage, and Modulus of Elasticity of High-Performance Concrete." *ACI Materials Journal,* 98(6), pp. 440 - 449.

54. Huo, X. S. O., Zhu, P., Ung, F., and Wasserman, E. P. (2006). "Case Study of a High-Performance Concrete Bridge in Tennessee." *Practice Periodical on Structural Design and Construction*, 11(4), pp. 229 - 237.
55. Ibrahim, N., Omenzetter, P., and Liscombe, P. (2015). "Monitoring System for In-Situ Measurement of Creep and Shrinkage Effects in a Prestressed Concrete Bridge." *Proceedings of 20th Australasian Conference on the Mechanics of Structures and Materials*, Toowoomba, Australia, pp.767- 771.
56. International Federation for Structural Concrete (*fib*). (2013). *fib Model Code for Concrete Structures 2010*, Wilhelm Ernst & Sohn, Berlin, Germany.
57. Jin, S., Cha, S., and Jung H. (2018). "Improvement of Concrete Creep Prediction with Probabilistic Forecasting Method Under Model Uncertainty." *Construction and Building Materials*, 184(2018), pp. 617 - 633.
58. Lopez, A. N. M., Silva, E. F., Dal Molin, D. C. C., and Filho, R. D. T. (2013). "Shrinkage-Reducing Admixture: Effects on Durability of High-Strength Concrete." *ACI Materials Journal*, 110(4), pp. 365 - 374.
59. Kang, T. and Huang, Y. (2012). "Computer Modeling of Post-Tensioned Structures." *Proceedings of 4th International Conference on Computer Modeling and Simulation (ICCMS 2012)*, IPCSIT 22 (2012), Singapore.
60. Kang, T. H. K., Huang, Y., Shin, M., Lee, J. D., and Chor, A. S. (2015). "Experimental and Numerical Assessment of Bonded and Unbonded Post-Tensioned Concrete Members." *ACI Structural Journal*, 112 (6), pp. 735 - 757.
61. Kim, S. H., Park, S. Y., Park, Y. H., and Jeon, S. J. (2019). "Friction Characteristics of Post-Tensioning Tendons in Full-Scale Structures." *Engineering Structures*, 183(2019), pp. 389 - 397.
62. Kim, S. H., Park, S. Y., Kim, S. T., and Jeon, S. J. (2022). "Analysis of Short-Term Prestress Losses in Post-tensioned Structures Using Smart Strands." *International Journal of Concrete Structures and Materials*, 16 (1).
63. Kioumarsi M, Azarhomayun, F., Haji, M., and Shekarchi, M. (2020). "Effect of Shrinkage Reducing Admixture on Drying Shrinkage of Concrete with Different w/c Ratios." *Materials*, 13(24), pp. 5721.
64. Klausen, A. and Kanstad, T. (2021). "The Effect of Shrinkage Reducing Admixtures on Drying Shrinkage, Autogenous Deformation, and Early Age Stress Development of Concrete." *Structural Concrete*, 22(Suppl. 1), pp. 596 - 606.
65. Kosmatka, S. H., Kerkhoff, B., and Wilson, M. L. (2011). *Design and Control of Concrete Mixtures,* 15th Edition, Portland Cement Association (PCA), Skokie, Illinois.
66. LARSA. (2021). *LARSA 4D User's Guide*. LARSA, Inc., Melville, New York.
67. Lee, A. and Robertson, I. N. (1995). *Instrumentation and Long-Term Monitoring of the North Halawa Valley Viaduct*, Research Report UHM/CE/95-0, University of Hawaii, Honolulu, Hawaii.
68. Li, S., Yang, Y., Pu, Q., Yang, D., Sun., B., and Li, X. (2018). "Three-Dimensional Nonlinear Creep and Shrinkage Effects of a Long-Span Prestressed Concrete Box Girder Bridge." *Structural Concrete*. 20(2019), pp. 638 - 649.
69. Lin T. Y. and Burns, N. (1991). *Design of Prestressed Concrete Structures*, 3rd Edition, John Wiley & Sons, New York
70. Liu, Y. (2018). *Finite-Element Modeling of Early-Age Concrete Behavior*, PhD. Dissertation, Auburn University, Auburn, Alabama.

71. LUSAS. (2022). “Prestress / Post-tensioning”, Engineering analysis + design software, < https://www.lusas.com/products/information/post-tensioning.html> (Accessed on 5-19-2023 at 8:42 pm).
72. Ma, J. and Dehn, F. (2017). “Shrinkage and Creep Behavior of an Alkali-Activated Slag Concrete.” *Structural Concrete*, 18(3).
73. Mato, F. M., Cornejo, M. O., and Sanchez, J. N. (2011). “Design and Construction of Composite Tubular Arches with Network Suspension System: Recent Undertakings and Trends.” *Journal of Civil Engineering and Architecture*, 5(3), pp. 191 - 214.
74. Meyerson, R., Weyers, R. E., Mokaram, D. W., and Lane, D. S. (2002). *Evaluation of Models for Predicting (Total) Creep of Prestressed Concrete Mixtures*, Report no VTRC 03-CR5, Virginia Transportation Research Council, Charlottesville, Virginia.
75. MIDAS Information Technology. (2019). *Time Dependent Material (Creep/Shrinkage),* midas Civil Online Manual - Civil structure design system, <http://manual.midasuser.com/EN_Common/Civil/875/index.htm> (Accessed on 4-19-2023 at 8:50 pm).
76. Mohammed, A. H., Tayşi, N., Nassani, D. E., and Hussein, A. K. (2017). “Finite Element Analysis and Optimization of Bonded Post-Tensioned Concrete Slabs.” *Cogent Engineering*, 4(1).
77. Mokarem, D. W., Weyers, R. E., and Lane, D. S. (2005). “Development of a Shrinkage Performance Specifications and Prediction Model Analysis for Supplemental Cementitious Material Concrete Mixtures.” *Cement and Concrete Research*, 35(2005), pp. 918 - 925.
78. Naaman, A. E. (2012). *Prestressed Concrete Analysis and Design – Fundamentals*, 2nd Edition, Techno Press, 3000, Ann Arbor, Michigan.
79. Neville, A. M. (1996). *Properties of Concrete*, 5th Edition, Pearson Education Limited, England.
80. Nmai., C., Tomita, R., Hondo, F., and Buffenbarger, J. (1998). “Shrinkage-Reducing Admixtures.” *Concrete International*, 20(4), pp. 31 - 37.
81. PCI. (2023). “West Seventh Street Bridge.” <https://www.pci.org/PCI/Project_Resources/Project_Profile/Project_Profile_Details.aspx?ID=23426> (Accessed on 6-24-2023).
82. Per Tveit. (2006). “An Introduction to the Network Arch.” <https://home.uia.no/pert/index.php/My_Publications> (Accessed on 2-18-2021)
83. Per Tveit. (2009). “Genesis and Development of the Network Arch Concept.” sixthstreetviaduct.org (n.d.) Sixth Street Viaduct Replacement Project < https://www.sixthstreetviaduct.org/> (Accessed on 1-13-2022 at 7:00 pm).
84. Post-Tensioning Institute (PTI). (2006). *Post-Tensioning Manual*, 6th Edition, Phoenix, Arizona.
85. RILEM Technical Committee TC-242-MDC. (2015). “RILEM Draft Recommendation: TC-242-MDC Multi-Decade Creep and Shrinkage of Concrete: Material Model and Structural Analysis”. *Materials and Structures*, 48, pp. 753 - 770.
86. Robertson, I. N. and Li, X. (2005). “Shrinkage and Creep Predictions Evaluated Using 10-Year Monitoring of the North Halawa Valley Viaduct.” *ACI SP-227 Shrinkage and Creep of Concrete*, pp.143 - 162.
87. Rongbing, B. and Jian, S. (2005). “Synthesis and Evaluation of Shrinkage-Reducing Admixture for Cementitious Materials.” *Cement and Concrete Research*, 35(2005), pp. 445 - 448.

88. Saha, A. K. (2018). “Effect of Class F Fly Ash on the Durability Properties of Concrete.” *Sustainable Environment Research,* 28(1), pp. 25 - 31.
89. Sakata, K., Tsubaki, T., Inoue, S., and Ayano, T. (2001). “Prediction Equations for Creep and Shrinkage in Concrete of Wide-Ranging Strength.” *Proceedings of Japanese Society of Civil Engineers,* 690(53), pp. 145 - 166.
90. Sakata, K., Ayano, T., Imamoto, K., and Sato, Y. (2009). “Database of Creep and Shrinkage Based on Japanese Research in Creep, Shrinkage and Durability Mechanics of Concrete and Concrete Structures.” *Proceedings of the 8th International Conference on Creep, Shrinkage and Durability Mechanics of Concrete and Concrete Structures. Creep, Shrinkage and Durability Mechanics of Concrete and Concrete Structures*, Ise-Shima, Japan, 30/09/2008, 2, pp. 1253 - 1274.
91. Sakata, K. and Shimomura, T. (2004). “Recent Progress in Research on and Code Evaluation of Concrete Creep and Shrinkage in Japan.” *Journal of Advanced Concrete Technology*, 2(2), pp.133 - 140.
92. Sakthivel, T., Gettu, R., and Pillai, R. G. (2019). “Compressive Strength and Elastic Modulus of Concretes with Fly Ash and Slag.” *Journal of Institute of Engineers of India (Series A)*.
93. Saliba, J., Roziere, E., Grondin, F., and Loukili, A. (2011). “Influence of Shrinkage-Reducing Admixtures on Plastic and Long-Term Shrinkage.” *Cement and Concrete Composites*, 33, pp. 209 - 217.
94. Siegel, A. F., and Wagner, M. R. (2022). *Chapter 11 - Correlation and Regression: Measuring and Predicting Relationships of Practical Business Statistics*, 8th Edition, pp. 313 - 370.
95. Sousa, H., Bento, J., and Figueiras, J. (2014). “Assessment and Management of Concrete Bridges Supported by Monitoring Data-Based Finite Element Modeling.” *Journal of Bridge Engineering*, 19(6).
96. Sundt Construction. (2023). “West 7th Street Bridge”, <https://www.sundt.com/projects/west-7th-street-bridge/> (Accessed on 8-15-2023 at 8:00 pm).
97. Tadros, M. K., Al-Omaishi, N., Seguirant, S. J., and Gallt, J. G. (2003). *Prestress Losses in Pretensioned High-Strength Concrete Bridge Girders,* NCHRP Report 496, Transportation Research Record, Washington, DC.
98. Tazawa, E., Yonekura, A., and Tanaka, S. (1989). “Drying Shrinkage and Creep of Concrete Containing Granulated Blast Furnace Slag.” *ACI Symposium Publication*, 114 (1), pp. 1325 - 1343.
99. Tazawa, E. (1999). *Autogenous Shrinkage of Concrete*, Taylor & Francis, New York.
100. Tong, G., Chen, Z., Lu, S., and Yao, R. (2018). “Monitoring and Analysis of Long-Term Prestress Losses in Post-Tensioned Concrete Beams.” *Measurement,* 122, pp. 573 - 581.
101. Varennes, M. (2011). *Design of a Single-Track Railway Network Arch Bridge According to Eurocodes*, MSc. Thesis, Royal Institute of Technology, Sweden.
102. Vecchio, F. J., Gauvreau, P., and Liu, L. (2006). “Modeling of Unbonded Post-Tensioned Concrete Beams Critical in Shear.” *ACI Structural Journal*, 103(1), pp. 57 - 64.
103. Videla, C. and Aguilar, C. (2005). “Effectiveness of shrinkage-reducing admixtures on Portland pozzolan cement concrete.” *Materiales De Construcción*, 55(278), pp. 13 - 28.
104. Yousefpour, H., Helwig, T. A., and Bayrak, O. (2015). “Construction stresses in the world’s first precast network arch bridge.” *PCI Journal*, 60 (5), pp. 30 - 47.

105. Zhou, Z., He, J., Chen, G., and Ou, J. (2009). "A Smart Steel Strand for the Evaluation of Prestress Loss Distribution in Post-Tensioned Concrete Structures." *Journal of Intelligent Material Systems and Structures*, 20(November), pp. 1901 - 1912.
106. Zhu, L., Wang, J. J., Li, X., Zhao, G. Y., and Huo, X. J. (2020). "Experimental and Numerical Study on Creep and Shrinkage Effects of Ultra High-Performance Concrete Beam." *Composites Part B*, 184(2020).

APPENDICES

APPENDIX A

CEMENT, GGBFS, AND FLY ASH MILL REPORTS

A.1 Cement

Table A-1. Cement Mill Report

Portland Cement Type I/II (Production Period: 2/01/021 to 2/28/2021)					
Standard Requirements					
Chemical Data			**Physical Data**		
Item	Spec. Limits	Results	Item	Spec. Limits	Results
SiO_2 (%)		18.9	Air content of mortar (volume %)	12.0 max	8
Al_2O_3 (%)	6.0 max	4.9	Blaine fineness (m^2/kg)	260.0 min	410
Fe_2O_3 (%)		3.07	Autoclave expansion (%)	0.8 max	0.05
CaO (%)		61.6	Compressive strength (MPa/psi):		
MgO (%)	6.0 max	2.8	1 day		15.7 [2276]
SO_3 (%)	3.0 max	3.83	3 days	12.0 [1740] min	26.8 [3890]
Loss of ignition (%)	3.5 max	2.1	7 days	19.6 [2760] min	31.8 [4614]
Na_2O (%)		0.278	28 days (previous month)	25.0 [4060] min	39.2 [5679]
K_2O (%)		0.99	Time of setting (minutes)		
Insoluble residue (%)	1.5 max	0.25	(Vicat) Initial	45-375	107
CO_2 (%)		1.5	(Vicat) Final		223
Limestone (%)	5.0 max	3.6			
$CaCO_3$ in limestone (%)	70.0 min	97.0			
Inorganic process addition (%)	5.0 max	0.0	Mortar Bar Expansion (ASTM C1038) (%)*	0.02 max	0.006
Potential phase composition			Base Cement Phase Composition		
C_3S (%)		57	C_3S (%)		57
C_2S (%)		11	C_2S (%)		12
C_3A (%)	8 max	8	C_3A (%)		8
C_4AF (%)		9	C_4AF (%)		9
Optional Requirements					
Item	Spec. Limits	Results	Item	Spec. Limits	Results
Equiv. Alkalies	A	0.69	False Set (%)	50 min	
			Retained 325 (%)		4.41
Additional Data					
Type	Limestone		Inorganic Processing Addition		
Amount	3.6		0.0		
SiO_2 (%)	1.4		Specific gravity (g/cm^3)		3.15
Al_2O_3 (%)	0.6				
Fe_2O_3 (%)	0.2				
CaO (%)	49.2				
SO_3 (%)	0.4				

A.2. Ground Granulated Blast Furnace Slag (GGBFS)

Table A-2. Slag Cement Mill Report

Slag Cement Grade 100 - Cemplus (Production Period: 2/01/021 to 2/28/2021)					
Standard Requirements - Slag					
Chemical Data			**Physical Data**		
Item	Spec. Limits	Results	Item	Spec. Limits	Results
Sulfide Sulfur (S) (%)	2.5 max	0.6			
Sulfate Sulfur (as SO_3) (%)		1.5	Air content of mortar (volume %)	12.0 max	5
Added Sulfate Sulfur (as SO_3) (%)			Blaine fineness (m^2/kg)	260.0 min	533
Inorganic process addition (%)	5.0 max		Retained 325 (%)		1.67
SiO_2 (%)		36.23	Compressive strength (MPa/psi):		
Al_2O_3 (%)		11.22	7 days		24.7 [3584]
Fe_2O_3 (%)		0.65	28 days (previous month)		40.6 [5894]
CaO (%)		38.22	Slag Activity Index (%) (SAI)		
Na_2O (%)		0.283	7 days		73.1
K_2O (%)		0.453	28 days (previous month)	95 min	100.3
Standard Requirements – Reference Cement					
Chemical Data			Physical Data		
Item	Spec. Limits	Results	Item	Spec. Limits	Results
Equiv. Alkalies	A	0.86	Blaine fineness (m^2/kg)	260.0 min	390
Potential phase composition					
C_3S (%)		57	Compressive strength (MPa/psi):		
C_2S (%)		13	7 days		33.9 [4915]
C_3A (%)		8	28 days (previous month)		40.4 [5854]
C_4AF (%)		9			
Additional Data					
Item			Item		Results
Type	Inorganic Processing Addition		Specific gravity (g/cm^3)		2.91
Amount	0.0		0.0		0.02
SiO_2 (%)			Autoclave expansion (%)		
Al_2O_3 (%)					
Fe_2O_3 (%)					
CaO (%)					
SO_3 (%)					

A.3. Fly Ash

Table A-3. Fly Ash Mill Report

ASTM C618/AASHTO M295 Testing of Monroe Fly Ash			
Sample Date:	12/1 – 12/31/20	Report Date:	2/10/21
Sample Type:	Monthly	MTRF ID:	48MO
Sample ID:			
Chemical Analysis	**Results**	**ASTM Limit Class F/C**	**AASHTO Limit Class F/C**
Silicon Dioxide (SiO_2) (%)	40.45		
Aluminum Oxide (Al_2O_3) (%)	20.91		
Iron Oxide (Fe_2O_3) (%)	10.74		
Sum (SiO_2+Al_2O_3+Fe_2O_3) (%)	72.10		
Sulfur Trioxide (SO_3) (%)	1.92		
Calcium Oxide (CaO) (%)	16.82		
Magnesium Oxide (MgO) (%)	3.12		
Sodium Oxide (Na_2O) (%)	1.07		
Potassium Oxide (K_2O) (%)	1.07		
Sodium Oxide Equivalent (Na_2O+0.658K_2O) (%)	1.77		
Moisture(%)	0.11	3.0 max	3.0 max
Loss on ignition (%)	1.72	6.0 max	5.0 max
Available Alkalies, as Na_2O_e (%)	0.91	Not Required	1.5 max
Physical Analysis			
Fineness, % retained on 45-µm sieve	16.76	34 max	34 max
Strength Activity Index – 7- or 28-day requirement			
7 day, % of control	90	75 min	75 min
28 day, % of control	90	75 min	75 min
Water Requirement, % of control	96	105 max	105 max
Autoclave Soundness (%)	-0.08	0.8 max	0.8 max
Density (g/cm^3)	2.65		

APPENDIX B

STRAIN AND TEMPERATURE DATA COLLECTED FROM THE 2ND AVENUE BRIDGE MEMBERS

B.1 Measured Strain in the Post-tensioned Knuckles

Table B-1. RSE of the Measured and Calculated Total Shrinkage Strain in the Upper Knuckles

Upper Knuckle	Shrinkage Model	Residual Standard Error (RSE) of Total Shrinkage Strains							
		T-1	T-2	T-3	M-1	M-2	B-1	B-2	B-3
SE Upper Knuckle (TG-1)	CEB-FIP 2010	30	61	36	30	25	59	32	34
	RILEM B4	232	196	222	275	270	308	276	281
NE Upper Knuckle (TG-5)	CEB-FIP 2010	91	35	117	33	73	16	18	32
	RILEM B4	167	285	140	282	186	253	254	229
SW Upper Knuckle (TG-6)	CEB-FIP 2010	109	103	50	111	79	69	33	69
	RILEM B4	363	357	210	364	332	321	282	321
NW Upper Knuckle (TG-10)	CEB-FIP 2010	25	66	21	46	100	79	89	95
	RILEM B4	270	209	236	289	209	321	333	339

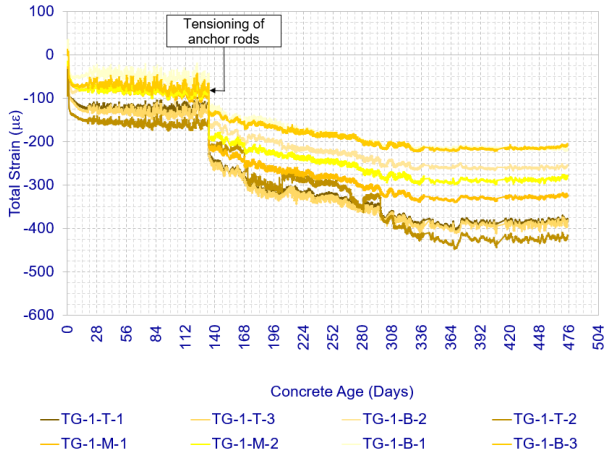

(a) At the SE knuckle - TG-1

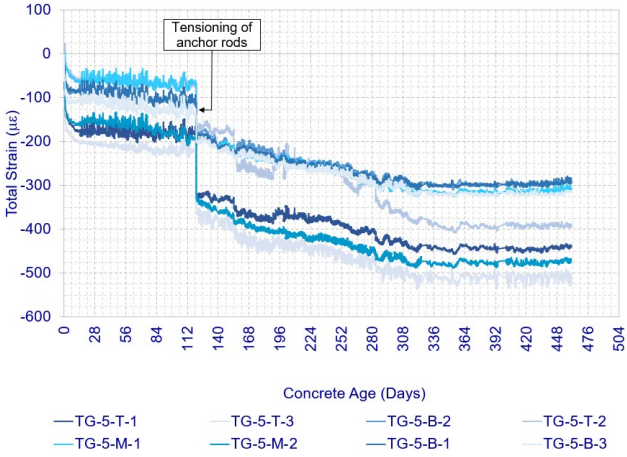

(b) At the NE knuckle - TG-5

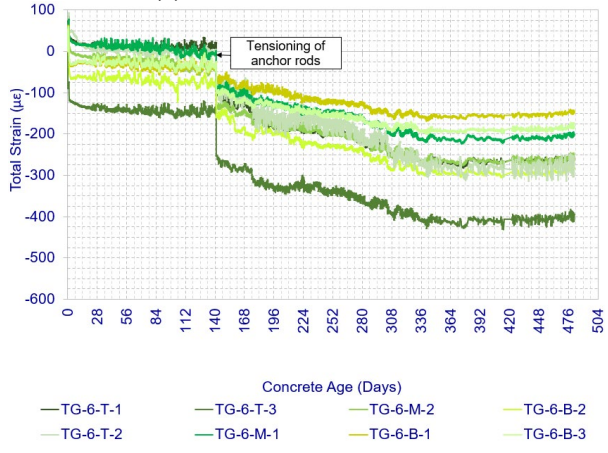

(c) At the SW knuckle - TG-6

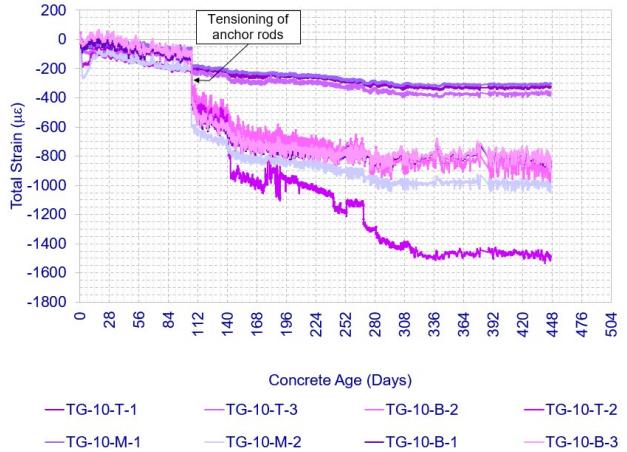

(d) At the NW knuckle - TG-10

Figure B-1. Measured strain in the post-tensioned upper knuckles.

APPENDIX C

PRESTRESS LOSSES IN POST-TENSIONED MEMBERS

C.1. Prestress Losses Due to Friction

The prestress force applied at the jacking ends of a post-tensioned member varies along its length due to friction losses between the tendons and the ducts. These friction losses arise from two effects: intentional curvature of the tendons and unintended curvature of the duct (wobble effect). The tendon curvature resulting from the tendon profile and the unintended curvature due to the wobble effect are illustrated in Figure C-1. The stress in a tendon at any point after accounting for friction losses is determined using Eq. (C-1).

$$\boldsymbol{T_x = T_0 e^{(\mu\alpha + Kx)}} \qquad \text{Eq. C-1}$$

where,

α	=	total angular change from jacking end to point x (radians)
μ	=	curvature friction coefficient
K	=	wobble friction coefficient
T_0	=	prestressing force at stressing end
T_x	=	prestressing force at point x
x	=	length of tendon from stressing end to point x

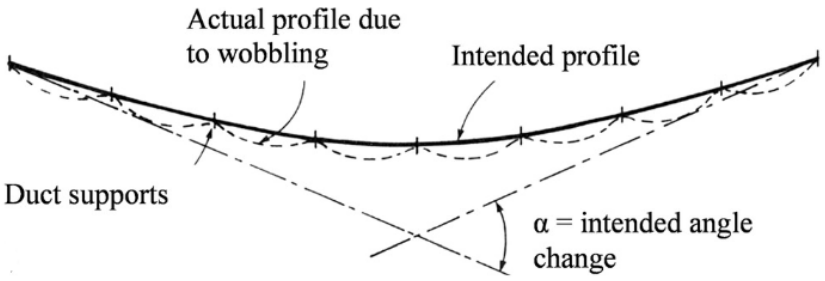

Figure C-1. Intended and unintended curvature of the tendon profile (Dundu 2015).

Table C-1 presents typical coefficients for μ and k based on prestressing steel type and post-tensioned duct type. In some cases, friction coefficients are determined through field measurements (Kim et al. 2019). For a tendon with a varying profile in both the horizontal and vertical planes, the total angular change is equal to the resultant of the horizontal and vertical curvatures (Caltrans 2014). For a straight tendon, the prestress loss due to intended curvature is zero ($\alpha = 0$); however, prestress loss due to the wobble effect remains. Overall, prestress loss due to friction increases with increasing tendon length, tendon curvature, and friction coefficient.

Table C-1. Recommended Friction Coefficients (ACI 2016)

Type of Prestressing Steel	Corrugated Metal Duct		Corrugated Plastic Duct		Smooth Steel Pipe		Smooth Plastic Pipe		No Duct Plastic Sheathing	
	μ	k (per ft)	μ	k (per ft)	μ	k (per ft)	μ	k (per ft)	μ	k (per ft)
Strand	0.15 to 0.25	0.00005 to 0.0003	0.10 to 0.14	0.00005 to 0.0003	0.25 to 0.30	0	0.10 to 0.14	0	-	-
Strad in precast elements and constant curvature tendons	0.15 to 0.25	0.00005 to 0.0003	0.10 to 0.14	0.00005 to 0.0003	-	-	-	-	-	-
External tendons, bare dry strand	-	-	-	-	0.25 to 0.30	0	0.12 to 0.15	0	-	-
Lubricated strand	0.12 to 0.18	0.00005 to 0.0003	-	-	0.20 to 0.25	0	-	-	-	-
Strand coated and extruded	0.01 to 0.05	0.00005 to 0.0003	0.01 to 0.05	0.00005 to 0.0003	0.01 to 0.05	0	0.01 to 0.05	0	0.01 to 0.07	0.00005 to 0.0003
Bars, deformed, smooth, and round	0.30	0 to 0.0002	0.30	0 to 0.0002	-	-	-	-	-	-

Figure C-2a illustrates the stress distribution in a straight tendon, or in a tendon with very small curvature, after friction losses when stressed from one end. The maximum stress occurs at the stressing end and corresponds to the jacking stress (f_{jack}), while the minimum stress occurs at the dead end (f_L).

Figure C-2b illustrates the stress distribution in a straight tendon, or in a tendon with very small curvature, after friction losses when stressed from both ends, where A denotes the first stressing end and B denotes the second stressing end. As shown in Figure C-2b, the tendon stress distribution is symmetric about the midpoint of the tendon. The maximum stress occurs at the two stressing ends (f_{jack} A and f_{jack} B), and the minimum stress occurs at the midpoint of the beam ($f_L/2$).

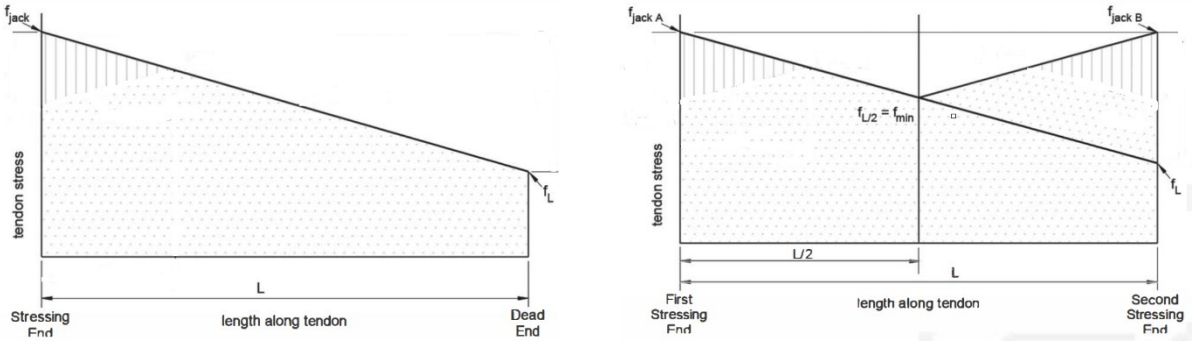

(a) Stressed from one end (b) Stressed from both ends

Figure C-2. Variation of stress in a straight tendon or a tendon with negligible curvature due to friction losses, considering (a) stressed from one end and (b) stressed from both ends (ACI 2016).

For the straight tendon, or a tendon with very small curvature, the friction intensity is constant along the tendon length (Figure C-2). In contrast, for a curved tendon, the friction intensity varies along the tendon length. When evaluating friction losses in a curved tendon, the tendon is divided into segments over which the friction intensity is assumed to be constant. Figure C-3 illustrates the stress distribution developed in a parabolic tendon after stressing. As shown in Figure C-3, the friction intensity for a parabolic tendon varies along its length and is therefore calculated separately for individual segments, such as from the inflection point to the low point, from the low point to the high point, and other corresponding segments.

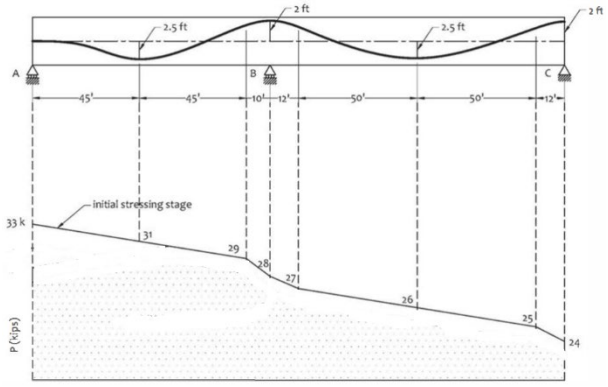

Figure C-3. Stress distribution in tendons reflecting variable friction intensity (ACI 2016).

C.2. Prestress Losses Due to Anchorage Set

When tendons are stressed and anchored, the movement of the strands within the anchorage is referred to as the anchorage set. As a result of this anchorage set, the tendon shortens and a portion of the tendon stress is lost. During anchorage seating, friction acting on the tendon occurs in the opposite direction of the friction that acts during stressing (ACI 2016). ACI (2016) recommends an anchorage set of 1/4 in. for tendons stressed using a power seating device and 3/8 in. for tendons stressed using jacks.

Figure C-4a illustrates the tendon stress distribution after accounting for friction and anchorage losses in a straight tendon, or a tendon with negligible curvature, stressed from one end. The tendon stress at the stressing end after anchorage set loss (Δf_{pA}) is denoted as f_{anchor}. The maximum tendon stress (f_{max}) occurs at a distance x from the stressing end, which is referred to as the distance influenced by the anchorage set. For a short tendon with negligible friction losses, this influence distance may extend to the dead end, whereas for a longer tendon the influence distance is shorter (ACI 2016).

Figure C-4b shows the variation of tendon stress after friction and anchorage losses for a straight tendon, or a tendon with negligible curvature, stressed from both ends, where A represents the first stressing end and B represents the second stressing end. As shown in Figure C-4b, the tendon stress distribution is symmetric about the midpoint of the tendon.

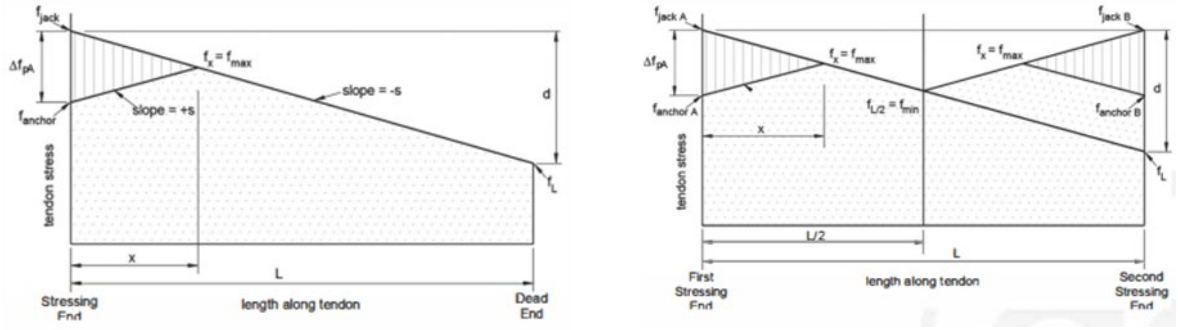

(a) Stressed from one end (b) Stressed from both ends

Figure C-4. Variation of stress in a straight tendon or a tendon with negligible curvature after friction and anchorage set losses considering (a) stressed from one end and (b) stressed from both ends (ACI 2016).

The anchorage set (ΔA) is determined by integrating the tendon stress from the stressing end to the distance influenced by the anchorage set (x), and dividing the result by the elastic modulus of the prestressing steel (E_{ps}) (ACI 2016). This quantity corresponds to the shaded area shown in Figure C-4a divided by E_{ps}, as expressed in Equation (C-2).

$$\boldsymbol{\Delta A = \frac{\Delta f_{pA} x}{2 E_{ps}}} \qquad \text{Eq. C-2}$$

For a given tendon segment, the slope of the stress line after anchorage set is equal in magnitude and opposite in direction to the slope of the stress line after friction losses (see Figure C-4a). For a straight tendon, or a tendon with negligible curvature, the slope of the stress line (s) is constant along the entire tendon length and is given by Equation (C-3).

$$\boldsymbol{s = \frac{f_{jack} - f_L}{L} = \frac{\frac{\Delta f_{pA}}{2}}{x}} \qquad \text{Eq. C-3}$$

where,

f_{jack} = prestressing force at the stressing end
f_L = prestressing force at the dead end
Δf_{pA} = change in stress at the stressing end due to the anchorage set
L = length of the tendon
x = length along the tendon affected by the anchorage set

Combining Eq. C-2 and Eq. C-3, the anchorage set loss (Δf_{pA}) is calculated using Eq. C-4.

$$\boldsymbol{\Delta f_{pA} = 2\sqrt{\frac{E_{ps}(f_{jack} - f_L)\Delta A}{L}}} \qquad \text{Eq. C-4}$$

Unlike a straight tendon, the slope of the stress line after friction losses in a curved tendon varies along the tendon length. Therefore, an iterative approach is required to determine the prestress loss due to anchorage set in a curved tendon (Aalami 2004).

C.3. Prestress Losses due to Elastic Shortening of Concrete

During post-tensioning, the concrete member shortens while the tendon is elongated during the stressing operation. Therefore, a tendon does not experience elastic shortening as a result of its own stressing. However, when tendons are stressed sequentially, previously stressed tendons shorten due to the subsequent stressing of other tendons. This phenomenon is referred to as elastic shortening loss. Elastic shortening loss in each tendon may be calculated using approximate methods or more rigorous methods that account for the stressing sequence and tendon profile. Considering the tendon path and the sequential stressing of the post-tensioned members of the 2nd Avenue Bridge, only the more accurate methods for calculating elastic shortening losses are discussed in this study. Equations (C-5) through (C-8) are used to compute elastic shortening losses.

For a concrete beam with straight tendons, if N denotes the total number of stressed tendons, the elastic shortening loss in the jth tendon due to stressing of the (j+1)th tendon is calculated using Equation (C-5) (Naaman 2012; Evans and Bennett 1958).

$$\left(\Delta f_{pES}\right)_{j\rightarrow j+1} = n_{pi}\frac{f_{pj+1}A_{pj+1}}{A_c}\left(1+\frac{e_{hj}e_{hj+1}}{r_h^2}+\frac{e_{vj}e_{vj+1}}{r_v^2}\right) \qquad \text{Eq. C-5}$$

The total loss in the j^{th} tendon is calculated using Eq.C-6.

$$\left(\Delta f_{pES}\right)_{j} = \sum_{k=j+1}^{N} n_{pi}\frac{f_{pk}A_{pk}}{A_c}\left(1+\frac{e_{hj}e_{hk}}{r_h^2}+\frac{e_{vj}e_{vk}}{r_v^2}\right) \qquad \text{Eq. C-6}$$

where,

A_c	=	area of concrete section (use net area for better accuracy)
A_{pk}	=	area of the k^{th} tendon
e_{hj}, e_{hk}	=	horizontal eccentricities of the j^{th} and k^{th} tendons with respect to the centroid of the concrete section
e_{vj}, e_{vk}	=	vertical eccentricities of the j^{th} and k^{th} tendons with respect to the centroid of the concrete section
E_{ci}	=	elastic modulus of concrete at the age of stressing
E_{ps}	=	elastic modulus of prestressing steel

f_{pk} = stress in the k^{th} tendon immediately after the last tendon has been stressed

n_{pi} = modular ratio at time of prestress = E_{ps}/E_{ci}

r_h = horizontal radius of gyration of concrete section (net section properties may be used for better accuracy)

r_v = vertical radius of gyration of concrete section (net section properties may be used for better accuracy)

In a concrete beam with curved tendons, if N is the number of stressed tendons, the elastic shortening loss in the j^{th} tendon due to the stressing of the $(j+1)^{th}$ tendon is calculated using Eq. C-7 (Naaman 2012 and Evans and Bennett 1958).

$$\left(\Delta f_{pES}\right)_{j\rightarrow j+1} = n_{pi}\frac{f_{pj+1}A_{pj+1}}{A_c}\left\{1 + \int_0^L\left(\frac{e_{hj}e_{hj+1}}{r_h^2} + \frac{e_{vj}e_{vj+1}}{r_v^2}\right)\right\} \qquad \text{Eq. C-7}$$

The total loss in the j^{th} tendon is calculated using Eq. C-8.

$$\left(\Delta f_{pES}\right)_j = \sum_{k=j+1}^{N} n_{pi}\frac{f_{pk}A_{pk}}{A_c}\left\{1 + \int_0^L\left(\frac{e_{hj}e_{hk}}{r_h^2} + \frac{e_{vj}e_{vk}}{r_v^2}\right)dx\right\} \qquad \text{Eq. C-8}$$

where,

L = span of the beam

x = distance to any point on the beam from one support

The accurate methods of calculating elastic shortening losses, as given from Eq. C-5 to Eq. C-8 assumed the strain compatibility between the tendon and the concrete. However, if the tendons are unbonded at the time of stressing, the tendons do not undergo strain changes similar to those of the concrete. For unbonded tendons, the elastic shortening losses are calculated using Eq. C-9 (ACI 2010).

$$\Delta f_{pES} = K_{es}\frac{E_{ps}}{E_{ci}}f_{cpa} \qquad \text{Eq. C-9}$$

where,

K_{es} = an averaging factor for post-tensioned members

= 0.5 for post-tensioned members when tendons are stressed in a sequential order to the same tension

= vary from 0 to 0.5 for other PT procedures

f_{cpa} = average compressive concrete stress at the center of gravity of the tendons immediately after the prestress has been applied to the concrete

AASHTO (2020) recommends an averaging factor of $(N-1)/2N$, where N is the number of sequentially stressed tendons.

C.4. Time-Dependent Losses Due to Steel Relaxation

Prestressing steel undergoes a relaxation phenomenon over time, the magnitude of which depends on the stress level in the tendon. Because tendon stress continuously changes throughout the service life of the structure, the relaxation rate also varies. Concrete creep, concrete shrinkage, and superimposed loads contribute to changes in tendon stress, thereby leading to additional prestress loss in the steel.

Commercially available prestressing strands are classified as low-relaxation or stress-relieved based on their relaxation characteristics. For low-relaxation steel, losses due to relaxation are generally small relative to other time-dependent prestress losses. The Precast/Prestressed Concrete Institute (PCI) has published building code requirements for post-tensioned concrete that specify a lump-sum prestress loss of 15 to 25 ksi, excluding friction losses. The PCI Design Handbook further recommends an estimated total prestress loss of 25 to 50 ksi for normal-weight concrete components (ACI 2016).

Losses due to relaxation of tendons is determined using Eq. C-10 (PCI 2010).

$$\boldsymbol{\Delta f_{pRE} = C\left[K_{re} - J\left(\Delta f_{pSH} + \Delta f_{pCR} + \Delta f_{pES}\right)\right]} \qquad \text{Eq. C-10}$$

where,

K_{re} = factor dependent upon the tendon type (see Table C.2)

J = factor that accounts for the stress change due to instantaneous elastic shortening and time-dependent creep and shrinkage (see Table C.2)

C = coefficient calculated based on the f_{pi}/f_{pu} where f_{pi} is the prestressing steel stress immediately after anchorage seating loss, and f_{pu} is the ultimate strength of prestressing steel

= $1 + 9(\frac{f_{pi}}{f_{pu}} - 0.7)$ for a stress-relieved strand with $0.75 \geq \frac{f_{pi}}{f_{pu}} \geq 0.70$

= $\left[\frac{(\frac{f_{pi}}{f_{pu}})}{0.19}\right]\left[\frac{(\frac{f_{pi}}{f_{pu}})}{0.85} - 0.55\right]$ for a stress-relieved strand with $0.70 > \frac{f_{pi}}{f_{pu}} \geq 0.51$

= $\frac{(\frac{f_{pi}}{f_{pu}})}{4.25}$ for a stress-relieved strand with $\frac{f_{pi}}{f_{pu}} < 0.51$

= $\left[\frac{(\frac{f_{pi}}{f_{pu}})}{0.21}\right]\left[\frac{(\frac{f_{pi}}{f_{pu}})}{0.90} - 0.55\right]$ for a low-relaxation strand with $\frac{f_{pi}}{f_{pu}} \geq 0.54$

$= \frac{(\frac{f_{pi}}{f_{pu}})}{4.25}$ for a stress-relieved strand with $\frac{f_{pi}}{f_{pu}} \leq 0.54$

Δf_{pSH} = prestress loss due to concrete shrinkage

Δf_{pCR} = prestress loss due to concrete creep

Δf_{pES} = prestress loss due to elastic shortening

Table C-2. Values of K_{re} and J (PCI 2010)

Tendon Type	K_{re}, psi (MPa)	J
Grade 270, stress-relieved strand or wire	20,000 (138)	0.150
Grade 250, stress-relieved strand or wire	18,500 (128)	0.140
Grade 240 or 235, stress-relieved wire	17,600 (121)	0.130
Grade 270, low-relaxation strand	5,000(34)	0.040
Grade 250, low-relaxation wire	4,630 (32)	0.037
Grade 240 or 235, low-relaxation wire	4,400 (30)	0.035
Grade 145 or 1 60, stress-relieved bar	6,000 (41)	0.050

C.5. Evaluation of Immediate Prestress Losses in Post-tensioned Tie Girders

Immediate prestress losses due to friction, anchorage set, and elastic shortening resulting from sequential post-tensioning of the west tie girder are discussed. Commercially available software is used to calculate friction and anchorage set losses in the tie girder tendons. Elastic shortening losses in each tendon are calculated using the method described in Section C.3.

Tendon forces after accounting for friction losses, anchorage set losses, and elastic shortening are evaluated at the midspan and at the instrumented locations in the west tie girder. These forces are then used to calculate the stresses developed in the tie girder during post-tensioning. Prestress losses due to friction and anchorage set are evaluated only for the west tie girder tendons stressed during PT Stage 1-1 and PT Stage 1-2.

C.5.1. Prestress Losses Due to Friction and Anchorage Set

LARSA 4D was used to calculate prestress losses due to friction and anchorage set in the west tie girder tendons during post-tensioning. Figure C-5 shows the tendon layout in the west tie girder as defined in LARSA 4D. The tie girder was modeled using beam elements with rectangular cross-sections, while the lower knuckles were modeled using beam elements with equivalent rectangular sections.

(a) Elevation view

(b) Plan view

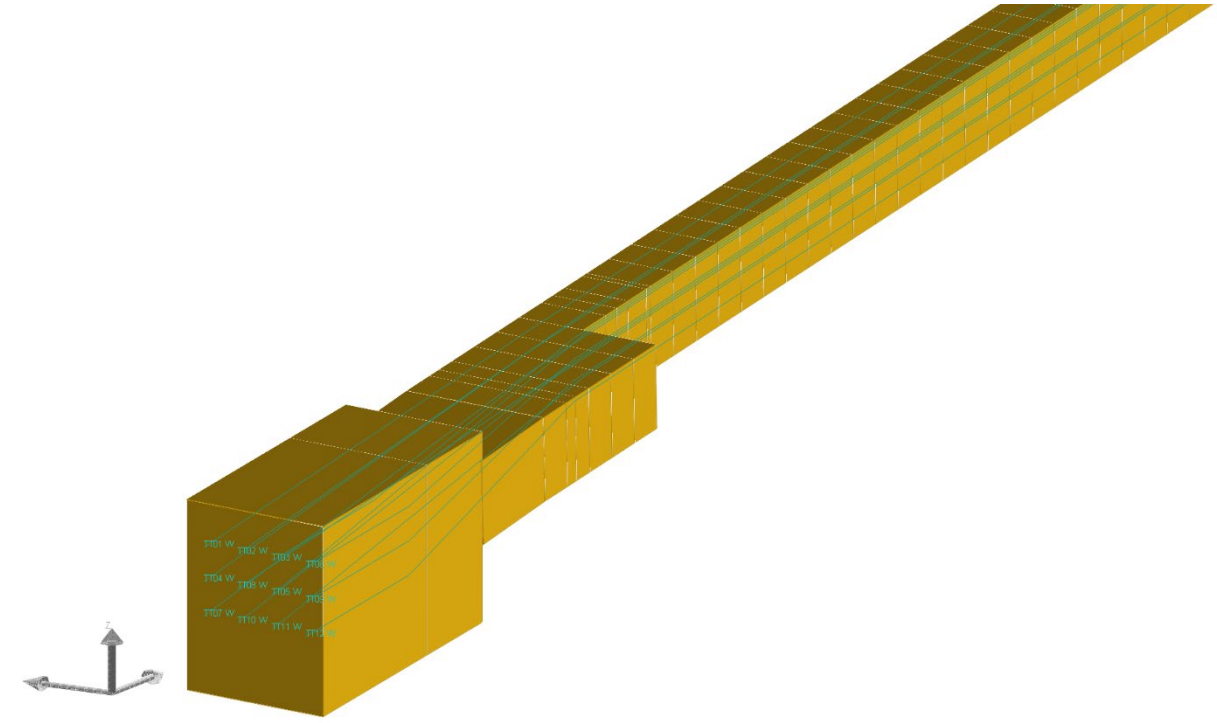

(c) Isometric view (at SW knuckle end)

Figure C-5. Tendon layout defined in LARSA for the west tie girder; (a) Elevation view, (b) Plan view, and (c) Isometric view at SW knuckle.

The *Tendon Geometry* and *Tendon Path* options in LARSA need to be correctly defined when calculating friction and anchorage set losses.

C.5.1.1. Tendon Geometry

The Tendon Geometry window in LARSA 4D is used to define tendon properties, including elastic modulus and cross-sectional area; stressing parameters, such as jacking force and jacking end; friction characteristics, including wobble and curvature friction coefficients; and anchorage set. The input parameters listed in Table C-3 were used to define the tendon geometry. These values correspond to the properties of the prestressing tendons used in the tie girders and the post-tensioning procedures implemented during construction.

Each tendon in the tie girders was stressed with a jacking force of 780 kips. Both tie girders were stressed from one end: the west tie girder from the southwest (SW) knuckle and the east tie girder from the southeast (SE) knuckle. Each tendon consisted of 19 strands installed in the anchorage plate and stressed using hydraulic jacks.

According to ACI Committee 423, an anchorage set of 3/8 in. (0.375 in.) is recommended for tendons stressed using jacks without a power seating device (ACI 2016). ACI Committee 423 also recommends a wobble coefficient ranging from 0.00005/ft to 0.00030/ft and a curvature friction coefficient ranging from 0.10/rad to 0.14/rad for strands in corrugated plastic ducts, similar to those used in the tie girders.

Based on a friction test conducted on a single tendon in the west tie girder (TT08) to determine appropriate friction parameters prior to stressing, a wobble coefficient of 0.0004/ft and a curvature friction coefficient of 0.15/rad were selected for TT08. Because all tendons in the tie girder were similar, the same friction parameters were applied to all tendons.

Table C-3. Input Parameters Used to Define the Tendon Geometry of Tie Girders

Input Parameter in LARSA	Value
Type of Strand	Post-tension (internal)
Prestressing Steel Elastic Modulus (E_{ps}) (ksi)	28,500
Strand Area (per strand) (in.^{2})	0.217
# of Strands	19
Jacking End	Start
Jacking Force @ Start	780 kips
Anchor Set (in.)	0.375 in.
Wobble Coefficient (per ft)	0.0004
Curvature Friction Coefficient (per rad)	0.15
Peak-stress Ratio[1] - Ends	0.7
Peak-stress Ratio[1] - Interior	0.7
[1] - Peak-stress Ratio = Tendon stress/ultimate strength (Typically kept below 0.7)	

C.5.1.2. Tendon Path

The tendon path was defined relative to the geometry of its housing element, namely the tie girder and lower knuckles. Based on the defined tendon path, the curvature of the tendon (α) was calculated. Using the specified tendon geometry and tendon path, the variation of tendon force along the tendon length was computed. LARSA follows the calculation procedures described in Sections C.1 and C.2 to determine friction and anchorage set losses.

Figure C-6a shows the force distribution in tendon TT08, which was stressed during PT Stage 1-1, after accounting for friction and anchorage set losses. For TT08, the force at the stressing end after these losses is 706.17 kips, corresponding to a loss of approximately 73.83 kips (9.5%) from

the initial jacking force of 780 kips. The force at the dead end is 687.01 kips, representing a loss of approximately 92.99 kips (11.9%) relative to the jacking force. Based on the force variation along the tendon length, a maximum tendon force of 742.98 kips occurs at a distance of 102.72 ft from the stressing end. Symmetric localized prestress losses are observed at a distance of 32 ft–8 in. from each end of the tendon. These losses correspond to friction effects associated with changes in the TT08 tendon path (see Figure D-2 for the TT08 tendon layout).

Figure C-6b shows the force distribution in tendons stressed during PT Stage 1-2 after friction and anchorage set losses. Similar to TT08, changes in tendon path result in localized prestress losses. For tendons TT06 and TT09, the tendon paths change at approximately 10 ft and 29 ft–8 in. from each end (see Figure D-2 for the tendon layouts). Consequently, two distinct prestress losses are observed at these locations, as shown in Figure C-6b. Overall, changes in the tendon path in the plan view contributed more significantly to friction losses than changes in the tendon path in the elevation view.

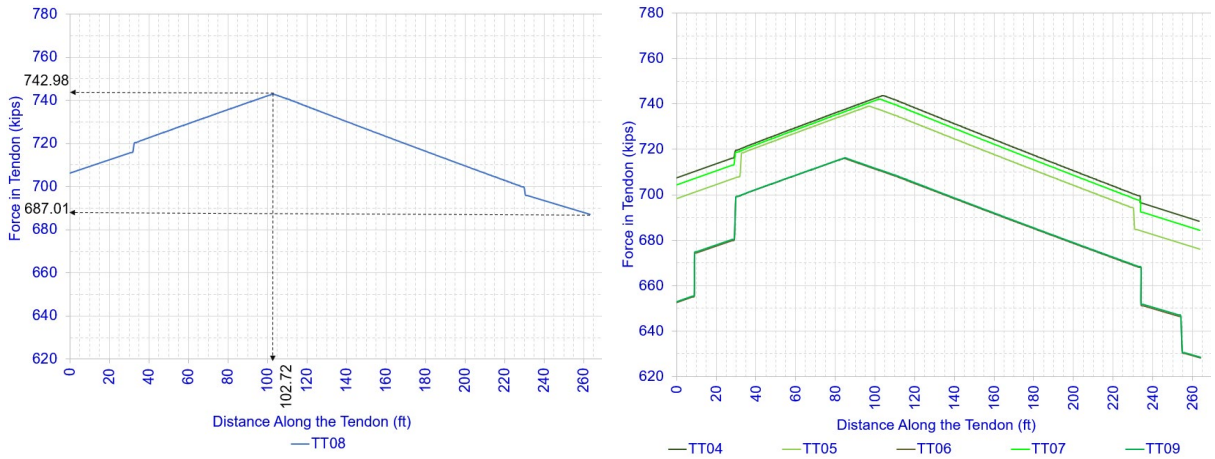

(a) PT Stage 1-1 (b) PT Stage 1-2

Figure C-6. Force variation along the tendon length (a) PT Stage 1-1 and (b) PT Stage 1-2 stressing.

Table C-4 shows the force in the tendons stressed during PT Stage 1-1 and PT Stage 1-2 after friction and anchorage set losses, at selected key locations (stressed end, dead end, and maximum force location).

Table C-4. Force in West Tie Girder Tendons Stressed During PT Stage 1-1 and PT Stage 1-2 After Friction and Anchorage Set Losses

Tendon	Force Before Anchor Set (kips)		Force After Anchor Set (kips)		Friction Loss (kips) (% of Jacking Force)	Anchorage Set Loss (kips) (% of Jacking force)	Maximum Force in Tendon (kips)	Location of the Maximum Force (ft)
	At Stressed End (Jacking Force)	At Dead End	At Stressed End	At Dead End				
TT04	780	688.33	707.37	688.33	11.8	9.3	743.56	103.64
TT05	780	675.97	698.20	675.97	13.3	10.5	739.01	96.64
TT06	780	628.00	652.42	628.00	19.5	16.4	716.07	83.65
TT07	780	684.33	704.26	684.33	12.3	9.7	742.00	102.66
TT08	780	687.01	706.17	687.01	11.9	9.5	742.99	102.66
TT09	780	628.31	652.78	628.31	19.4	16.3	716.37	84.67

C.5.2. Force After Friction and Anchorage Set Losses at Instrumented Locations

Table C-5 summarizes friction and anchorage set losses for tendons stressed during PT Stage 1-1 and PT Stage 1-2 at midspan and at the instrumented locations in the west tie girder (TG-8 and TG-9). The corresponding percentage losses relative to the applied jacking force are also provided.

Table C-5. Friction and Anchorage Set Losses in the West Tie Girder Tendons Stressed During PT Stage 1-1 and PT Stage 1-2

Tendon	Friction and Anchorage Set Losses (kips)			Friction and Anchorage Set Losses (% of Jacking Force)		
	At Midspan	At TG-8	At TG-9	At Midspan	At TG-8	At TG-9
TT04	52.86	55.58	78.36	6.8	7.1	10.0
TT05	52.86	55.58	78.36	6.8	7.1	10.0
TT06	79.25	81.90	103.84	10.2	10.5	13.3
TT07	48.28	51.04	74.05	6.2	6.5	9.5
TT08	47.11	49.87	72.93	6.0	6.4	9.3
TT09	78.95	81.60	103.65	10.1	10.5	13.3

Table C-6 presents the tendon forces after accounting for friction and anchorage set losses for tendons stressed during PT Stage 1-1 and PT Stage 1-2 at midspan and at the instrumented locations in the west tie girder (TG-8 and TG-9).

Table C-6. Tendon Force After Friction and Anchorage Set Losses in the West Tie Girder Tendons Stressed During PT Stage 1-1 and PT Stage 1-2

Tendon	Tendon Force after Friction and Anchorage Set Losses (kips)		
	At Midspan	At TG-8	At TG-9
TT04	727.14	724.42	701.64
TT05	727.14	724.42	701.64
TT06	700.75	698.10	676.16
TT07	731.72	728.96	705.95
TT08	732.89	730.13	707.07
TT09	701.05	698.40	676.35

C.5.3. Average Tendon Force After Friction and Anchorage Set Losses

The average tendon force after friction and anchorage set losses is calculated as the area under the tendon force curve divided by the tendon length. Figure C-7 illustrates the calculation of the average tendon force for tendon TT08 after friction and anchorage set losses. Based on this calculation, an average tendon force of 719.04 kips (174.40 ksi) is obtained for TT08.

Table C-7 summarizes the average tendon forces after friction and anchorage set losses for all 12 tendons and includes the deviation of the average tendon force from the applied jacking force. For TT08, the average tendon force is 7.8% lower than the applied jacking force.

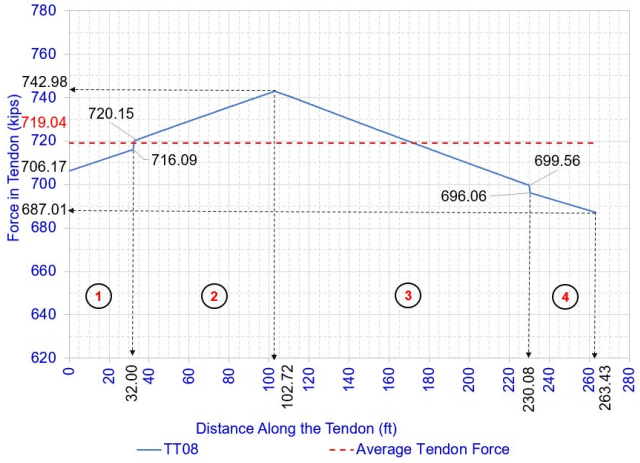

Area of region 1 (kips-ft)	=	0.5×(706.17+716.09)×32.00	=	22756
Area of region 2 (kips-ft)	=	0.5×(720.15 + 742.98)×(102.72-32.00)	=	51736
Area of region 3 (kips-ft)	=	0.5×(742.98+699.56)×(230.08 -102.72)	=	91861
Area of region 4 (kips-ft)	=	0.5×(696.06+687.01)×(263.43 -230.08)	=	23064
Total Area below the tendon force variation curve (kips-ft)	=	22756 + 51736 + 91861 + 23064	=	189417
Average force in TT08 (kips)	=	189417/263.43	=	719.04

Note: Length of TT08 = 263.43 ft Area of a tendon = 4.123 in.^{2}

Figure C-7. Average tendon force calculation for TT08.

Table C-7. Average Tendon Force in the West Tie Girder Tendons Stressed During PT Stage 1-1 and PT Stage 1-2 After Friction and Anchorage Set Losses

Tendon	Average Tendon Force		Deviation From the Jacking Force	
	kips	ksi	kips	%
TT04	719.95	174.62	60.05	7.7
TT05	713.30	173.00	66.70	8.6
TT06	687.09	166.65	92.91	11.9
TT07	717.88	174.12	62.12	8.0
TT08	719.04	174.40	60.96	7.8
TT09	687.46	166.74	92.54	11.9

C.5.4. Prestress Losses Due to Elastic Shortening During Post-tensioning

In this section, elastic shortening losses during the sequential post-tensioning of the tie girders are calculated using Equations (C-8) and (C-9). For these calculations, only the presence of the tie girders was considered. Figure C-8 shows the tie girder cross-section with the tendon layout.

During PT Stage 1-1, tendon TT08 was stressed. During PT Stage 1-2, tendons TT05, TT04, TT09, TT06, and TT07 were stressed in the specified sequence. At PT Stage 1-1, no elastic shortening occurs in TT08 due to its own stressing operation. During PT Stage 1-2, when tendons TT05 through TT07 were stressed, all previously stressed tendons underwent elastic shortening, except for TT07. Consequently, all tendons except TT07 experienced elastic shortening due to post-tensioning prior to the bridge move. However, only TT08 was grouted before PT Stage 1-2. Accordingly, the elastic shortening loss in TT08 was calculated using Equation (C-8), while the elastic shortening losses in TT05, TT04, TT09, and TT06 were calculated using Equation (C-9).

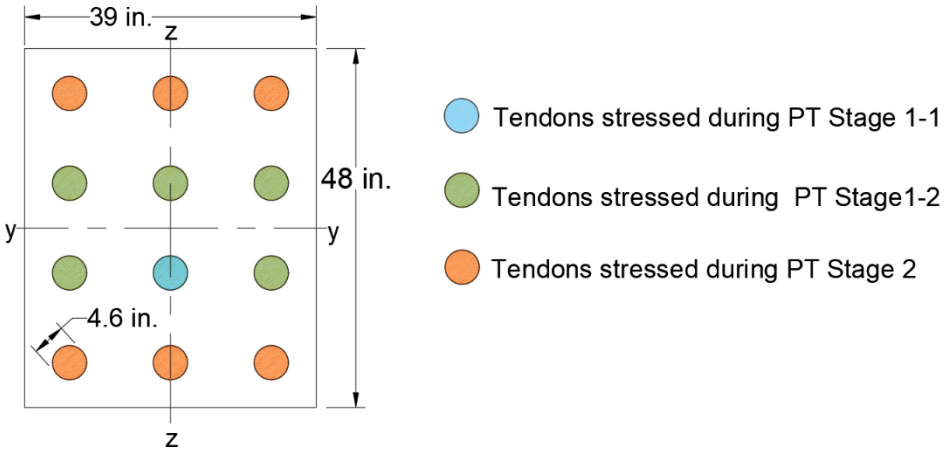

Figure C-8. Tendons stressed during post-tensioning stages.

Table C-8 summarizes the section and material properties of the tie girders used for each post-tensioning stage. The net section area of the tie girder was 1,672.57 in² at PT Stage 1-1. At PT Stage 1-2, the net section area was updated to 1,689.19 in² to account for grouting of TT08. Accordingly, a concrete area of 1,689.19 in² was used in the elastic shortening loss calculations for PT Stage 1-2. The elastic moduli measured from 4 × 8 in. concrete cylinders at the post-tensioning ages were used to calculate the modular ratio (see Appendix E). The elastic modulus of the prestressing steel was taken as 28,500 ksi.

The level of prestress in the j^{th} tendon at the time the $(j+1)^{th}$ tendon was stressed was assumed to be equal to the tendon stress after accounting for friction and anchorage set losses, without

consideration of time-dependent losses. For example, the tendon force in TT08 at midspan was taken as 732.89 kips (see Table C-6) when calculating the elastic shortening loss in TT08 due to stressing of TT05. This force reflects only friction and anchorage set losses and does not account for time-dependent losses occurring in TT08 between PT Stages 1-1 and 1-2.

Table C-8. Tie Girder Section Properties and Material Properties Used in the Elastic Shortening Calculations

Girder Section Property	During PT Stage 1-1	During PT Stage 1-2
Net area of concrete, A_c (in.^{2})	1672.57	1689.19
Net moment of inertia, I_{yy} (in.^{4})	323263.16	323883.43
Net moment of inertia, I_{zz} (in.^{4})	212781.72	212806.70
Radius of gyration, r_{yy} (in.^{4})	13.90	13.85
Radius of gyration, r_{zz} (in.^{4})	11.28	11.22
Centroid of the net section about y-y axis (measured from the girder bottom), (in.)	24	23.95
Centroid of the net section about z-z axis (measured from the girder right edge), $\bar{y}$ (in.)	19.5	19.5
Elastic modulus of concrete (West tie girder)[1], E_c (ksi)	NA[2]	6406.190
Modular ratio (West tie girder)	NA[2]	4.45

[1] – See Appendix E.
[2] - Only TT08 was stressed at PT Stage 1-1. Therefore, no elastic shortening losses were calculated at PT Stage 1-1. No elastic shortening losses were calculated after PT Stage 2.

APPENDIX D

GEOMETRY AND DETAILS OF THE POST-TENSIONED MEMBERS

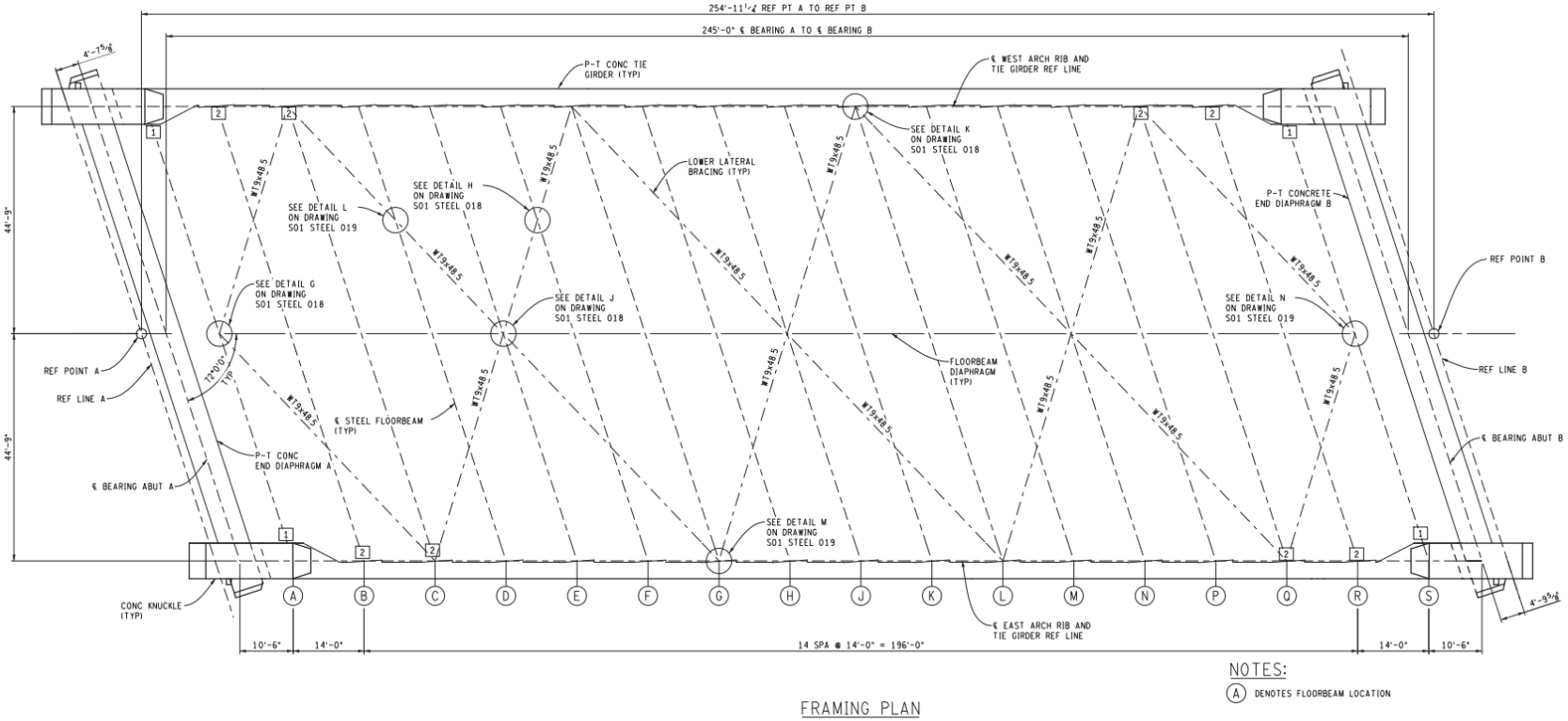

Figure D-1. Framing plan of the 2nd Avenue Bridge.

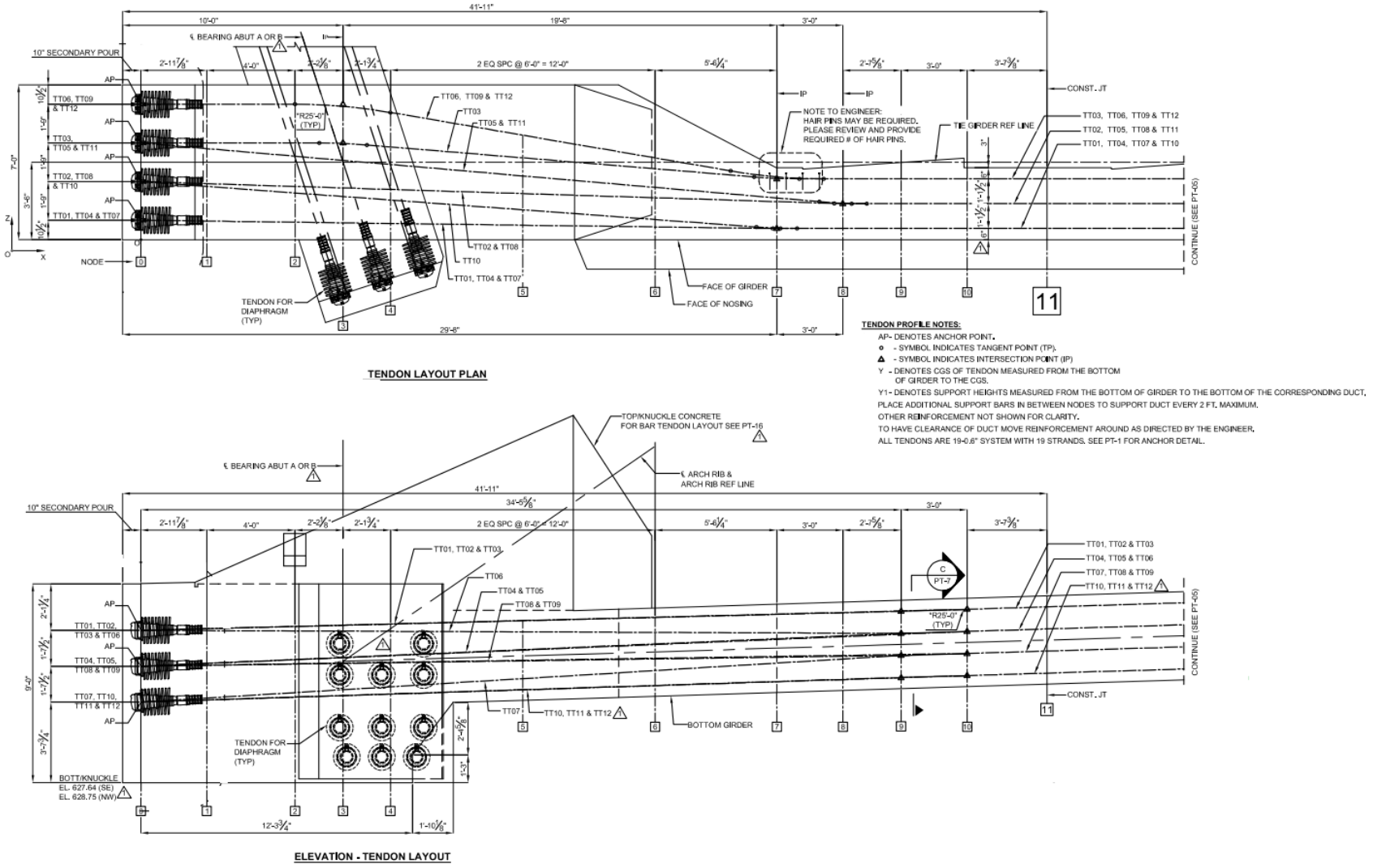

Figure D-2. Tie girder and knuckles -Tendon layout.

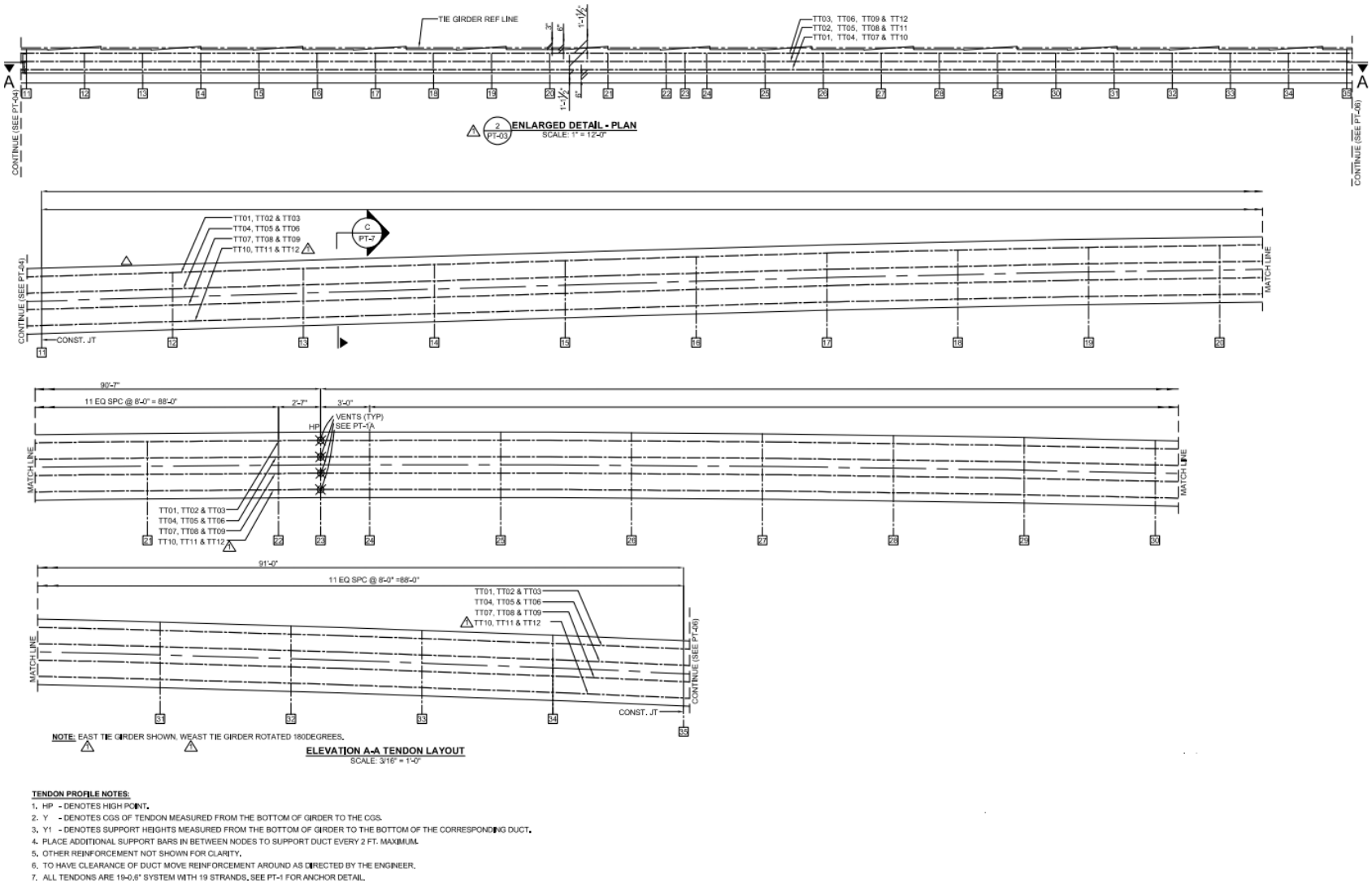

TENDON PROFILE NOTES:

1. HP - DENOTES HIGH POINT.
2. Y - DENOTES CGS OF TENDON MEASURED FROM THE BOTTOM OF GIRDER TO THE CGS.
3. Y1 - DENOTES SUPPORT HEIGHTS MEASURED FROM THE BOTTOM OF GIRDER TO THE BOTTOM OF THE CORRESPONDING DUCT.
4. PLACE ADDITIONAL SUPPORT BARS IN BETWEEN NODES TO SUPPORT DUCT EVERY 2 FT. MAXIMUM.
5. OTHER REINFORCEMENT NOT SHOWN FOR CLARITY.
6. TO HAVE CLEARANCE OF DUCT MOVE REINFORCEMENT AROUND AS DIRECTED BY THE ENGINEER.
7. ALL TENDONS ARE 19-0.6" SYSTEM WITH 19 STRANDS. SEE PT-1 FOR ANCHOR DETAIL.

Figure D-2. Tie girder and knuckles -Tendon layout (cont.).

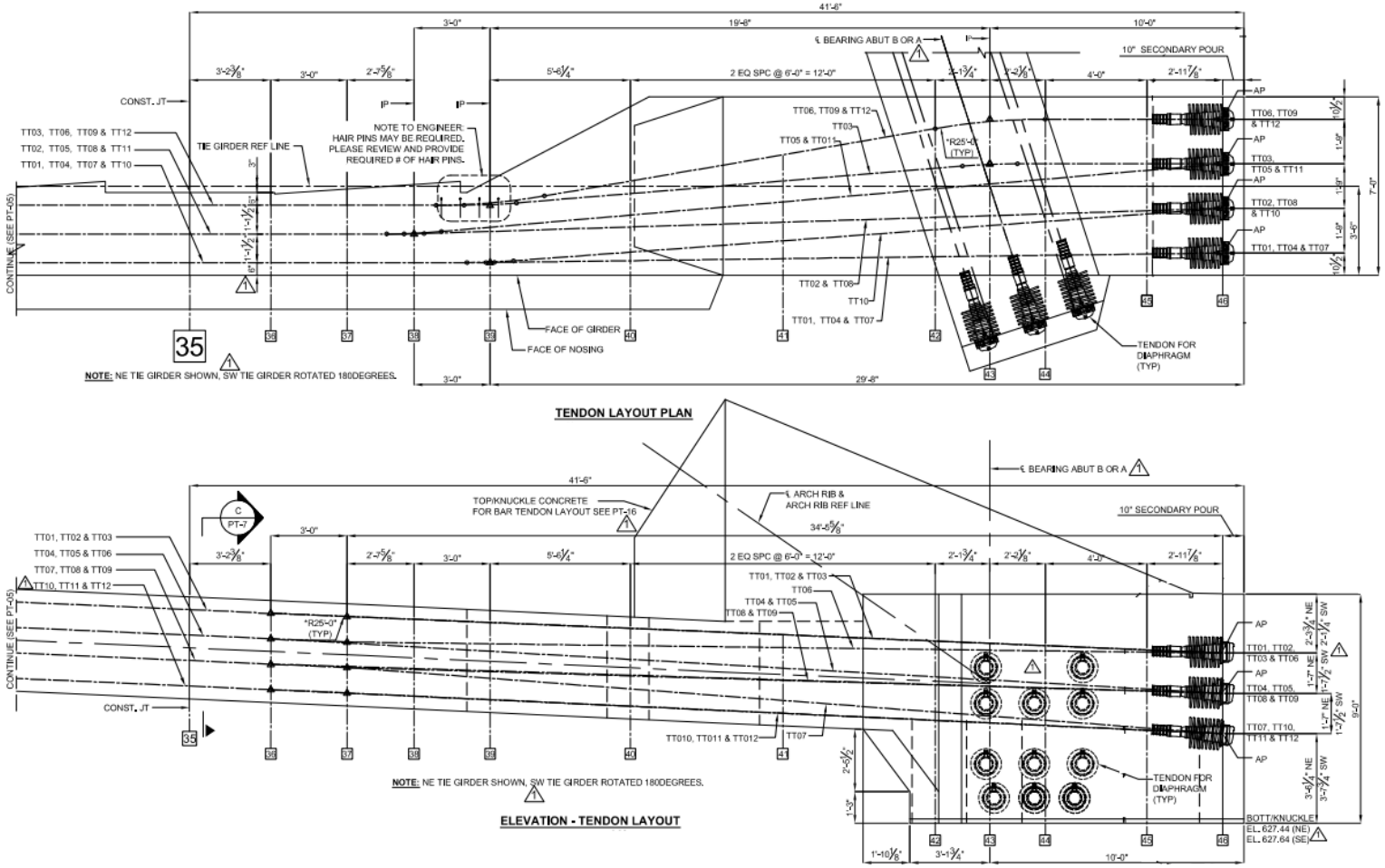

TENDON PROFILE NOTES:

1. AP- DENOTES ANCHOR POINT.
2. ⊙ - SYMBOL INDICATES TANGENT POINT (TP).
3. ⊠ - SYMBOL INDICATES INTERSECTION POINT (IP)
4. Y - DENOTES CGS OF TENDON MEASURED FROM THE BOTTOM OF GIRDER TO THE CGS.
5. Y1- DENOTES SUPPORT HEIGHTS MEASURED FROM THE BOTTOM OF GIRDER TO THE BOTTOM OF THE CORRESPONDING DUCT.
6. PLACE ADDITIONAL SUPPORT BARS IN BETWEEN NODES TO SUPPORT DUCT EVERY 2 FT. MAXIMUM.
7. OTHER REINFORCEMENT NOT SHOWN FOR CLARITY.
8. TO HAVE CLEARANCE OF DUCT MOVE REINFORCEMENT AROUND AS DIRECTED BY THE ENGINEER.
9. ALL TENDONS ARE 19-0.6" SYSTEM WITH 19 STRANDS, SEE PT-1 FOR ANCHOR DETAIL.

Figure D-2. Tie girder and knuckles -Tendon layout (cont.).

APPENDIX E

MATERIAL TEST DATA

E.1 Fresh Concrete Properties of the Mix Used in Post-tensioned Members

Table E.1 and Table E.2 show the fresh concrete properties measured by MDOT and Z-contractors during the casting of tie girders, end diaphragms, and knuckles.

Table E.-1. Fresh Concrete Properties of the Mix Used in Post-tensioned Members as Measured by MDOT

Section	Slump flow (in.)	Air content (%)	Concrete temp (^{0} F)	Air temp (^{0} F)
West tie girder	21	7.1	51	32
	17	7.1	54	32
East tie girder	22.5	7	51	33
	24.5	6.3	51	36
North diaphragm	22	5.3	68	70
	23.5	5.1	69	71
	24.5	5.7	68	72
South diaphragm	24	5.2	61	60
	25	6.6	62	63
	22	6.2	65	67
Lower SW knuckle	23.5	5.3	53	50
Upper SW knuckle	22.5	6.3	58	48
Lower SE knuckle	26.5	6	58	45
	23	7.8	59	43
Upper SE knuckle	24.5	6.4	54	27
Lower NW knuckle	24	6.8	51	43
Upper NW knuckle	22	5.8	59	41
Lower NE knuckle	24.5	5.8	59	52
	18	7.3	59	54
Upper NE knuckle	18.5	5.7	59	39

Table E-2. Fresh Concrete Properties of the Mix Used in Post-tensioned Members as Measured by Z-Contractors

Section	Truck ID	Pump	Air content (%)	Concrete temp (^{0}F)	Spread (in.)	J Ring (in.)	Rapid (mm)	Notes
West tie girder	1	Before	6.4	51	22	20	2	-
		After	7.5	-	-	-	-	-
	3	Before	7.6	51	-	-	-	-
		After	7	-	-	-	-	
East tie girder	1	Before	5.5/4.5	50	19.5	18.5	2	AEA added
		After	5.5	-	-	-	-	-
	2	Before	6/4.5	50	21	19.5	2	AEA added
		After	6	-	-	-	-	-
	3	Before	5/5.5	-	-	-	-	AEA added
		After	-	-	-	-	-	-
	4	Before	6.8	-	-	-	-	-
		After	-	-	-	-	-	-
	5	Before	-	-	20	-	-	-
		After	-	-	-	-	-	-
	8	Before	5.5	50	21.5	20.5	2	-
		After	-	-	-	-	-	-
North Diaphragm	15	Before	6.9	60	21.5	20	1	-
		After	6.8	-	-	-	-	-
	16	Before	6.7	-	-	-	-	-
		After	6.1	-	-	-	-	-
	22	Before	6.2	65	22.5	21	1	-
		After	-	-	-	-	-	-
	26	Before	6.7	67	22	19	1	-
		After	-	-	-	-	-	-

Table E-2. Fresh Concrete Properties of the Mix Used in Post-tensioned Members as Measured by Z-Contractors

Section	Truck ID	Pump	Air content (%)	Concrete temp (^{0}F)	Spread (in.)	J Ring (in.)	Rapid (mm)	Notes
South Diaphragm	1	Before	5.2	60	24.5	24	4	-
		After	6	-		-	-	-
	2	Before	5.9	59	24.5	-	-	-
		After	5.7	-	-	-	-	-
	7	Before	7	59	24.5	24	5	-
		After	-	-	-	-	-	-
	11	Before	6.8	-	24	22	3	-
		After	-	-	-	-	-	-
Lower SW Knuckle	1	Before	5.8	60	22	22	3	-
		After	6.8		21.5	21	1	-
	2	Before	6	55	23	22.5		-
	3	Before	7.1	55	20.5	20	1	-
	7	Before	8	56	21	21	2	-
Lower SE Knuckle	1	Before	6.8	56	24.5	25	7	-
	2	Before	7.5	56	24	25	10	-
	3	Before	6.3	57	-	-	-	-
	4	Before	7	-	24	24.5	5	-
	5	Before	7	56	24	23.5	6	-
Lower NW Knuckle	1	Before	7.7	54	20	20	1	-
		After	6.1	-	-	-	-	-
	3	Before	6.5	51	23	22	4	-
		After	5.9	-	-	-	-	-
	5	Before	6.2	53	22	22	2	-
Upper NW Knuckle	1	Before	5.8	52	22	20.5	3	-
		After	6.5	-	-	-	-	-
	2	Before	-	-	23	-	-	-
	3	Before	7.9	52	24	23	4	-

Table E-2. Fresh Concrete Properties of the Mix Used in Post-tensioned Members as Measured by Z-Contractors

Section	Truck ID	Pump	Air content (%)	Concrete temp (^{0}F)	Spread (in.)	J Ring (in.)	Rapid (mm)	Notes
Lower NE Knuckle	1	Before	5.9	59	21	19	4	-
		After	6.8	-	-	-	-	-
	3	Before	6.6	59	21.5	21.5	2	-
		After	5.8	-	-	-	-	-
	6	Before	7.2	59	18	16	0	-
Upper NE Knuckle	1	Before	6.1	57	19.5	18	2	-
		After	5.4	-	-	-	-	-
	2	Before	7.6	54	18	16.5	2	-

E.2. Compressive Strength of the Mix Used in Post-tensioned Members

Table E.3. shows the compressive strength of cylinders fabricated and cured under the laboratory experimental program at WMU.

Table E-3. Compressive Strength of the Mix Used in Post-tensioned Members as Measured by WMU

Cylinder Set	Age (days)	Compressive Strength of 4×8 in. Cylinders (psi)			Mean Compressive Strength (psi)	Standard Deviation (psi)	COV (%)
		1	2	3			
Set 0 (ASTM)	7	7410	7350	7210	7323	84	1.14
	28	10970	11090	9710	10590	624	5.89
Set 1 (ASTM)	7	6370	6340	6440	6383	42	0.66
	28	11290	11210	10620	11040	299	2.71
	68	12580	11680	12670	12310	447	3.63
	168	8650	10050	-	9350[1]	700	7.49
	284	18940	21200	-	20070	1130	5.63
Set 1 (ASTM+ Laboratory)	28	11690	11200	10800	11230	364	3.24
	68	12480	11680	11580	11913	403	3.38
	168	11580	10790	-	11185	395	3.53
	284	11440	12660	12520	12207	545	4.47
Set 2 (Field)	22	5370	5720	6360	5817	410	7.05
	29	6150	6080	6220	6150	57	0.93
	68	8740	8500	8600	8613	98	1.14
Set 4 (Laboratory)	7	7580	7260	7620	7487	161	2.15
	14	9260	9810	9720	9597	241	2.51
	21	10180	10510	9760	10150	307	3.02
	28	10040	-	-	10040	-	-
	47	11350	11250	11320	11307	42	0.37
	56	11570	11180	11490	11413	168	1.47
	147	12530	11890	11720	12047	349	2.89
	263	12520	11760	-	12140	380	3.13

COV – Coefficient of variation

[1] – The test results are questionable. These results will not be used in any calculations.

Table E.4 and Table E.5 show the compressive strength of cylinders tested by MDOT and Z-Contractors, respectively.

Table E-4. Compressive Strength of the Mix Used in Post-tensioned Members as Measured by MDOT

Section	Age (days)	Compressive Strength (psi)						Mean Compressive Strength (psi)	Standard Deviation (psi)	COV (%)
		Cylinder 1	Cylinder 2	Cylinder 3	Cylinder 4	Cylinder 5	Cylinder 6			
West Tie Girder	7	5530	5170	5840	5910	-	-	5613	293	5.22
	14	8100	8260	8780	8940	-	-	8380	376	4.49
	28	9970	9730	11220	10010	-	-	10307	585	5.67
	56	11970	11370	12530	13150	-	-	11957	724	6.06
East Tie Girder	7	5680	5940	5690	5690	-	-	5770	112	1.93
	14	8480	8510	8290	8170	-	-	8427	154	1.82
	28	10410	9960	10020	10110	-	-	10130	173	1.71
	56	11640	12060	11770	11640	-	-	11823	178	1.50
South Diaphragm	7	8150	8020	7520	7620	8130	8160	7933	263	3.31
	14	10570	11140	10050	10170	10990	10880	10633	409	3.85
	28	12670	12640	11620	11870	12730	13030	12427	504	4.05
	56	14970	15750	13810	14560	15150	14420	14777	610	4.13
North Diaphragm	7	8400	8610	7710	7730	6840	7080	7728	637	8.25
	14	11050	11280	10300	10620	9630	10070	10492	564	5.37
	28	13280	13070	12670	12900	12640	11980	12757	412	3.23
	56	14670	15230	14700	16020	15170	14890	15113	458	3.03
Lower SW Knuckle	7	7160	7200	-	-	-	-	7180	20	0.28
	14	-	-	-	-	-	-	-	-	-
	28	11410	11500	-	-	-	-	11455	45	0.39
	56	12540	12600	-	-	-	-	12570	30	0.24
Upper SW Knuckle	7	4940	4710	-	-	-	-	4825	115	2.38
	14	7090	7170	-	-	-	-	7130	40	0.56
	28	9640	9640	-	-	-	-	9640	0	0.00
	56	12190	11950	-	-	-	-	12070	120	0.99
Lower SE Knuckle	7	5880	5690	5800	5700	-	-	5768	78	1.35
	14	-	-	-	-	-	-	-	-	-
	28	10430	10760	10120	10030	-	-	10335	287	2.77
	56	11330	11180	11100	11110	-	-	11180	92	0.82

Table E-4. Compressive Strength of the Mix Used in Post-tensioned Members as Measured by MDOT

Section	Age (days)	Compressive Strength (psi)						Mean Compressive Strength (psi)	Standard Deviation (psi)	COV (%)
		Cylinder 1	Cylinder 2	Cylinder 3	Cylinder 4	Cylinder 5	Cylinder 6			
Upper SE Knuckle	7	5650	5540	-	-	-	-	5595	55	0.98
	14	8090	8160	-	-	-	-	8125	35	0.43
	28	10110	9950	-	-	-	-	10030	80	0.80
	56	11410	12570	-	-	-	-	11990	580	4.84
Lower NW Knuckle	7	5460	5560	-	-	-	-	5510	50	0.91
	14	-	-	-	-	-	-	-	-	-
	28	9810	9770	-	-	-	-	9790	20	0.20
	56	11260	10870	-	-	-	-	11065	195	1.76
Upper NW Knuckle	7	5760	6040	-	-	-	-	5900	140	2.37
	14	8840	9300	-	-	-	-	9070	230	2.54
	28	11920	12540	-	-	-	-	12230	310	2.53
	56	12500	13080	-	-	-	-	12790	290	2.27
Lower NE Knuckle	7	6550	6320	6450	6460	-	-	6445	82	1.27
	14	-	-	-	-	-	-	-	-	-
	28	11000	11010	11020	10530	-	-	10890	208	1.91
	56	12800	12700	12380	11840	-	-	12430	374	3.01
Upper NE Knuckle	7	6240	5720	-	-	-	-	5980	260	4.35
	14	9240	9110	-	-	-	-	9175	65	0.71
	28	10910	10990	-	-	-	-	10950	40	0.37
	56	12790	13430	-	-	-	-	13110	320	2.44

Table E-5. Compressive Strength of the Mix Used in Post-tensioned Members as Measured by Z Contractors

Section	Age (days)	Compressive Strength (psi)						Mean Compressive Strength (psi)	Standard Deviation (psi)	COV (%)
		Cylinder 1	Cylinder 2	Cylinder 3	Cylinder 4	Cylinder 5	Cylinder 6			
West Tie Girder	7	5400	5420	6350	5360	-	-	5633	415	7.36
	14	-	-	-	-	-	-	-	-	-
	28	9150	9640	10600	10790	-	-	10045	676	6.73
	56	10140	10390	11970	12100	-	-	11150	891	7.99
East Tie Girder	7	5360	5530	6330	6360	-	-	5895	454	7.70
	14	-	-	-	-	-	-	-	-	-
	28	10670	10840	12110	11800	-	-	11355	613	5.40
	56	10810	10890	11990	12010	-	-	11425	576	5.04
South Diaphragm	7	7180	7170	7090	6760	7390	7650	7207	272	3.78
	14	-	-	-	-	-	-	-	-	-
	28	8340	8450	13540	12630	14040	14290	11882	2520	21.21
	56	9740	9510	14450	13720	14510	14690	12770	2245	17.58
North Diaphragm	7	7290	7420	7430	7420	6250	6310	7020	526	7.49
	14	-	-	-	-	-	-	-	-	-
	28	13020	12680	10580	10770	11710	12450	11868	932	7.86
	56	13980	14880	13500	14630	13340	14130	14077	554	3.93
Lower SW Knuckle	7	6490	6700	7230	7080	6030	6030	6593	465	7.06
	14	-	-	-	-	-	-	-	-	-
	28	11423	11576	11869	11813	10423	10597	11284	569	5.04
	56	-	-	-	-	-	-	-	-	-
Upper SW Knuckle	7	6840	6700	6450	6070	-	-	6515	292	4.49
	14	-	-	-	-	-	-	-	-	-
	28	11610	11350	11160	11350	-	-	11368	160	1.41
	56	11850	11660	11950	12110	-	-	11893	163	1.37
Lower SE Knuckle	7	4710	4740	5030	4920	5480	5620	5083	349	6.87
	14	-	-	-	-	-	-	-	-	-
	28	9543	9595	9943	9780	10260	10320	9907	301	3.04
	56	-	-	-	-	-	-	-	-	-

Table E-5. Compressive Strength of the Mix Used in Post-tensioned Members as Measured by Z Contractors

Section	Age (days)	Compressive Strength (psi)						Mean Compressive Strength (psi)	Standard Deviation (psi)	COV (%)
		Cylinder 1	Cylinder 2	Cylinder 3	Cylinder 4	Cylinder 5	Cylinder 6			
Upper SE Knuckle	7	6580	6480	6680	6610	-	-	6588	72	1.09
	14	-	-	-	-	-	-	-	-	-
	28	11170	11280	11560	11370	-	-	11345	143	1.26
	56	-	-	-	-	-	-	-	-	-
Lower NW Knuckle	7	5556	5480	5631	5551	6023	6033	5712	227	3.98
	14	-	-	-	-	-	-	-	-	-
	28	10560	10680	10650	10640	10840	11000	10728	148	1.38
	56	11180	11240	11480	11670	11610	11660	11473	197	1.72
Upper NW Knuckle	7	5370	5560	5120	-	-	-	5350	180	3.37
	14	-	-	-	-	-	-	-	-	-
	28	10600	10530	9380	9240	-	-	9938	630	6.34
	56	12280	12010	10550	10780	-	-	11405	751	6.58
Lower NE Knuckle	7	5918	6050	6210	6250	6119	6269	6136	123	2.01
	14	-	-	-	-	-	-	-	-	-
	28	11449	11646	11581	11734	11519	11554	11581	91	0.79
	56	-	-	-	-	-	-	-	-	-
Upper NE Knuckle	7	6335	6230	6590	6540	-	-	6424	147	2.29
	14	-	-	-	-	-	-	-	-	-
	28	9600	9750	10480	10450	-	-	10070	399	3.96
	56	11560	11610	11870	11850	-	-	11723	139	1.18

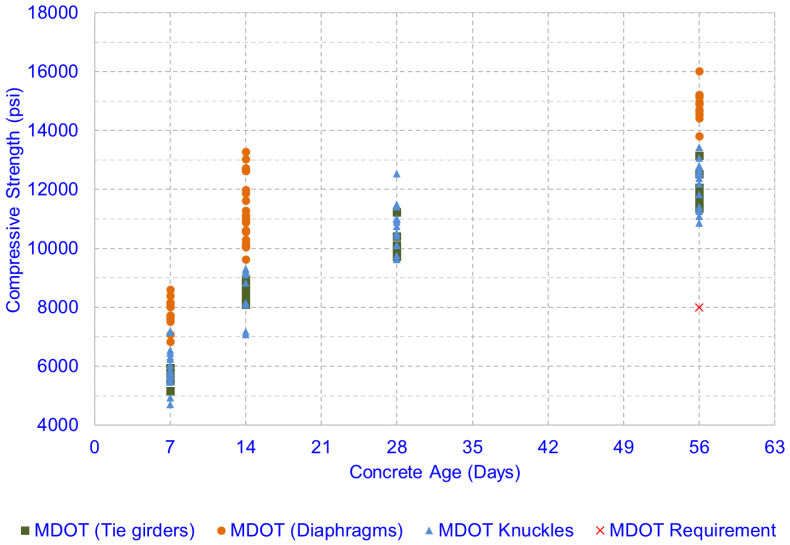

Figure E-1. Compressive strength of the mix used in post-tensioned members as measured by MDOT.

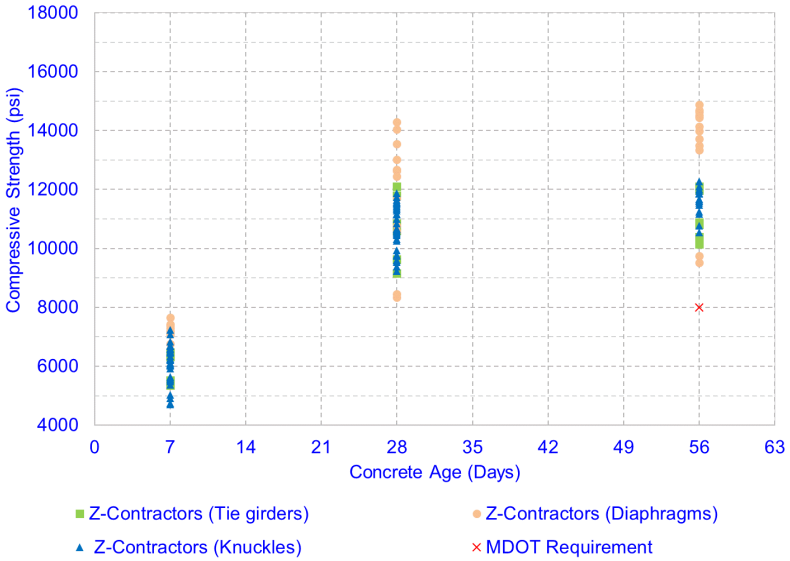

Figure E-2. Compressive strength of the mix used in post-tensioned members as measured by Z-Contractors.

E.3. Static Modulus of Elasticity (MOE) of the Mix Used in Post-tensioned Members as Measured by WMU

Table E.6 shows the MOE and Poisson's ratio of cylinders fabricated and cured under the laboratory experimental program at WMU.

Table E-6. Static Modulus of Elasticity (MOE) and Poisson's Ratio of the Mix Used in Post-tensioned Members as Measured by WMU

Cylinder Set	Age (days)	MOE of 4×8 in. Cylinders (ksi)			Average MOE (ksi)	Standard Deviation (psi)	COV (%)	Poisson's Ratio of 4×8 in. Cylinders		Average Poisson's Ratio
		1	2	3				1	2	
Set 0 (ASTM)	7	6472	5834	-	6153[1]	319	5.19	0.23	0.21	0.22
	28	7087	7026	-	7056	31	0.44	0.22	0.22	0.22
Set 1 (ASTM)	7	5642	5327	-	5484	157	2.87	0.21	0.19	0.20
	28	7020	6979	-	6999	21	0.29	0.22	0.21	0.22
	68	7274	7473	-	7373	99	1.35	-[2]	-[2]	-[2]
	168	7078	7078	7104	7086	12	0.17	-[2]	-[2]	-[2]
	284	7575	7406	-	7490	84	1.13	-[2]	-[2]	-[2]
Set 1 (ASTM+ Laboratory)	7	5642	5327	-	5484	157	2.87	0.21	0.19	0.20
	28	6082	6204	-	6143	61	0.99	0.21	0.21	0.21
	68	6304	6251	-	6278	26	0.42	-[2]	-[2]	-[2]
	170	6463	6349	-	6406	57	0.89	-[2]	-[2]	-[2]
	284	6510	6573	-	6542	32	0.48	-[2]	-[2]	-[2]
Set 2 (Field)	22	5597	6225	-	5911[1]	314	5.31	0.22	0.22	0.22
	30	5436	5216	-	5326	110	2.07	0.20	0.19	0.20
	68	5826	5876	-	5851	25	0.42	-[2]	-[2]	-[2]
	170	6886	7299	-	7093	207	2.91	-[2]	-[2]	-[2]
Set 4 (Laboratory)	7	5863	6051	-	5957	94	1.58	0.20	0.20	0.20
	14	6445	6398	-	6422	24	0.37	0.22	0.21	0.22
	21	6824	6150	-	6487[1]	337	5.20	0.22	0.21	0.22
	47	6524	6893	-	6708	185	2.75	-[2]	-[2]	-[2]
	56	6996	6985	-	6990	6	0.08	-[2]	-[2]	-[2]
	149	7497	7346	-	7422	75	1.02	-[2]	-[2]	-[2]
	263	7260	7415	-	7338	77	1.05	-[2]	-[2]	-[2]

COV – Coefficient of variation
[1] – The test results were not within 5% of the average.
[2] – The Poisson's ratio was not measured after 30 days of concrete age due to channel failure in the testing machine.

APPENDIX F

TRUCKLOAD CONFIGURATIONS USED FOR LOAD TESTING

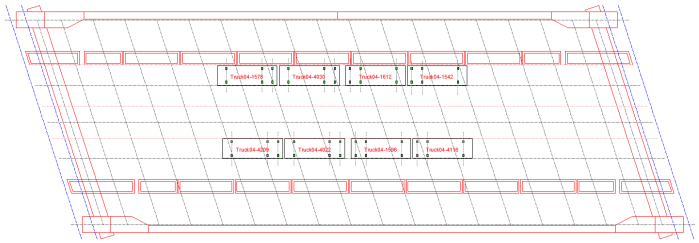

(a) Truckload configuration 1 for TG-2, -3, -4, -6, -8, and -9, EM-SM-2, and -7, and WH-SM-7

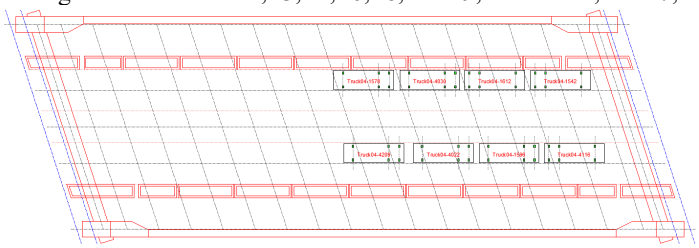

(b) Truckload configuration 2 for TG-10

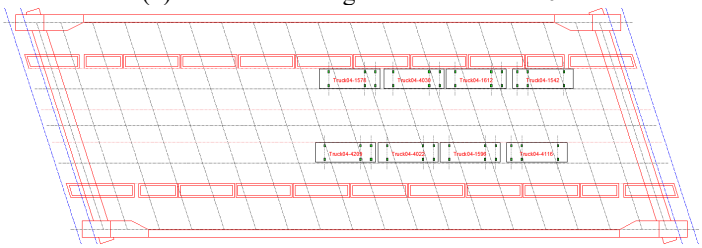

(c) Truckload configuration 3 for WH-SM-4, -6, -8

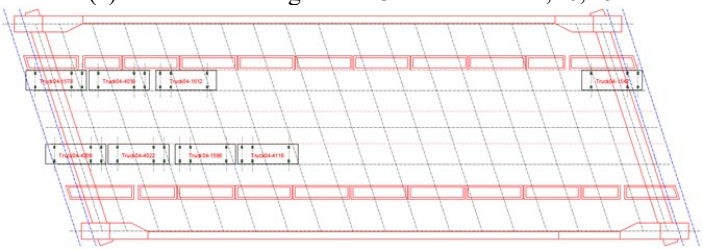

(d) Truckload configuration 4 for WH-SM-2

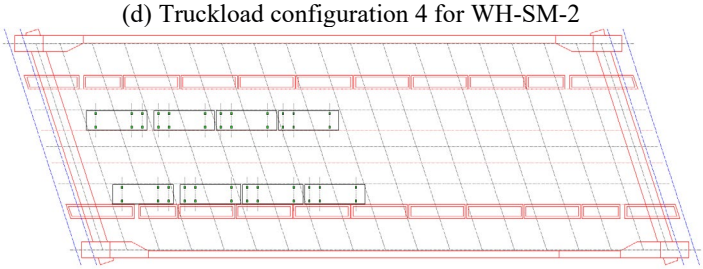

(e) Truckload configuration 5 for TG-1

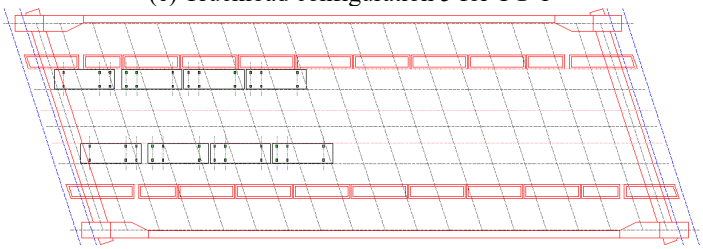

(f) Truckload configuration 6 for TG-7

Figure F-1. Truckload configurations used during the load testing.

APPENDIX G

THERMAL MONITORING DATA

G.1 Thermal Monitoring Data in the Lower Southwest (SW) Knuckle

Figure G-1 shows the temperature and the temperature difference measured in the lower part of the SW knuckle. The maximum temperature is less than 150° F, and the maximum temperature difference is less than 35° F.

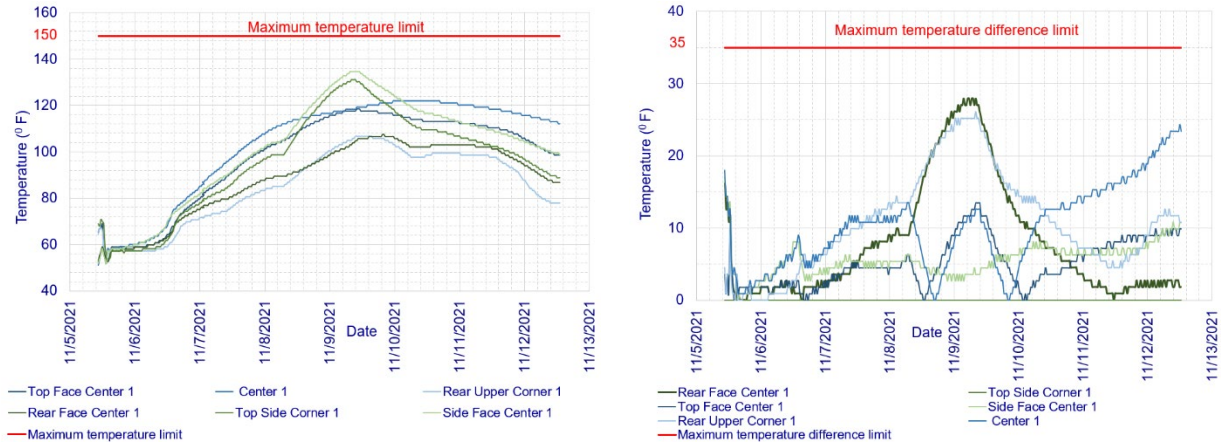

(a) Temperature (b) Temperature difference

Figure G-1. (a) Temperature and (b) temperature difference.

G.2 Thermal Monitoring Data in the Upper Southwest (SW) Knuckle

Figure G-2 shows the temperature and the temperature difference measured in the upper part of the SW knuckle. The temperature data recorded using VWGs at TG-6 is also shown. The maximum temperature is less than 150° F, and the maximum temperature difference is less than 35° F.

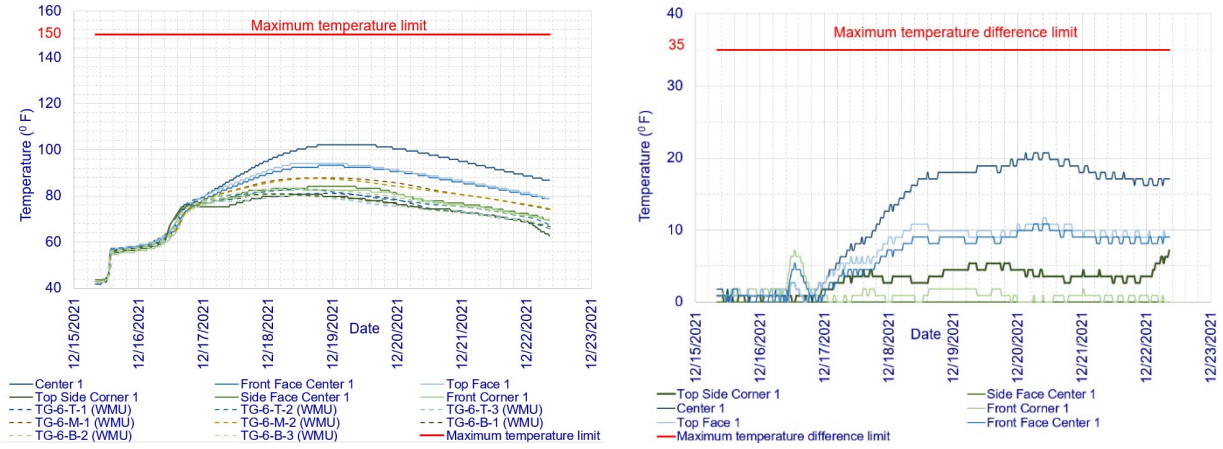

(a) Temperature (b) Temperature difference

Figure G-2. (a) Temperature and (b) temperature difference.

G.3 Thermal Monitoring Data in the Lower Northwest (NW) Knuckle

Figure G-3 shows the temperature and the temperature difference measured in the lower part of the NW knuckle. The maximum temperature is less than 150° F, and the maximum temperature difference is less than 35° F.

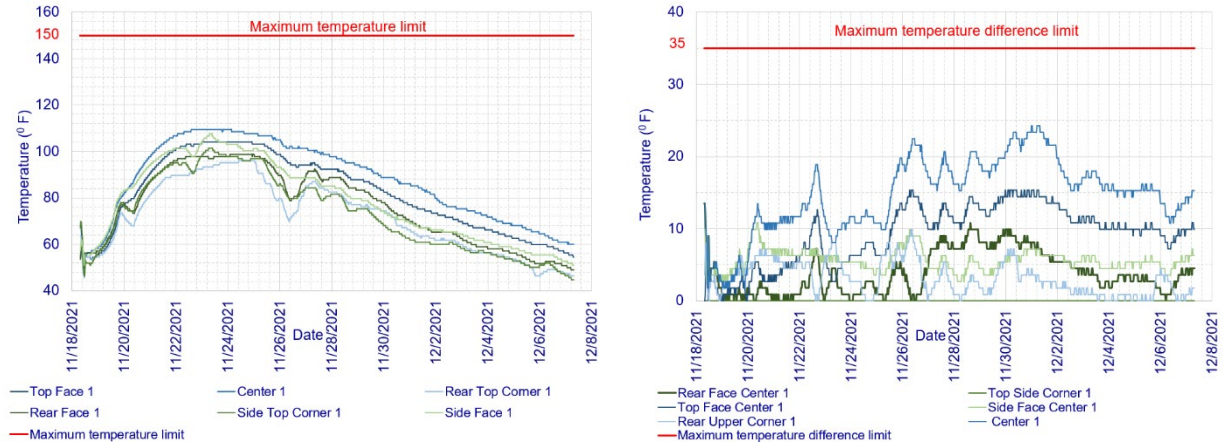

(a) Temperature (b) Temperature difference

Figure G-3. (a) Temperature and (b) temperature difference.

G.4 Thermal Monitoring Data in the Upper Northwest (NW) Knuckle

Figure G-4 shows the temperature and temperature difference measured in the upper part of the NW knuckle. Temperature data recorded using VWGs at TG-10 are also shown. The maximum temperature measured is less than 150° F, and the maximum temperature difference is less than 35° F.

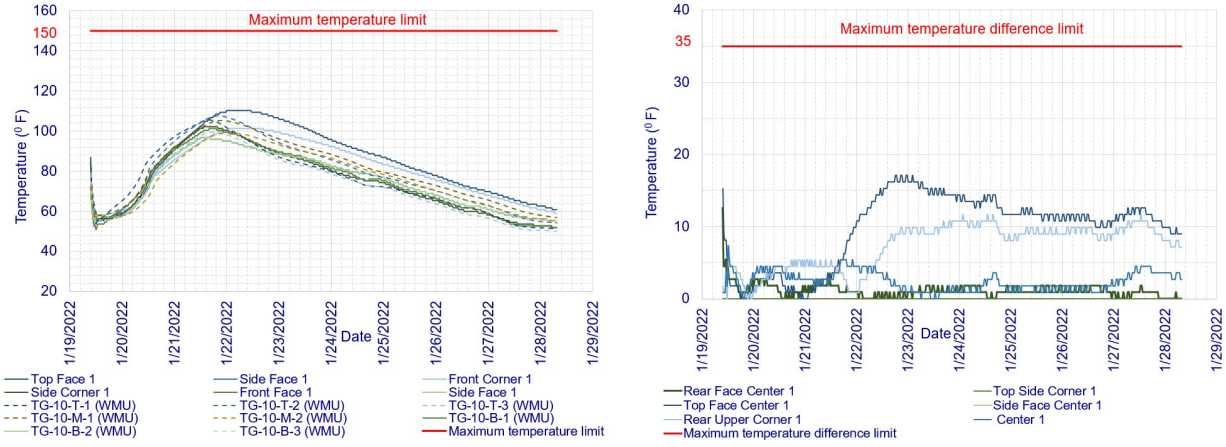

(a) Temperature (b) Temperature difference

Figure G-4. (a) Temperature and (b) temperature difference.

G.5 Thermal Monitoring Data in the Lower Southeast (SE) Knuckle

Figure G-5 shows the temperature and temperature difference measured in the lower part of the SE knuckle. The maximum temperature measured is less than 150° F. The maximum temperature difference is less than 35° F, except at the lower SE knuckle, where the temperature difference briefly exceeded the limit and reached 37° F.

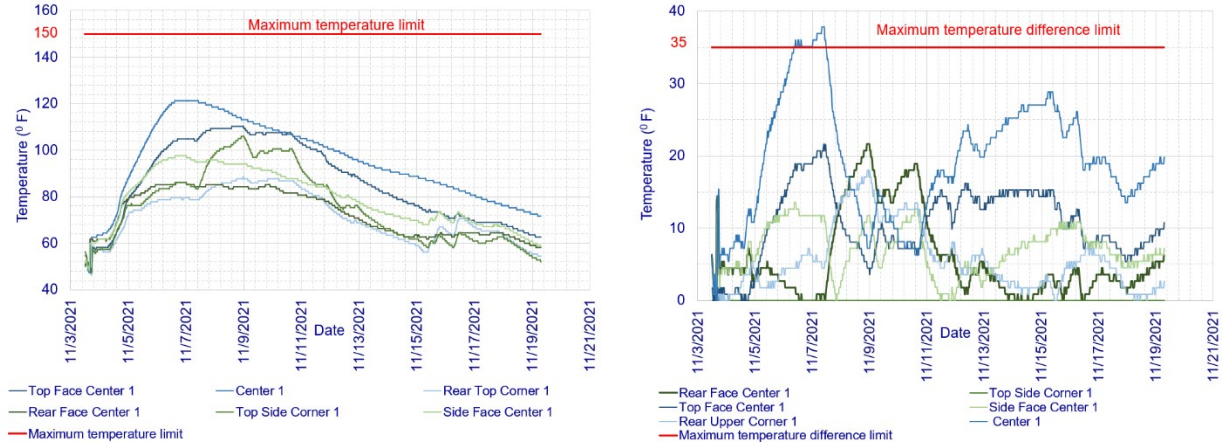

(a) Temperature (b) Temperature difference

Figure G-5. (a) Temperature and (b) temperature difference measured.

G.6 Thermal Monitoring Data in the Upper Southeast (SE) Knuckle

Figure G-6 shows the temperature and temperature difference measured in the upper part of the SE knuckle using thermal sensors. Temperature data collected from the VWGs at TG-1 for the upper SE knuckle are also shown. The maximum temperature measured in the upper SE knuckle is less than 150° F, and the maximum temperature difference is less than 35° F.

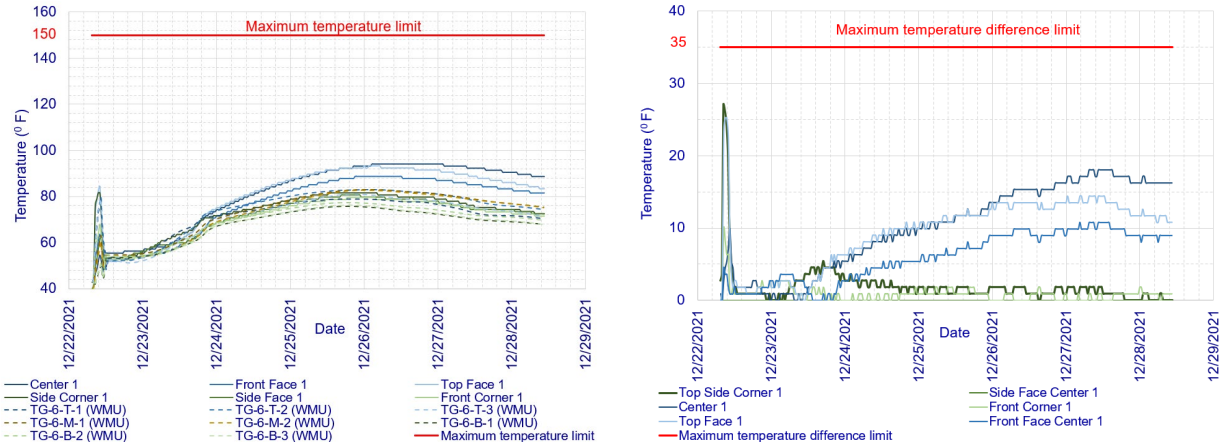

(a) Temperature (b) Temperature difference

Figure G-6. (a) Temperature and (b) temperature difference.

G.7 Thermal Monitoring Data in the Lower Northeast (NE) Knuckle

Figure G-7 shows the temperature and temperature difference measured in the lower part of the NE knuckle using thermal sensors. The maximum temperature measured in the lower NE knuckle is less than 150° F, and the maximum temperature difference is less than 35° F.

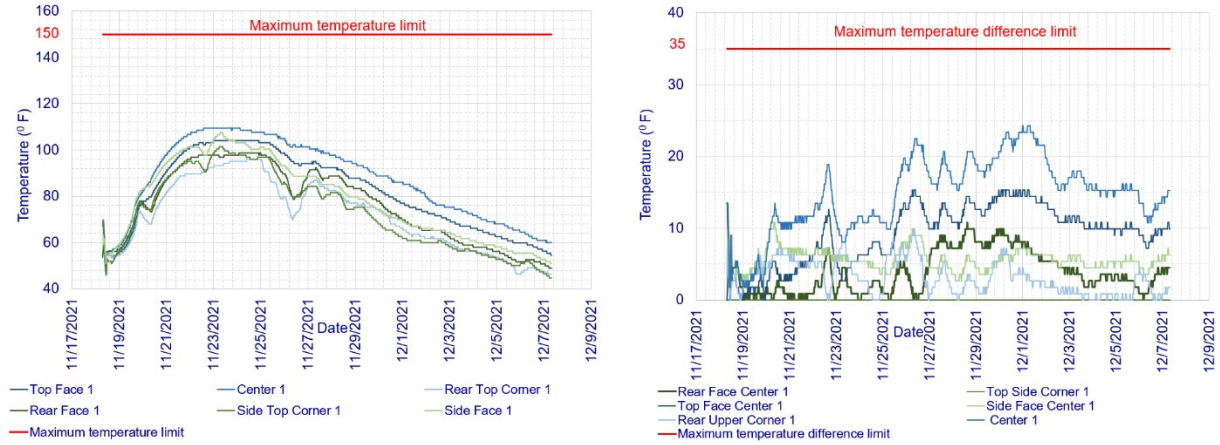

(a) Temperature (b) Temperature difference

Figure G-7. (a) Temperature and (b) temperature difference.

G.8 Thermal Monitoring Data in the Upper Northeast (NE) Knuckle

Figure G-8 shows the temperature and temperature difference measured in the upper part of the NE knuckle using thermal sensors. Temperature data collected from the VWGs at TG-5 for the upper NE knuckle are also shown. The maximum temperature measured in the upper NE knuckle is less than 150° F, and the maximum temperature difference is less than 35° F.

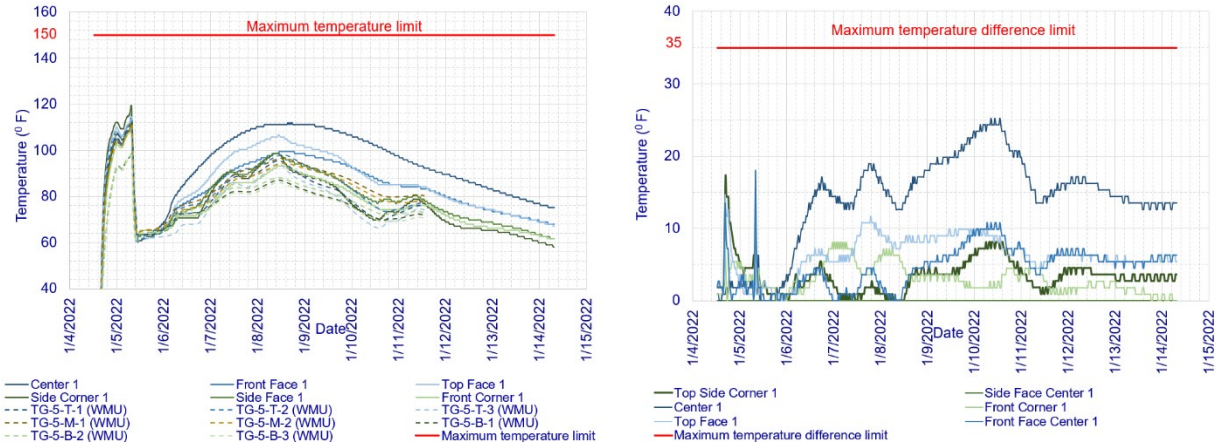

(a) Temperature (b) Temperature difference

Figure G-8. (a) Temperature and (b) temperature difference.

G.9 Thermal Monitoring Data in the West Tie Girder

Figure G-9 shows the temperature and temperature difference measured in the west tie girder using thermal sensors and VWGs. The thermal sensor in the west tie girder is located closer to TG-9 VWG locations. As shown in Figure G-9, the temperature data collected from the thermal sensors are in close agreement with the VWG temperature data for the west tie girder. The maximum temperature measured in the east tie girder is less than 150° F, and the maximum temperature difference in the east tie girder is less than 35° F.

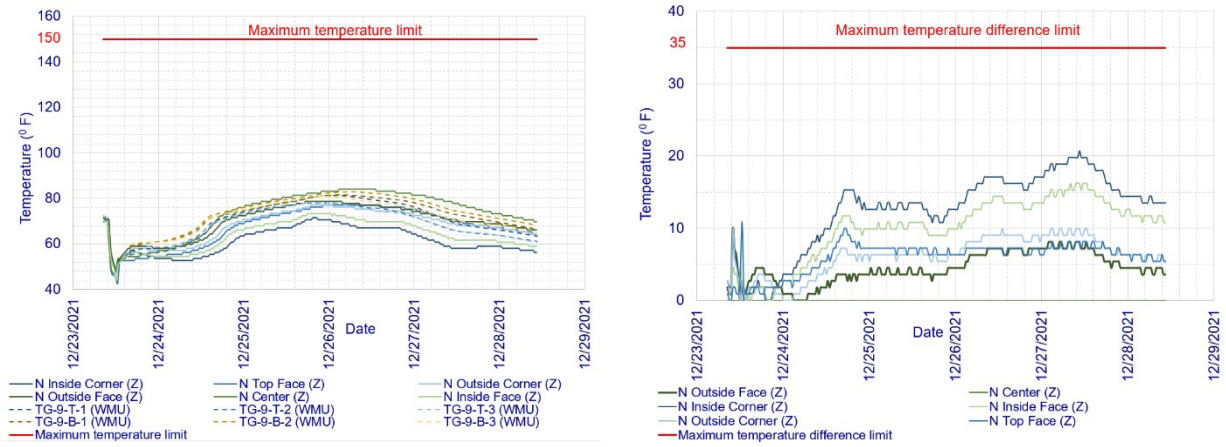

(a) Temperature (b) Temperature difference

Figure G-9. (a) Temperature and (b) temperature difference.

G.10 Thermal Monitoring Data in the East Tie Girder

Figure G-10 shows the temperature and temperature difference measured in the east tie girder using thermal sensors and VWGs. The thermal sensor in the east tie girder is located at the midpoint between the TG-2 and TG-3 VWG locations. As shown in Figure G-10, the temperature data collected from the thermal sensors are in close agreement with the VWG temperature data for the east tie girder. The maximum temperature measured in the east tie girder is less than 150° F, and the maximum temperature difference in the east tie girder is less than 35° F.

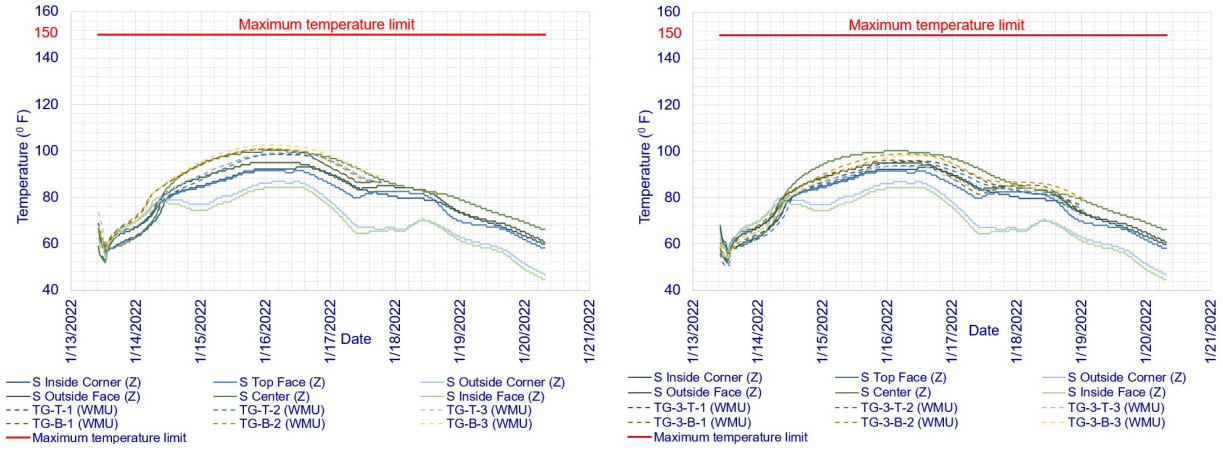

(a) Temperature – At TG-2

(b) Temperature difference – At TG-3

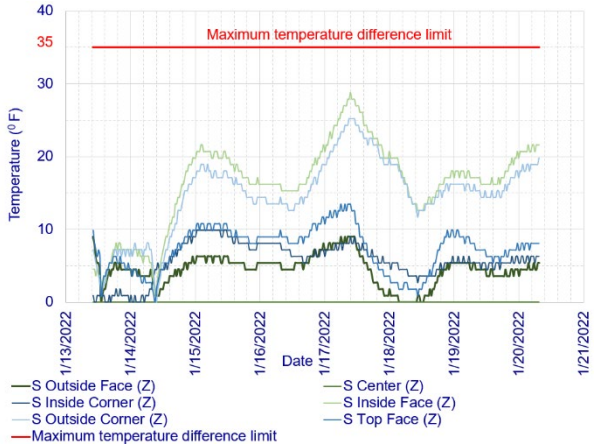

(c) Temperature difference

Figure G-10. (a) Temperature and (b) temperature difference.

G.11 Thermal Monitoring Data in the South End Diaphragm

Figure G-111 shows the temperature and temperature difference measured in the south end diaphragm using thermal sensors and VWGs. Thermal sensors were installed at two locations in the north end diaphragm: one at one-third of the diaphragm span and the other at two-thirds of the diaphragm span. However, only one set of thermal sensor data is available, and the corresponding sensor location is unknown. Therefore, the temperature data recorded at the TG-12 VWG location were used for comparison with the thermal sensor data. The results indicate that the maximum temperature measured in the west tie girder is less than 150° F and that the maximum temperature difference measured in the north end diaphragm is less than 35° F.

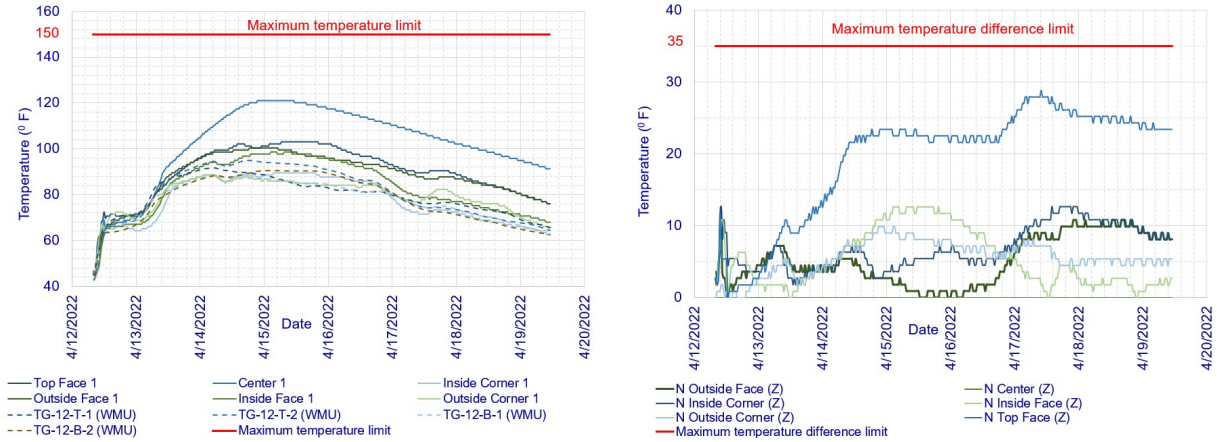

(a) Temperature (b) Temperature difference

Figure G-11. (a) Temperature and (b) temperature difference.

G.12 Thermal Monitoring Data in the North End Diaphragm

Figure G-12 shows the temperature and temperature difference measured in the north end diaphragm using thermal sensors and VWGs. Thermal sensors were installed at two locations in the north end diaphragm: one at one-third of the diaphragm span and the other at two-thirds of the diaphragm span. However, only one set of thermal sensor data is available, and the corresponding sensor location is unknown. Therefore, the temperature data recorded at the TG-15 VWG location were used for comparison with the thermal sensor data. The results indicate that the maximum temperature measured in the west tie girder is less than 150° F and that the maximum temperature difference measured in the north end diaphragm is less than 35° F.

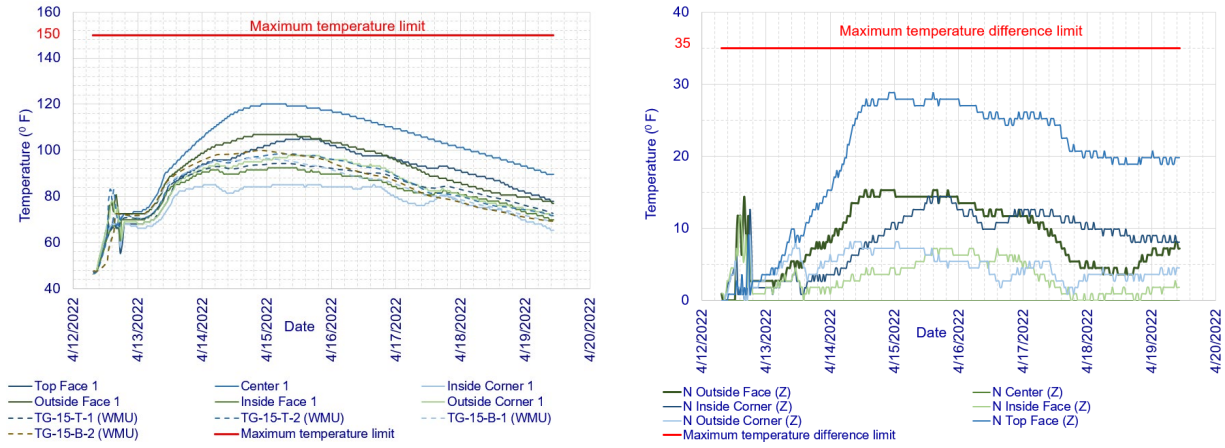

(a) Temperature (b) Temperature difference

Figure G-12. (a) Temperature and (b) temperature difference.

APPENDIX H

OPERATIONAL LIMITS FOR THE BRIDGE

H.1 Stresses in the Knuckles at the End of Construction

Table H-1. Change in Strain at TG-1 Sensor Location Due to Static Loads

Activity	Strain Change (με)							
	TG-1-T-1	TG-1-T-2	TG-1-T-3	TG-1-M-1	TG-1-M-2	TG-1-B-1	TG-1-B-2	TG-1-B-3
Anchor rod tensioning	-105.081	-129.639	-159.359	-145.397	-84.622	-127.553	-58.755	-77.453
End of construction	-358.537	-351.001	-334.579	-326.736	-335.098	-312.070	-307.336	-338.390

Table H-2. Change in Strain at TG-5 Sensor Location Due to Static Loads

Activity	Strain Change (με)							
	TG-5-T-1	TG-5-T-2	TG-5-T-3	TG-5-M-1	TG-5-M-2	TG-5-B-1	TG-5-B-2	TG-5-B-3
Anchor rod tensioning	-137.357	-90.766	-168.646	-127.810	-151.263	-78.437	-55.042	-49.777
End of construction	-139.956	-261.209	-149.057	-130.584	-153.147	-112.917	-121.245	-135.619

Table H.-3. Change in Strain at TG-6 Sensor Location Due to Static Loads

Activity	Strain Change (με)							
	TG-6-T-1	TG-6-T-2	TG-6-T-3	TG-6-M-1	TG-6-M-2	TG-6-B-1	TG-6-B-2	TG-6-B-3
Anchor rod tensioning	-124.159	-119.981	-127.505	-90.367	-84.660	-26.219	-52.415	-47.951
End of construction	-172.012	-190.154	-150.729	-123.793	-150.129	-85.702	-143.979	-111.973

Table H-4. Change in Strain at TG-10 Sensor Location Due to Static Loads

Activity	Strain Change (με)							
	TG-10-T-1	TG-10-T-2	TG-10-T-3	TG-10-M-1	TG-10-M-2	TG-10-B-1	TG-10-B-2	TG-10-B-3
Anchor rod tensioning	-138.924	-295.254	-135.337	-124.133	-448.955	-428.732	-397.578	-453.693
End of construction	-135.936	-1128.292	-155.659	-136.343	-464.233	-420.214	-500.918	-397.984

Table H-5. Stresses at TG-1 Sensor Location Due to Static Loads

Activity	MOE (ksi)	Stress Developed at TG-1 Cross Section Due to Construction Activity (psi)							
		TG-1-T-1	TG-1-T-2	TG-1-T-3	TG-1-M-1	TG-1-M-2	TG-1-B-1	TG-1-B-2	TG-1-B-3
Anchor rod tensioning	5851	-743	-297	-752	-711	-611	-358	-343	-272
End of construction	6542	-1034	-1607	-987	-818	-703	-700	-754	-602
Total Stress at the end of Construction		**-1777**	**-1904**	**-1739**	**-1529**	**-1314**	**-1058**	**-1097**	**-874**

Table H-6. Stresses at TG-5 Sensor Location Due to Static Loads

Activity	MOE (ksi)	Stress Developed at TG-5 Cross Section Due to Construction Activity (psi)							
		TG-5-T-1	TG-5-T-2	TG-5-T-3	TG-5-M-1	TG-5-M-2	TG-5-B-1	TG-5-B-2	TG-5-B-3
Anchor rod tensioning	5851	-804	-531	-987	-748	-885	-459	-322	-291
End of construction	6542	-916	-1709	-975	-854	-1002	-739	-793	-887
Total Stress at the end of Construction		**-1719**	**-2240**	**-1962**	**-1602**	**-1887**	**-1198**	**-1115**	**-1178**

Table H-7. Stresses at TG-6 Sensor Location Due to Static Loads

Activity	MOE (ksi)	Stress Developed at TG-6 Cross Section Due to Construction Activity (psi)							
		TG-6-T-1	TG-6-T-2	TG-6-T-3	TG-6-M-1	TG-6-M-2	TG-6-B-1	TG-6-B-2	TG-6-B-3
Anchor rod tensioning	6990	-868	-839	-891	-632	-592	-183	-366	-335
End of construction	7422	-1277	-1411	-1119	-919	-1114	-636	-1069	-831
Total Stress at the end of Construction		**-2145**	**-2250**	**-2010**	**-1550**	**-1706**	**-819**	**-1435**	**-1166**

Table H-8. Stresses at TG-10 Sensor Location Due to Static Loads

Activity	MOE (ksi)	Stress Developed at TG-6 Cross Section Due to Construction Activity (psi)							
		TG-10-T-1	TG-10-T-2	TG-10-T-3	TG-10-M-1	TG-10-M-2	TG-10-B-1	TG-10-B-2	TG-10-B-3
Anchor rod tensioning	6990	-971	-2064	-946	-868	-3138	-2997	-2779	-3171
End of construction	7422	-1009	-8374	-1155	-1012	-3446	-3119	-3718	-2954
Total Stress at the end of Construction		**-1980**	**-10438**	**-2101**	**-1880**	**-6584**	**-6116**	**-6497**	**-6125**

H.2 Stresses in the PT Tie Girders at the End of Construction

Table H-9. Change in Strain at TG-2 Sensor Location Due to Static Loads

Activity	Strain Change (με)					
	TG-2-T-1	TG-2-T-2	TG-2-T-3	TG-2-B-1	TG-2-B-2	TG-2-B-3
Stage 1-1 post-tensioning	-131.778	-121.519	-108.407	-96.127	-60.451	-72.734
Stage 1-2 post-tensioning	-299.771	-297.516	-345.884	-337.184	-334.679	-354.835
Deck pour E1, E2, E3, E4, E5, and E6	44.149	44.700	49.299	53.753	55.621	51.449
Stage 2 post-tensioning	-251.307	-265.688	-299.585	-299.613	-298.786	-321.167
Deck pour A1, A2, B1, B2, D1, and D2	45.011	37.145	41.566	73.644	69.306	53.328
Deck pour D3, D4, D5, and D6	19.666	42.613	33.842	9.888	11.315	9.095
West sidewalk- pour B, C, D, E, and S	22.309	39.102	34.770	22.944	21.666	22.249
East sidewalk- pour H, J, K, L, and T	32.803	51.171	43.559	32.468	32.904	29.810
West sacrificial nosing- pour U	-13.753	-30.840	-25.130	-16.238	-10.575	-13.829
East sacrificial nosing- pour U	-126.952	-59.835	28.266	-98.073	29.890	36.325
West side barrier railing construction West planter boxes- pour R	Data were not recorded for these activities[1].					
East side barrier railing construction	54.754	52.632	14.106	27.467	25.594	-16.506
East planter boxes- pour R	8.576	8.368	4.687	10.614	8.354	8.958
Plinths on the east side	46.581	48.490	17.447	23.795	27.501	17.342
Plinths on the west side	46.852	50.187	30.983	22.827	12.359	6.050
Low-profile center median construction	44.093	43.366	24.202	19.477	11.441	5.478

[1] Data was not recorded in the east tie girder sensors (i.e., TG-2, TG-3, and TG-4) during the west side barrier construction and west planter box construction due to an issue with the *slave node*. However, similar activity on the east side caused tension in the west tie girder, with magnitudes ranging from 78 to 306 psi, and reduced the overall compression stress. Therefore, removing this from the calculations provides an upper bound for the compression.

Additionally, in these calculations, the small tension values generated during hanger tensioning were neglected.

Table H-10. Change in Strain at TG-3 Sensor Location Due to Static Loads

Activity	Strain Change (με)							
	TG-3-T-1	TG-3-T-2	TG-3-T-3	TG-3-M-1	TG-3-M-2	TG-3-B-1	TG-3-B-2	TG-3-B-3
Stage 1-1 post-tensioning	-105.081	-129.639	-159.359	-145.397	-84.622	-127.553	-58.755	-77.453
Stage 1-2 post-tensioning	-358.537	-351.001	-334.579	-326.736	-335.098	-312.070	-307.336	-338.390
Deck pour E1, E2, E3, E4, E5, and E6	63.840	57.962	42.299	51.758	57.325	62.473	51.455	60.735
Stage 2 post-tensioning	-286.975	-288.521	-284.267	-303.309	-293.854	-307.695	-294.119	-307.938
Deck pour A1, A2, B1, B2, D1, and D2	61.316	44.631	41.099	50.984	56.713	61.247	61.130	66.665
Deck pour D3, D4, D5, and D6	34.286	40.197	15.247	9.027	12.552	14.107	8.111	10.147
West sidewalk- pour B, C, D, E, and S	36.668	40.187	19.541	19.038	24.276	23.292	14.833	15.139
East sidewalk- pour H, J, K, L, and T	48.449	52.013	32.808	30.728	37.001	28.463	33.586	35.295
West sacrificial nosing- pour U	-26.938	-31.833	-14.776	-15.178	-17.952	-12.540	-11.721	-14.850
East sacrificial nosing- pour U	29.077	-74.372	-144.258	-140.282	27.904	-100.748	29.136	40.911
West side barrier railing construction West planter boxes- pour R	Data was not recorded for these activities.							
East side barrier railing construction	18.883	49.856	51.041	55.769	16.351	18.162	31.039	34.000
East planter boxes- pour R	5.746	8.441	8.742	9.752	5.977	9.607	6.156	9.811
Plinths on the east side	22.292	46.746	42.333	40.868	11.074	13.726	32.156	28.238
Plinths on the west side	33.600	45.658	43.716	43.372	24.032	18.441	13.223	3.074
Low-profile center median construction	26.610	41.192	41.863	41.838	18.783	16.534	8.646	6.653

Table H-11. Change in Strain at TG-4 Sensor Location Due to Static Loads

Activity	Strain Change (με)					
	TG-4-T-1	TG-4-T-2	TG-4-T-3	TG-4-B-1	TG-4-B-2	TG-4-B-3
Stage 1-1 post-tensioning	-142.839	-122.735	-99.891	-115.120	-63.844	-78.984
Stage 1-2 post-tensioning	-283.636	-304.517	-361.557	-291.946	-340.156	-370.805
Deck pour E1, E2, E3, E4, E5, and E6	36.053	49.935	54.452	62.574	53.497	52.428
Stage 2 post-tensioning	-244.012	-270.485	-316.932	-301.352	-311.937	-338.125
Deck pour A1, A2, B1, B2, D1, and D2	34.045	36.075	41.371	78.922	72.210	61.559
Deck pour D3, D4, D5, and D6	10.827	37.650	28.997	15.472	8.889	8.072
West sidewalk- pour B, C, D, E, and S	11.978	30.588	29.594	25.023	17.566	17.740
East sidewalk- pour H, J, K, L, and T	25.807	42.602	42.738	29.880	39.109	35.410
West sacrificial nosing- pour U	-20.813	-23.029	-20.031	-18.223	-11.617	-14.641
East sacrificial nosing- pour U	-126.703	-47.636	34.859	-111.647	33.799	41.967
West side barrier railing construction	Data was not recorded for these activities.					
West planter boxes- pour R						
East side barrier railing construction	46.349	47.458	15.614	17.102	35.459	21.712
East planter boxes- pour R	6.241	5.531	5.311	8.741	9.076	7.865
Plinths on the east side	36.098	40.851	19.895	18.715	31.850	9.235
Plinths on the west side	34.099	39.696	29.807	10.637	22.940	2.987
Low-profile center median construction	34.749	36.332	24.297	12.082	15.553	2.657

Table H-12. Change in Strain at TG-9 Sensor Location Due to Static Loads

Activity	Strain Change (με)					
	TG-9-T-1	TG-9-T-2	TG-9-T-3	TG-9-B-1	TG-9-B-2	TG-9-B-3
Stage 1-1 post-tensioning	-154.095	-101.783	-95.324	-130.698	-55.222	-71.789
Stage 1-2 post-tensioning	-321.493	-304.382	-288.082	-307.074	-317.258	-276.460
Deck pour E1, E2, E3, E4, E5, and E6	45.563	37.039	60.731	50.825	47.186	94.610
Stage 2 post-tensioning	-315.563	-275.163	-285.178	-348.042	-321.674	-325.553
Deck pour A1, A2, B1, B2, D1, and D2	46.847	39.686	51.176	85.839	93.217	97.101
Deck pour D3, D4, D5, and D6	15.690	17.284	5.941	5.230	4.961	10.780
West sidewalk- pour B, C, D, E, and S	52.364	50.240	40.935	39.601	35.184	77.085
East sidewalk- pour H, J, K, L, and T	37.618	40.906	68.006	18.597	21.222	77.582
West sacrificial nosing- pour U	45.608	-45.641	-129.192	54.780	28.807	-123.081
East sacrificial nosing- pour U	4.514	5.728	5.165	8.298	9.074	6.485
West side barrier railing construction	7.960	9.141	10.041	11.291	11.868	11.574
West planter boxes- pour R	13.211	21.393	21.257	13.836	12.733	14.672
East side barrier railing construction	14.918	35.205	37.573	18.869	21.913	14.477
East planter boxes- pour R	5.109	6.068	6.073	5.970	4.335	4.282
Plinths on the east side	24.190	41.089	43.690	17.676	22.704	22.657
Plinths on the west side	33.488	42.209	42.741	9.065	13.378	27.919
Low-profile center median construction	30.109	40.191	38.350	6.925	12.249	19.145

Table H-13. Stresses at TG-2 Sensor Location Due to Static Loads

Activity	MOE (ksi)	Stress Developed at TG-2 Cross Section Due to Construction Activity (psi)					
		TG-2-T-1	TG-2-T-2	TG-2-T-3	TG-2-B-1	TG-2-B-2	TG-2-B-3
Stage 1-1 post-tensioning	6990	-921	-849	-758	-672	-423	-508
Stage 1-2 post-tensioning	7422	-2225	-2208	-2567	-2503	-2484	-2634
Deck pour E1, E2, E3, E4, E5, and E6		328	332	366	399	413	382
Stage 2 post-tensioning		-1865	-1972	-2224	-2224	-2218	-2384
Deck pour A1, A2, B1, B2, D1, and D2		334	276	309	547	514	396
Deck pour D3, D4, D5, and D6		146	316	251	73	84	68
West sidewalk- pour B, C, D, E, and S		166	290	258	170	161	165
East sidewalk- pour H, J, K, L, and T		243	380	323	241	244	221
West sacrificial nosing- pour U		-102	-229	-187	-121	-78	-103
East sacrificial nosing- pour U		-942	-444	210	-728	222	270
West side barrier railing construction		Data was not recorded for these activities.					
West planter boxes- pour R							
East side barrier railing construction		406	391	105	204	190	-123
East planter boxes- pour R		64	62	35	79	62	66
Plinths on the east side		346	360	129	177	204	129
Plinths on the west side		348	372	230	169	92	45
Low-profile center median construction		327	322	180	145	85	41
Total Stress at the end of Construction		**-3348**	**-2602**	**-3340**	**-4043**	**-2932**	**-3969**

Table H-14. Stresses at TG-3 Sensor Location Due to Static Loads

Activity	MOE (ksi)	Stress Developed at TG-3 Cross Section Due to Construction Activity (psi)							
		TG-3-T-1	TG-3-T-2	TG-3-T-3	TG-3-M-1	TG-3-M-2	TG-3-B-1	TG-3-B-2	TG-3-B-3
Stage 1-1 post-tensioning	6990	-735	-906	-1114	-1016	-592	-892	-411	-541
Stage 1-2 post-tensioning	7422	-2661	-2605	-2483	-2425	-2487	-2316	-2281	-2512
Deck pour E1, E2, E3, E4, E5, and E6		474	430	314	384	425	464	382	451
Stage 2 post-tensioning		-2130	-2141	-2110	-2251	-2181	-2284	-2183	-2286
Deck pour A1, A2, B1, B2, D1, and D2		455	331	305	378	421	455	454	495
Deck pour D3, D4, D5, and D6		254	298	113	67	93	105	60	75
West sidewalk- pour B, C, D, E, and S		272	298	145	141	180	173	110	112
East sidewalk- pour H, J, K, L, and T		360	386	243	228	275	211	249	262
West sacrificial nosing- pour U		-200	-236	-110	-113	-133	-93	-87	-110
East sacrificial nosing- pour U		216	-552	-1071	-1041	207	-748	216	304
West side barrier railing construction		Data was not recorded for these activities.							
West planter boxes- pour R									
East side barrier railing construction		140	370	379	414	121	135	230	252
East planter boxes- pour R		43	63	65	72	44	71	46	73
Plinths on the east side		165	347	314	303	82	102	239	210
Plinths on the west side		249	339	324	322	178	137	98	23
Low-profile center median construction		197	306	311	311	139	123	64	49
Total Stress at the end of Construction		**-2899**	**-3273**	**-4374**	**-4225**	**-3226**	**-4358**	**-2813**	**-3143**

Table H-15. Stresses at TG-4 Sensor Location Due to Static Loads

Activity	MOE (ksi)	Stress Developed at TG-4 Cross Section Due to Construction Activity (psi)					
		TG-4-T-1	TG-4-T-2	TG-4-T-3	TG-4-B-1	TG-4-B-2	TG-4-B-3
Stage 1-1 post-tensioning	6990	-998	-858	-698	-805	-446	-552
Stage 1-2 post-tensioning	7422	-2105	-2260	-2683	-2167	-2525	-2752
Deck pour E1, E2, E3, E4, E5, and E6		268	371	404	464	397	389
Stage 2 post-tensioning		-1811	-2008	-2352	-2237	-2315	-2510
Deck pour A1, A2, B1, B2, D1, and D2		253	268	307	586	536	457
Deck pour D3, D4, D5, and D6		80	279	215	115	66	60
West sidewalk- pour B, C, D, E, and S		89	227	220	186	130	132
East sidewalk- pour H, J, K, L, and T		192	316	317	222	290	263
West sacrificial nosing- pour U		-154	-171	-149	-135	-86	-109
East sacrificial nosing- pour U		-940	-354	259	-829	251	311
West side barrier railing construction		Data was not recorded for these activities.					
West planter boxes- pour R							
East side barrier railing construction		344	352	116	127	263	161
East planter boxes- pour R		46	41	39	65	67	58
Plinths on the east side		268	303	148	139	236	69
Plinths on the west side		253	295	221	79	170	22
Low-profile center median construction		258	270	180	90	115	20
Total Stress at the end of Construction		**-3959**	**-2928**	**-3456**	**-4100**	**-2849**	**-3981**

Table H-16. Stresses at TG-9 Sensor Location Due to Static Loads

Activity	MOE (ksi)	Stress Developed at TG-9 Cross Section Due to Construction Activity (psi)					
		TG-9-T-1	TG-9-T-2	TG-9-T-3	TG-9-B-1	TG-9-B-2	TG-9-B-3
Stage 1-1 post-tensioning	5821	-897	-592	-555	-761	-321	-418
Stage 1-2 post-tensioning	6406	-2059	-1950	-1845	-1967	-2032	-1771
Deck pour E1, E2, E3, E4, E5, and E6		292	237	389	326	302	606
Stage 2 post-tensioning	6542	-2064	-1800	-1866	-2277	-2104	-2130
Deck pour A1, A2, B1, B2, D1, and D2		306	260	335	562	610	635
Deck pour D3, D4, D5, and D6		103	113	39	34	32	71
West sidewalk- pour B, C, D, E, and S		343	329	268	259	230	504
East sidewalk- pour H, J, K, L, and T		246	268	445	122	139	508
West sacrificial nosing- pour U		298	-299	-845	358	188	-805
East sacrificial nosing- pour U		30	37	34	54	59	42
West side barrier railing construction		52	60	66	74	78	76
West planter boxes- pour R		86	140	139	91	83	96
East side barrier railing construction		98	230	246	123	143	95
East planter boxes- pour R		33	40	40	39	28	28
Plinths on the east side		158	269	286	116	149	148
Plinths on the west side		219	276	280	59	88	183
Low-profile center median construction		197	263	251	45	80	125
Total Stress at the end of Construction		**-2560**	**-2120**	**-2295**	**-2743**	**-2248**	**-2007**

H.3 Stresses in the PT End Diaphragms at the End of Construction

Table H-17. Change in Strain at TG-11 Sensor Location Due to Static Loads

Activity	Strain Change (με)			
	TG-11-T-1	TG-11-T-2	TG-11-B-1	TG-11-B-2
End of post-tensioning	-433.094	-298.492	-400.244	-277.455
End of construction	-42.581	-197.423	57.369	-50.595

Table H-18. Change in Strain at TG-12 Sensor Location Due to Static Loads

Activity	Strain Change (με)			
	TG-12-T-1	TG-12-T-2	TG-12-B-1	TG-12-B-2
End of post-tensioning	-400.225	-226.603	-500.639	-330.897
End of construction	-97.985	-183.925	111.776	-46.742

Table H-19. Change in Strain at TG-13 Sensor Location Due to Static Loads

Activity	Strain Change (με)			
	TG-13-T-1	TG-13-T-2	TG-13-B-1	TG-13-B-2
End of post-tensioning	-445.018	-300.180	-409.053	-240.730
End of construction	-25.720	-116.696	27.249	-83.480

Table H-20. Change in Strain at TG-14 Sensor Location Due to Static Loads

Activity	Strain Change (με)			
	TG-14-T-1	TG-14-T-2	TG-14-B-1	TG-14-B-2
End of post-tensioning	-316.287	-403.862	-277.915	-376.357
End of construction	-108.546	-64.754	-79.769	3.629

Table H-21. Change in Strain at TG-15 Sensor Location Due to Static Loads

Activity	Strain Change (με)			
	TG-15-T-1	TG-15-T-2	TG-15-B-1	TG-15-B-2
End of post-tensioning	-248.007	-345.274	-388.481	-469.217
End of construction	-220.009	-59.845	-21.523	44.230

Table H-22. Change in Strain at TG-16 Sensor Location Due to Static Loads

Activity	Strain Change (με)			
	TG-16-T-1	TG-16-T-2	TG-16-B-1	TG-16-B-2
End of post-tensioning	-280.710	-424.446	-259.397	-392.155
End of construction	-96.852	-24.907	-46.119	7.075

Table H-23. Stresses at TG-11 Sensor Location Due to Static Loads

Activity	MOE (ksi)	Stress Developed at TG-11 Cross Section Due to Construction Activity (psi)			
		TG-11-T-1	TG-11-T-2	TG-11-B-1	TG-11-B-2
End of post-tensioning	6990	-3027	-2086	-2798	-1939
End of construction	7422	-316	-1465	426	-376
Total Stress at the end of Construction		**-3343**	**-3552**	**-2372**	**-2315**

Table H-24. Stresses at TG-12 Sensor Location Due to Static Loads

Activity	MOE (ksi)	Stress Developed at TG-12 Cross Section Due to Construction Activity (psi)			
		TG-12-T-1	TG-12-T-2	TG-12-B-1	TG-12-B-2
End of post-tensioning	6990	-2798	-1584	-3499	-2313
End of construction	7422	-727	-1365	830	-347
Total Stress at the end of Construction		**-3525**	**-2949**	**-2670**	**-2660**

Table H-25. Stresses at TG-13 Sensor Location Due to Static Loads

Activity	MOE (ksi)	Stress Developed at TG-13 Cross Section Due to Construction Activity (psi)			
		TG-13-T-1	TG-13-T-2	TG-13-B-1	TG-13-B-2
End of post-tensioning	6990	-3111	-2098	-2859	-1683
End of construction	7422	-191	-866	202	-620
Total Stress at the end of Construction		**-3302**	**-2964**	**-2657**	**-2302**

Table H-26. Stresses at TG-14 Sensor Location Due to Static Loads

Activity	MOE (ksi)	Stress Developed at TG-14 Cross Section Due to Construction Activity (psi)			
		TG-14-T-1	TG-14-T-2	TG-14-B-1	TG-14-B-2
End of post-tensioning	6990	-2211	-2823	-1943	-2631
End of construction	7422	-806	-481	-592	27
Total Stress at the end of Construction		**-3016**	**-3304**	**-2535**	**-2604**

Table H-27. Stresses at TG-15 Sensor Location Due to Static Loads

Activity	MOE (ksi)	Stress Developed at TG-15 Cross Section Due to Construction Activity (psi)			
		TG-15-T-1	TG-15-T-2	TG-15-B-1	TG-15-B-2
End of post-tensioning	6990	-1734	-2413	-2715	-3280
End of construction	7422	-1633	-444	-160	328
Total Stress at the end of Construction		**-3366**	**-2858**	**-2875**	**-2952**

Table H-28. Stresses at TG-16 Sensor Location Due to Static Loads

Activity	MOE (ksi)	Stress Developed at TG-16 Cross Section Due to Construction Activity (psi)			
		TG-16-T-1	TG-16-T-2	TG-16-B-1	TG-16-B-2
End of post-tensioning	6990	-1962	-2967	-1813	-2741
End of construction	7422	-719	-185	-342	53
Total Stress at the end of Construction		**-2681**	**-3152**	**-2155**	**-2689**